UNIVERSITY OF BELGRADE

FACULTY OF CHEMISTRY

Ljubica D. Anđelković

THEORETICAL INVESTIGATION OF THE JAHN-TELLER EFFECT AND THE INFLUENCE OF THE JAHN-TELLER DISTORTION ON THE PROPERTIES OF CHEMICAL SYSTEMS

Doctoral Dissertation

Belgrade, 2015

UNIVERZITET U BEOGRADU

HEMIJSKI FAKULTET

Ljubica D. Anđelković

TEORIJSKO PROUČAVANJE *JAHN-TELLER*-OVOG EFEKTA I NJEGOVOG UTICAJA NA OSOBINE HEMIJSKIH SISTEMA

doktorska disertacija

Beograd, 2015

Supervisors

_____

Dr Maja Gruden-Pavlović, associate professor
Faculty of Chemistry, University of Belgrade

_____

Dr Matija Zlatar, assistant research professor
Center for Chemistry, Institute of Chemistry, Technology and Metallurgy, University of Belgrade

Committee members

_____

Dr Pablo García-Fernández, assistant research professor
Universidad de Cantabria, Departamento CITIMAC, Santander, Cantabria (Spain)

_____

Dr Miloš Milčić, associate professor
Faculty of Chemistry, University of Belgrade

Date _____.

Acknowledgements

This thesis was conceived and conducted at the Faculty of Chemistry, University of Belgrade (Department of General and Inorganic Chemistry). The subject for this thesis was proposed by Dr Maja Gruden-Pavlović, Associate Professor at the Faculty of Chemistry, University of Belgrade and Dr Matija Zlatar, Assistant Research Professor at the Center for Chemistry, Institute of Chemistry, Technology and Metallurgy, University of Belgrade.

I would like to gratefully and sincerely thank Dr Maja Gruden-Pavlović and Dr Matija Zlatar for their guidance, understanding, patience, and most importantly, their friendship. Their mentorship was paramount in providing a well-rounded experience consistent my long-term career goals. They encouraged me to not only grow as a computational chemist but also as an independent researcher.

I would like to thank Dr Pablo García-Fernández for his assistance and guidance in getting a wider breadth of experience, valuable discussions and accessibility. I would also like to acknowledge Dr Miloš Milčić, who has been a source of encouragement, not only during this thesis project but also during my undergraduate studies. I am gratefully indebted to them for their precious comments on this thesis.

Many thanks to Dr Comandante Saša, Dr Badža, Dr Makijaveli, Dr in spec. Stepinac, Filip and Milena for their concern and enthusiasm in the past years. These friends and co-workers also provided for some much needed humor and entertainment in what could have otherwise been a somewhat stressful laboratory environment. It was fundamental in supporting me during these difficult moments. "I think this is the beginning of a beautiful friendship."

I would also like to thank Boža and Milica for valuable help in the technical editting of this thesis.

My gratitude goes to Nick Vlastaras who patiently revised and corrected English in my thesis. Thanks to him this thesis attained an "English shape".

I must express my profound gratefulness to my parents for providing me with unconditional support, unflagging love and continuous encouragement throughout my life and my years of study. This achievement would not have been possible without them. Thank you.

I would like to thank Krikor for believing in me and supporting me. His encouragement and tolerance were undeniably a testament of his unyielding devotion.

This thesis is dedicated to my son Dragutin, for whom it has become a necessity.

Theoretical investigation of the Jahn-Teller effect and the influence of the Jahn-Teller distortion on the properties of chemical systems

SUMMARY

Quantum mechanical description of the changes in electronic structure due to distortions in molecular shape and vice versa is given in the form of the vibronic coupling theory. Probably, the most famous concept based on this theory is the Jahn−Teller (JT) effect. The JT theorem states that a molecule with a degenerate electronic state spontaneously distorts along a non-totally symmetric vibrational coordinates. This removes the degeneracy and lowers the energy. In fact, the vibronic coupling, correlation between electronic states and vibrational motion of nuclei, describes all spontaneous symmetry breaking distortions, attributed to the JT, Renner-Teller and pseudo JT effects. The consequences of the JT effect are far-reaching. JT effect affects the high magneto-resistance in manganites, superconductivity in fullerides, aromaticity, molecular stereochemistry, reactivity, magnetic properties of molecules, as well as many other properties. It should be emphasized that the JT effect has inspired very significant scientific discoveries, e.g. the concept of high-temperature superconductivity. The significance of the JT effect is increasingly recognized, hence, quantifying the distortion and getting insight into the mechanism lies at the heart of modern investigations. In this thesis, the JT effect and its consequences on the structure and properties of organic and inorganic molecules, aromaticity, excitonic coupling and excitation energy transfer are studied.

The JT effect was analyzed and the JT parameters were determined for the JT active cyclobutadienyl radical cation ($C_4H_4^{+\bullet}$), cyclopentadienyl radical ($C_5H_5^{\bullet}$), benzene cation ($C_6H_6^{+}$), benzene anion ($C_6H_6^{-}$), tropyl radical ($C_7H_7^{\bullet}$), anions and cations of corannulene and coronene ($C_{20}H_{10}^{-}$, $C_{20}H_{10}^{+}$, $C_{24}H_{12}^{-}$ and $C_{24}H_{12}^{+}$), small metal and metalloid clusters (Na_3, Ag_3, As_4^- , Sb_4^-), hexaflurocuprat(II) ion ($[CuF_6]^{4-}$), manganese chelate complex ($[Mn(acac)_3]$) and the organometallic compound cobaltocene ($CoCp_2$) by the means of

multideterminantal Density Functional Theory (DFT) approach. The validation of multideterminantal DFT method was performed by systematic investigation of the influence of the exchange-correlation functional (LDA, BP86, BLYP, OPBE and B3LYP) on the determination of the JT parameters and comparison with available data from the literature. JT distortion is a consequence of the electronic factors, but also essentially depends on the geometry of the investigated molecule. The choice of functional is directly associated with a specific chemical problem, however it is concluded that in the analysis of the JT distortion all used functionals give qualitatively satisfactory results.

The analysis of the multimode JT problem in As_4^- and Sb_4^-, $C_5H_5^{\bullet}$, $C_6H_6^+$, $C_6H_6^-$, $C_7H_7^{\bullet}$, $C_{20}H_{10}^-$, $C_{20}H_{10}^+$, $C_{24}H_{12}^-$ and $C_{24}H_{12}^+$ was performed by the means of the Intrinsic Distortion Path (IDP) model. All the required information, to calculate the vibronic coupling coefficients is contained in the minimum energy lower-symmetry structure. This structure is the real minimum on the potential energy surface, allowing normal mode analysis in the straightforward manner. The correlation of the normal modes in the minimum energy structure with the high symmetry normal modes according to the epikernel principle, has been described. With this model, it is possible to directly separate the contributions of the different normal modes to the JT distortion, their energy contributions to the JT stabilization energy along a relevant particular path of distortion and the forces responsible for the distortion, giving further insight into the origin and mechanism of the vibronic coupling. The distortion is always dominated by the modes that fulfill symmetry requirements, according to the JT theory. If there are several appropriate vibrations, harder modes will always be more important in the beginning of the distortion, because they reduce energy in the most efficient way, while the softer modes are important in the second part of the distortion, leading the molecule to the minimum energy conformation. Therefore, the importance of all JT active normal modes needs to be included in the analysis of the JT effect.

Thorough study of the influence of the JT distortions on the aromaticity is presently of the utmost importance due to the increasing development of material chemistry, for example considering magnetism and structure of graphenes. The aromaticity in $C_6H_6^+$, $C_6H_6^-$, $C_5H_5^{\bullet}$, $CoCp_2$, fullerene cation and anion, As_4^- and Sb_4^- is investigated. The changes of the most popular magnetic criteria, Nucleus-Independent Chemical Shifts

(NICS), were scanned along the particular path of distortion, IDP. The deeper inspection of the magnetic criteria along the IDP indicate that antiaromaticity decreases with increasing deviation from the high-symmetry to lower-symmetry point on the potential energy surface, for all investigated species. Thus, the JT effect can be surely considered as the unique mechanism of lowering the antiaromaticity. In order to fully understand the aromaticity of the JT active molecules, it is necessary to include detailed analysis of the JT effect. The analysis performed along the particular distortion path, IDP, enables predicting properties of many aromatic systems, from small organic and inorganic molecules, to fullerenes and complicated nano-structures.

The new model that combines excitonic coupling and molecular vibrations is developed, i.e. excitonic coupling is studied from the JT perspective. Excitonic coupling is analyzed in the model system – benzene dimer and the proposed model is validated. The purpose of the new developed model is to represent and predict the properties of coupled identical chromophores based on intrinsic features of the constituting monomers alone. Therefore, the new model is allowing to study much larger systems, relevant in the biology and technology. This approach, in the combination with the time-dependent DFT (TD-DFT) calculations, provides prediction of the properties of coupled chromophores with the high precision.

The results given in this thesis indicate that, in addition to the experimental techniques, quantum chemical methods based on the DFT play important role in the analysis and design of the systems with desired properties. Detailed analysis of the properties of molecules prone to the JT distortion by theoretical methods that reliably describe the JT effect, as well as the observed properties of molecular systems, is a way to a better understanding of the new materials.

Keywords: Jahn-Teller effect, Aromaticity, Excitonic coupling, Multideterminantal Density Functional Theory, Intrinsic Distortion Path (IDP), Vibronic model for excitonic coupling

Area of science: Chemistry

Sub-area of science: Inorganic chemistry

UDC number: 546

Teorijsko proučavanje *Jahn-Teller*-ovog efekta i njegovog uticaja na osobine hemijskih sistema

REZIME

Kvantno-mehanički opis promena u elektronskoj strukturi kao posledica distorzije molekula i obrnuto dat je u formi teorije vibronske sprege. *Jahn-Teller*-ov (JT) efekat je verovatno najpoznatiji koncept zasnovan na ovoj teoriji. Po JT teoremi svi nelinearni molekuli sa degenerisanim elektronskim stanjem spontano se distorguju duž vibracija koje nisu totalno simetrične, pri čemu dolazi do uklanjanja degeneracije uz sniženje energije.U stvari, vibronska sprega, korelacija između elektronskih stanja i pomeraja jezgara, opisuje sve spontane distorzije molekulskih sistema i odnosi se na JT efekat, *Renner-Teller*-ov efekat i pseudo JT efekat. Posledice JT efekta su dalekosežne. JT efekat utiče na visoku magneto-otpornost manganita, superprovodljivost fulerida, aromatičnost, stereohemiju molekula, reaktivnost, magnetne osobine molekula, kao i mnoge druge osobine. Treba istaći da je JT efekat inspirisao veoma značajna naučna otkrića, na primer, koncept visoko-temperaturne superprovodljivosti. Značaj JT efekta se sve više prepoznaje, stoga, kvantifikovanje distorzije i dobijanje uvida u njen mehanizam se nalazi u centru modernih istraživanja. U okviru ove teze, analiziran je JT efekat i njegove posledice na strukturu i osobine organskih i neorganskih molekula, aromatičnost, ekscitonsku spregu i prenos energije ekscitacije.

JT efekat je analiziran i izračunati su JT parametri za ciklobutadienil radikal katjon ($C_4H_4^{+\bullet}$), ciklopentadienil radikal ($C_5H_5^{\bullet}$), benzen katjon ($C_6H_6^{+}$), benzen anjon ($C_6H_6^{-}$), tropil radikal ($C_7H_7^{\bullet}$), anjone i katjone koranulena i koronena ($C_{20}H_{10}^{-}$, $C_{20}H_{10}^{+}$, $C_{24}H_{12}^{-}$ and $C_{24}H_{12}^{+}$), male metalne i metaloidne klastere (Na_3, Ag_3, As_4^-, Sb_4^-), heksafluorokuprat(II) jon ($[CuF_6]^{4-}$), helatni kompleks mangana ($[Mn(acac)_3]$) i organometalno jedinjenje kobaltocen ($CoCp_2$) primenom multideterminantne teorije funkcionala gustine (eng. *Density Functional Theory*, DFT). Validacija multideterminantnog DFT metoda je izvedena uz sistematsko ispitivanje uticaja različitih

DFT funkcionala (LDA, BP86, BLYP, OPBE i B3LYP) na izračunavanje JT parametara i poređenje sa dostupnim podacima iz literature. JT distorzija je posledica elektronskih faktora, ali takođe bitno zavisi i od geometrije ispitivanog molekula. Iako je izbor DFT funkcionala direktno povezan sa konkretnim hemijskim problemom, pri analizi JT distorzije, svi ispitivani funkcionali daju kvalitativno zadovoljavajuće rezultate.

Izvedena je analiza uticaja većeg broja vibracija odgovornih za distorziju molekula primenom modela Svojstvenog puta distorzije (eng. *Intrinsic Distortion Path*, IDP) u As_4^-, Sb_4^-, $C_5H_5^{\bullet}$, $C_6H_6^+$, $C_6H_6^-$, $C_7H_7^{\bullet}$, $C_{20}H_{10}^-$, $C_{20}H_{10}^+$, $C_{24}H_{12}^-$ i $C_{24}H_{12}^+$. Sve potrebne informacije pri izračunavanju koeficijenata vibronske sprege sadržane su u strukturi minimalne energije. Kod IDP modela referentna struktura je distorgovana, nisko-simetrična struktura minimalne energije, koja predstavlja pravi minimum na površini potencijalne energije, pa je vibraciona analiza jednoznačna. Opisan je i način korelacije normalnih modova u strukturi minimalne energije sa normalnim modovima u višoj simetriji, saglasno epikernel principu. Ovim modelom moguće je direktno odvojiti doprinose različitih vibracija JT distorziji, njihov energetski doprinos JT stabilizacionoj energiji duž puta distorzije i odrediti sile odgovorne za JT distorziju, dajući bolji uvid u poreklo i mehanizam vibronske sprege. Distorzija je uvek vođena vibracijama koje ispunjavaju simetrijske uslove na osnovu JT teoreme. Ako postoji više JT aktivnih vibracija, vibracije viših frekvencija dominiraju na početku distorzije jer snižavaju energiju molekula na najefikasniji način, dok su vibracije nižih frekvencija važne u drugom delu distorzije, vodeći molekul do konformacije minimalne energije. Dakle, u analizi JT efekta moraju se uključiti sve JT aktivne vibracije.

Zbog sve bržeg razvoja nauke o materijalima, ispitivanje uticaja JT efekta na aromatičnost je od sve većeg značaja, posmatrajući npr. magnetizam i strukturu grafena. Ispitivana je aromatičnost u $C_6H_6^+$, $C_6H_6^-$, $C_5H_5^{\bullet}$, $CoCp_2$, fuleren katjonu i anjonu, As_4^- i Sb_4^-. Promene hemijskih pomeranja nezavisnih od jezgra (NICS), kao najpopularnijeg magnetnog kriterijuma aromatičnosti, praćene su duž svojstvenog puta distorzije, IDP modela. Detaljna analiza magnetnog kriterijuma duž IDP modela ukazuje na antiaromatičnost ispitivanih vrsta, koja se smanjuje sa sniženjem simetrije na površini potencijalne energije. JT efekat se može zasigurno smatrati jedinstvenim mehanizmom sniženja antiaromatičnosti JT aktivnih molekula. Dakle, u cilju potpunog razumevanja aromatičnosti JT aktivnih molekula, neophodno je uključiti i detaljnu analizu JT efekta.

Analiza aromatičnosti izvedena duž svojstvenog puta distorzije omogućava predviđanja svojstava mnogih aromatičnih sistema, od malih organskih i neorganskih molekula, do fulerena i komplikovanih nano-struktura.

Razvijen je model koji kombinuje ekscitonsku spregu i molekulske vibracije, odnosno proučavana je ekscitonska sprega iz JT perspektive. Ekscitonsko kuplovanje je analizirano na model sistemu – dimeru benzena i izvedena je validacija razvijenog modela. Svrha razvijenog modela jeste da se razumeju i predvide osobine spregnutih hromofora preko svojstava monomerne jedinice. Dakle, novi model omogućava proučavanje većih sistema od velike biološke i tehnološke važnosti. Ovakav pristup, u kombinaciji sa proračunima koji se zasnivaju na vremenski zavisnoj DFT metodi (TD-DFT), omogućava predviđanja svojstava spregnutih hromofora sa velikom preciznošću.

Rezultati ove teze ukazuju da kvantno hemijske teorijske metode, bazirane na Teoriji funkcionala gustine, pored eksperimentalnih tehnika, imaju bitnu ulogu pri analizi i dizajnu molekulskih sistema sa željenim svojstvima. Detaljna analiza osobina molekula koji podležu JT distorziji putem teorijskih metoda koji pouzdano opisuju, kako JT efekat, tako i posmatrane osobine molekulskih sistema, predstavlja put ka boljem razumevanju novih materijala.

Ključne reči: *Jahn-Teller*-ov efekat, Aromatičnost, Ekscitonsko kuplovanje, Multideterminantna Teorija funkcionala gustine, Svojstveni put distorzije (IDP), Vibronski model za ekscitonsko kuplovanje

Naučna oblast: Hemija

Uža naučna oblast: Neorganska hemija

UDK broj: 546

Contents

1. Introduction

Language of chemistry is composed of a vast number of concepts that have become an integral part of what is considered to be a chemical intuition, enabling easy understanding of different chemical phenomena and rationalization of both, experimental and theoretical results. Usefulness of various chemical concepts goes even further, as their employment is frequently the first step towards a prediction of new properties, at least in a qualitative manner. From these reasons, it is evident why computational studies are often focused to seek origin, accurate determination of such concepts, and their precise definitions in quantum mechanical terms. The interconnection between molecular geometry and electronic structure is in the very center of theoretical chemistry. Quantum mechanical description of the changes in electronic structure due to distortions in molecular shape and vice versa is given in the form of the vibronic coupling theory.[1, 2] Probably, the most famous concept based on this theory is the Jahn−Teller (JT) effect.[3] The JT theorem states that degenerate electronic states of non-linear molecules are energetically unstable with respect to the nuclear displacements which lift the orbital degeneracy. In fact, the vibronic coupling, correlation between electronic states and vibrational motion of nuclei, describes all spontaneous symmetry breaking distortions,[1] attributed to the JT,[3] Renner-Teller (RT)[4] and pseudo JT (PJT) effects[5]. Thus, in general, the JT type distortions include proper JT distortions of molecules in a degenerate electronic state, PJT distortions in a non-degenerate electronic states, and RT distortions in linear systems.[1] There are many cases in which the separation of electronic states and nuclear movement would lead to the lack of explanation of many physical and chemical phenomena, such as ferroelectric phase transitions in perovskite crystals, colossal magneto-resistance in manganites,[6] superconductivity in fullerides,[7-10] molecular stereochemistry, reactivity, magnetic properties of molecules, structure and spectroscopy of impurity centers, conical intersections in photochemistry, and many other interesting phenomena[11, 12]. It should be emphasized that the JT effect has inspired very significant scientific discoveries, e.g. the concept of high-temperature superconductivity.[13, 14] The significance of the JT effect is increasingly recognized, hence, quantifying the distortion and getting insight into the mechanism lies at the heart of modern investigations.

It is noteworthy to mention that, despite great effort has been made in the development of the different experimental techniques,[1, 15] the experimental investigation of the JT effect still presents a very difficult task. On the other hand, rapid progress in computational science, combined with advances in a development of the electronic structure theory, made computational chemistry inevitable for studying the vibronic coupling, either as a partner to the experiment, or to provide an insight into the physical origin of the problem. From a broad palette of electronic structure methods, Density Functional Theory (DFT)[16, 17] emerged into the mainstream of quantum chemical methods, mainly because it gives a good compromise between accuracy of the results and computational economy. However, the application of DFT for the vibronic coupling, and especially for the treatment of the degenerate electronic states, requires special caution. Therefore, special approaches, like multideterminantal-DFT (MD-DFT) are needed.[18, 19] In addition, the accuracy of DFT calculations, predominantly depends on the suitability of the approximations made for the exchange-correlation (XC) functional. The choice of XC functional to be used in practice depends primary on the chemical nature of the system and the problem under study. Unfortunately, since none of the present-day XC functional was constructed to deal with the vibronic coupling effects, the special attention should be paid in the study of the JT effect within the framework of DFT.

The proper determination of the symmetry breaking distortions of molecules, as well as its influence on various properties, that are inherently related to the geometry, provides better understanding of various fundamental phenomena. The present thesis reports on the state-of-art in the field of the JT effect and the influence of the JT distortion on the various chemical properties. In particular, the objectives of this thesis are assessment of different density functional approximations for determination of the JT effect, as well as, addressing several, until now, not well understood phenomena related to the JT effect – the multimode JT effect, influence of the JT distortions on the aromaticity/antiaromaticity, and relationship between the symmetry breaking, JT type distortions and excitation energy transport.

The multimode JT problem is related to the fact that molecular distortions are only in the ideal case described by the movements of nuclei along one normal mode. Nevertheless, in the realistic situations, there are several JT active modes, and it is not possible to known *a priori* the individual role of different normal modes in the observed

JT induced properties. Herein, application of the Intrinsic Distortion Path (IDP) model[19-22] is presented and it is shown that it is possible directly to separate the contributions of the different vibrations to the JT distortion and to determine the forces which drive the distortion. It is important to stress that in all cases investigated in this thesis, a general trend is observed in the involvement of different types of vibrations, regardless of the diversity of a system at the hand.

Thorough study of the influence of the JT distortions on the aromaticity is presently of the utmost importance due to the increasing development of material chemistry, and substantial differences in aromatic/antiaromatic behavior of the JT active molecules. It should not be disregarded that the JT effect lies in the origin of the symmetry breaking processes, thus the proper picture of aromatic character of the JT active species cannot be made without including the JT distortion. Substantial differences in aromatic/antiaromatic behavior of the JT active molecules lead to the different reaction pathways, i.e. aromatic species are prone to high electrophilic aromatic substitutions, but show low reactivity in addition reactions, thus the analysis of vibonic coupling and aromaticity along the particular distortion path has shown to be essential. In order to not loose important, chemical features, the IDP model is employed for analysis of the JT distortion impact on the aromaticity.

The influence of vibronic coupling on the energy transfer, a theory combining excitonic coupling theory and the JT theory by forming PJT type systems is developed and introduced in this thesis. The nature of the interaction between individual chromophores determines the efficiency of energy and charge transfer, essential chemical processes acting in biological and manmade artificial materials. The extent of excitonic coupling between chromophores, for example, controls light harvesting and energy transfer in natural and artificial photosynthesis. A detailed understanding of the physical effects determining the electronic properties of the model dimer, its excited states and the role of vibronic coupling is an essential prerequisite for the successful investigation of more complex systems. The new developed model predicts the properties of the dimer through the simple interpretation of the monomer characteristics and its intrinsic features. This will allow for the study of the properties of isolated molecules by looking for systems with improved excitation transfer properties.

The thesis is divided in an introductory part containing Chapters 2-5, results and discussion part containing Chapters 6-9, and general conclusion presented in Chapter 10. Chapters 2-5 describe the investigated concepts and techniques when studying JT effect and its influence on the properties of the chemical systems, vibronic coupling theory (Chapter 2), DFT (Chapter 3), aromaticity (Chapter 4) and excitonic coupling (Chapter 5). Chapters 6-9 constitute the main part of the work and can be divided in four parts, where the MD-DFT procedure for the determination of the JT distortion in small aromatic organic radicals, anions and cations of corannulene and coronene, organometallic compound, metal and metaloid clusters and Werner type complexes with different XC functionals is given in Chapter 6, the treatment of the multimode JT problem in square-planar arsenic and antimony anionic clusters, small, organic, aromatic, radicals and open-shell corannulenes and coronenes by the means of MD-DFT and IDP is shown in Chapter 7, the influence of the JT effect on the aromaticity of benzene cation and anion, cyclopentadienyl radical, cobaltocene, fullerene ions and square-planar arsenic and antimony clusters is given in Chapter 8 and the new model combining excitonic coupling theory and JT theory, as well as the results obtained for the benzene dimer can be found in Chapter 9.

2. Vibronic Coupling Theory

Vibronic interaction, the correlation existing between the movement of electrons and nuclei, represents a very complicated problem in molecular and solid state physics and chemistry. Many issues can be easily solved by the decoupling of electronic and nuclear wavefunction using the adiabatic approximation.[23]

The basis of the vibronic coupling theory is strictly connected to the solution of the non-relativistic time independent many-body Schrödinger equation:

$$\hat{H}\Psi\left(\{\vec{R}_\alpha\},\{\vec{r}_i,\vec{\sigma}_i\}\right) = E\Psi(\{\vec{R}_\alpha\},\{\vec{r}_i,\vec{\sigma}_i\})$$

Eq. 2.1.

where the many-body wavefunction Ψ is a function of all the spatial coordinates of nuclei, $\vec{R}_\alpha$, (α = 1, …, M) and spatial and spin coordinates of electrons, $\vec{r}_i, \vec{\sigma}_i$, ($i$ = 1, …, N) for a system containing M nuclei and N electrons. The Hamiltonian ($\hat{H}$), a sum of all possible interactions between electrons and nuclei, can be written as

$$\hat{H} = \hat{T}_R(\vec{R}) + \hat{H}_r(\vec{r}) + \hat{V}(\vec{r},\vec{R})$$

Eq. 2.2.

$\hat{T}_R$ is the kinetic energy of the nuclei that depends only on the nuclear coordinates, $\vec{R}$, $\hat{H}_r$ represents the part of the Hamiltonian that depends only on the electronic coordinates, $\vec{r}$. For the sake of simplicity, the particular coordinate dependence of the first and second term in the total Hamiltonian will not be explicitly shown since it is given using indexes. $\hat{V}(\vec{r},\vec{R})$ takes into account the nuclei-nuclei and nuclei-electron interaction.

$$\hat{T}_R = \sum_{\alpha=1}^{M} \frac{-\nabla^2_{\vec{R}_\alpha}}{2M_\alpha}$$

Eq. 2.3.

$$\hat{H}_r = \sum_{i=1}^{N}\left(\frac{-\nabla^2_{\vec{r}_i}}{2} + \frac{1}{2}\sum_{j=1}^{N}\frac{1}{|\vec{r}_i - \vec{r}_j|}\right)$$

Eq. 2.4.

$$\hat{V}(\vec{r},\vec{R}) = \frac{1}{2}\sum_{\alpha=1}^{M}\sum_{i=1}^{N}\frac{Z_\alpha Z_\beta}{|\vec{R}_\alpha - \vec{R}_\beta|} - \frac{1}{2}\sum_{i=1}^{N}\sum_{\alpha=1}^{M}\frac{Z_\alpha}{|\vec{r}_i - \vec{R}_\alpha|}$$

Eq. 2.5.

where $\vec{R}_\alpha$ are the positions of the M nuclei, $\vec{r}_i$ the positions of the *N* electrons, and Z_α and M_α the corresponding nuclear charges and masses, respectively.

2.1. Adiabatic Approximation

It is a dream of researchers to find the reasonable solutions of Schrödinger equation. Since a large number of variables are involved in the Schrödinger equation, and even electronic and nuclear variables are coupled in the equation, solving it represents a very complex and demanding task. The first step in solving it is to take into account various approximations, among which the most important one is obtained by decoupling the dynamics of the electrons and the nuclei, known as Born-Oppenheimer approximation.[24] The essence of the approximation lies on the fact that the nuclei are much heavier than the electrons. In most cases the timescale of the response of the electrons is a few orders of magnitude faster than that of the nuclei, which allows the dynamics of the electrons and nuclei to be decoupled, and thus nuclei can be treated as classical particles and can be considered as static with respect to quantum particle electrons. Since the wavefunction depends on one spin and three spatial coordinates for every electron assuming fixed nuclear positions, finding the solution of the Schrödinger equation is still complicated.

2.1.1. Crude Adiabatic Approximation

The total Hamiltonian (Eq. 2.2.) can be rewritten:

$$\hat{H} = \hat{T}_R + \hat{H}_r + \hat{V}(\vec{r},\vec{R}_0) + \hat{W}'(\vec{r},\vec{R})$$

Eq. 2.1.1.1.

where,

$$\hat{W}'(\vec{r},\vec{R}) = \hat{V}(\vec{r},\vec{R}) - \hat{V}(\vec{r},\vec{R}_0)$$

Eq. 2.1.1.2.

is the vibronic Hamiltonian, and $\vec{R}_0$ is fixed nuclear geometry.

In order to solve the complete Schrödinger equation, the trial solution is used:

$$\Psi(\vec{r},\vec{R}) = \sum_m \chi_m(\vec{R})\varphi_m(\vec{r})$$

Eq. 2.1.1.3.

The exact solution to the problem, without losing any information, can only be found when $m \to \infty$ (an infinite basis) which is obviously impossible to perform in practice.

Substituting the total wavefunction from Eq. 2.1.1.3. into the total Hamiltonian (Eq. 2.2.), after some simple transformations, leads to the set of coupled equations:

$$\left(\hat{T}_R + E_m(R_0) + \widehat{W}'_{mm}\right)\chi_m(\vec{R}) + \sum_{k\neq m} \widehat{W}'_{km}\,\chi_k(\vec{R}) = E\chi_m(\vec{R})$$

Eq. 2.1.1.4.

The previous equation defines the nuclear movement where the diabatic (first term in the left hand expression) and vibronic (second term in the left hand expression) terms play the role of potential energy terms. The vibronic matrix represents the potential that static nuclei observe from their interaction with the electrons and the diabatic matrix is the delay in the electronic wavefunction to adapt to moving nuclei. In the Crude Adiabatic (CA) approximation,[23, 24] the off-diagonal elements of $\widehat{W}'$, the second term in the left hand expression of Eq. 2.1.1.4., are neglected. In order to evaluate the total Hamiltonian, the total wavefunction can be expressed as,

$$\Psi(\vec{r},\vec{R}) \approx \Psi^{CA}(\vec{r},\vec{R}) = \chi(\vec{R})\varphi(\vec{r})$$

Eq. 2.1.1.5.

Obviously, the problem is reduced to a simple equation, providing the nuclear wavefunction for the different electronic states *m*,

$$\left(\hat{T}_R + E'_m(R)\right)\chi_m(\vec{R}) = E\chi_m(\vec{R})$$

Eq. 2.1.1.6.

where $E'_m(R) = E_m(R_0) + \langle\varphi_m(\vec{r})\left|\widehat{W}'_{mm}\right|\varphi_m(\vec{r})\rangle$ is the electronic potential in which the nuclei move.

The CA approximation leads to the very crude vibronic matrix, and the calculated energy surface, E'_m, is far from describing those of a real molecule.

2.1.2. Born-Oppenheimer Approximation

In the Born-Oppenheimer (BO) approximation, the total wavefunction is expressed as following,

$$\Psi(\vec{r},\vec{R}) = \sum_m \chi_m(\vec{R})\varphi_m(\vec{r},\vec{R})$$

Eq. 2.1.2.1.

where $\chi_m(\vec{R})$ represent the nuclear functions, and $\varphi_m(\vec{r},\vec{R})$ are the electronic functions. The electronic wavefunction can be obtained solving the Schrödinger equation,

$$\left(\hat{H}_r + \hat{V}(\vec{r},\vec{R})\right)\varphi_m(\vec{r},\vec{R}) = \hat{H}_e\varphi_m(\vec{r},\vec{R}) = E_m(\vec{R})\varphi_m(\vec{r},\vec{R})$$

Eq. 2.1.2.2.

The problem to solve is:

$$(\hat{T}_R + \hat{H}_e)\sum_m \varphi_m(\vec{r},\vec{R})\chi_m(\vec{R}) = E\sum_m \varphi_m(\vec{r},\vec{R})\chi_m(\vec{R})$$

Eq. 2.1.2.3.

Applying the kinetic energy operator, $\hat{T}_R$, to one of the terms of the total wavefunction from Eq. 2.1.2.1., the following is obtained,

$$\begin{aligned}\hat{T}_R\varphi_m(\vec{r},\vec{R})\chi_m(\vec{R}) &= -\frac{\hbar^2}{2M}\left(\frac{\partial}{\partial R}\right)^2\varphi_m(\vec{r},\vec{R})\chi_m(\vec{R}) \\ &= -\frac{\hbar^2}{2M}\left(\frac{\partial^2\varphi_m}{\partial R^2}\chi_m + 2\frac{\partial\varphi_m}{\partial R}\frac{\partial\chi_m}{\partial R} + \varphi\frac{\partial^2\chi_m}{\partial R^2}\right)\end{aligned}$$

Eq. 2.1.2.4.

Since the nuclear mass is at least 1840 times that of the electron, the nuclear speed is much smaller. Accordingly, electrons adjust their positions to the nuclear arrangement almost immediately. In other words, the electronic wavefunction does not depend on the nuclear momentum, and the first and second terms in Eq. 2.1.2.4., called the non-adiabatic operators, can be neglected. The total wavefunction is reduced to only one term, as following,

$$\Psi(\vec{r},\vec{R}) \approx \Psi^{BO}(\vec{r},\vec{R}) = \chi(\vec{R})\varphi(\vec{r},\vec{R})$$

Eq. 2.1.2.5.

Introducing the BO wavefunction into the total Hamiltonian results in,

$$\left(\hat{T}_R + \hat{H}_e\right)\varphi\left(\vec{r},\vec{R}\right)\chi\left(\vec{R}\right) = \varphi\left(\vec{r},\vec{R}\right)\frac{\hbar^2}{2M}\frac{\partial^2\chi\left(\vec{R}\right)}{\partial R^2} + \hat{H}_e\varphi\left(\vec{r},\vec{R}\right)\chi\left(\vec{R}\right) = E\varphi\left(\vec{r},\vec{R}\right)\chi\left(\vec{R}\right)$$

Eq. 2.1.2.6.

Multiplying both sides of the previous equation by φ^*, and integrating with respect to $\vec{r}$, leads to:

$$\hat{H}_e\left(\vec{R}\right)\varphi\left(\vec{r},\vec{R}\right) = E_e\left(\vec{R}\right)\varphi\left(\vec{r},\vec{R}\right)$$

Eq. 2.1.2.7.

$$\hat{H}_N\chi\left(\vec{R}\right) = E\chi\left(\vec{R}\right)$$

Eq. 2.1.2.8.

with,

$$\hat{H}_e = \hat{H}_r + \hat{V}(\vec{r},\vec{R})$$

Eq. 2.1.2.9.

$$\hat{H}_N = \hat{T}_R + E_e\left(\vec{R}\right)$$

Eq. 2.1.2.10.

where $E_e\left(\vec{R}\right)$ is usually called the Adiabatic Potential Energy Surface (APES) and plays the role of a potential in the nuclear equation.

2.2. Vibronic Coupling Constants

In order to discuss the APES, it is customary to set a frozen reference geometry, $\vec{R}_{HS}$. This nuclear configuration of an *N*-atomic molecule typically belongs to a high symmetry (HS) point group, G_{HS}, especially when talking about the JT and PJT effects. The full Hamiltonian is divided in the reference part, $\hat{H}^{HS}$, and the vibronic contribution, $\hat{W}$:

$$\hat{H} = \hat{H}^{HS} + \hat{W}$$

Eq. 2.2.1.

$\hat{H}^{HS}$ is valid for the $\vec{R}_{HS}$ configuration, and $\hat{W}$ describes changes occurring with the distortion. The vibronic coupling models are all based on a perturbative approach to the Eq. 2.2.1:

$$\widehat{H} = \widehat{H}^{HS} + \sum_{k=1}^{3N-6} \left(\frac{\partial \widehat{V}}{\partial \vec{Q}_{HSk}}\right)_{HS} \vec{Q}_{HSk} + \frac{1}{2} \sum_{k,l=1}^{3N-6} \left(\frac{\partial^2 \widehat{V}}{\partial \vec{Q}_{HSk} \partial \vec{Q}_{HSl}}\right)_{HS} \vec{Q}_{HSk}\, \vec{Q}_{HSl} + \cdots$$

Eq. 2.2.2.

Vibronic coupling operator is expressed as a Taylor expansion along the normal coordinates, $\vec{Q}_{HSk}$.[i]

Considering that the ground state eigenfunction of $\widehat{H}^{HS}$ with energy, E^0, is f-fold degenerate, $\Psi_i^{HS,0} = \left|\Gamma_{HS}^{elect} m_i\right\rangle$, where Γ_{HS}^{elect} represents the irreducible representation (irrep) of the ground state and m_i is the component, *i*=1,…,f. According to the second order perturbation theory, the matrix elements, H_{ij}, for the wavefunctions, $\Psi_i^{HS,0}$, are given by the equation:

$$H_{ij} = E^0 \delta_{ij} + \sum_{i,j=1}^{f} \left\langle \Psi_i^{HS,0} \middle| \widehat{W} \middle| \Psi_j^{HS,0} \right\rangle + \sum_{i=1}^{f} \sum_{p \neq 0} \frac{\left| \left\langle \Psi_i^{HS,0} \middle| \widehat{W} \middle| \Psi_i^{HS,p} \right\rangle \right|^2}{E^0 - E^p} + \cdots$$

Eq. 2.2.3.

where 0 denotes the ground state, and *p* excited states.

For the purpose of calculating the APES around $\vec{R}_{HS}$ (or in general around any point $\vec{R}_X$), the following secular equation has to be solved:

$$\begin{vmatrix} H_{11} - E & H_{12} & \cdots & H_{1f} \\ H_{21} & H_{22} - E & \cdots & H_{2f} \\ \vdots & \vdots & \vdots & \vdots \\ H_{f1} & H_{f2} & \cdots & H_{ff} - E \end{vmatrix} = 0$$

Eq. 2.2.4.

Keeping the terms up to second order in $\vec{Q}_{HSk}$, Eq. 2.2.3. reads:

[i] The *N*-atomic molecule has 3*N*-6 normal coordinates (3*N*-5 for the linear molecules) which can be classified according to the corresponding irreps, Γ_{HSk}^{vib}, of the point group G_{HS}. In order to differentiate the symmetry of electronic states and vibrations, superscripts are added, e.g. Γ^{elect} and Γ^{vib}.

$$H_{ij} = E^0\delta_{ij} + \sum_{k=1}^{3N-6}\sum_{i,j=1}^{f}\left\langle \Psi_i^{HS,0}\left|\left(\frac{\partial\hat{V}}{\partial\vec{Q}_{HSk}}\right)_{HS}\right|\Psi_j^{HS,0}\right\rangle \vec{Q}_{HSk} + \frac{1}{2}\sum_{k=1}^{3N-6}\sum_{i=1}^{f}\left\langle \Psi_i^{HS,0}\left|\left(\frac{\partial^2\hat{V}}{\partial\vec{Q}^2{}_{HSk}}\right)_{HS}\right|\Psi_i^{HS,0}\right\rangle \vec{Q}^2{}_{HSk} + \frac{1}{2}\sum_{\substack{k,l=1\\k\neq l}}^{3N-6}\sum_{i,j=1}^{f}\left\langle \Psi_i^{HS,0}\left|\left(\frac{\partial^2\hat{V}}{\partial\vec{Q}_{HSk}\partial\vec{Q}_{HSl}}\right)_{HS}\right|\Psi_j^{HS,0}\right\rangle \vec{Q}_{HSk}\vec{Q}_{HSl} + \sum_{k=1}^{3N-6}\sum_{i=1}^{f}\sum_{p\neq 0}\frac{\left|\Psi_i^{HS,0}\left|\left(\frac{\partial\hat{V}}{\partial\vec{Q}_{HSk}}\right)_{HS}\right|\Psi^{HS,p}\right\rangle\right|^2}{E^0 - E^p}\vec{Q}^2{}_{HSk}$$

Eq. 2.2.5.

The matrix elements in Eq. 2.2.5. are the vibronic coupling constants. Obviously, the vibronic coupling constants define the APES. Furthermore, some of them have clear physical meaning, as it will be explained bellow.

If we rewrite Eq. 2.2.5., the following is obtained:

$$H_{ij} = E^0\delta_{ij} + \sum_{k=1}^{3N-6}\sum_{i,j=1}^{f}F_{ij}^k\vec{Q}_{HSk} + \frac{1}{2}\sum_{k=1}^{3N-6}\sum_{i=1}^{f}G_{ii}^{kk}\vec{Q}^2{}_{HSk} + \frac{1}{2}\sum_{\substack{k,l=1\\k\neq l}}^{3N-6}\sum_{i,j=1}^{f}G_{ij}^{kl}\,\vec{Q}_{HSk}\vec{Q}_{HSl} + \frac{1}{2}\sum_{k=1}^{3N-6}\sum_{i=1}^{f}\sum_{p\neq 0}K_v\,\vec{Q}^2{}_{HSk}$$

Eq. 2.2.6.

F_{ij}^k are the linear vibronic coupling constants, which reflect the force that the electrons of the state *i* create over the nuclei when they move following the normal coordinate $\vec{Q}_{HSk}$, see Subsection 2.2.1. for detailed discussion. G_{ii}^{kk}= K_0 is the harmonic force constant, see Subsection 2.2.2. for detailed discussion. G_{ij}^{kl} are called the quadratic vibronic coupling constants, which usually influence the shape of the APES in the JT active nonlinear molecules, producing the warping of the Mexican hat. Quadratic instability may take place in nonlinear molecules when linear vibronic constants are negligible.[1] For linear molecules, the linear vibronic constants are always zero because the non-totally

symmetric normal modes are odd and the degenerate states are even. However, the quadratic terms differ from zero, and this may lead to the instability of the linear configurations in the case of sufficiently strong coupling, referred to the RT effect.[4] K_v is the vibronic force constant, which depict the linear PJT coupling of the ground state with excited states, see Subsection 2.2.2.

Eq. 2.2.5. can be reduced by the symmetry rules, which allow identifying the non-zero vibronic coupling constants. The Hamiltonian is invariant under all symmetry operations in the corresponding point group. Hence, the operator $\partial\hat{V}/\,\partial\vec{Q}_{HSk}$ transforms according to the irrep Γ_{HSk}^{vib} of the normal coordinate $\vec{Q}_{HSk}$. Similarly, the operator $\partial^2\hat{V}/\,\partial\vec{Q}_{HSk}\partial\vec{Q}_{HSl}$ is a basis for the reducible representation obtained by the direct product $\Gamma_{HSk}^{vib} \otimes \Gamma_{HSk}^{vib} \subset \Gamma_r$. The matrix elements in Eq. 2.2.5. are only different from zero for:

$$\Gamma_{HS}^{elect} \otimes \Gamma_{HS}^{elect} \otimes \Gamma_{HSk}^{vib} \subset A_1$$

Eq. 2.2.7.

or in the case of the quadratic vibronic coupling constants for:

$$\Gamma_{HSk}^{vib} \otimes \Gamma_{HSl}^{vib} \otimes \Gamma_{HS}^{elect} \otimes \Gamma_{HS}^{elect} \subset A_1$$

Eq. 2.2.8.

2.2.1. The Slope of the Adiabatic Potential Energy Surface

The slope of the APES is defined as a derivative of energy over Cartesian coordinates. According to the Hellmann-Feynman theorem,[25, 26] the derivative of the total energy with respect to a parameter, λ, is related to the expectation value of the derivative of the Hamiltonian with respect to λ:

$$\frac{\partial E}{\partial \lambda} = \langle \Psi \left| \frac{\partial \hat{H}}{\partial \lambda} \right| \Psi \rangle$$

Eq. 2.2.1.1.

The force can be expressed in the direction of the normal coordinate, $\vec{Q}$:

$$\vec{F} = -\frac{\partial E}{\partial \vec{Q}} = -\left(\frac{\partial T}{\partial \vec{Q}} + \frac{\partial V_{en}}{\partial \vec{Q}} + \frac{\partial V_{ee}}{\partial \vec{Q}} + \frac{\partial V_{nn}}{\partial \vec{Q}} \right)$$

Eq. 2.2.1.2.

Although the perturbational theory was not invoked, the integral in Eq. 2.2.1.2. is identical to the linear vibronic coupling constants defined in Eq. 2.2.5., and hence the force approach is alternative to the perturbational formulation.[27, 28] The origin of the JT effect is a non-null symmetry-breaking force appearing in every nonlinear system in a degenerate electronic state.

The potential energy operator contains three parts: nuclear-nuclear Coulomb repulsion ($\hat{V}_{nn}$), electron-nuclear interactions ($\hat{V}_{en}$), and electron-electron repulsion ($\hat{V}_{ee}$). Since $\hat{V}_{ee}$ does not depend on the $\vec{Q}$, $\partial \hat{V}_{ee} / \partial \vec{Q} = 0$, and $\hat{V}_{nn}$ is not a function of the electronic coordinate. As the wavefunctions are orthonormal, linear vibronic coupling constant is:

$$\vec{F} = -\frac{\partial E}{\partial \vec{Q}} = -\langle \Psi \left| \frac{\partial \hat{V}}{\partial \vec{Q}} \right| \Psi \rangle = -\left(\langle \Psi \left| \frac{\partial \hat{V}_{en}}{\partial \vec{Q}} \right| \Psi \rangle + \frac{\partial V_{nn}}{\partial \vec{Q}} \right)$$

$$= -\left(\int \rho\,(\vec{r}) \frac{\partial V_{en}(\vec{r}, \vec{Q})}{\partial \vec{Q}} d\vec{r} + \frac{\partial V_{nn}}{\partial \vec{Q}} \right)$$

Eq. 2.2.1.3.

For any $\vec{Q}$ that is not totally symmetric, $\partial \hat{V}_{nn} / \partial \vec{Q} = 0$. Therefore, $\hat{V}_{nn}$ contributes to the slope of APES only for totally symmetric distortions. If the ground state is non-degenerate, $\langle \Psi \left| \frac{\partial \hat{V}_{en}}{\partial \vec{Q}} \right| \Psi \rangle \neq 0$, again only if $\vec{Q}$ is totally symmetric. Consequently, for any stationary point on the APES, the point group does not change along any reaction path[12]. If the ground state is degenerate, representing the particular scenario of the JT effect, for the slope to differentiate from zero, $\vec{Q}$ might be a basis for a non-totally symmetric representation. Although in such case, $\partial \hat{V}_{nn} / \partial \vec{Q} = 0$, second integral in the Eq. 2.2.1.3., $\langle \Psi \left| \frac{\partial \hat{V}_{en}}{\partial \vec{Q}} \right| \Psi \rangle \neq 0$. If non-totally symmetric $\vec{Q}$ belongs to one of the irreps which is a component of the direct product $\Gamma_{HS}^{elect} \otimes \Gamma_{HS}^{elect}$, these normal coordinates are JT active. The spontaneous distortion along the JT active coordinates leads to a descent in symmetry and removes the degeneracy of the ground state. Moreover, the energy will be lowered if the system is distorted in that direction. Using the group theory considerations, it is possible to know when the linear coupling constants are non-zero.

Jahn and Teller[3] studied all degenerate states for the all symmetry point groups and showed that for any molecular system with orbital degeneracy, there is at least one non-

totally symmetric normal coordinate for which $\langle \Psi \left| \frac{\partial \hat{V}_{en}}{\partial \vec{Q}} \right| \Psi \rangle \neq 0$, except in linear systems. This, was latter expressed in the well-known JT theorem[3]:

"Any nonlinear system which is in a degenerate state will couple to a non-symmetrical vibration that will reduce the energy of the molecule"

The JT problems are classified according to the irreps of the electronic states and normal modes that are coupled, $\Gamma \otimes \gamma$.[1] Since the slope of the APES at the HS point differs from zero, this highly symmetric configuration is not a stationary point.

When the symmetry is lowered, the wavefunction is no longer degenerate, and the linear vibronic coupling constants will be zero unless the normal coordinate $\vec{Q}$ becomes totally symmetric in the new point group. The lower symmetry (LS) point group of the minimum, G_{LS}, can be easily predicted from the correlation tables for the symmetry descent. In other words, the point group of lower symmetry configuration is the one in which the normal mode becomes totally symmetric. If there are several possibilities for a descent in symmetry, G_{LS} is the highest one with removed degeneracy according to the epikernel principle.[1, 29, 30]

The reason why the JT effect is usually considered to have a purely electrostatic origin can be found with deeper inspection of the Eq. 2.2.1.3. As already stated above, for the HS configuration in a JT problem, the first term in the Eq. 2.2.1.3. is the linear vibronic coupling constant, while the second is null due to the symmetry considerations. However, it must be taken into account that the expectation values of all operators included in Eq. 2.2.1.2. change during a geometry change:

$$\frac{\partial V_{ee}}{\partial \vec{Q}} = \langle \frac{\Psi}{\partial \vec{Q}} \left| \hat{V}_{ee} \right| \Psi \rangle + \langle \Psi \left| \hat{V}_{ee} \right| \frac{\Psi}{\partial \vec{Q}} \rangle$$

Eq. 2.2.1.4.

$$\frac{\partial T}{\partial \vec{Q}} = \langle \frac{\Psi}{\partial \vec{Q}} \left| \hat{T} \right| \Psi \rangle + \langle \Psi \left| \hat{T} \right| \frac{\Psi}{\partial \vec{Q}} \rangle$$

Eq. 2.2.1.5.

and the Hellman-Feymann theorem only shows that the force for a particular geometry exclusively depends on the electron-nuclei interaction and electron density for that point, Eq. 2.2.1.3. After an infinitesimal distortion has taken place in the system due to this

force, the electron density is also changed (as expressed through the PJT effect[1]), and all terms in Eq. 2.2.1.2. start contributing to the changes in energy, as seen trivially, for example when writing the energy functional in DFT. Thus, and as stressed previously in the literature,[31] when discussing the variations of geometry of a particular system one should not consider that the forces are merely electrostatic. In the multimode JT problem different distortion modes play different roles with respect to the terms in Eq. 2.2.1.2., as it will be shown in Chapter 7, Section 7.2. for the case of small, organic radicals. In particular, it can be found that some modes stabilize the molecule very strongly through the electron-nuclear interactions, while others play more subtle roles allowing the relaxation of electron-electron and kinetic energy terms through changes in the electron density.

2.2.2. The Curvature of the Adiabatic Potential Energy Surface

The presentation of the APES curvature, or force constant, $K_k = K_0 + K_v$, in the direction $\vec{Q}_{HSk}$ at $\vec{R}_{HS}$, is given by the following equation:

$$K = \frac{1}{2}\frac{\partial^2 E}{\partial \vec{Q}^2{}_k} = \frac{1}{2}\frac{\partial}{\partial \vec{Q}_k}\langle \Psi \left| \frac{\partial \hat{V}}{\partial \vec{Q}_k} \right| \Psi \rangle = \langle \Psi \left| \frac{\partial^2 \hat{V}}{\partial \vec{Q}^2{}_k} \right| \Psi \rangle + \langle \frac{\partial \Psi}{\partial \vec{Q}_k} \left| \frac{\partial \hat{V}}{\partial \vec{Q}_k} \right| \Psi \rangle + \langle \Psi \left| \frac{\partial \hat{V}}{\partial \vec{Q}_k} \right| \frac{\partial \Psi}{\partial \vec{Q}_k} \rangle$$

Eq. 2.2.2.1.

where $\frac{\partial \Psi}{\partial \vec{Q}_k}$ is the first order correction to the wavefunction in perturbational theory:

$$\frac{\partial \Psi}{\partial \vec{Q}_k} = \Psi + \sum_p \frac{\langle \Psi \left| \frac{\partial \hat{V}}{\partial \vec{Q}_k} \right| \Psi^p \rangle}{E^0 - E^p} \Psi$$

Eq. 2.2.2.2.

K_0 and K_v are given by the following Eqs.:

$$G_{ii}^{kk} = K_0 = \left\langle \Psi_i^{HS,0} \left| \left(\frac{\partial^2 \hat{V}}{\partial \vec{Q}^2{}_{HSk}} \right)_{HS} \right| \Psi_i^{HS,0} \right\rangle$$

Eq. 2.2.2.3.

$$K_v = 2\frac{\left| \Psi_i^{HS,0} \left| \left(\frac{\partial \hat{V}}{\partial \vec{Q}_{HSk}} \right)_{HS} \right| \Psi^{HS,p} \right\rangle \Big|^2}{E^0 - E^p}$$

Eq. 2.2.2.4.

K_0, which is always different from zero and positive as the $\partial^2\hat{V}/\partial\vec{Q}^2{}_{HSk}$ is totally symmetric, tends to bring the system back to the more symmetrical situation.[1] If the vibronic coupling is ignored, the HS configuration would be the most stable configuration of the system.

K_v is always negative, due to the nominator $E^0 - E^p$. Since there are always some excited states of the same irrep as the ground state, K_v is different from zero and thus, shows that the vibronic terms favor instability. Taking into account that $K_0 > 0$, the only possibility for the appearance of a spontaneous instability that breaks the symmetry of a system is $K_0 < |K_v|$. This situation refers to the PJT effect. The importance of the PJT effect should not be underestimated. Its most common application is the explanation of the shape of molecules[1, 32] and solids,[1, 33] including linear systems where it has been shown to be stronger than the RT effect.[32] The observation of symmetry-forbidden transitions due to vibronic coupling[34] or the barrier controlling tunneling in JT systems are directly or strongly influenced by the PJT effect.[35] It is also used to explain transition states in reactions,[12] and has given rise to the discovery of new materials like the vibronic spin-crossover systems.[36]

The difference between JT and PJT effects resides in their physical meaning. While the JT effect describes the forces that electrons produce when the system displays a degenerate state (Subsection 2.2.1.), the PJT describes the energetics associated with the change in the distribution of electrons.[37]

2.3. Relevant Theory of the $E \otimes (b_1 + b_2)$ Jahn-Teller Problem. Case Study: Square-planar Molecules

In pursuance of an explanation on how the vibronic coupling theory can be applied for qualitative analysis, the particular scenario, i.e. $E \otimes (b_1 + b_2)$ JT problem, will be shown in detail.

The square-planar As_4^- and Sb_4^-, have ^2E_g ground state in D_{4h} point group, and six normal modes that are classified into A_{1g}, B_{1g}, B_{2g}, B_{2u} and E_u irreps. The symmetric product of the E_g electronic state transforms as A_{1g}+B_{1g}+B_{2g}. These three vibrations in square-planar structures are depicted on Figure 2.3.1., using the vibrational energy distribution representation.[38]

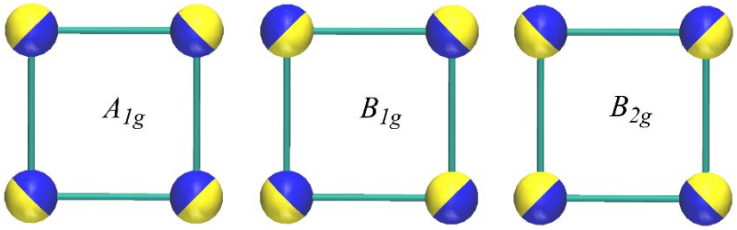

Figure 2.3.1. Vibrational energy distribution representation of the A_{1g}, B_{1g} and B_{2g} normal modes. The different colors indicate the direction of the displacement vector; the volume of the spheres is proportional to the contribution made by the individual nuclei to the energy of the vibrational mode.

Vibrations that belong to both B_{1g} and B_{2g} irreps in D_{4h} point group will distort square-planar structure to a structure with D_{2h} symmetry, however b_{1g} will lead to rhombus and b_{2g} to rectangular structure, Figure 2.3.2.

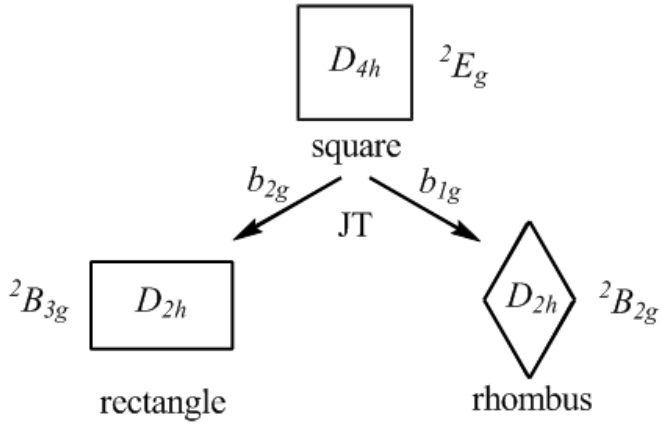

Figure 2.3.2. JT distortion of the square-planar As_4^- and Sb_4^-.

Totally symmetric coordinate does not distort the symmetry, however, in principle, needs to be taken into account since its vibronic coupling constant is not zero by symmetry. The JT $E\otimes(a_1+b_1+b_2)$ problem in As_4^- and Sb_4^- is one of the simplest examples of the multimode problem. Taking into account coupling coefficients for D_{4h} point group (Table 2.3.1.), and labelling two wavefunctions of the E_g term transforming as x^2-y^2 and xy, as B_{2g} and B_{3g}, respectively, according to the irreps in D_{2h} point group in which the E_g state will split (Figure 2.2.), the vibronic coupling matrix W, takes the form:

$$W = \begin{vmatrix} F_{b_{1g}}Q_{b_{1g}} + F_{a_{1g}}Q_{a_{1g}} & F_{b_{2g}}Q_{b_{2g}} \\ F_{b_{2g}}Q_{b_{2g}} & -F_{b_{1g}}Q_{b_{1g}} + F_{a_{1g}}Q_{a_{1g}} \end{vmatrix}$$

Eq. 2.3.1.

where three vibronic coupling constants have been introduced:

$$F_{b_{1g}} = \langle \psi_{B_{2g}} \left| \frac{\partial \hat{H}}{\partial Q_{b_{1g}}} \right| \psi_{B_{2g}} \rangle = - \langle \psi_{B_{3g}} \left| \frac{\partial \hat{H}}{\partial Q_{b_{1g}}} \right| \psi_{B_{3g}} \rangle$$

Eq. 2.3.2.

$$F_{b_{2g}} = \langle \psi_{B_{2g}} \left| \frac{\partial \hat{H}}{\partial Q_{b_{2g}}} \right| \psi_{B_{3g}} \rangle = \langle \psi_{B_{3g}} \left| \frac{\partial \hat{H}}{\partial Q_{b_{2g}}} \right| \psi_{B_{2g}} \rangle$$

Eq. 2.3.3.

$$F_{a_{1g}} = \langle \psi_{B_{2g}} \left| \frac{\partial \hat{H}}{\partial Q_{a_{1g}}} \right| \psi_{B_{2g}} \rangle = \langle \psi_{B_{3g}} \left| \frac{\partial \hat{H}}{\partial Q_{a_{1g}}} \right| \psi_{B_{3g}} \rangle$$

Eq. 2.3.4.

JT parameters, JT radius, R_{JT}, and JT stabilization energy, E_{JT}, the energy difference between minimum energy conformation and the energy at the degeneracy point, Figure 2.3.3., of each vibration are given by:

$$R_{JT_i} = \frac{F_i}{K_i}$$

Eq. 2.3.5.

$$E_{JT_i} = \frac{F_i^2}{2K_i}$$

Eq. 2.3.6.

Table 2.3.1. Coupling coefficients for D_{4h} point group.

Vibration	El. state component	$E_g \otimes E_g$			
		$B_{2g}B_{2g}$	$B_{2g}B_{3g}$	$B_{3g}B_{2g}$	$B_{3g}B_{3g}$
b_{1g}		$1/\sqrt{2}$	0	0	$-1/\sqrt{2}$
b_{2g}		0	$1/\sqrt{2}$	$1/\sqrt{2}$	0
a_{1g}		$1/\sqrt{2}$	0	0	$1/\sqrt{2}$

APES has two kinds of stationary points which feature rhombic and rectangular distortions. Neglecting possible second-order interaction with the a_{1g} vibration,[1, 39] as shown by *ab initio* results to be a correct assumption for the As_4^- and Sb_4^-, one of those stationary points will be minimum structure and the other saddle point, depending on the values of E_{JT}, or vibronic coupling constants of b_{1g} and b_{2g} modes. The vibronic coupling

constants, F_i, and force constants of JT active vibrations, K_i completely define the potential energy surface.

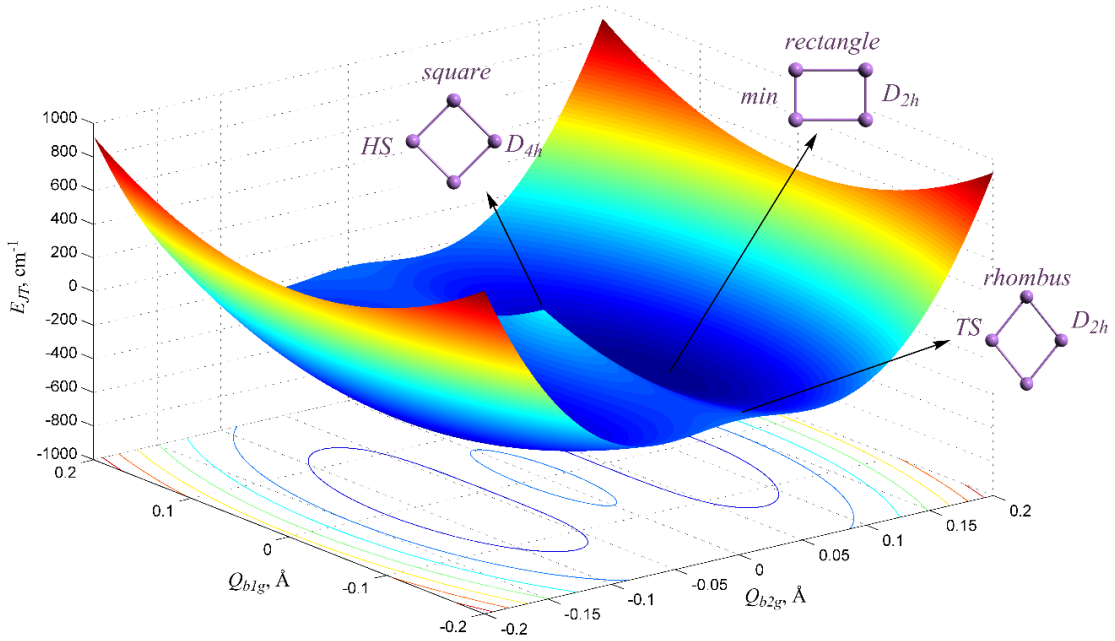

Figure 2.3.3. 3D APES of Sb_4^- in the space of JT active b_{1g} and b_{2g} normal modes; vibronic coupling parameters are taken from LDA Intrinsic Distortion Path (IDP) model and numerical values will be given in Chapter 7, Section 7.1.; HS have square, minima (*min*) rectangular and transition states (*TS*) rhombic geometries.

2.4. Relevant theory of the $E \otimes e$ Jahn-Teller Problem. Case Study: Octahedral Molecules

Another characteristic situation in which the perturbational approach to the vibronic coupling plays an essential role is $E \otimes e$ JT problem, which can be explained without difficulty using an octahedral hexaflurocuprat(II) ion.

The ground electronic state of the hexaflurocuprat(II) ion, in the O_h point group, is ^2E_g. According to the group theory consideration, $E \otimes E$ expands the following irreps:

$$E_g \otimes E_g = A_{1g} \oplus [A_{2g}] \oplus E_g$$

Eq. 2.4.1.

in the O_h symmetry group. The distortion coordinate is, thus, e_g. According to the previous Equation, the matrix elements in Eq. 2.2.5. differ from zero when considering normal modes belonging to a_{1g} and e_g. It should be noted that a_{1g} vibration will not lead to any descent in symmetry, and can only produce the change of interatomic distances. Normal

modes, a_{1g} and e_g, in octahedral structures are presented on Figure 2.4.1., using the vibrational energy distribution representation.[38]

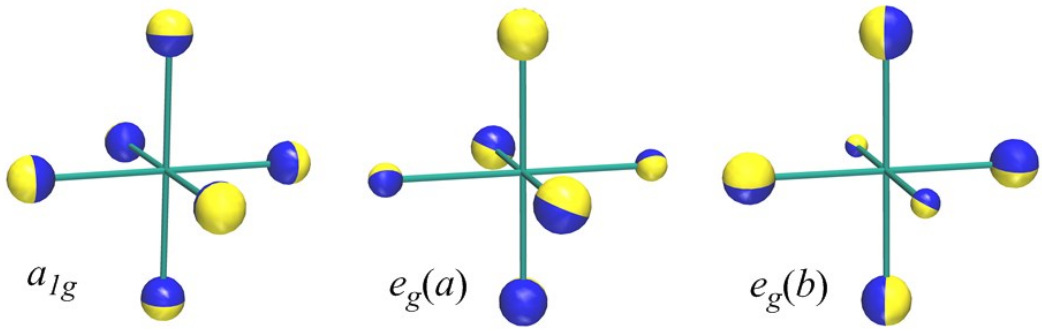

Figure 2.4.1. Vibrational energy distribution representation of the a_{1g} and e_g normal modes. The different colours indicate the direction of the displacement vector; the volume of the spheres is proportional to the contribution made by the individual nuclei to the energy of the vibrational mode.

Using the correlation table for the O_h point group, it can be easily seen that the descent in symmetry goes to the D_{4h}. The electronic state will split into $^2A_{1g}$ and $^2B_{1g}$, compressed and elongated geometry, respectively, Figure 2.4.2.

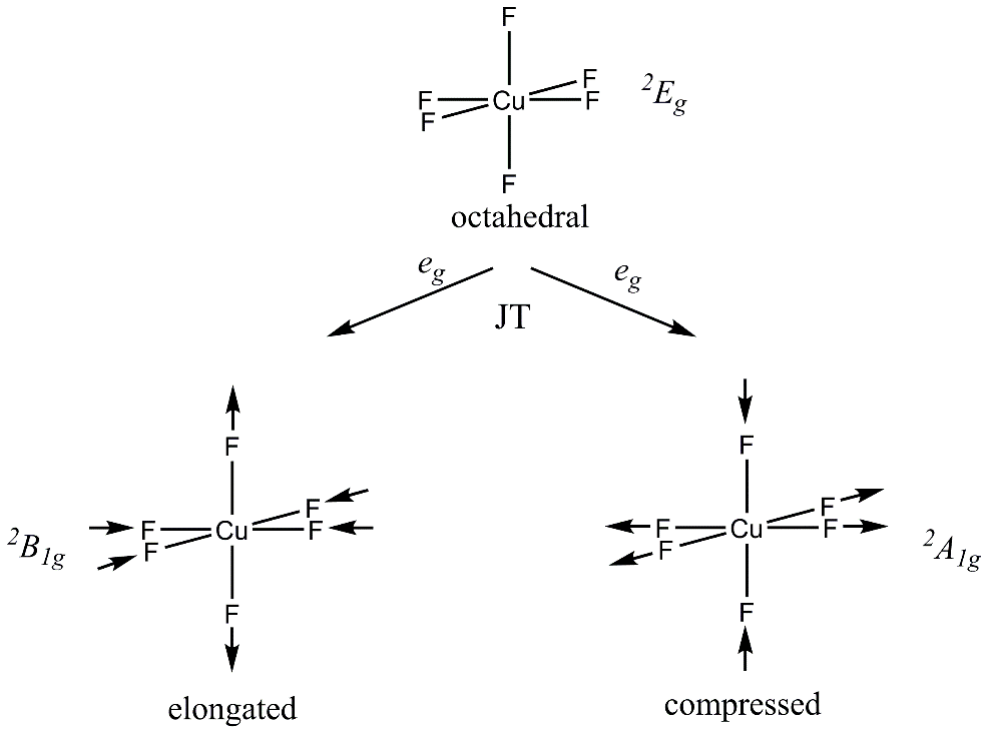

Figure 2.4.2. JT distortion of the octahedral hexaflurocuprat(II) ion.

Taking into account coupling coefficients for O_h point group, Table 2.4.1., we can easily find that the W matrix is:

$$W = \begin{vmatrix} FQ_a & FQ_b \\ FQ_b & -FQ_a \end{vmatrix}$$

Eq. 2.4.1.

Table 2.4.1. Coupling coefficients for O_h point group.

Vibration	El. state component	$E_g \otimes E_g$			
		AA	*AB*	*BA*	*BB*
e_g	*a*	$-1/\sqrt{2}$	0	0	$1/\sqrt{2}$
	b	0	$1/\sqrt{2}$	$1/\sqrt{2}$	0

The potential energy as a function of a distortion along Q_a and Q_b is:

$$E = E^0 + \frac{1}{2}K(\vec{Q}^2{}_a + \vec{Q}^2{}_b) \pm F\left[(\vec{Q}^2{}_a + \vec{Q}^2{}_b)\right]^{\frac{1}{2}}$$

Eq. 2.4.2.

The change in energy along Q_a, or Q_b, or along any linear combination of Q_a and Q_b is the same. In the Eq. 2.4.2. only quadratic forms of Q_a and Q_b play a role, and thus the energy of a distortion along $-Q_a$ is the same as along Q_a. Therefore, the APES takes a form of Mexican-hat surface, without any warping, Figure 2.4.3. This is the particular scenario, so-called dynamic JT problem, where the vibronic matrix is restricted to the harmonic approximation, and only linear terms are taken into the consideration. In the dynamic JT effect, molecule resonates between two or more equivalent modes of distortion. Although the vibronic coupling model is very useful in the consideration and explanation of the dynamic JT effect, at least in a qualitative manner, the distortion cannot be directly observed.

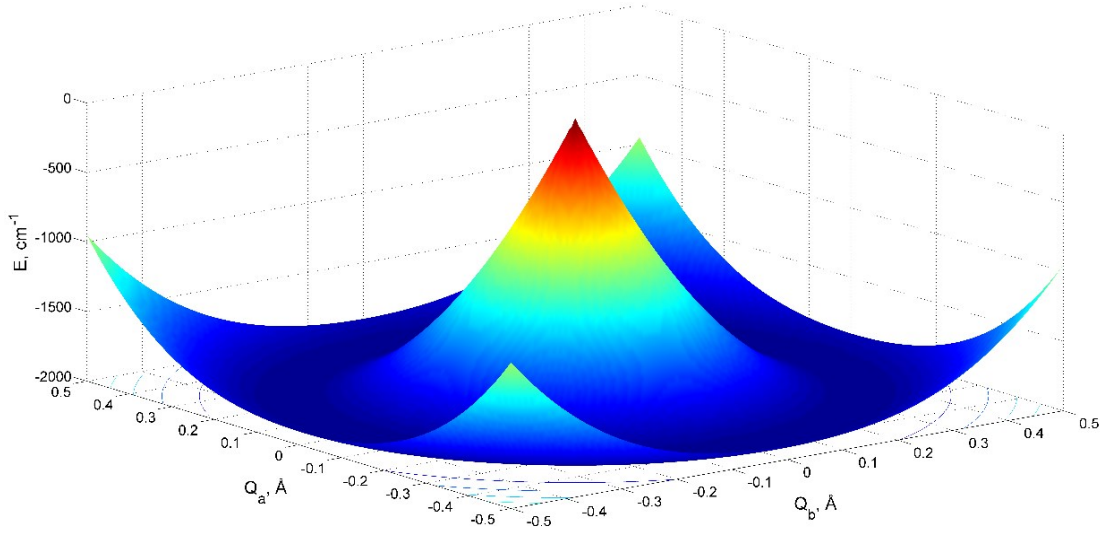

Figure 2.4.3. A descriptive 3D APES for linear $E \otimes e$ JT effect.

When higher order vibronic constants of the normal coordinates are not zero, and have to be taken into account, the APES is no longer flat, and the warping occurs, Figure 2.4.4. The equivalent minima are replaced by the three wells separated by three saddle points. In the case of static JT effect, the molecule remains distorted in a particular way long enough for the distortion to be detected experimentally. According to the group theory, the condition for a static JT effect is a non-vanishing second-order vibronic coupling. However, elastic anharmonicity (third-order term) is also very important in warping of the APES, and often even more prominent than the quadratic vibronic terms.[35]

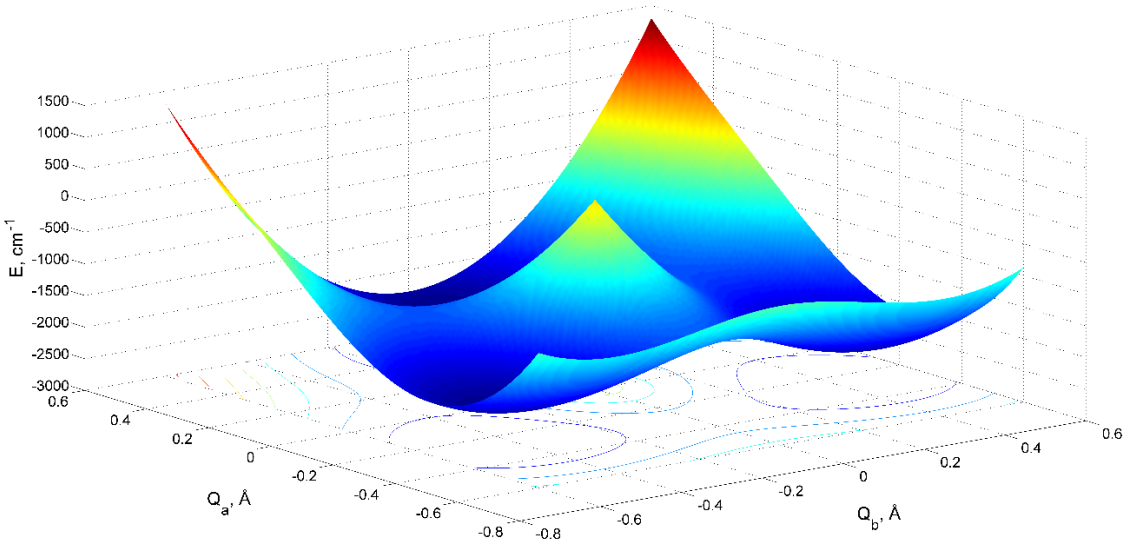

Figure 2.4.4. A descriptive 3D APES for quadratic $E \otimes e$ JT effect.

2.5. Pseudo Jahn-Teller Two Level Problem

In order to illustrate the concept of the PJT effect, the coupling between the non-degenerate ground state and only one excited state, belonging to different symmetries, separated by an energy gap 2Δ, and coupled by a vibrational motion, Q, with appropriate symmetry as explained above in the Section 2.2., Subsection 2.2.2. The vibronic coupling matrix W, takes the form:

$$W = \begin{vmatrix} -\Delta & FQ \\ FQ & \Delta \end{vmatrix}$$

Eq. 2.5.1.

and the energy of the system is:

$$E = \frac{1}{2} K_0 \vec{Q}^2 \pm \left[(\Delta^2 + F^2 \vec{Q}^2) \right]^{\frac{1}{2}}$$

Eq. 2.5.2.

where, K_0 is the primary force constants, and F is the linear PJT coupling constant between ground and considered excited state, see Eqs. 2.2.5. and 2.2.6. for the definitions. From the last Eqs. it is obvious that the PJT correction to the energy is quadratic, in contrast to the JT correction which was linear (if only linear vibronic coupling is considered). In addition, the final wavefunctions will become an admixture of Ψ and Ψ^p, hence in the absence of PJT coupling the electronic wavefunctions, and consequently all the derived properties, e.g. electron density would remain frozen to their values at the reference geometry. Depending on the value of the linear vibronic constant F, with respect to 2Δ and K_0, two different situation may arise concerning the shape of the APES, illustrated on the Figure 2.5.1. The first situation is weak PJT effect, where the coupling between the ground and excited state is small resulting in a reduction of the frequency of the ground state vibrations, along with an increment of the one corresponding to the excited state, and there is no instability of the reference HS nuclear configuration. The second situation arises when there is a strong enough coupling, and the curvature of the ground state becomes negative leading to the instability of the reference HS point, Figure 2.5.1.

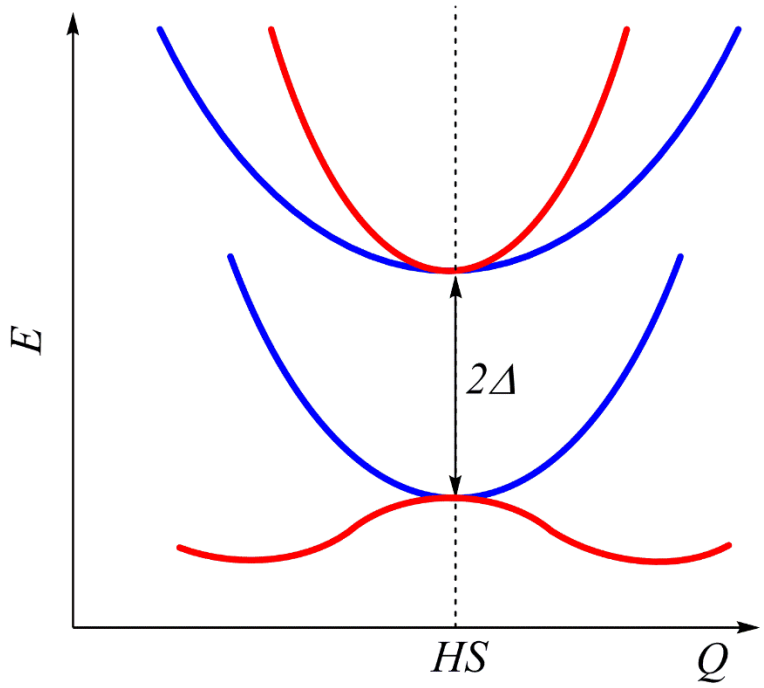

Figure 2.5.1. Qualitative description of weak (blue) and strong (red) PJT coupling.

2.6. The Intrinsic Distortion Path

The group theory allows finding the irrep of the non-totally symmetric vibrations in the HS conformation, which are JT active and remove the degeneracy and lead to a stabilization of the system by lowering the symmetry. In order to get a detailed picture on the interaction between the deformation of the electron distribution and the displacements of the nuclei one needs to go beyond the group theory consideration. Thus, computational studies can be successfully applied in order to obtain APES of the JT active molecules.

The IDP method[19-21] is based on the fact that all the information about the vibronic coupling at the HS nuclear arrangement is also contained in the distorted LS minimum energy structure. The reference point for the method is, thus, the LS configuration, a true minimum on the potential energy surface, and the distortion is given as a superposition of all totally symmetric normal modes in the LS point group, connecting the HS configuration with the LS structure.

This particular reaction path, which starts from HS geometry and ends in the LS minimum, uses the simplified quadratic energy surface, instead of the full *ab initio* energy surface:

$$E_{JT} = \sum_i \frac{1}{2} K_i^{LS} \left[\vec{Q}_i^{LS}(HS)\right]^2$$

Eq. 2.6.1.

where $\vec{Q}_i^{LS}(HS)$ is the HS geometry expressed in terms of the LS vibrational modes. The potential energy surface has a simple analytical form and it is possible to directly distinguish the contributions of the different vibrations to the JT distortion, the forces at the HS point, as well as how these forces change along a relevant particular path of distortion.

Since the force is derivative of the energy over the Cartesian coordinates, it is straightforward to obtain the total force at the HS point directly. The force which drives the nuclei toward the minimum stationary points on the potential energy surface can be projected on either HS or LS normal modes, denoted as F_i^{HS} and F_i^{LS}, respectively. Since the physical meaning of the linear vibronic coupling constant is the force along the particular, usually HS normal mode,[1] the linear vibronic constants, can be evaluated as

F_i^{HS}. The two forces defined via HS and LS normal modes, although clearly different, are connected:

$$\vec{F}^{LS} = \mathbf{J}\vec{F}^{HS}$$

Eq. 2.6.2.

where $\vec{F}^{LS}$ and $\vec{F}^{HS}$ are column vectors with magnitudes of corresponding forces as elements, and $\mathbf{J}$ is a (3*N*-6) x (3*N*-6) Dushinsky matrix[40] which correlates the HS and LS normal modes:

$$\mathbf{J} = \left(\vec{\mathrm{Q}}^{LS}\right)^{\mathrm{T}}\vec{Q}^{HS}$$

Eq. 2.6.3.

The JT distortion, $\vec{R}_{JT}$, the distortion vector between the HS and LS points, is expressed in terms of either LS or HS normal modes:

$$\vec{R}_{JT} = \sum_i r_{JT,i}^{LS}\,\vec{Q}_i^{LS} = \sum_i r_{JT,i}^{HS}\,\vec{Q}_i^{HS}$$

Eq. 2.6.4.

where $r_{JT,i}$ is the contribution of the displacements along the mass-weighted LS or HS normal coordinate to the $\vec{R}_{JT}$, or in other words the JT radius of the mode.

3. Density Functional Theory

The development of new physical and numerical algorithms and strong computer processors induces increase in using *ab initio* methods in computational modeling of physical and chemical properties of molecules.[41] The quantum mechanical (QM) methods, which are used to describe the wavefunction of the system, successfully explain the experimental data, and allow the prediction of the properties of matter in experimentally inaccessible conditions.[41] Although these methods are highly accurate,[42-45] they are very time consuming and limited by system size, thus the need for accurate, versatile, but less time consuming method has appeared. When calculating the properties related to the ground state of molecules, e.g. geometry and electronic structure, Density Functional Theory (DFT)[16, 17] has emerged into the mainstream of QM approaches and nowadays DFT represents one of the most popular and successful QM methods.[16, 17, 46-51]

A key goal of most electronic structure theory is to solve the non-relativistic time independent many-body Schrödinger equation and the conventional QM approaches employ the wavefunction as the central quantity. Contrary to the wavefunction based methods, DFT, as the central observable, uses the electron density, $\rho(r)$, which uniquely determines the Hamiltonian, and thus all properties of the system. Regardless of how many electrons the system possesses, the electron density is always three dimensional. $\rho(r)$, integrated over all space, gives the total number of electrons N:

$$N = \int \rho(r) dr$$

Eq. 3.1.

In late 1920s and beginning of 1930s Thomas,[52] Fermi,[53] Dirac[54] and Wigner[55] stated that the electronic energy can be expressed in terms of the electronic density. The relevance of the simple Thomas-Fermi model is not in computing the ground state energy and density but more as an indicator that the energy can be determined purely using the electron density. This approach is extremely simple and qualitatively correct for atoms. However it does not predict a binding energy for molecules, and the proof is not rigorous. J. C. Slater intuitively proposed in 1951[56] to represent the potential of exchange and correlation by the cubic root of the electronic density. This modification was motivated

by the theory of the homogeneous electronic gas, introduced by Thomas and Fermi, and particularly characterized by the introduction of its exchange potential. Slater's work simplified the Hartree-Fock (HF) method in a way that the exchange potential is calculated locally from the one third power of the density. This is the Hartree-Fock-Slater method, or Xα method.

3.1. Hohenberg-Kohn Theorem

After more than 40 years from the first Thomas-Fermi model, Hohenberg and Kohn set up the foundations of DFT which allows expressing the electronic Hamiltonian as a functional of $\rho(r)$.[57] Their theory relies on two main theorems. First theorem states that external potential, V_{ext}, the interaction of electrons and nuclei, uniquely determines $\rho(r)$. Second one states that the ground state electron density can be found using a variational principle.

In the electronic Hamiltonian only V_{ext} depends explicitly on the nuclear configuration. As a consequence of the first theorem, the whole electronic Hamiltonian can be expressed as a functional of $\rho(r)$. Briefly, knowledge of $\rho(r)$ implies knowledge of the wavefunction and V_{ext}, and hence of all other observables.

For any given ground state density $\rho_0(r)$ it is possible to calculate the corresponding ground state wavefunction $\Psi_0(r_1, r_2, \ldots, r_N)$, which means that all ground state observables are functionals of $\rho_0(r)$, too. If there is another external potential, V'_{ext}, which differs from V_{ext} by more than a constant and can also give the same ground state electron density, there are two different Hamiltonians, $\hat{H}$ and $\hat{H}'$, with the same ground state electron density, but with two different wavefunctions, Ψ and Ψ':

$$E_0 < \langle \Psi' | \hat{H} | \Psi' \rangle = \langle \Psi' | \hat{H}' | \Psi' \rangle + \langle \Psi' | \hat{H} - \hat{H}' | \Psi' \rangle$$
$$= E'_0 + \int \rho(r)[V_{ext}(r) - V'_{ext}(r)]\, dr$$

Eq. 3.1.1.

where E_0 and E'_0 are the ground state energies for $\hat{H}$ and $\hat{H}'$, respectively. Similarly:

$$E_0' < \langle \Psi | \hat{H}' | \Psi \rangle = \langle \Psi | \hat{H}' | \Psi \rangle + \langle \Psi | \hat{H}' - \hat{H} | \Psi \rangle = E_0 - \int \rho(r)[V_{ext}(r) - V_{ext}'(r)]\, dr$$

Eq. 3.1.2.

Adding Eqs. 5.1.1. and 5.1.2. the following contradiction is obtained:

$$E_0 + E_0' < E_0' + E_0$$

Eq. 3.1.3.

This obvious nonsense leads us to the conclusion that there are no two different external potentials that give the same ground state electron density. Thus, $\rho(r)$ uniquely determines external potential, and all ground state properties.

The total energy of the system can be written explicitly as a function of $\rho(r)$:

$$E[\rho(r)] = T[\rho(r)] + V_{ne}[\rho(r)] + V_{ee}[\rho(r)] = \int \rho(r) V_{ext}(r) dr + F_{HK}\,[\rho(r)]$$

Eq. 3.1.4.

where

$$F_{HK}[\rho(r)] = T[\rho(r)] + V_{ee}[\rho(r)]$$

Eq. 3.1.5.

Since $F_{HK}[\rho(r)]$ only depends on $\rho(r)$ and is independent from V_{ext}, $F_{HK}[\rho(r)]$ is a universal functional of $\rho(r)$.

The second theorem shows that the ground state energy can be obtained variationally, with the density that minimizes the total energy being the exact ground state density, which is expressed as:

$$E_0[\rho_0] \leq E_{V_{ext}}[\rho]$$

Eq. 3.1.6.

Suppose the ground state wavefunction is Ψ and its electron density is $\rho(r)$. Thus the $\rho(r)$ uniquely determines V_{ext}. If there is another wavefunction, Ψ', with an arbitrary variation from Ψ and its electron density is $\rho'(r)$, then the following can be obtained:

$$\langle \Psi' | \hat{H} | \Psi' \rangle = \int \rho'(r) V_{ext}(r) dr + F_{HK}\,[\rho'(r)] = E[\rho'(r)] \geq E[\rho(r)]$$

Eq. 3.1.7.

Obviously, the energy will reach the minimum only when the electron density is the ground state electron density.

If the universal functional $F_{HK}[\rho(r)]$ was known, the determination of the ground state energy and electron density would be an easy task since it requires only the minimization of a functional of the 3-dimensional density function.

3.2. The Kohn-Sham Equations

The determination of universal functional $F_{HK}[\rho(r)]$ presented one of the main problems in DFT. Most of the models, such as Thomas-Fermi approximation, were not able to reproduce the kinetic energy of the system. In 1965, Kohn and Sham[58] suggested the solution to this problem by re-introducing the idea of non-interacting electrons moving in an effective field, which enabled the calculation of the kinetic energy and transformed DFT into a practical electronic structure theory.

The functional $F_{HK}[\rho(r)]$ is a sum of the kinetic energy of non-interacting electron (T_s), the Coulomb energy ($E^{Coulomb}$), and all the many-body quantum effects which are summarized into the exchange and correlation energy term (E_{xc}). The total energy of the system is:

$$E[\rho(r)] = \int \rho(r)V_{ext}(r)dr + F_{HK}\,[\rho(r)]$$

$$= \int \rho(r)V_{ext}(r)dr + T_s[\rho(r)] + E^{Coulomb}[\rho(r)] + E_{xc}[\rho(r)]$$

Eq. 3.2.1.

The effective potential, V^{eff}, can be defined as follows,

$$V^{eff} = \frac{\delta\{\int \rho(r)V_{ext}(r)dr + E^{Coulomb}[\rho(r)] + E_{xc}[\rho(r)]\}}{\delta\rho(r)}$$

$$= V_{ext}(r) + \int \frac{\rho(r')}{|r - r'|}dr' + V_{xc}(r)$$

Eq. 3.2.2.

where $V_{xc}(r)$ is the exchange-correlation potential.

The main equation in Kohn-Sham (KS) DFT which is the one-electron Schrödinger-like equation can be expressed as:

$$\left[-\frac{1}{2}\nabla^2 + V^{eff}\right]\Phi_i = \epsilon_i \Phi_i$$

Eq. 3.2.3.

The functions Φ_i are the Kohn-Sham one-electron orbitals, and the ϵ_i's are the energies of the KS one-electron orbitals.

The $\rho(r)$ is defined as follows,

$$\rho(r) = \sum_{i=1}^{N} |\Phi_i|^2$$

Eq. 3.2.4.

Finally, the total energy can be written as:

$$E = \sum_{i=1}^{N} \epsilon_i - \frac{1}{2}\iint \frac{\rho(r)\rho(r')}{|r - r'|} + E_{xc}[\rho(r)] - \int V_{xc}(r)\rho(r)dr$$

Eq. 3.2.5.

The Eqs. 3.2.2., 3.2.3., and 3.2.4. are KS equations and they must be solved self-consistently in order to obtain KS orbitals. The general procedure is to begin with an initial guess of the electron density, construct the V^{eff} and then get the KS orbitals. The electron density is obtained based on these orbitals and the process is repeated until convergence is achieved. Once the final electron density is obtained, the total energy can be easily calculated. The KS equations recast the many-body Schrödinger equation into a set of coupled, single-particle equations and isolate all many-body interaction into the XC density functional. For exact functional, and for exact external potential, KS orbitals would give exact ground state electron density and energy. Unfortunately, the uniform functional that would give exactly the same answer as the Schrödinger equation for the ground state of any system, is not affordable. Since, E_{xc} term, which includes the non-classical aspects of the electron-electron interaction along with the kinetic energy of the real system different from the non-interacting system, is not known exactly, an approximation needs to be used.

3.3. Exchange-Correlation Functionals

The only unknown term for obtaining the exact energy within DFT is E_{xc}, in which all complexity is hidden.[59] Many proposals have been made for describing this XC

energy, and by now there is an almost endless list of approximated functionals with varying levels of complexity, separated into a number of classes. A useful way for E_{xc} categorization, "Jacob's ladder", has been proposed by Perdew,[60] where XC functionals are grouped hierarchically according to their complexity on rungs of a ladder, from the simplest to the most sophisticated, Figure 3.3.1. Furthermore, XC functionals can be categorized into *non-empirical* (formulated only by satisfying some physical rules) and *empirical* (made by fitting to the known results of atomic or molecular properties).

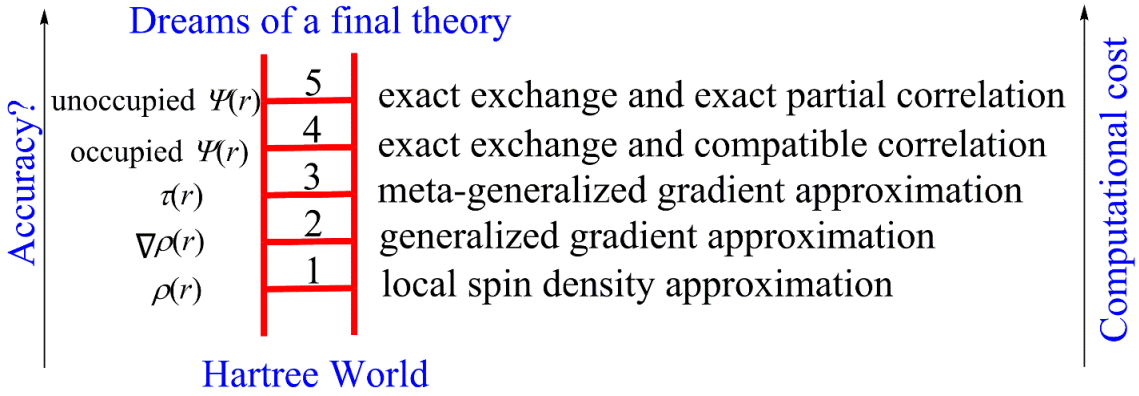

Figure 3.3.1. Jacobs's ladder of density functional approximations.

3.3.1. Local Spin Density Approximation (LDA)

LDA[61] depends solely upon the value of the electron density at each point in space. Within this approximation a real inhomogeneous system is divided into infinitesimal volumes and the electron density in each of the volumes is taken to be constant. The E_{xc} for the density within each volume is assumed to be the E_{xc} obtained from the uniform electron gas for that density:

$$E_{xc}^{\mathrm{LDA}}[\rho(r)] = \int \rho(r)\epsilon_{xc}^{unif}\left(\rho(r)\right)dr$$

Eq. 3.3.1.1.

where ϵ_{xc}^{unif} is the XC energy per particle of the interacting uniform electron gas of density $\rho(r)$. The E_{xc} is decomposed into exchange, E_x, and correlation, E_c, terms linearly,

$$E_{xc} = E_x + E_c$$

Eq. 3.3.1.2.

The analytical expression for the exchange energy, E_x, is known exactly[54, 56]:

$$E_x^{\mathrm{LDA}}[\rho(r)] = -\frac{3}{4}\left(\frac{3}{\pi}\right)^{1/3} \int \rho^{4/3}(r)\, dr$$

Eq. 3.3.1.3.

The calculation of the E_c is not straightforward and only limiting expressions for the correlation density are known exactly, leading to numerous different approximations for correlation energy per particle. In the high- and low-density limits corresponding to infinitely-weak and infinitely-strong correlation, energy density is, respectively[17]:

$$\epsilon_c = A\ln(r_s) + B + r_s(C\ln(r_s) + D)$$

Eq. 5.3.1.4.

$$\epsilon_c = \frac{1}{2}\left(\frac{g_0}{r_s} + \frac{g_1}{r_s^{3/2}} + \cdots\right)$$

Eq. 5.3.1.5.

where the Wigner-Seitz radius, r_s, is related to the density as follows,

$$\frac{4}{3}\pi r_s^3 = \frac{1}{\rho}$$

Eq. 5.3.1.6.

Accurate quantum Monte Carlo simulations for the energy of homogeneous electron gas have been performed for several intermediate values of the density, providing accurate values of the correlation energy density.[62] The most favored LDA's to the correlation energy density interpolate these accurate values obtained from simulation while reproducing the exactly known limiting behavior. Various approaches, using different analytic forms for ϵ_c, have generated several LDA's for the correlation functional, and Vosko-Wilk-Nusair (VWN)[61] represents the most popular one.

Generally, LDA provides good geometries, although bond lengths are usually underestimated, vibrational frequencies or charge densities. However, the LDA is not a good approximation for systems with weak bonds or for prediction of the thermodynamic properties.

3.3.2. Generalized Gradient Approximation (GGA)

Since the KS density is non-local, and a purely local approximation seemed not to be enough, the further approximation needed to be introduced. The most frequently used way is to introduce the gradient of the density to create the Generalized Gradient Approximation (GGA) in which the potentials depends both on the value of the density, and on the value of the gradient of the density in a point of the space. GGAs usually correct the results obtained at LDA level of theory. However, it should be pointed out that the use of GGA functionals does not always mean an improvement over the LDA results. In this work we will show that for most of the systems studied, e.g. small, aromatic, organic radicals, organometallic compound, metalloid clusters, the choice of a specific GGA, e.g. BP86[63, 64] or OPBE,[65] does not affect the final results.

3.3.3. The Hybrid Functionals

The hybrid functionals represent the class of DFT approximations obtained by linear combination of the exact exchange interaction calculated from the HF theory and E_x and E_c from standard functionals. The exact exchange, taken from the HF and incorporated into the hybrids, is expressed as follows,

$$E_x^{\mathrm{HF}} = -\frac{1}{2}\sum_{i,j}\iint \Psi_i^*(r_1)\Psi_j^*(r_1) - \frac{1}{r_{12}}\Psi_i(r_2)\Psi_j(r_2)dr_1dr_2$$

Eq. 3.3.2.1.

One of the most commonly used version of hybrids is B3LYP,[63] which stands for Becke, 3-parameter, and Lee-Yang-Parr.

Although the computational cost of hybrids is much higher in comparison to the LDA and GGA functionals, such approximations have been shown to offer noticeably improved performance over LDA and GGA levels of theory for the calculations of gas phase properties of molecules and solids.[66-69]

Nowadays, more sophisticated approximations to the XC functionals have appeared, e.g. meta-GGAs and meta-hybrids. The meta-functional is referred typically to one that includes a dependence on the kinetic energy density, i.e. on the Laplacian of the orbitals.[41]

3.4. DFT Calculation of the Jahn-Teller Ground State Properties – MD-DFT Method

The group theory consideration can be used for a qualitative discussion about JT distortion, although the degree of the distortion and how big the energy gain is due to the descent in symmetry remain unknown. The first goal in the analysis and characterization of the JT system is the determination of the JT parameters which quantify the potential energy surface: the E_{JT}, which gives energy stabilization due to the JT effect, the warping barrier (Δ) which gives the energy difference between two minima LS structures, and the JT radius (R_{JT}), which shows a direction and magnitude of the distortion, Figure 3.4.1. These parameters are directly connected to the vibronic coupling constants discussed in Chapter 2, and their relationship depends on the model used. For example, using the second order Taylor expansion around the HS point, the JT parameters for $E \otimes e$ are:[1]

$$R_{JT}^{min} = \frac{|F|}{K - 2|G|}$$

Eq. 3.4.1.

$$R_{JT}^{TS} = -\frac{|F|}{K + 2|G|}$$

Eq. 3.4.2.

$$E_{JT} = \frac{F^2}{2(K - 2|G|)}$$

Eq. 3.4.3.

$$\Delta = \frac{4E_{JT}|G|}{K + 2|G|}$$

Eq. 3.4.4.

These expressions are typically used in the MD-DFT analysis of the $E \otimes e$ JT problem.[18] However, similar equations taking into account for example anharmonicity, as well as for other type of the JT problems can be found in literature.[1]

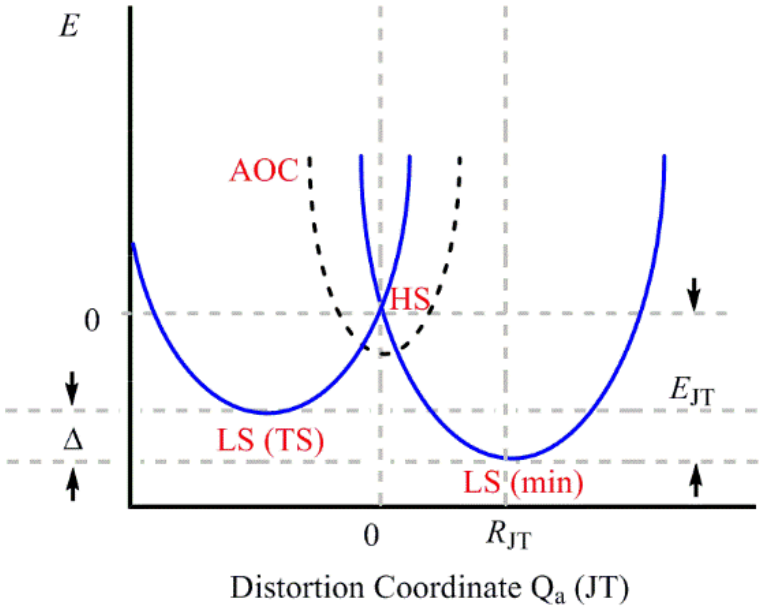

Figure 3.4.1. Qualitative cross section through the potential energy surface, along JT active distortion coordinate Q_a; Definition of the JT parameters - the JT stabilization energy, E_{JT}, the warping barrier, Δ, the JT radius, R_{JT}.

To obtain these variables it is necessary either to perform the experiment, and fit the results to the proposed model, or to carry out a computational study. The experimental determination of the JT distortion is very difficult and there is no consistency between the different methods. Therefore, preference is given to the theoretical simulations,[70] either to complement the experiment, or to understand and seek the microscopic origin of the vibronic coupling effects. In spite of the general success in application of the DFT, the modern alternative to the wavefunction-based *ab initio* methods, in variety of tasks in chemistry and physics, there are still somewhat troublesome issues, like treatment of the excited states, weak interactions, and degenerate states. Substantial progress in dealing with these issues has been made lately.[71] Degeneracy of electronic states is particularly difficult to deal, and consequently requires special caution.[72-74] DFT can rigorously treat degenerate states either by reformulation of original Hohenberg-Kohn theorem using constrain search formalism[75] or sub-system ensemble DFT.[76, 77] MD-DFT, developed by Daul et al.,[18] successfully treats the degenerate states and offers fast and easy way to calculate properties of medium-to-large sized molecules. Numerous JT active molecules have been accurately analyzed by the means of MD-DFT.[18-21, 78-80]

The underlying idea of the MD-DFT approach in the analysis of the JT distortion is to know geometries and energies of the HS and LS points on the APES and the

calculation procedure consists of the three steps. Shwarz[81] and Baerends[82] pointed out that a single determinant KS-DFT is insufficient in the description of degenerate electronic states. Thus, the electronic state of the HS configuration requires to be represented with more than one Slater determinants. It was proposed to use the average of configuration (AOC) SCF calculation,[18] where the degenerate orbitals are equally populated, leading to a homogenous distribution of electrons over the components of the degenerate irreducible representation, in order to retain the A_1 symmetry of the total electron density in the HS point group. E.g. for e^3 electronic configuration, 1.5 electrons are placed into each of the two *e* orbitals. Obviously, AOC type calculation approximates the electronic structure, if the vibronic coupling would not be present. The AOC approach gives a proper geometry of HS species (step 1), but using simply the energy obtained in this way would be false,[83] and consequently the JT stabilization energy is not the energy difference between the HS and LS points. This issue is due to the self-interaction error (SIE) present in the approximate exchange, which is sometimes referred to as overestimation of the delocalization by approximate DFT. In approximate DFT the Coulomb interaction is treated exactly, while the exchange part is approximated and for a single electron these two terms should cancel each other. The residual interaction of the electron with itself, SIE, will always artificially stabilize the energy of systems having fractional number of electrons compared to the corresponding ones with integer number of electrons. In order to compare the LS geometries with HS structure, the unpaired electron needs to be distinguishably placed in one of the degenerate orbitals. To tackle this problem, a single point calculation imposing the HS symmetry on the nuclear geometry and the LS on the electron density, should be used (step 2). This gives the energy of a Slater determinant with an integer electron orbital occupancy. The last, straightforward step, involves geometry optimization of the LS structure with the proper occupation of KS orbitals. This yields the different LS geometries and energies that correspond to the minimum and to the transition state on the potential energy surface, respectively. The E_{JT} is the difference in energy obtained in the second and last step for the structures with the same electron distribution. In order to quantify the JT distortion, a vector $\vec{R}_{JT}$ is defined as the vector between the HS and LS nuclear configurations. The $\vec{R}_{JT}$ is given by the length of the distortion vector between the HS and the LS minimum

energy configurations. The MD-DFT calculation scheme for the particular example of the JT effect in hexaflurocuprat(II) ion, $[CuF_6]^{4-}$, is presented in Figure 3.4.2.

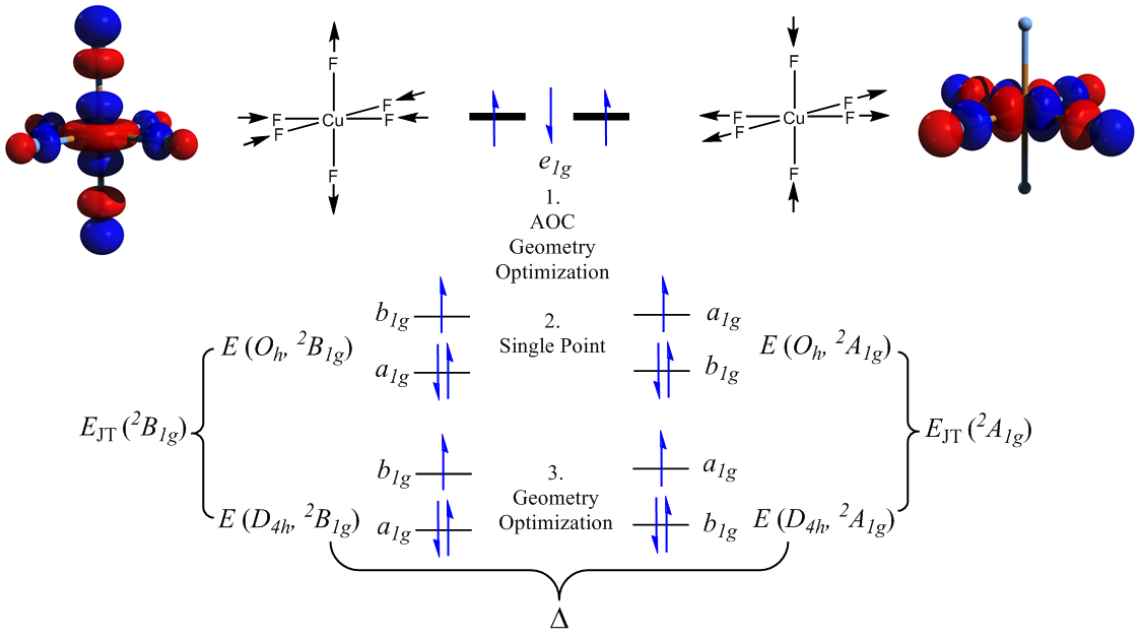

Figure 3.4.2. MD-DFT approach for the calculation of the JT parameters for the $O_h \rightarrow D_{4h}$ distortion of $[CuF_6]^{4-}$ ion.

3.5. DFT Calculations of the Excited State Properties

In the last few decades DFT has become the method of choice for calculation of the ground state properties of large molecules, by replacing the interacting many-electron problem with an effective single particle problem that can be promptly solved. Officially, classic DFT formalism can only predict properties of the ground electronic states, and cannot describe excited electronic states. Concerning electron excitations, DFT was first used in the framework of ΔSCF approach.[51, 84-86] Another method which has been proven to perform well in the determination and understanding of excited state properties of coordination compounds, and is also computationally cheap, is Ligand Field Density Functional Theory.[87] The most popular DFT based method for the calculations of excited states is the Time-Dependent Density Functional Theory (TD-DFT).[88-94] Unfortunately, as in the ground state DFT, the exact form of the effective potential remains secluded, and the approximations have to be administered in order to get access to nonlinear optics

properties, and via linear-response theory introduced to TD-DFT,[95] to excited state information of medium- to large-sized molecules.

The major application of TD-DFT is the evaluation of vertical excitation energies and the calculation of the electronic absorption spectra.[96, 97] TD-DFT is not only capable for simulation of vertical transition energies,[98] but also for predicting excited state structures,[99] investigation of the excited state potential energy surfaces, emission wavelengths,[96] dipole moments,[100] and circular dichroism spectra of chiral molecules[101, 102]. Photochemical reaction mechanisms certainly represent the challenging task for TD-DFT. However, nowadays it is possible to perform mixed TD-DFT/classical trajectory surface-hopping calculations in order to get better insight of the potential mechanisms and reaction branching ratios.[103-107] Recently proposed subsystem formulation of TD-DFT[108] has shown to be very successful for the calculations of multi-chromophoric systems.[109, 110] TD-DFT, a relatively young technique, has become a hot topic in the world of quantum chemistry since it can provide accurate results at a low computer cost. Still, there are cases where it failed to reproduce the experimentally obtained data.[111, 112]

4. Aromaticity

Aromaticity and its antipode, antiaromaticity, examples of chemical concepts,[113-117] are vastly used to intuitively describe chemical bonding in organic chemistry. Delocalized electronic structure of aromatic compounds yields enhanced planarity, equalized bond lengths, enhanced stability, favoring of substitution instead of addition that would be typical for isolated double bonds, and the ability to sustain ring currents when exposed to external magnetic fields. In spite of diverse utilization of aromaticity and antiaromaticity, these two concepts are still mainly applicable to molecules with an even number of electrons. The Hückel Molecular Orbital (MO) theory proposed that species with 4n+2 π electrons are aromatic, whereas structures with 4n π electrons are defined as antiaromatic.[118, 119] Molecules with odd number of π electrons are supposed to show antiaromaticity.[120-123]

Removal of one electron from 4n+2 π system should result in a 4n+1 π system, and transition from aromaticity to antiaromaticity is expected. Understanding this transition and relation between 4n+2 π and 4n+1 π systems is connected fundamentally to the understanding of concepts of aromaticity and antiaromaticity. Detachment of electron from typical aromatic molecule, which is closed shell, planar, highly symmetric and with degenerate frontier orbitals, will lead to a 4n+1 π molecule in a degenerate electronic state that is subject to the JT effect. Since the JT theorem states that a molecule with a degenerate electronic state distorts along non-totally symmetric vibrational coordinates by removing the degeneracy and lowering the energy, it is obvious that the JT effect is in sharp contrast to the aromaticity. In other words, the JT effect induces unequalization of bond lengths, leading to the stabilization of the system upon distortion. The detailed analysis how the JT distortions influence the antiaromaticity will be shown in Chapter 8, where the answer to the question whether the JT effect can be regarded as the origin of the antiaromaticity in the systems with 4n+1 π electrons will be given.

Although the Hückel rules of aromaticity, based on a number of electrons in π MOs, are very appealing due to their simplicity, they actually neither quantify nor give physical explanation of this intriguing effect. Because of the importance of aromaticity, there have been many attempts to rationalize it and to derive a universal quantitative measure of it.[114, 115, 117, 124] Aromatic compounds possess specific magnetic properties such as: proton

chemical shifts, magnetic susceptibility exaltation, nucleus-independent chemical shifts (NICS) and ring current plots.[125-128] Beside vastly used magnetic properties, there are also other criteria for the definition and analysis of aromaticity: structural (geometric) criterion, energetic criterion - enhanced stability (large resonance energy), as well as the determination of the most significant $T_{x,y}$ (translationally)- and R_z (rotationally)-allowed occupied→unoccupied MO transitions[129] and adaptive natural density partitioning analysis[130], and so forth. Each of these properties can be used to probe the aromaticity of a molecule, though unfortunately, they do not need to be consistent with each other.

Computed NICS indices are presently the most widely used and are a very efficient tool for the exploration of this phenomenon. NICS index is the negative of magnetic shielding which is computed at a point of interest in space. The diamagnetic and paramagnetic effects of the ring currents associated with aromatic and antiaromatic features (i.e., shielding and deshielding of nuclei) can be determined according to the calculated NICS index. Negative NICS values in interior positions of rings indicate the presence of induced diatropic ring currents, or aromaticity, whereas positive values denote paratropic ring currents and antiaromaticity. The more negative the NICS values, the more aromatic the rings are. NICS parameters can be computed at selected points inside or around molecules, typically at ring centers and above. NICS values calculated at the geometrical center of the ring are denoted as NICS(0).[131] Similarly, NICS values at 1 Å above the perpendicular plane of the rings are defined as NICS(1), and the $NICS(1)_{zz}$ tensor component has been presented to provide better insight of the overall molecular magnetic properties. It was suggested that this latter quantity gives the best measure of aromaticity among the different NICS related definitions.[132] NICS(0) and $NICS(1)_{zz}$ values describe rather different effects. It is likely that $NICS(1)_{zz}$ values account mainly for the π aromaticity effect, while NICS(0) results better reflect both, the σ and π aromaticity or antiaromaticity effects.

Initially aimed to describe properties of planar organic cyclic compounds, with 4n+2 π electrons, concept of aromaticity, has been extended to 4n triplet aromaticity,[133] pericyclic transition states,[134] Möbius aromaticity,[135] 3D and spherical aromaticity,[136] as well as to the aromaticity of inorganic compounds[137-139]. In spite of a large number of papers devoted to the aromaticity of these various systems, the molecules prone to the JT distortion are relatively infrequently studied.[120-122] In attempt of seeking the origin,

explanation and understanding of these two confronting phenomena, the influence of the JT distortion on the aromaticity in small organic radicals, organometallic compound, fullerene ions and inorganic clusters will be given in details in the Chapter 8.

5. Excitonic Coupling

Conjugated π-systems are deservedly the subject of extensive experimental and theoretical studies, considering that π-conjugated smart materials have become increasingly important in everyday life.[140-152] A comprehensive collection of their electronic spectra and electronic and structural properties has been presented over decades, with regard to their remarkable applicability in organic light-emitting diodes (OLED)[153], in semi-conducting layers of field-effect transistors (FET),[140, 151, 154, 155] as well as in organic solar cells which are being developed as cheap substitutes for silicon-based solar cells. However, the low energy conversion efficiency of organic solar cells is the main bottleneck, which still limits their usage. This is partially due to rather inefficient excitation energy transport (EET)[150, 156] within the organic materials. For designing improved organic materials, all occurring processes and the effects determining their efficiency need to be ascertained and eventually well understood.

To investigate EET pathways in organic materials theoretically, the first step is the calculation of the excitonic coupling (EC) between individual chromophores using quantum chemical methods for the excited states of the system, because the qualitative character and the quantitative rate of EET is determined by EC.[144, 157, 158] EET usually occurs from an electronically excited molecule to a non-excited spatially close molecule with lower excitation energy via Förster, when Coulomb coupling dominates, or Dexter-type (exchange coupling), or both transfer mechanisms between excitonically coupled dimers.[159] In general, two types of EET are distinguished, in-coherent and coherent EET[160]. The first is often described as "hopping" of excitation energy from one site to the other, i.e. the exciton is localized on one monomer unit due to its geometry relaxation and then transferred dynamically to a neighboring site. The latter one is usually understood in terms of delocalized excited electronic states over several chromophores and the monomer units remain structurally identical. However, most real cases of practical importance belong to intermediate situations.

In EC theory, the Hamiltonian of two monomer units in a coupled dimer is separated into intramolecular and intermolecular contributions as follows,

$$\hat{H}_{exciton} = \sum_{m} \hat{H}_m(R) + \frac{1}{2}\sum_{mn} \hat{V}_{mn}(R)$$

Eq. 5.1.

H_m describes each individual monomer, while V_{mn} describes all Coulomb interactions between coupled monomer units. If only the electronic part of the interaction between monomer 1 and 2 is considered,

$$\hat{V}_{mn} = \hat{V}_{12}^{el-el}$$

Eq. 5.2.

It follows that,

$$\langle \Phi_{1a2a} | \hat{V}_{12}^{el-el} | \Phi_{1b2b} \rangle = V_{exciton}$$

Eq. 5.3.

where Φ_{1a2a} is an anti-symmetric expansion of the electronic states of the dimer, and $V_{exciton}$ is electronic coupling matrix element between the two states. Expansion of the Hamiltonian in the two-state basis of degenerate coupled excited states and diagonalization gives the eigenvalues of the coupled states as

$$\varepsilon_{\pm} = E_{ex} \pm V_{exciton}$$

Eq. 5.4.

where E_{ex} is the energy of the uncoupled states. In the two-state dimer case, the energy difference between the coupled states corresponds to $2V_{exciton}$. Electronic coupling matrix element depends on the intermolecular coordinates. In the weak coupling case,[161] where the relaxation energy of the donor is significantly higher than the electronic coupling between donor and acceptor, the rate for the EET is given by Fermi's golden rule[162]:

$$k_{\mathrm{EET}} = \frac{2\pi}{\hbar} |V_{exciton}|^2 J_{\mathrm{EET}}$$

Eq. 5.5.

J_{EET} represents the Franck-Condon weighted density, i.e. the overlap of the bands of the donor fluorescence and acceptor absorption spectra. $V_{exciton}$, electronic coupling matrix element between the two neutral excited (NE) states, Frenkel excitations, depends on the intermolecular separation, R, and individual transition dipole moments, $\vec{D}$, as it is given by well-known Förster formula[163, 164],

$$V_{exciton} = \frac{\vec{D}_1\vec{D}_2}{R_{12}^3} - 3\frac{(\vec{D}_1\vec{R}_{12})(\vec{R}_{12}\vec{D}_2)}{R_{12}^5}$$

Eq. 5.6.

Besides NE states, the energy transfer properties can also be influenced by charge transfer (CT) states, and thus both kinds of states and their mutual interaction are necessary for the proper description of EET. The definitions of NE and CT states for excitonically coupled dimer in a localized picture is straightforward.[165] In NE state, where an electron is excited from an occupied orbital of one monomer unit to a virtual orbital of itself, Figure 5.1., no charge separation occurs. If an electron is excited from one monomer unit to another, CT state can be defined, Figure 5.1. According to the definition of the CT state, it can be supposed that CT excitation includes a charge separation, which sometimes can lead to the wrong conclusion. However, it is possible that a CT state includes simultaneous excitation from one monomer unit to another in a dimer system. Briefly, an excitation from monomer 1 to monomer 2, and an excitation from 2 to 1 may introduce same amount of charge separation and compensate each other, and thus dipole moment of the system remains unaltered. This situation takes the place when the monomers are symmetrical to each other e. g. when the system has a center of inversion or a mirror plane. The insight into the corresponding orbitals represents a usual way to distinguish the character of an excited state related to the excitation. The qualitatively correct excited state character can be predicted in a simple way if the corresponding orbitals are localized to each monomer. The complication arises if some of the corresponding orbitals are delocalized over the dimer, especially when symmetry is used for the calculation of the reference wavefunction, and the specification of the excited state character cannot be easily determined.

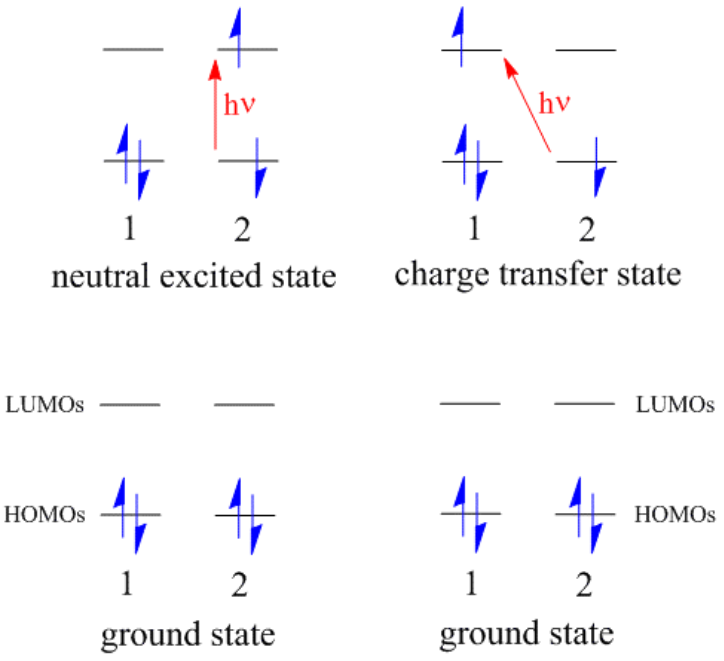

Figure 5.1. Schematic representation of neutral excited (NE) and charge transfer (CT) states.

In summary, the calculation of EC between individual chromophores, which determines the qualitative character and the quantitative rate of EET, can be obtained from quantum chemical calculations of the excited states of the system, but there are three basic problems: (1) An accurate description of excited states is in general not straightforward. (2) The huge size of the molecular systems prohibits the use of accurate theoretical methods. (3) This type of analysis necessarily requires a picture of locally excited states of the individual chromophores. Quantum-chemical calculations, however, typically yield a delocalized picture, which prohibits, or at least severely complicates, the extraction of ECs.

Two major competing energetic effects determine whether the excited state is localized on one site of the dimer: EC and geometry relaxation. Depending on the relative size of these contributions, the dimer either relaxes its geometry leading to localization of the excited state on one site, or the monomer units remain structurally identical and the excited state stays delocalized. Since EC is strongly distance dependent, it is clear that the distance between the sites tunes also the ratio between these two energetic contributions.

In order to understand the geometry relaxation of an electronically excited dimer, or equivalently, the localization of the exciton, it is necessary to explicitly take nuclear motion into account. Many theories exist for the description of EET processes[160], however, only a very few studies are available that consider both electronic and vibrational contributions to the energy transfer process in a rigorous, quantum mechanical way.[158, 166-168] Typically, the effect of vibrations is often included as dynamic disorder in the electronic coupling.[169, 170] The coupling between electronic and vibrational degrees of freedom is generally quantified by the so-called non-adiabatic couplings,[171] and structural, symmetry-breaking distortions can be explained in this framework by JT and PJT theory.[1] Thus, the understanding of the localization mechanism of excited states and the driving forces responsible for it, in the framework of the established PJT formalism and Förster's degenerate perturbation theory approach[164], is not a simple task. The model for the reliable description, interpretation and prediction of EC taking into account vibronic coupling, and the interplay between these two effects was developed and the theory lying behind can be found in the Chapter 9, Section 9.1.

6. Results and Discussion: The Choice of the Exchange-Correlation Functional for the Determination of the Jahn-Teller Parameters by DFT

The accuracy of DFT calculations predominantly depends on the suitability of the approximations made for the XC functional. In contrast to the wavefunction based methods, DFT lacks a procedure to systematically improve the accuracy, and one of the biggest skills in employing DFT to reproduce and predict various properties of molecules, is the proper choice of XC functional. Much of the research in the field of DFT is devoted to developing new XC functionals, which will yield to the results of better quality. Different XC functionals give more or less accurate results for the different problems under study.[172-177] The choice of XC functional to be used in practice depends primarily on the chemical nature of the system and the problem under study. Having in mind the importance of the JT effect, proper determination of the JT parameters represents a fundamental task in order to get deeper insight into the vibronic coupling. Definition of the JT parameters is given on Figure 3.2., and their relation to the vibronic coupling constants are shown in Chapter 2. MD-DFT can be successfully employed for simulations in systems where electron degeneracy or near-degeneracy requires use of multideterminantal approaches, but the selection of XC functional is still crucial for the quality of the results. It is noteworthy that none of the present-day approximate XC functional was constructed to deal with the vibronic coupling effects, and thus, there are no guarantees when selecting XC approximation, but some general guidelines in analysis of the JT effect in the simple and efficient way are offered.

In order to clarify which XC functional should be used for study of the JT effect within MD-DFT framework, the molecules which differ in the nature of chemical bonding, range of E_{JT}, symmetry of distortion, and also type of the JT problems ($E\otimes(b_1+b_2)$, $E\otimes e$) were chosen. Results for small, aromatic, organic radicals, C_nH_n (n=4-7); corannulene anion and cation ($C_{20}H_{10}^-$ and $C_{20}H_{10}^+$) and coronene anion and cation ($C_{24}H_{12}^-$ and $C_{24}H_{12}^+$) are given in Table 6.1. MD-DFT results for small metal clusters - sodium cluster (Na_3) and silver cluster (Ag_3); arsenic and antimony clusters (As_4^- and Sb_4^-); Werner type complexes - hexaflurocuprat(II) ion ($[CuF_6]^{4-}$); tris(acetylacetonato)manganese(III) ($[Mn(acac)_3]$) and organometallic compound -

bis(cyclopentadienyl)cobalt(II) (cobaltocene, $CoCp_2$) are presented in Table 6.2. The XC functionals used for the determination of the JT parameters are LDA characterized by the VWN parameterization,[61] and GGAs, such as BP86,[63, 64] BLYP,[63, 178] OPBE[65] and hybrid B3LYP[179, 180]. It is noteworthy that the experimental determination of the JT parameters is very difficult and there are often uncertainties in the values, because they are obtained from fitting to different models. Conversely, theoretical values fall within a broad range, hence, it is often hard to say which value is the reference one.

Cyclobutadienyl radical cation ($C_4H_4^{+\bullet}$), cyclopentadienyl radical ($C_5H_5^{\bullet}$), benzene cation ($C_6H_6^{+}$), benzene anion ($C_6H_6^{-}$), tropyl radical ($C_7H_7^{\bullet}$), $C_{20}H_{10}^{-}$, $C_{20}H_{10}^{+}$, $C_{24}H_{12}^{-}$ and $C_{24}H_{12}^{+}$ have a single electron or a hole in a doubly degenerate highest occupied molecular orbital, representing the family of the JT active hydrocarbon rings. Unlike the $C_5H_5^{\bullet}$, $C_6H_6^{+}$, $C_6H_6^{-}$, $C_7H_7^{\bullet}$, $C_{20}H_{10}^{-}$, $C_{20}H_{10}^{+}$, $C_{24}H_{12}^{-}$ and $C_{24}H_{12}^{+}$ which are the examples of $E\otimes e$ problem, $C_4H_4^{+\bullet}$ presents paradigm of $E\otimes(b_1+b_2)$ JT problem (see Chapter 2, Section 2.3).

The previous CASSCF calculation for $C_4H_4^{+\bullet}$ revealed the E_{JT} of 2637 cm^{-1},[181] which is in agreement with our results. $C_5H_5^{\bullet}$ is one of the most studied JT active molecules both experimentally and theoretically. The results by Miller et al. who used dispersed fluorescence spectroscopy are considered to be benchmark result (E_{JT}=1237 cm^{-1}).[182] MD-DFT calculation at LDA level of theory gives the value of 1244 cm^{-1}, which is even better than the values obtained by high level *ab initio* calculations.[182, 183] The calculated data for $C_6H_6^{+}$ are in accordance to the previous theoretical studies, which report the value of E_{JT} between 700 and 1000 cm^{-1}.[184-186] The experimentally estimated JT stabilization energy for $C_7H_7^{\bullet}$ is 1043 cm^{-1}, whereas a previously theoretically obtained value is 1374 cm^{-1}.[187] The obtained values for the JT parameters with different XC functionals are consistent (Table 6.1), except for the case of B3LYP where an overestimation of E_{JT} can be noticed. This is not surprising, as B3LYP has a tendency to overestimate the exchange and correlation energies of localized electrons.[188] In the case of $C_6H_6^{+}$, different XC functionals lead to a different ground electronic state in the D_{2h} point group. LDA gives the $^2B_{2g}$ state, whereas GGA and B3LYP give $^2B_{3g}$ as the minimum on the potential energy surface, Table 6.1. As the values of the warping barrier are in the range from -39.5 cm^{-1} to 29.1 cm^{-1}, the JT effect can be considered as dynamic, independent of the choice of the XC functional used. The warping barrier is

experimentally reported to be 8 cm^{-1}, and the $^2B_{2g}$ state to be a minimum,[189] although this result has to be taken with caution since the experimental techniques are often ambiguous in the investigation of the JT effect. In all cases good agreement with both experimental and theoretical data is achieved.[181, 182, 184-187, 189-198]

The JT parameters for $C_{20}H_{10}^-$, $C_{20}H_{10}^+$, $C_{24}H_{12}^-$ and $C_{24}H_{12}^+$ do not depend significantly on a selection of XC functionals, except in the case of B3LYP where slightly higher values were noticed, Table 6.1. This is in agreement with the results on the JT active small aromatic organic radicals. In the case of $C_{20}H_{10}^-$, Yoshizawa et al. calculated E_{JT} of 952 cm^{-1} with B3LYP functional.[199] HF and MP2//HF calculations highly overestimated E_{JT} with the values of 2525 and 3984 cm^{-1}, respectively.[200] MD-DFT E_{JT} values are in the range of 404-540 cm^{-1}, depending on the chosen XC functional, Table 6.1. The warping barrier between the five equivalent minima is experimentally estimated to be 18 cm^{-1} using electron spin resonance (ESR) spectroscopy,[201] and previous DFT/B3LYP value[199] was 2.4 cm^{-1}. The warping barrier obtained with MD-DFT method is close to zero, or at least very small, independently of the choice of XC functional used. This is in accordance with the group theory analysis for the JT molecules with C_5 main axes in the HS nuclear arrangement.[19] The E_{JT} values for $C_{20}H_{10}^+$ are slightly higher in comparison to the results obtained for $C_{20}H_{10}^-$, at all levels of theory, Table 6.1. Different ground states obtained by different XC functionals (Table 6.1.) are due to the very small warping barriers, which are in the range of the precision of the calculation. According to earlier DFT/B3LYP study,[202] the values of E_{JT} for $C_{24}H_{12}^-$ and $C_{24}H_{12}^+$ were 645 and 484 cm^{-1}, respectively, which is in very good agreement with the MD-DFT computations, Table 6.1. Regarding $C_{24}H_{12}^-$, Sato et al. obtained the JT stabilization energy to be 2395 cm^{-1} at MP2//HF level.[203] The MD-DFT E_{JT} values fall in the range of 290-410 cm^{-1}, Table 6.1. Former *ab initio* calculations revealed that C_{2h} represents the global minimum point on the potential energy surface, and the energy barrier between C_{2h} and D_{2h} structures was reported to be less than 0.8 cm^{-1}.[203] The MD-DFT calculations revealed even smaller value of 0.3 cm^{-1}. The JT effect was not observed in the ESR spectra, even at low temperature.[201, 204] According to the observed hyperfine coupling (HFC) constants all hydrogen atoms are equivalent due to the very small warping barrier. The pseudorotation about the D_{6h} JT crossing makes the HFC constant averaged.

Table 6.1. Results of the DFT calculations performed to analyze the JT effect of minimum on the potential energy surface for small, aromatic, organic radicals, C_nH_n (n=4-7), corannulene anion and cation ($C_{20}H_{10}^-$ and $C_{20}H_{10}^+$) and coronene anion and cation ($C_{24}H_{12}^-$ and $C_{24}H_{12}^+$); the JT parameters E_{JT} and Δ are given in cm^{-1} and R_{JT} in $(amu)^{1/2}$Å.

	Distortion		LDA	BP86	BLYP	OPBE	B3LYP
$C_4H_4^{+\bullet}$	$D_{4h}\rightarrow D_{2h}$	E_{JT}	2418	2470	2497	2413	2649
		Δ	2595.5	2046.2	2220.4	1902.7	1842.2
		R_{JT}	0.31	0.32	0.33	0.31	0.32
$C_5H_5^\bullet$	$D_{5h}\rightarrow C_{2v}$	E_{JT}	1244	1302	1303	1300	1686
		Δ	0.0	-0.8	-0.8	-1.6	0.0
		R_{JT}	0.25	0.26	0.27	0.26	0.27
$C_6H_6^+$	$D_{6h}\rightarrow D_{2h}$	E_{JT}	879	885	880	891	970
		Δ	29.1	-37.1	-8.1	-62.9	-39.5
		R_{JT}	0.27	0.28	0.28	0.28	0.28
$C_6H_6^-$	$D_{6h}\rightarrow D_{2h}$	E_{JT}	788	834	857	824	925
		Δ	38.7	39.5	40.3	33.1	17.7
		R_{JT}	0.19	0.19	0.19	0.19	0.29
$C_7H_7^\bullet$	$D_{7h}\rightarrow C_{2v}$	E_{JT}	853	923	936	917	1123
		Δ	0.0	0.0	0.0	0.0	0.0
		R_{JT}	0.16	0.17	0.17	0.16	0.18
$C_{20}H_{10}^-$	$C_{5v}\rightarrow C_s$	E_{JT}	405	417	424	410	540
		Δ	1.6	1.6	0.0	1.6	0.8
		R_{JT}	0.32	0.31	0.30	0.30	0.34
$C_{20}H_{10}^+$	$C_{5v}\rightarrow C_s$	E_{JT}	548	536	525	551	665
		Δ	2.4	0.0	0.8	0.0	1.6
		R_{JT}	0.53	0.51	0.49	0.53	0.58
$C_{24}H_{12}^-$	$D_{6h}\rightarrow D_{2h}$	E_{JT}	290	302	315	302	410
		Δ	12.1	5.6	8.9	12.9	0.8
		R_{JT}	0.12	0.13	0.14	0.13	0.15
$C_{24}H_{12}^+$	$D_{6h}\rightarrow D_{2h}$	E_{JT}	287	302	304	303	401
		Δ	12.9	6.4	7.3	12.1	0.0
		R_{JT}	0.19	0.20	0.20	0.20	0.22

The electronic structures of Na_3 and Ag_3 molecules are determined primarily by the behavior of three valence electrons (one donated by each Na or Ag atom). In the HS, D_{3h} point group, sodium and silver clusters are in the degenerate electronic states. The JT distortion leads to the splitting of the degenerate state $^2E_1'$ into $^2A_1$ and $^2B_2$ with a descent in symmetry to C_{2v}. According to the DFT calculations, the $^2B_2$ state is the global minimum, while the transition state on the potential energy surface is $^2A_1$. Analyzing the influence of different XC functionals for Na_3 and Ag_3 clusters revealed that BLYP approximation overestimates the JT stabilization energy, the warping barrier and the JT

radius, Table 6.2., and the geometry differs significantly. The DFT results at BLYP level give one bond length to be 6.5 Å and other two 3.3 Å and one angle with the value of 164.5° and other two 7.3°, which are far from the results obtained with the other applied XC approximations and reference values.[205] The same trend was observed for the Ag_3 molecule. Hence, the BLYP is shown to be less accurate than other applied XC functionals. In both cases, good agreement with previous theoretical studies is obtained,[1, 35, 205-210] with the exception of the aforementioned BLYP, Table 6.2.

Arsenic and antimony anionic four-member rings, As_4^- and Sb_4^-, have a single electron in a doubly degenerate HOMO, leading to ^2E_g ground electronic state, in perfect square-planar nuclear configurations that belong to the D_{4h} point group. Hence, these molecules are JT unstable, and distort to the conformations of lower, D_{2h} symmetry, with the rectangular or rhombic geometries. ^2E_g ground electronic state splits into two non-degenerate electronic states, $^2B_{3g}$ and $^2B_{2g}$ in D_{2h} point group (see Chapter 2, Section 2.3.). MD-DFT results are summarized, in Table 6.2. In all cases rectangle, with $^2B_{3g}$ electronic state is the minimum structure, while $^2B_{2g}$ rhombus is the transition state on the potential energy surface. Calculated JT stabilization energies are consistent to each other, independently of the chosen XC functional.

Table 6.2. Results of the DFT calculations performed to analyze the JT effect of minimum on the potential energy surface for Na_3, Ag_3, As_4^-, Sb_4^-, $[CuF_6]^{4-}$, $[Mn(acac)_3]$ and $CoCp_2$; the JT parameters E_{JT} and Δ are given in cm^{-1} and R_{JT} in $(amu)^{1/2}$Å.

	Distortion		LDA	BP86	BLYP	OPBE	B3LYP
Na_3	$D_{3h}\rightarrow C_{2v}$	E_{JT}	961	1006	1456	708	1182
		Δ	345.2	365.4	759.8	169.4	450.9
		R_{JT}	3.92	4.36	14.27	2.48	5.49
Ag_3	$D_{3h}\rightarrow C_{2v}$	E_{JT}	504	686	966	806	889
		Δ	167.0	289.6	514.6	345.2	394.4
		R_{JT}	2.01	3.39	9.26	4.42	4.97
As_4^-	$D_{4h}\rightarrow D_{2h}$	E_{JT}	703	846	775	948	840
		Δ	774.3	496.2	648.8	149.1	299.7
		R_{JT}	0.09	0.09	0.09	0.09	0.09
Sb_4^-	$D_{4h}\rightarrow D_{2h}$	E_{JT}	556	518	644	528	579
		Δ	596.8	322.9	490.9	133.7	148.2
		R_{JT}	0.08	0.09	0.09	0.09	0.09
$[CuF_6]^{4-}$	$O_h\rightarrow D_{4h}$	E_{JT}	2417	3467	2917	9327	2604
		Δ	804.1	1246.1	1312.3	7337.3	991.3
		R_{JT}	1.89	2.53	2.74	14.05	2.26
$[Mn(acac)_3]$	$D_3\rightarrow C_2$	E_{JT}	1756	1626	1601	843	1785
		Δ	360.5	325.0	313.8	424.3	333.9
		R_{JT}	1.26	1.44	1.45	2.06	1.29
$CoCp_2$	$D_{5h}\rightarrow C_{2v}$	E_{JT}	814	762	694	838	728
		Δ	0	0	-0.8	-1.6	-2.4
		R_{JT}	0.35	0.34	0.32	0.35	0.34

It is a well-known fact of coordination chemistry that hexa-coordinated copper(II) and manganese(III) complexes exibit a strong JT coupling. In the O_h point, the copper(II) ion has a ^2E_g electronic ground state. After descent in symmetry to D_{4h}, the electronic state splits into $^2A_{1g}$ and $^2B_{1g}$, compressed and elongated geometry, respectively. The values for the warping barrier, Δ, Table 6.2., unambiguously indicate that the APES is not flat, thus the state $^2B_{1g}$ is energy minimum, whereas $^2A_{1g}$ is the transition state. The octahedral Cu(II) units in the crystals of K_2CuF_4, Ba_2CuF_6, and so forth, were originally misinterpreted as compressed by EPR measurements and X-ray data.[211-213] More elaborate investigations, including Extented X-Ray Absorption Fine Structures (EXAFS) measurements[214-216] and DFT calculations[217] showed that, in fact, the local octahedra are elongated. However, it should be pointed out that complete understanding of the electronic structure of K_2CuF_4 is difficult considering only isolated $[CuF_6]^{4-}$ fragment, without considering the effects of the electrostatic potential of the rest of the lattice,[217]

unlike the case of $KZnF_3:Cu^{2+}$ where elongated $[CuF_6]^{4-}$ complexes are formed due to the static JT effect.[218] The evaluated E_{JT} values are in the range of 2400-3400 cm^{-1} for all used functionals, with the exception of OPBE, which gives a very high JT stabilization energy. Experimentally estimated E_{JT} from UV-Vis spectra are found to be 2082.5 or 2195.5 cm^{-1} (E_{JT} are extracted from UV-Vis transition using the relation $E \approx 4E_{JT}$).[219, 220] Thus, to explain the differences in R_{JT}, the bond distances in $[CuF_6]^{4-}$ at HS and LS nuclear configurations were analyzed and then compared with the available experimental data, Table 6.3.[221, 222] It can be clearly seen (Table 6.3.) that the LDA gives the most accurate geometry. The OPBE gives quite good results for the equatorial bonds in the D_{4h} global minimum structure with absolute deviations from experimental data of 0 Å. However, axial bond distances are too long (≈4.4 Å), indicating the great discrepancy. This discrepancy can be explained by high negative charge of the complex ion, which is only partially compensated by the conductor like screening solvation model (COSMO) model (see Computational Details Section). COSMO model was employed in order to partially simulate the environmental effects in the crystal lattice of highly negative charged complex.[223] It should be mentioned that without COSMO, fluoride ions as ligands dissociate in D_{4h} symmetry. Other GGA functionals, as well as B3LYP show bigger deviation in the observed equatorial bond distances, and more accurate results for bond lengths in the axial position.

Table 6.3. Calculated DFT and experimental bond lengths (Å) in $[CuF_6]^{4-}$.

$[CuF_6]^{4-}$	LDA	BP86	PW91	BLYP	OPBE	B3LYP	EXP[221]	EXP[222]
O_h, Cu-F	2.01	2.10	2.10	2.10	2.12	2.10	2.02	2.05
D_{4h}, ax-Cu-F	2.28	2.45	2.44	2.51	4.37	2.40	2.22	2.30
D_{4h}, eq-Cu-F	1.91	1.96	1.96	1.97	1.93	1.96	1.92	1.93

The other Werner-type complex, $[Mn(acac)_3]$, has D_3 symmetry with a $^2E_1$ ground state. Because of the JT effect, the symmetry decreases to C_2, whereby the ground state splits into ^2A and ^2B. An axial elongation corresponds to the ^2A state, the minimum on the potential energy surface, while the transition state, compressed octahedron, is in the ^2B electronic state, higher in energy by 313-425 cm^{-1}, Table 6.2., which is in a good agreement with a previous DFT study.[224] The DFT calculations at the OPBE level clearly underestimate the JT stabilization energies, Table 6.2. The differences in the values of the JT parameters can be explained by the differences in the geometries obtained with the

different level of theory. It is well-known that inclusion of gradient corrections leads to bond elongation compared to the LDA results.[176] The overlays of the crystal structure[225] and structures computed at the LDA and OPBE levels are presented in Figure 6.1. Obviously, the structure obtained with LDA matches better to the X-ray structure, which is a confirmation that LDA tends to give better geometries for Werner-type complexes.[176, 226] Therefore, the proper determination of geometry not only in a metric data but also in conformation of the ligands is very important in the determination of JT parameters.

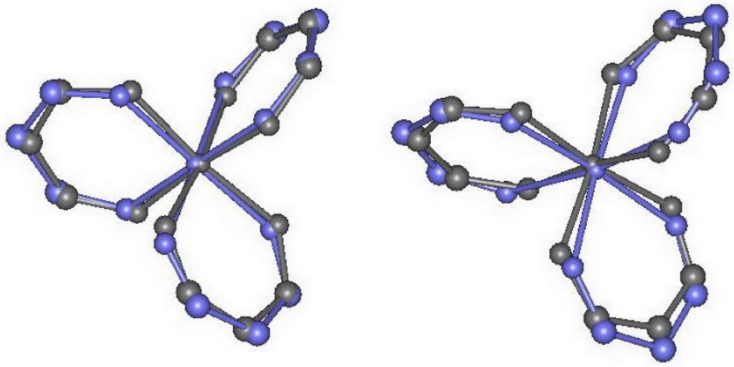

Figure 6.1. Overlay of experimental X-ray (gray) with LDA optimized (light blue) global minimum structure (left) and OPBE optimized (light blue) global minimum structure (right).

$CoCp_2$ possesses two possible HS conformations, eclipsed (D_{5h}) and staggered (D_{5d}). The presented results are limited to $CoCp_2$ in D_{5h} symmetry, as DFT calculation revealed that the eclipsed conformation is more stable and the JT effect does not depend on the rotation of the rings.[80] Similar to the cases of organic radicals, values of the JT parameters in this organometallic compound do not depend significantly on a choice of XC functionals, Table 6.2. The different ground states obtained using different functional (Table 6.2.) are due to the very small warping barriers, which are in the range of the precision of the calculation. Negligible warping barrier is expected because second order vibronic coupling constant is zero in D_{5h} point group.[19] The calculated parameters, Table 6.2., are in agreement with the value of 1050 cm^{-1} estimated from the solid state EPR spectra.[227] In contrast to, for example $C_5H_5^{\bullet}$, the experimental value for $CoCp_2$ cannot be considered as a benchmark, as the experimental results are strongly dependent on the diamagnetic host matrix.[227] This is clearly an example of experimental difficulties in the quantification of the JT parameters.

6.1. Conclusion

All molecules under study belong to the JT active species, and they represent completely different chemical systems; hence, the obtained results can be assumed as general.

For small, aromatic, organic, radicals and anions and cations of corannulene and coronene, the JT parameters do not depend on a choice of the XC functional. The results obtained by the means of MD-DFT are mutually consistent, regardless of the level of theory, and are in good agreement with the results of previous studies, both experimental and theoretical.

DFT analysis of the JT effect in small metal clusters, Na_3 and Ag_3, gives acceptable results for all applied XC functionals, except for BLYP which clearly gives wrong geometries of the distorted structures. Thus, one should be careful in using BLYP for the quantification of the JT distortion in such cases.

Particular choice of the XC functional for the determination of the JT parameters in square-planar arsenic and antimony anionic clusters is not crucial.

The LDA tends to give better geometries for Werner-type compounds in comparison to the GGA and hybrid functionals. The GGA functionals always yield longer bonds and, hence, worse agreement with the experimental data for Werner-type species. Thus, great attention should be given to the choice of the XC functional for the analysis of the JT effect and determination of the JT parameters in Werner-type complexes.

Obtained JT parameters for organometallic compound, cobaltocene, are consistent regardless of the performed XC functional.

To obtain reliable results, the LDA performs remarkably well, as it provides the best geometries for both the HS and LS species. The difficulties in the determination of the JT parameters are not to be found in the definition of degenerate states, but in the determination of the precise geometry of the HS and LS points.

6.2. Computational Details

The DFT calculations have been carried out using the Amsterdam Density Functional program package, ADF2010.01.[228-230] Geometry optimization of all investigated molecules was performed using LDA characterized by the VWN parameterization,[61] and GGAs, such as BP86,[63, 64] BLYP,[63, 178] OPBE[65] and hybrid B3LYP[179, 180]. An all electron

Triple-zeta Slater-type orbitals (STO) plus one polarization function (TZP) basis set has been used for all atoms. All calculations were spin-unrestricted. Separation of the orbital and the geometrical symmetry, as used in the calculation of the energies of the HS nuclear configurations is done using SYMROT subblock in the QUILD program, version 2010.01,[175] provided in the ADF2010.01 program package. Analytical harmonic frequencies[231, 232] were calculated in order to ascertain that LS structure corresponds to the stationary points on the potential energy surface. COSMO,[233-235] as implemented in ADF,[236] with the dielectric constant of water $\varepsilon = 78.4$ was included in the DFT calculations in the case of hexafluorocuprat(II) ion, in order to partially simulate the environmental effects in the crystal lattice.[223]

7. Results and Discussion: Treatment of the Multimode Jahn-Teller Problem

The distortion from a HS nuclear arrangement, due to the JT effect, toward a LS energy minimum conformation is a displacement on the 3*N*-6 potential energy surface. In the ideal case, the distortion corresponds to the movements of nuclei along one normal mode that belongs to a non-totally symmetric irrep of the HS point group of molecule. The analysis of the structural distortion from the HS nuclear arrangements of the JT active molecules presents a challenge because of the superposition of the effects produced by many different normal modes. Briefly, complications arise when there are more than one vibration responsible for the distortion, a typical scenario when considering polyatomic molecules and almost a certainty when dealing with solid-state problems. As the dimension of the problem becomes much higher, the Mexican-hat representation of the APES is not appropriate anymore for the description of the distortion, and new effects may arise. The appraisal of the influence of different normal modes on the JT effect is referred to as a multimode problem. When there are several JT active modes, it is not possible to known *a priori* the individual role of normal modes in the observed JT induced properties. The profound and elegant theoretical studies have been carried out in order to tackle the multimode problem and quantify the role played by different normal modes in symmetry breaking processes, using interaction mode.[1, 23, 237] Recently, a new approach to analyse the multimode problem, called IDP model,[19-22] Chapter 2, Section 2.6., has been proposed. The reference point for the model is the LS configuration, a true minimum on the potential energy surface. All the required information, to calculate the vibronic coupling coefficients is contained in the LS structure, at least to a good approximation. Within the harmonic approximation the potential energy surface has a simple analytical form, so with this model, it is possible to directly separate the contributions of the different normal modes to the JT distortion, their energy contributions to the JT stabilization energy along a relevant particular path of distortion and the forces at the HS point, giving further insight into the origin and mechanism of the vibronic coupling.

7.1. Multimode Jahn-Teller Problem in Square-Planar Arsenic and Antimony Clusters

Arsenic and antimony anionic four-member rings, As_4^- and Sb_4^-, examples of $E \otimes (b_1 + b_2)$ multimode JT problem, have ^2E_g ground electronic state in the D_{4h} point group. Descent in symmetry goes to D_{2h}, with the rectangular or rhombic geometries. ^2E_g ground electronic state splits into the $^2B_{3g}$ and $^2B_{2g}$. The rectangle, with $^2B_{3g}$ electronic state is the minimum structure with no imaginary frequencies, while $^2B_{2g}$ rhombus is the transition state on the potential energy surface. Some XC functionals revealed that D_{2h} rhombus structure present subject of further symmetry reduction due to the pseudo JT distortion, with slightly puckered rhombus in C_{2v} symmetry and $^2B_1$ electronic state being additionally stabilized for around 300 cm^{-1}, Tables 7.1.1. and 7.1.2. Electronic energies of As_4^- and Sb_4^- calculated for HS and LS points, as well as their AOC energies, according to the calculation procedure explained in Chapter 3, Section 3.4. are listed in the Tables 7.1.1. and 7.1.2. The JT parameters calculated with different XC functionals are given in Chapter 6, Table 6.2. Considering that minimum rectangular structures arise as a consequence of a proper JT distortion, further analysis of combined JT/PJT effect is not necessary.

Table 7.1.1. Results of the DFT calculations performed to analyze the JT effect in As_4^-; Energies are in eV.

Occupations	State	Geometry	LDA	BP86	B3LYP
$e_g^{1.5}e_g^{1.5}$	^2E_g	D_{4h}	-19.424	-17.608	-20.642
$b_{2g}^2 b_{3g}^1$	$^2B_{3g}$	D_{4h}	-19.428	-17.608	-20.903
$b_{3g}^2 b_{2g}^1$	$^2B_{2g}$	D_{4h}	-19.381	-17.617	-20.937
$b_{2g}^2 b_{3g}^1$	$^2B_{3g}$	D_{2h}	-19.515	-17.713	-21.007
$b_{3g}^2 b_{2g}^1$	$^2B_{2g}$	D_{2h}	-19.419	-17.652	-20.970
$b_2^2 b_1^1 a_1$	$^2B_1$	C_{2v}	-19.444	-17.66	-20.970
$a_1^2 b_2^1 b_1$	$^2B_2$	C_{2v}	-19.779	-17.858	-21.075

Table 7.1.2. Results of the DFT calculations performed to analyze the JT effect in Sb_4^-; Energies are in eV.

Occupations	State	Geometry	LDA	BP86	B3LYP
$e_g^{1.5}e_g^{1.5}$	^2E_g	D_{4h}	-17.171	-15.502	-18.092
$b_{2g}^2 b_{3g}^1$	$^2B_{3g}$	D_{4h}	-17.164	-15.507	-18.311
$b_{3g}^2 b_{2g}^1$	$^2B_{2g}$	D_{4h}	-17.129	-15.506	-18.341
$b_{2g}^2 b_{3g}^1$	$^2B_{3g}$	D_{2h}	-17.233	-15.572	-18.383
$b_{3g}^2 b_{2g}^1$	$^2B_{2g}$	D_{2h}	-17.159	-15.532	-18.364
$b_2^2 b_1^1 a_1$	$^2B_1$	C_{2v}	-17.172	-15.532	-18.364
$a_1^2 b_2^1 b_1$	$^2B_2$	C_{2v}	-17.457	-15.678	-18.426

In order to understand these simplest examples of the multimode JT effect, IDP analysis was performed. E_{JT} obtained from IDP analysis is in a good agreement with DFT calculations, Table 7.1.3., for both, $As_4^{2-}$and Sb_4^{2-}, confirming validity of harmonic approximation employed in IDP model. An analysis of multimode problem in these systems revealed negligible contribution of a_{1g} normal mode, with R_{JT} less than 0.004 Å and stabilization energy of approximately 0.2 cm^{-1}.

Table 7.1.3. The JT stabilization energy, E_{JT} (cm^{-1}) and JT radius, R_{JT} (Å) for distortions of As_4^- and Sb_4^- from square-planar to rectangle and rhombus structures obtained by MD-DFT and IDP models with different XC functionals (LDA, BP86 and B3LYP).

		As_4^-		Sb_4^-	
	Structure	rhombus	rectangle	rhombus	rectangle
	El. State	B_{2g}	B_{3g}	B_{2g}	B_{3g}
LDA	E_{JT}(MD-DFT)	304.9	703.4	239.5	556.2
	E_{JT}(IDP)	329.2	756.6	258.2	519.8
	R_{JT}	0.120	0.086	0.140	0.084
BP86	E_{JT}(MD-DFT)	281.0	845.8	207.8	517.5
	E_{JT}(IDP)	580.1	732.0	184.2	480.1
	R_{JT}	0.130	0.090	0.117	0.086
B3LYP	E_{JT}(MD-DFT)	266.4	840.1	189.0	578.9
	E_{JT}(IDP)	222.7	825.6	123.2	562.4
	R_{JT}	0.104	0.093	0.096	0.090

Values of the vibronic constants and force constants, from IDP and MD-DFT, with different XC functionals, are presented in Table 7.1.4. With these parameters and vibronic coupling model described in Chapter 2, Section 2.3., potential energy surface in

the space of JT active b_{1g} and b_{2g} normal modes is constructed, Figure 7.1.1. The potential energy profile is essentially parabolic. Forces along the two JT active modes are changing linearly from HS D_{4h} nuclear configuration toward the corresponding D_{2h} stationary points. If distortions to rectangle and rhombus are considered independently, the JT problem shows features of single mode JT effect. However, in D_{4h} symmetry, this is truly multimode problem, and direction of the distortion is dictated by higher forces of harder b_{2g} mode, Table 7.1.4. As it could be expected, for softer b_{1g} mode somewhat larger distortion is needed to reach the stationary point on the potential energy surface, Table 7.1.3.

Table 7.1.4. Analysis of the JT effect in As_4^- and Sb_4^-: vibronic coupling constants of b_{1g} and b_{2g} normal modes, F_{b1g} and F_{b2g} (in $10^3 cm^{-1}/Å$), and force constants of b_{1g} and b_{2g} normal modes, K_{b1g} and K_{b2g} (in $10^3 cm^{-1}/Å^2$) obtained by IDP model and by MD-DFT with different XC functionals.

		As_4^-				Sb_4^-			
		F_{b1g}	K_{b1g}	F_{b2g}	K_{b2g}	F_{b1g}	K_{b1g}	F_{b2g}	K_{b2g}
LDA	IDP	5.629	48.1	17.564	202.8	3.797	27.9	12.391	147.8
	MD-DFT	5.082	42.3	16.358	190.2	3.421	24.4	13.242	157.6
BP86	IDP	6.004	43.4	16.342	181.0	3.132	26.6	11.173	129.3
	MD-DFT	4.323	33.2	18.796	208.8	3.552	30.4	12.035	139.9
M06-L	IDP	4.847	36.8	11.896	127.0	6.124	26.6	10.850	167.7
	MD-DFT	4.064	35.0	26.827	304.8	1.631	7.1	7.861	120.9
B3LYP	IDP	4.375	42.1	17.824	191.2	2.561	26.6	12.499	138.7
	MD-DFT	5.123	49.2	18.066	194.3	3.937	41.0	12.864	142.9

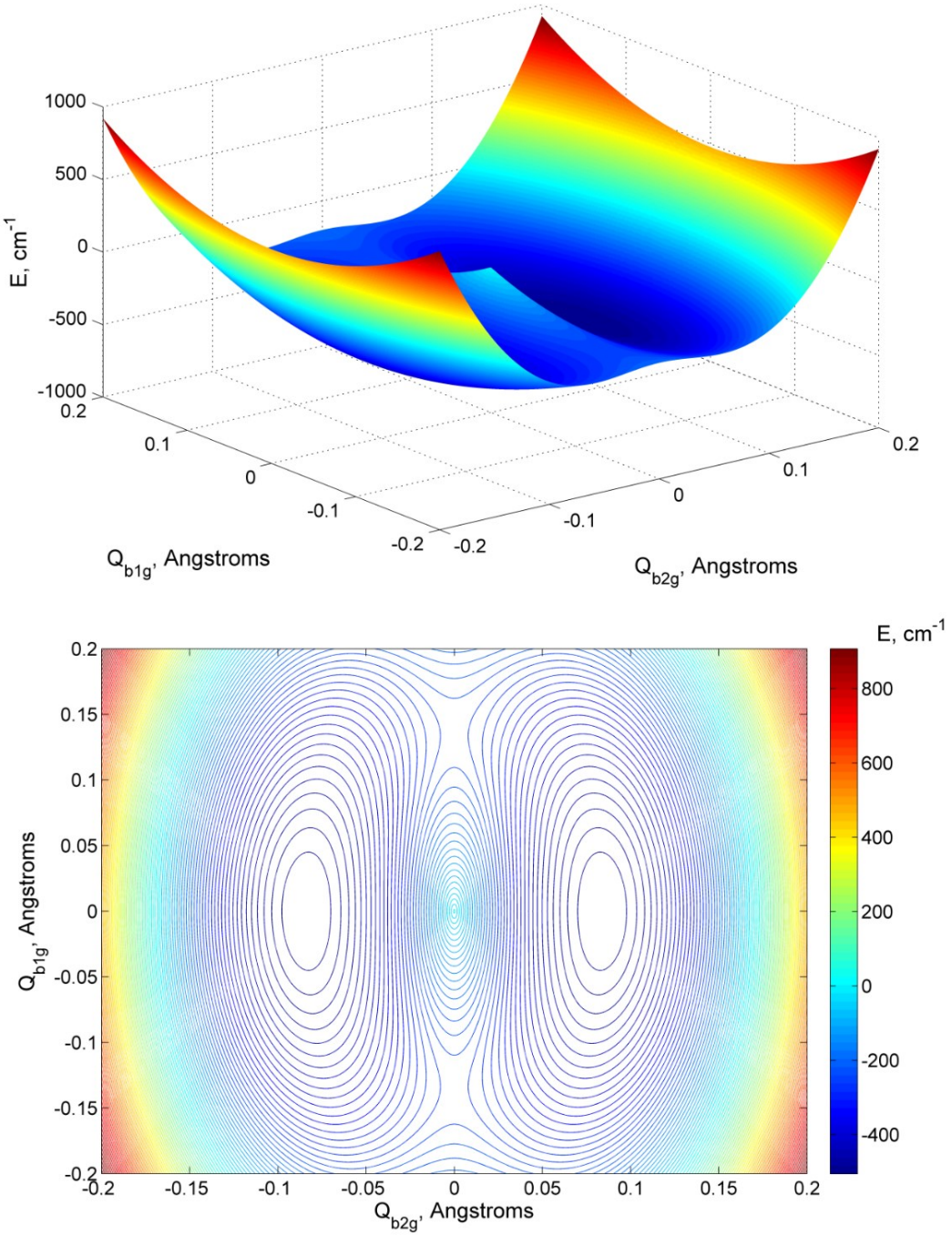

Figure 7.1.1. Potential energy surface of Sb_4^- in the space of JT active b_{1g} and b_{2g} normal modes, 3D (up) and 2D (down); vibronic coupling parameters are taken from LDA IDP model; minima have rectangular and transition states rhombic geometries.

7.1.1. Conclusion

The simplest multimode JT problem, $E \otimes (b_1 + b_2)$, in square-planar arsenic and antimony anionic clusters is investigated by the means of the IDP model. Although at the first glance one may assume that $E \otimes (b_1 + b_2)$ represents single mode effect, it is truly multimode problem since the direction of the distortion is guided with higher forces of harder vibration. The synergic effect of the MD-DFT and IDP allows for calculating of vibronic coupling constants and getting deeper insight into the origin and mechanism of the distortion.

7.1.2. Computational Details

All investigated molecules were optimized by DFT calculations using the Amsterdam Density Functional program package, ADF2013.01.[229, 230, 238] The LDA characterized by the VWN parameterization[61] was used for the symmetry-constrained geometry optimizations. In addition BP86[63, 64] and B3LYP[178, 179] XC functionals were employed. TZP basis set was used for all atoms. Separation of the orbital and the geometrical symmetry, as used in the calculation of the energies of the HS nuclear configurations, is done using SYMROT subblock in the QUILD program, version 2013.01,[239] provided in the ADF2013.01 program package. In all cases, the global minimum was confirmed by the absence of the imaginary frequency modes.

7.2. Multimode Jahn-Teller Problem in Small Aromatic Radicals

$C_5H_5^{\bullet}$, $C_6H_6^{+}$, $C_6H_6^{-}$ and $C_7H_7^{\bullet}$ are important species in organic chemistry but also are very interesting for spectroscopic and quantum chemistry studies. All of them have a single electron or a hole in a doubly degenerate highest occupied molecular orbital, leading to a degenerate state arising as a consequence of an addition or removal of an electron in the parent aromatic molecule, as in Figure 7.2.1., presenting paradigmatic examples of the $E \otimes e$ JT problem.

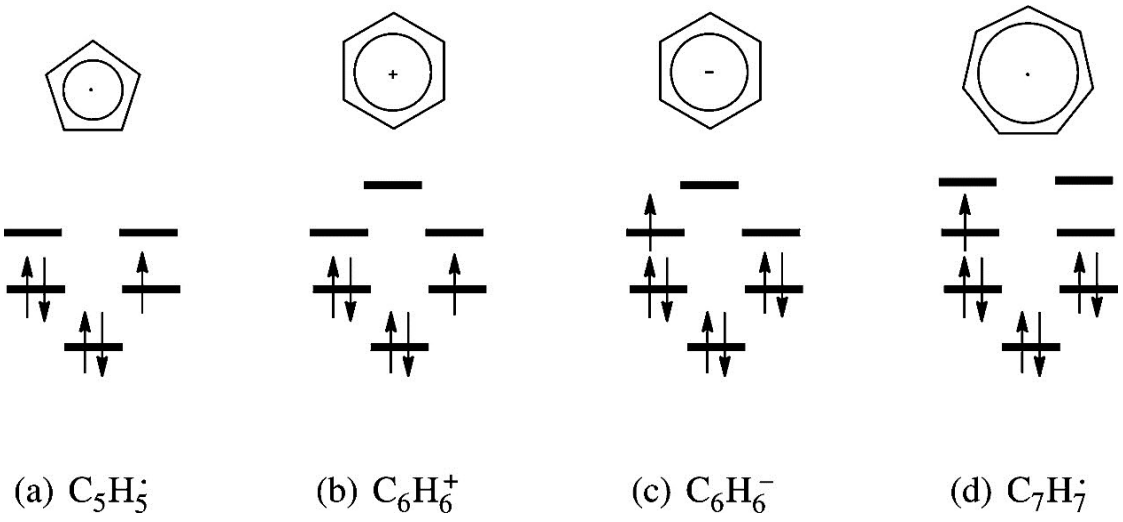

Figure 7.2.1. Structures of $C_5H_5^{\bullet}$, $C_6H_6^{+}$, $C_6H_6^{-}$ and $C_7H_7^{\bullet}$; a simple MO scheme is outlined.

To tackle the multimode problem in these molecules, the JT distortion is expressed as a linear combination of all totally symmetric normal modes in the LS minimum energy conformation by the means of the IDP model, Chapter 2, Section 2.6., allowing quantification and clarification of the role played by the different symmetry-breaking and totally symmetric vibrations in the global distortion.

In addition, the structural analysis is complemented by investigation of the different electronic interactions (electron-nuclei, electron-electron, etc.) present in the Hamiltonian, leading to a more complete and balanced view of the changes undergone by the system along the JT distortion.

7.2.1. Energy Component Analysis

In the time-independent, nonrelativistic, BO approximation, the molecular Hamiltonian operator, consists of a sum of the electron kinetic energy, the nuclear-nuclear Coulomb repulsion, the electron-nuclear interaction and the electron-electron repulsion operators. The energy of a system, which is the expectation value of the Hamiltonian operator, can be expressed as a sum of the expectation values of the corresponding operators. All of the quantities can be calculated with the Hartree-Fock, post Hartree-Fock, or DFT approaches. An analysis of the changes of these energy components during a chemical transformation helps to understand the nature of chemical bonding in a molecule. The studies along this line were performed for the analysis of the formation of covalent bonds,[240-242] to explain the Hund's rule,[243-245] aromaticity,[246, 247] different spin states of iron complexes,[248] PJT distortions,[249-255] DFT-based quantification of the steric and quantum effects,[256-262] and so forth. Nevertheless, energy component analysis was seldom used for the exploration of the JT effect.[263-265] Within the KS-DFT formalism,[17, 58] changes of the individual energy terms can be formulated as:

$$\Delta E = \Delta T_s + \Delta V_{KS} = \left(\Delta T_w + \Delta T_p\right) + \left(\Delta V_{elst} + \Delta V_{XC}\right)$$

Eq. 7.2.1.1.

$$\Delta V_{elst} = \Delta V_{en} + \Delta J + \Delta V_{nn}$$

Eq. 7.2.1.2.

where ΔT_s is change of the kinetic energy of a fictitious system of noninteracting electrons and ΔV_{KS} is a change of the KS potential energy that consists of the changes of the electron-nuclear potential energy (ΔV_{en}), changes of the classical Coulomb electron-electron repulsion (ΔJ), and changes of the exchange-correlation potential energy (ΔV_{XC}). ΔV_{en}, ΔJ and ΔV_{nn} are conveniently grouped together into the classical electrostatic term, ΔV_{elst}. ΔV_{XC} consists of the residual part of the true kinetic energy, sometimes referred to as the correlation kinetic energy,[17, 266, 267] and the nonclassical electrostatic interactions. ΔT_s is partitioned into the changes of the Weizsäcker kinetic energy ΔT_w[268] and the Pauli kinetic energy ΔT_p[256, 269-275]. Liu defined T_w as a steric energy from KS-DFT.[256] T_p, itself simply defined as $T_p = T_s - T_w$, is regarded as an extra kinetic energy required of the fermions by the Pauli exclusion principle.[256] T_w is consistent with Weisskopf's kinetic

energy pressure;[276] it is related to Bader's atoms in molecule approach[277] and and Fisher information theory[278, 279]. T_p appears in a definition of electron localization function.[280, 281] The fermionic quantum energy contribution can be defined as a $T_p + V_{XC}$.[256] DFT based quantification of the steric, electrostatic, and fermionic quantum energy contributions was applied in the analysis of various chemical problems.[256-262]

7.2.2. Distortion of Cyclopentadienyl Radical, Benzene Cation and Tropyl Radical

The ground electronic state of $C_5H_5^{\bullet}$, $C_6H_6^{+}$, and $C_7H_7^{\bullet}$ in a HS point group belongs to a double degenerate irrep which splits into two non-degenerate electronic states in LS point group. This yields two different LS geometries, usually referred as dienyl ($^2B_1$ $C_5H_5^{\bullet}$) and allyl ($^2A_2$ $C_5H_5^{\bullet}$) or elongated ($^2B_{2g}$ $C_6H_6^{+}$, $^2B_1$ $C_7H_7^{\bullet}$) and compressed ($^2B_{3g}$ $C_6H_6^{+}$, $^2A_2$ $C_7H_7^{\bullet}$) structures. The JT active distortion is the totally symmetric reaction coordinate in the LS point group. The other component of the double degenerate JT active distortion allows mixing of the two electronic states emerging from the degenerate ground state. This is summarized in Table 7.2.2.1.

Table 7.2.2.1. Summary of the group theory considerations for the JT distortions in $C_5H_5^{\bullet}$, $C_6H_6^{+}$, and $C_7H_7^{\bullet}$. Γ_{el} is irrep of the electronic state; Γ_{JT} is irrep of the JT active vibrations; N is the number of atoms in a molecule; N_{a1} is the number of totally symmetrical vibrations in the LS point group. One component of the degenerate pairs of vibrations in the HS becomes a_1 in the LS point group.

Molecule	Distortion	Γ_{el}	Γ_{JT}	$3N$-	N_{a1}	Origin of the LS a_1
$C_5H_5^{\bullet}$	$D_{5h} \rightarrow C_{2v}$	$E''_1 \rightarrow A_2+B_1$	$E'_2 \rightarrow A_1+B_2$	24	9	$4e'_2$, $2a'_1$, $3e'_1$
$C_6H_6^{+}$	$D_{6h} \rightarrow D_{2h}$	$E_{1g} \rightarrow$	$E_{2g} \rightarrow$	30	6	$4e_{2g}$, $2\ a_{1g}$
$C_7H_7^{\bullet}$	$D_{7h} \rightarrow C_{2v}$	$E''_2 \rightarrow A_2+B_1$	$E'_3 \rightarrow A_1+B_2$	36	13	$4e'_3$, $4e'_2$, $3e'_1$, $2a'_1$

The JT parameters, E_{JT}, Δ and R_{JT}, calculated by the means of MD-DFT and IDP are summarized in Table 7.2.2.2. Results using LDA are presented because particular choice of XC functional is not essential, as shown in Chapter 6. In all cases, E_{JT} obtained from IDP analysis is in a good agreement with DFT calculations, Table 7.2.2.2. The strongest stabilization is observed for $C_5H_5^{\bullet}$. As previously discussed (Chapter 6), these results are in great agreement with experimentally estimated values, e.g. E_{JT} for $C_5H_5^{\bullet}$ from dispersed fluorescence spectrum is 1237 cm^{-1}.[182] Essentially zero Δ for $C_5H_5^{\bullet}$ and

$C_7H_7^{\bullet}$ is consistent with vibronic coupling for D_{5h} and D_{7h} point groups.[19] For $C_6H_6^+$ Δ is very small, which is in accordance with previous studies.[186]

Table 7.2.2.2. Results of the DFT calculations performed to analyze the JT effect in $C_5H_5^{\bullet}$, $C_6H_6^+$, and $C_7H_7^{\bullet}$. The JT parameters E_{JT} and Δ are given in cm^{-1} and R_{JT} in $(amu)^{1/2}$Å.

Molecule	JT parameters	geometry, state	
	E_{JT}	$C_{2v}, {}^2A_2$	1244.5
	E_{JT}	$C_{2v}, {}^2B_1$	1244.5
	E_{JT}(IDP)	$C_{2v}, {}^2A_2$	1238.0
$C_5H_5^{\bullet}$	E_{JT}(IDP)	$C_{2v}, {}^2B_1$	1238.0
	Δ		0.0
	R_{JT}	$C_{2v}, {}^2A_2$	0.25
	R_{JT}	$C_{2v}, {}^2B_1$	0.25
	E_{JT}	$D_{2h}, {}^2B_{2g}$	879.2
	E_{JT}	$D_{2h}, {}^2B_{3g}$	831.6
	E_{JT}(IDP)	$D_{2h}, {}^2B_{2g}$	839.1
$C_6H_6^+$	E_{JT}(IDP)	$D_{2h}, {}^2B_{3g}$	791.1
	Δ		32.2
	R_{JT}	$D_{2h}, {}^2B_{2g}$	0.27
	R_{JT}	$D_{2h}, {}^2B_{3g}$	0.27
	E_{JT}	$C_{2v}, {}^2A_2$	853.3
	E_{JT}	$C_{2v}, {}^2B_1$	853.3
	E_{JT}(IDP)	$C_{2v}, {}^2A_2$	861.2
$C_7H_7^{\bullet}$	E_{JT}(IDP)	$C_{2v}, {}^2B_1$	862.2
	Δ		0.0
	R_{JT}	$C_{2v}, {}^2A_2$	0.16
	R_{JT}	$C_{2v}, {}^2B_1$	0.16

On the potential energy profile it is possible to distinguish two distinct regions (Figures 7.2.2.1.a, 7.2.2.2.a, 7.2.2.3.a). In the first region the energy is changing faster, and depending on the particular molecule, after 25-40% of the path most of the E_{JT} is obtained. An analysis of the multimode JT distortion shows that, regardless of the number of totally symmetric normal modes in LS minimum energy conformation, Table 7.2.2.1., three vibrations are most important for the distortion and for the E_{JT}: C-C stretch, C-C-C bend, and C-C-H bend (Figures 7.2.2.1.a, 7.2.2.2.a, 7.2.2.3.a, Figure 7.2.2.4. (for the case of $C_6H_6^+$); and Table 7.2.2.3.). These three vibrations are found to be the most important in the computational and experimental studies on $C_5H_5^{\bullet}$ and $C_6H_6^+$.[182, 184, 192] It should be pointed out that in these studies only those three normal modes are considered, while IDP

takes into account all possible normal modes. Initially, the most important JT active mode is the hardest of the three modes, the C-C stretch, while in the second region, where the system relaxes toward the global minimum, softer modes become more important, and the APES is flat. Monitoring changes of all the energy components along the IDP, Eqs. 7.2.1.1. and 7.2.1.2., gives a whole picture of what happens inside the molecule during the JT distortion. The results are presented in Figure 7.2.2.1.c,d for $C_5H_5^{\bullet}$, Figure 7.2.2.2.c,d for $C_6H_6^{+}$, and in Figure 7.2.2.3.c,d for $C_7H_7^{\bullet}$. Curves have been displaced vertically to make each energy component zero for the HS configuration, so that the stabilizing and destabilizing interactions along the distortion path can be clearly identified. A similar trend of the changes of energy components is observed for all of the molecules. Two regions are clearly differentiated in the $\Delta T/\Delta V$ profiles. Most of the total energy stabilization is achieved around the HS point when the distortion is driven by the lowering of ΔV and simultaneous increase of ΔT. The initial downward push is clearly due to the JT effect, which is due to the stabilization of the V_{elst}, and the C-C stretch is mainly involved in the distortion. After that, the contribution of the C-C stretch drops to the zero. The origin of this distortion is clearly associated to the electron-nuclear interaction, Figure 7.2.2.1., and occurs along the C-C stretch, as the active electrons occupy the space between the carbon atoms. Changes in the V_{XC} energy are an order of magnitude smaller than changes of the V_{elst} and are not important for the qualitative picture. The kinetic energy apparently favors the HS nuclear configuration. Changes in the T_s are directed with the changes of the T_p, which can be identified as the main opposing contribution to the JT distortion. If we look in more detail into changes of the V_{elst}, it can be seen that the main stabilization comes from the V_{en} which goes quickly down, to adapt to the nontotally symmetrical electron density, as expected from the theoretical considerations, Chapter 2. Two other electrostatic contributions, V_{ee} and V_{nn}, show the opposite tendency, thus giving in total smaller changes in the V_{elst}. However, after the initial push, the system reaccommodates leading to the strong reduction of the T_p, V_{ee}, and V_{nn}. While T_w almost did not change in the first region, it becomes destabilizing in the second region, and it is changed then parallel to the changes in the V_{elst}. Owing to this behavior of T_w, the total kinetic energy does not contribute globally to stabilize the system. On the other hand the T_p, V_{ee}, and V_{nn} repulsions clearly stabilize the system in the final run. In fact, the energy contribution due to the V_{en} interactions at the end is

positive, and the global stabilization seems to come from the electron-electron and nuclear readjustment. Obviously, the correct answer can only be obtained from looking at the whole path and understanding the changes undergone by the forces using the previously explained theory in Chapter 2. Thus, while the initial distortion is clearly associated with the usual JT distortions, in the second region softer, bending modes play a more important role, due to the changes of the density caused by the modification of the geometry in the first push. This leads to enhancing the effects of energy components with opposite signs, which are almost cancelling each other, yielding to the very small total energy variation. From the point of view of the JT theory, this also underlines the very important role of the PJT effect, associated to the density changes to obtain the final stabilization energy and barriers in JT systems.

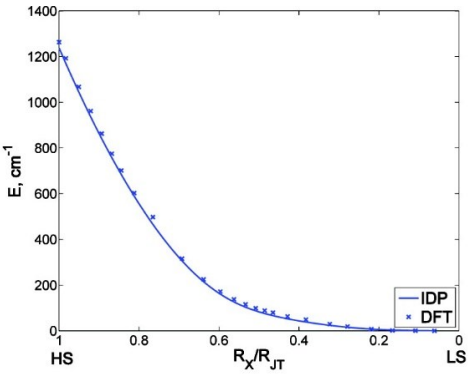

(a) Changes of the energy, IDP model and DFT results

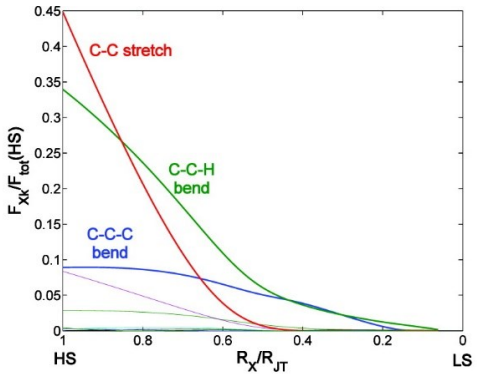

(b) Changes of the forces (normalized to the total distortion force at HS point) of the 9 a_1 normal modes in C_{2v}, along the IDP

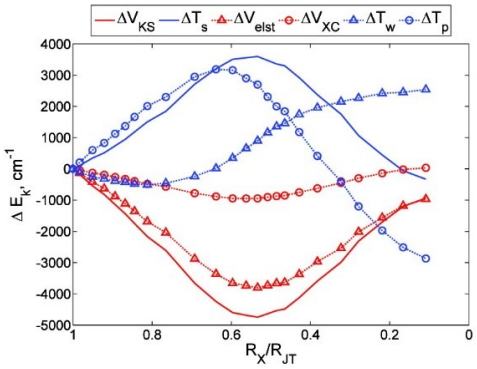

(c) Changes of the potential, kinetic energies, and their components along the IDP

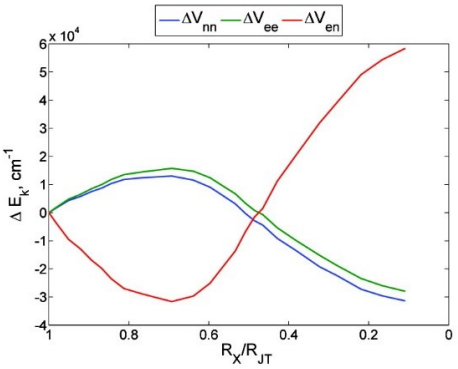

(d) Changes of the different electrostatic energy terms along the IDP

Figure 7.2.2.1. Intrinsic distortion path and energy component analysis of the JT $D_{5h}\rightarrow C_{2v}$ distortion in $C_5H_5^{\bullet}$.

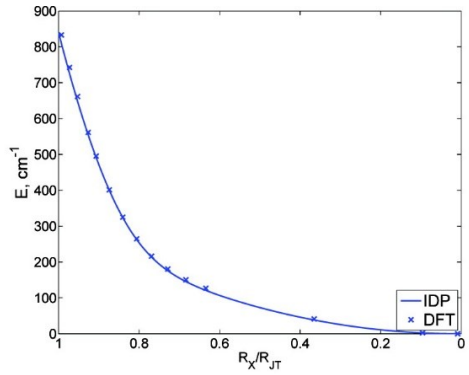

(a) Changes of the energy, IDP model and DFT results

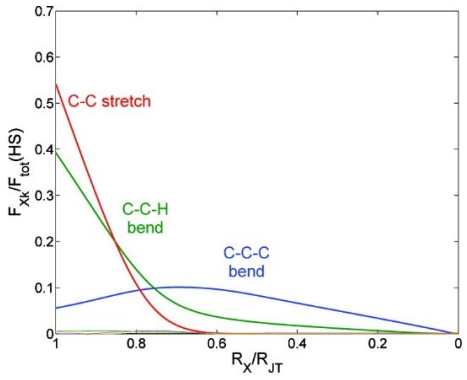

(b) Changes of the forces (normalized to the total distortion force at HS point) of the 6 a_g normal modes in D_{2h}, along the IDP

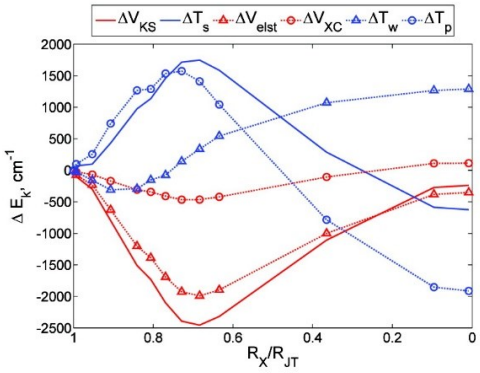

(c) Changes of the potential, kinetic energies, and their components along the IDP

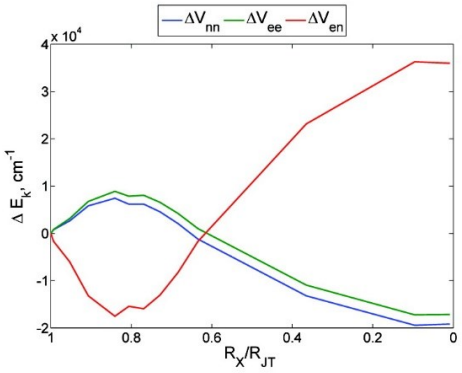

(d) Changes of the different electrostatic energy terms along the IDP

Figure 7.2.2.2. Intrinsic distortion path and energy component analysis of the JT $D_{6h} \rightarrow D_{2h}$ distortion in $C_6H_6^+$.

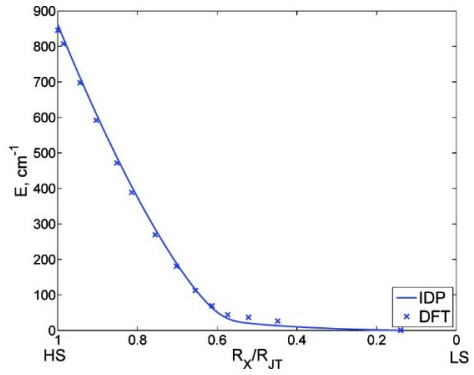

(a) Changes of the energy, IDP model and DFT results

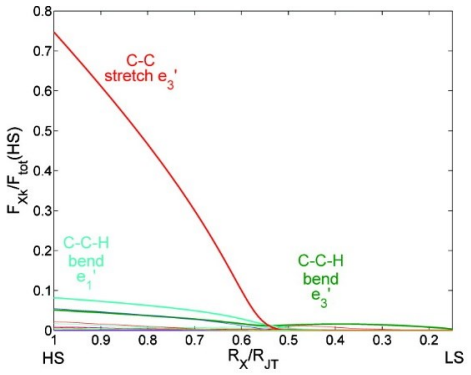

(b) Changes of the forces (normalized to the total distortion force at HS point) of the 13 a_1 normal modes in C_{2v}, along the IDP

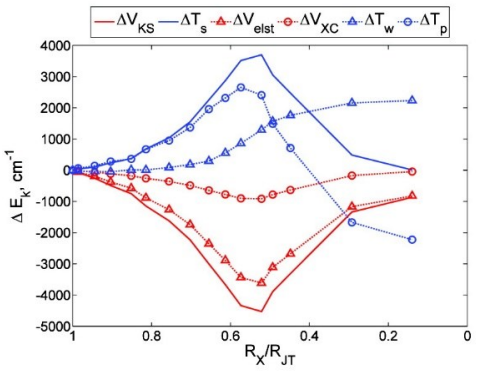

(c) Changes of the potential, kinetic energies, and their components along the IDP

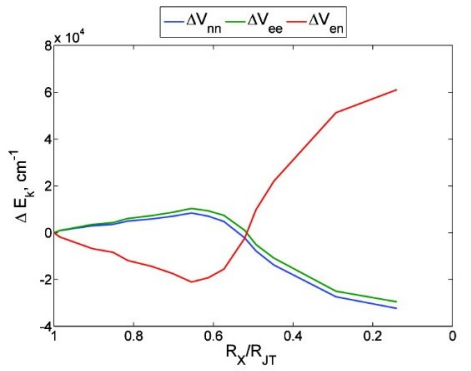

(d) Changes of the different electrostatic energy terms along the IDP

Figure 7.2.2.3. Intrinsic distortion path and energy component analysis of the JT $D_{7h} \rightarrow C_{2v}$ distortion in $C_7H_7^{\bullet}$.

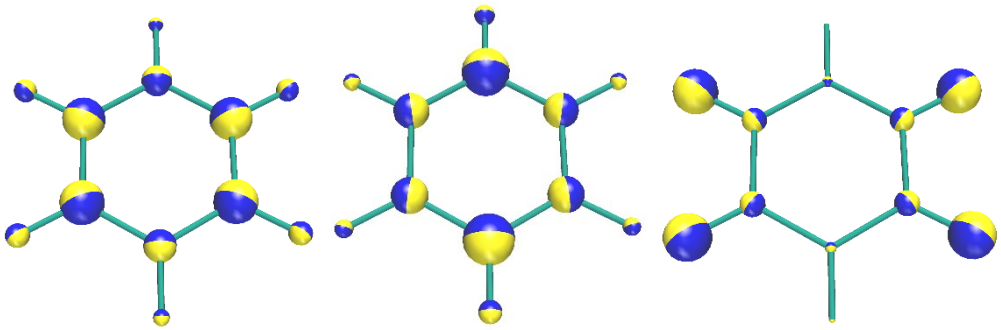

Figure 7.2.2.4. Vibrational energy distribution representation of the C-C stretch, C-C-C bend and C-C-H bend normal modes for $C_6H_6^+$. The different colours indicate the direction of the displacement vector; the volume of the spheres is proportional to the contribution made by the individual nuclei to the energy of the vibrational mode.

Table 7.2.2.3. Analysis of the multimode JT problem in $C_5H_5^{\bullet}$, $C_6H_6^+$, and $C_7H_7^{\bullet}$ by the LS totally symmetric normal modes in harmonic approximation. Frequencies of selected normal modes are in cm^{-1} as obtained from DFT calculations; contribution of the normal mode $\vec{Q}_k$ to the $\vec{R}_{JT}$ is given by c_k in %; E_k energy contribution of $\vec{Q}_k$ to the E_{JT} in %.

Assignment	molecule	HS-irrep	$\tilde{\nu}_k$ in LS	c_k	E_k
C-C-C bend	$C_5H_5^{\bullet}$	e'_2	831	24.19	19.99
	$C_6H_6^+$	e_{1g}	591	51.99	34.33
	$C_7H_7^{\bullet}$	e'_3	894	5.31	1.87
C-C-H bend	$C_5H_5^{\bullet}$	e'_2	1040	52.18	20.02
	$C_6H_6^+$	e_{1g}	1166	34.63	16.99
	$C_7H_7^{\bullet}$	e'_3	1234	30.53	3.92
C-C stretch	$C_5H_5^{\bullet}$	e'_2	1482	13.93	53.74
	$C_6H_6^+$	e_{1g}	1556	12.40	46.99
	$C_7H_7^{\bullet}$	e'_3	1234	44.07	87.55

7.2.3. Distortion of Benzene Anion

The benzene molecule, C_6H_6, with the D_{6h} nuclear arrangement has a double-degenerate highest occupied molecular orbital (HOMO), e_{1g}, and a double-degenerate lowest unoccupied molecular orbital (LUMO), e_{2u}. Therefore, $C_6H_6^-$ is JT unstable. $C_6H_6^-$ has $^2E_{2u}$ ground electronic state in conformation that belongs to the D_{6h} point group. As in the case of $C_6H_6^+$, the distortion coordinate is e_{2g}, and hence very similar distortion for both cases is expected. DFT results for the benzene anion are presented in Table 8.4. After

the descent in symmetry to D_{2h}, the electronic state splits into $^2B_{1u}$ and ^2A_u. As it can be seen from Table 7.2.3.1., the D_{2h} structure is not the most stable conformation of $C_6H_6^-$, and further reduction of symmetry occurs.

Table 7.2.3.1. Results of the DFT calculations performed to analyze the JT effect in $C_6H_6^-$. The JT parameters E_{JT} and Δ are given in cm^{-1} and R_{JT} in $(amu)^{1/2}$Å.

Molecule	JT parameters	geometry, state	
$C_6H_6^-$	E_{JT}	$D_{2h}, ^2A_u$	788.0
	E_{JT}	$D_{2h}, ^2B_{1u}$	735.6
	E_{JT}(IDP)	$D_{2h}, ^2A_u$	779.2
	E_{JT}(IDP)	$D_{2h}, ^2B_{1u}$	823.6
	Δ		38.7
	R_{JT}	$D_{2h}, ^2A_u$	0.19
	R_{JT}	$D_{2h}, ^2B_{1u}$	0.19
	$E_{JT/PJT}$	$C_2, ^2A_1$	1187.3
	$E_{JT/PJT}$	$D_2, ^2A$	1126.8
	$E_{JT/PJT}$(IDP)	$C_2, ^2A_1$	1060.5
	$E_{JT/PJT}$(IDP)	$D_2, ^2A$	1009.7
	Δ		46.8
	$R_{JT/PJT}$	$C_2, ^2A_1$	0.62
	$R_{JT/PJT}$	$D_2, ^2A$	0.57

Out of six totally symmetric normal modes in the D_{2h} point group, similar to the case of the cation, the influence of the same three normal modes is most significant. The IDP method for the JT distortion of $C_6H_6^-$, in Figure 7.2.3.1., reveals the same trend as in the previous cases. The distortion starts with the C-C stretch ($\tilde{\nu}$ (D_{2h}) = 1496 cm^{-1}, 23.27% to the R_{JT}, 69.16% to the E_{JT}), in Figure 7.2.3.1.b, and with stabilization of the electron-nuclear attraction, Figure 7.2.3.1.d. After 20% of the path, most of the energy stabilization is achieved, as in Figure 7.2.3.1.a. In the second region there is a strong reduction of the electron-electron, nuclear-nuclear, and Pauli kinetic energy. The difference to the case of cation is that the C-C-C bending is not as important ($\tilde{\nu}$ (D_{2h}) = 604 cm^{-1}, 9.58% to the R_{JT}, 5.21% to the E_{JT}), and C-C-H bending is dominating in this region ($\tilde{\nu}$ (D_{2h}) = 1093 cm^{-1}, 64.63% to the R_{JT}, 22.21% to the E_{JT}), as in Figure 7.2.3.1.d.

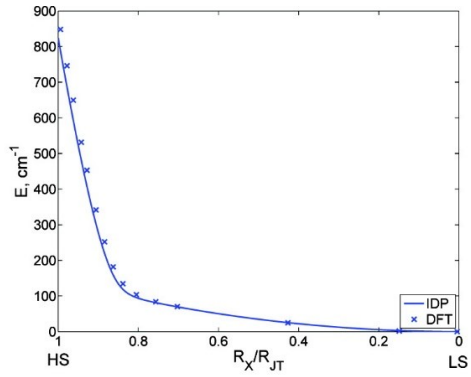

(a) Changes of the energy, IDP model and DFT results

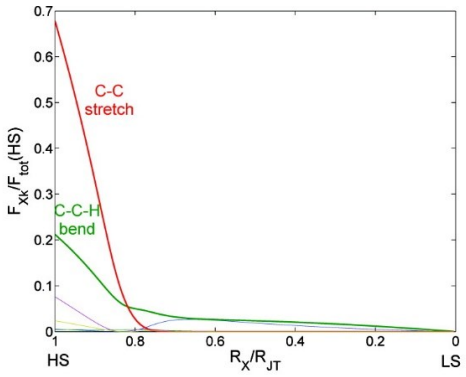

(b) Changes of the forces (normalized to the total distortion force at HS point) of the 6 a_g normal modes in D_{2h}, along the IDP

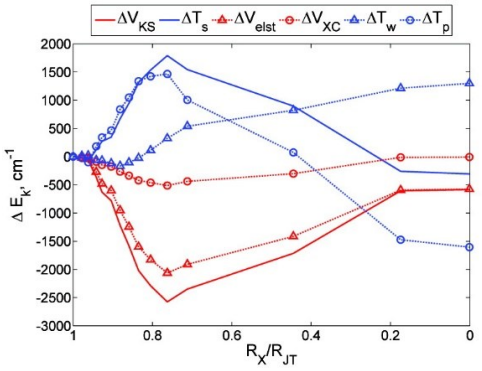

(c) Changes of the potential, kinetic energies, and their components along the IDP

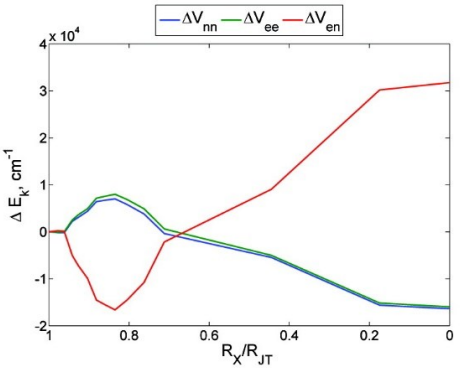

(d) Changes of the different electrostatic energy terms along the IDP

Figure 7.2.3.1. Intrinsic distortion path and energy component analysis of the JT $D_{6h}\rightarrow D_{2h}$ distortion in $C_6H_6^-$.

DFT calculations show the differences between the electronic structure of the benzene cation and anion. In the case of anion, LUMO, both in the D_{6h} and in D_{2h} configurations, is σ* (a_{1g}) MO as it could be expected from the electronic structure of the neutral benzene. Thus, the first excited state of anion is $^2A_{1g}$, which is estimated to lie around 0.1 eV above the ground $^2E_{2u}$ state in a D_{6h} configuration and 0.7 eV above the ground states in D_{2h} configurations. Due to the PJT coupling of the ground, π* electronic state with the excited σ* state, DFT frequency calculations reveal one imaginary e_{2u} frequency in D_{6h}, one a_u imaginary frequency in ^2A_u D_{2h} structure, and two imaginary frequencies in ^2B_u, one b_{1u} and one b_{1g} (pseudorotation around the JT cusp). Following the imaginary frequencies, the true stationary points on the APES were obtained. The out-

of-plane C_{2v} conformation, depicted in Figure 7.2.3.2.a, is the global minimum, which lies around 400 cm^{-1} below the planar D_{2h} structures. The out-of-plane conformation is more stable than the twisted D_2 conformation, in Figure 7.2.3.2.b, for 47 cm^{-1}. This situation is similar to the case of $C_6F_6^-$.[282]

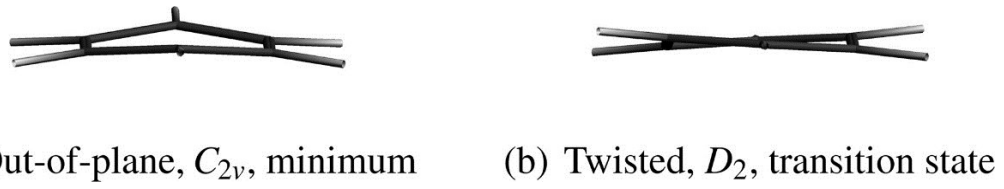

Figure 7.2.3.2. Graphical representation of the out-of-plane, C_{2v}, conformation (a) and twisted, D_2, conformation (b) of $C_6H_6^-$.

The relation between the structures of D_{2h}, C_{2v}, and D_2 symmetry on the APES is schematically shown in Figure 7.2.3.3. Twisted D_2 and planar D_{2h} (^2A_u) conformations are saddle points on the APES. D_{2h} ($^2B_{1u}$) planar conformation is second-order saddle point on the APES, which is indicated with dashed arrows in Figure 7.2.3.3. Both C_{2v} and D_2 point groups are subgroups of D_{2h} and D_{6h} point groups, and the puckering and twisting of $C_6H_6^-$ are consequence of the combined JT and PJT effects.

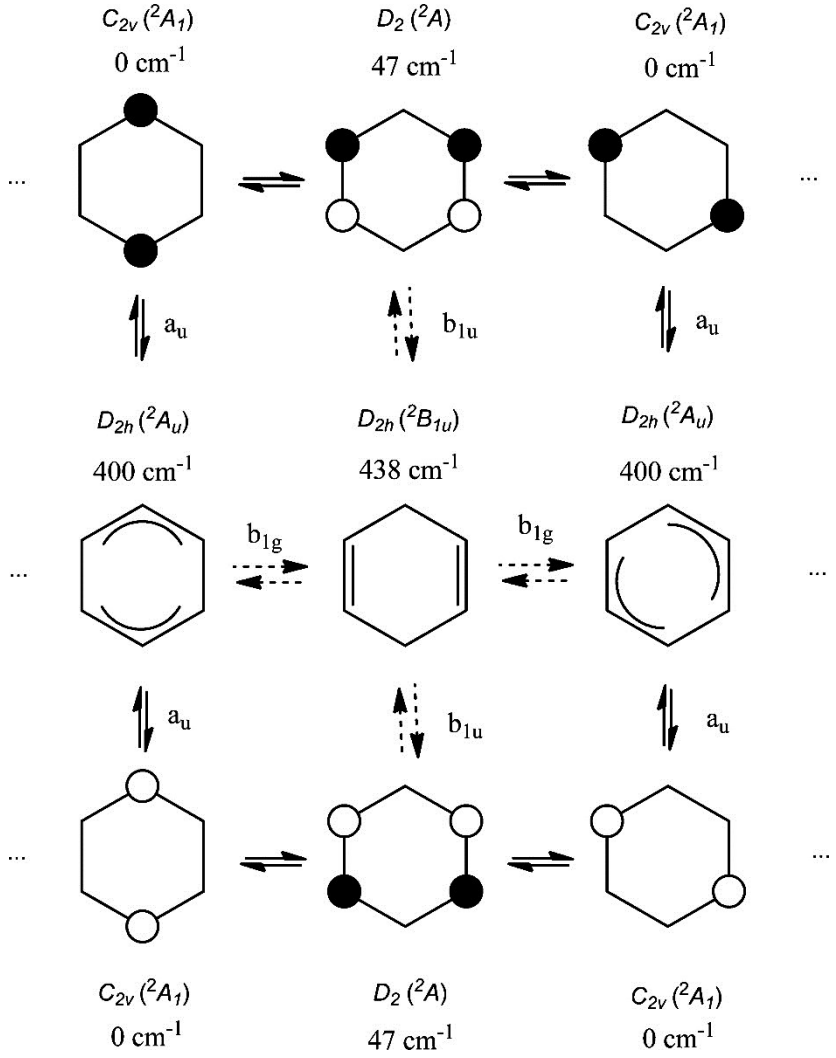

Figure 7.2.3.3. Relation between various structures of $C_6H_6^-$; open (white) and closed (black) circles represent carbon atoms lying below and above the mean plane of the $C_6H_6^-$; energies are given relative to the global minimum, C_{2v} structure, in cm^{-1}; D_{6h} structure lies 1190 cm^{-1} above the global minimum; the symmetry of the vibrations with negative force constants in D_{2h} structures and their direction is indicated.

To analyze the combined JT and PJT distortion of $C_6H_6^-$, $D_{6h}\rightarrow C_{2v}$ distortion, it is necessary to consider nine totally symmetric normal modes in C_{2v} minimum energy conformation. They correlate to the four e_{2g}, two a_{1g}, two b_{2u}, and one e_{2u} vibration in D_{6h}. Even though this distortion is more complicated than previously discussed cases, E_{JT} obtained from the IDP analysis, 1060 cm^{-1}, is still in rather good agreement with the value of 1187 cm^{-1} from MD-DFT calculations. Two distinct regions on the APES could be distinguished, in Figure 7.2.3.4.a. Very early along the IDP, c.a. after 5% of the path, a strong stabilization of around 500 cm^{-1} is achieved. In this region C-C stretch ($\tilde{\nu}$ (C_{2v}) =

1531 cm^{-1}, 1.3% to the R_{JT}, 25.9% to the E_{JT+PJT}) and C-C-H bending ($\tilde{\nu}$ (C_{2v}) = 1112 cm^{-1}, 3.9% to the R_{JT}, 10.4% to the E_{JT+PJT}) are dominating, in Figure 7.2.3.4.b. So, in this region, there is a proper JT distortion, similar to the previously described cases. In the second region the adiabatic energy surface is not flat, and energy gradually decreases for additional 500 cm^{-1}. In this region distortion is almost completely described with the out-of-plane normal mode ($\tilde{\nu}$ (C_{2v}) = 320 cm^{-1}, 90.9% to the R_{JT}, 51.2% to the E_{JT+PJT}). This out-of-plane vibration correlates to the modes with imaginary frequencies in D_{6h} or D_{2h} structures. All of the other vibrations have negligible influence on the both the distortion and the stabilization. The total stabilization energy is due to the stabilization of the electron-nuclear attraction along the path. This is because PJT π*-σ*mixing introduces additional bonding within a molecule. T_w and V_{XC} are also getting stabilized, while other energy components are opposing to the distortion, as in Figure 7.2.3.4.c,d.

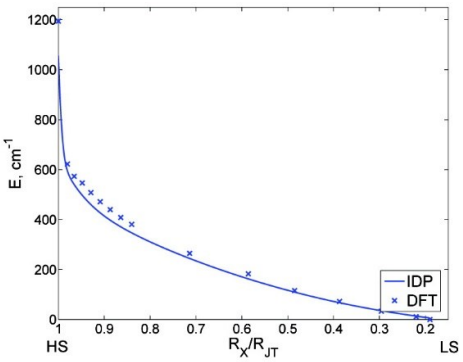

(a) Changes of the energy, IDP model and DFT results

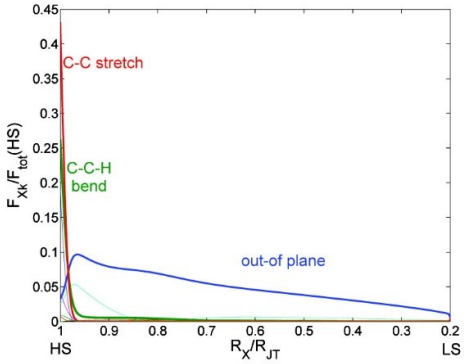

(b) Changes of the forces (normalized to the total distortion force at HS point) of the 9 a_1 normal modes in C_{2v}, along the IDP

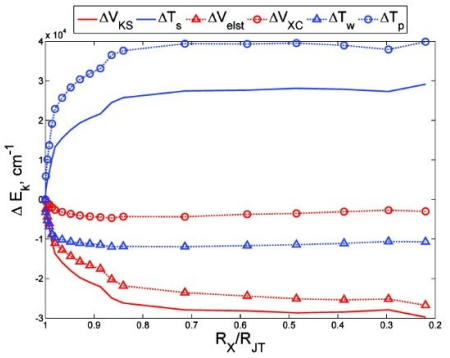

(c) Changes of the potential and kinetic energies along the IDP

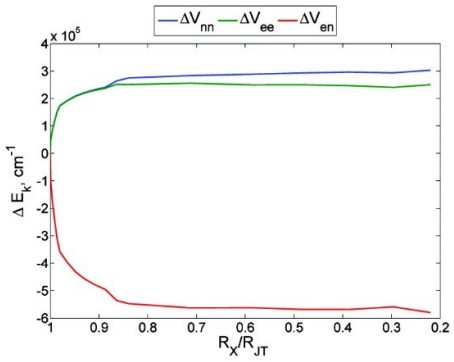

(d) Changes of the different potential energy terms along the IDP

Figure 7.2.3.4. Intrinsic distortion path and energy component analysis of the combined JT/PJT $D_{6h} \rightarrow C_{2v}$ distortion in $C_6H_6^-$.

7.2.4. Conclusion

In this Chapter, a general approach to analyze the multimode JT problem in the family of the JT active hydrocarbon rings, C_nH_n (n = 5-7), is presented. Additionally the examination of the systematic effects in the shape of the potential energy surfaces in these molecules was elucidated.

All considered species have a doubly degenerate electronic ground state which is coupled with vibrations of doubly degenerate irreps in the HS point group. Although the nature of chemical bonding is the same in all systems, they differ in the symmetry of the distortion, range of E_{JT}, the number of atoms, and hence the number of different normal modes that need to be considered in the IDP analysis. The results obtained by MD-DFT and IDP model are in a good agreement with the theoretical and experimentally estimated

values reported in the literature so far.[182, 184, 186, 187, 192] These results demonstrate the utility of this methodology, not only for the analysis of the proper JT effect, but also when PJT coupling is present. However, IDP method has not yet been explored in the cases where PJT or hidden JT effect.[36, 283, 284] The inspection of the IDP indicates that linearly JT active vibrations dominate along the path; harder ones are most important in the beginning, while softer ones take over along the path. Totally symmetric type vibrations appear not to be important. The contribution to the E_{JT} mainly originates from C-C stretch normal modes in C_nH_n molecules. The energy component analysis revealed that, while the electron-nuclear interactions are very important in the stabilization of the system around the HS point, other forces due to the electron-electron, nuclear-nuclear, and kinetic interactions are dominant in later stages of the distortion, although contributing very little to the total stabilization of the molecule through bending deformations. It can be concluded that, looking only at the values of individual energy components at HS and LS structures, without analyzing the details of their changes along the distortion path, chemically important features could be lost, and even wrong conclusions could be drawn. The correct answer can be obtained by inspection of the IDP, monitoring the changes of the contributions of the most important normal modes, in conjunction with energy component analysis. The subtle changes of the energy components are emerging as the outcome of the multimode JT effect in combination with changes in the electron density through the PJT effect. The assessment of the changes of individual energy components, in the combination with the IDP analysis of the multimode JT problem, gives an information about the main driving force for the distortion. This helps to rationalize the influence of different movements of nuclei on the electron density in a molecule.

7.2.5. Computational Details

The DFT calculations have been carried out using the Amsterdam Density Functional program package, ADF2010.01.[228-230] The LDA characterized by the VWN[61] parameterization have been used for the symmetry constrained geometry optimizations. TZP basis set has been used for all atoms. All calculations were spin-unrestricted. Separation of the orbital and the geometrical symmetry, as used in the calculation of the energies of the HS nuclear configurations is done using SYMROT subblock in the QUILD program, version 2010.01,[175] provided in the ADF2010.01 program package.

Analytical harmonic frequencies[231, 232] and normal modes at the LS stationary points were calculated. For the IDP analysis LDA geometries and information from corresponding frequency calculations were used. Values of the individual energy components were obtained from single-point LDA calculations, with 6-31G* basis set for all of the atoms, on the geometries obtained from the IDP analysis, using a NWChem program package, version 6.0.[285]

7.3. Multimode Jahn-Teller Problem in the Open-Shell Corannulenes and Coronenes

A rising technological area is focused and oriented on the electrical properties of fullerenes, graphene sheets, and similar carbon-based nanostructures, due to their outstanding properties and numerous ideas about their (potential) uses in nanotechnology.[286, 287] Consequently, the discovery and development of carbon nanostructures have stimulated studies on the chemistry of corannulene ([5]circulene, $C_{20}H_{10}$)[288, 289] and coronene ([6]circulene, $C_{24}H_{12}$),[290] Figure 7.3.1. Since $C_{20}H_{10}$ and $C_{24}H_{12}$ can be considered as fragments of fullerene (C_{60}) and graphite, respectively, the characterization of their electronic features is of the essential importance. $C_{20}H_{10}$ is a highly symmetric molecule (C_{5v} point group) representing the curvature in all known fullerenes and the end caps of nanotubes. It belongs to the family of polycyclic, strained, nonplanar aromatic hydrocarbons composed of five aromatic hexagons distributed around a central five-membered ring. $C_{24}H_{12}$, also known as a superbenzene, and molecular model of graphene sheets, consists of six aromatic hexagon rings symmetrically arranged around an inner six-membered ring (D_{6h} point group). Both molecules belong to an important class of functional organic materials, extensively studied for application in electronic devices.[291-294]

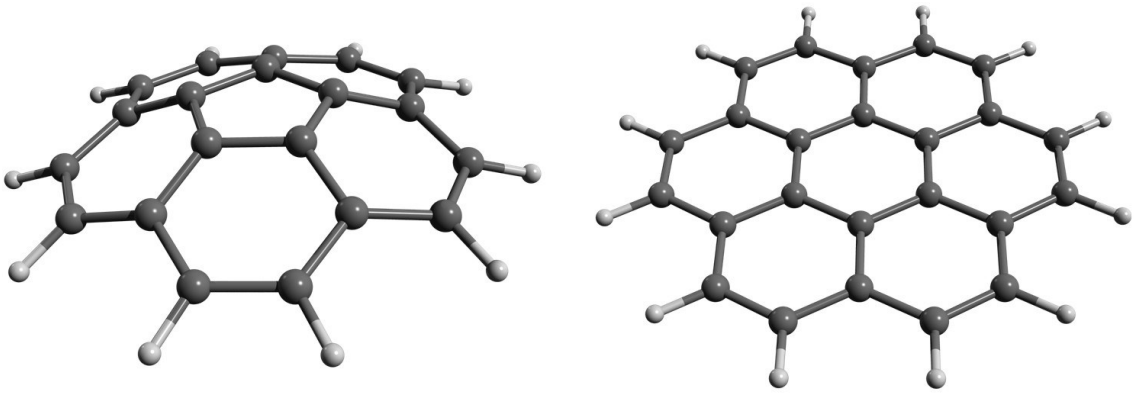

Figure 7.3.1. Structures of $C_{20}H_{10}$ and $C_{24}H_{12}$, respectively.

Because of their rich function, appearance in diverse natural environments, and search for new organic materials and superconductors, the study on the open-shell $C_{20}H_{10}$ and $C_{24}H_{12}$, with degenerate ground electronic states, have also attracted a great deal of attention.[295-300] Charged $C_{20}H_{10}$ and $C_{24}H_{12}$, i.e. $C_{20}H_{10}^{-}$, $C_{20}H_{10}^{+}$, $C_{24}H_{12}^{-}$ and $C_{24}H_{12}^{+}$, are species disposed to the multimode JT effect, thus, the determination, analysis, and getting further insight into the vibronic coupling in these molecules present a challenging task and interesting scientific topic.[199-203, 295, 300-308] Herein, the performance IDP model, Chapter 2, Section 2.6., in the analysis of the multimode JT problem in $C_{20}H_{10}^{-}$, $C_{20}H_{10}^{+}$, $C_{24}H_{12}^{-}$ and $C_{24}H_{12}^{+}$, is reported and the results are compared with the previous studies on $C_5H_5^{\cdot}$, $C_6H_6^{+}$, $C_6H_6^{-}$ (Chapter 6 and Section 7.2.), fullerene cation and fullerene anion.[20, 21, 79]

$C_{20}H_{10}^{-}$ and $C_{20}H_{10}^{+}$ have bowl-shaped structure (C_{5v} symmetry) with unpaired electron in e_1 doubly degenerate orbital. Due to the JT effect the symmetry is reduced to the C_s and $^2E_1$ ground state splits into two non-degenerate electronic states, $^2A'$ and $^2A''$, Figure 7.3.2. and Table 7.3.1. The electronic terms of planar $C_{24}H_{12}^{-}$ and $C_{24}H_{12}^{+}$ in D_{6h} symmetry are $^2E_{1g}$ and $^2E_{2u}$, respectively. The degenerate states of $C_{24}H_{12}^{-}$ and $C_{24}H_{12}^{+}$ split into non-degenerate electronic states upon elongated and compressed distortion from D_{6h} to D_{2h} symmetry, Figure 7.3.2. and Table 7.3.1.

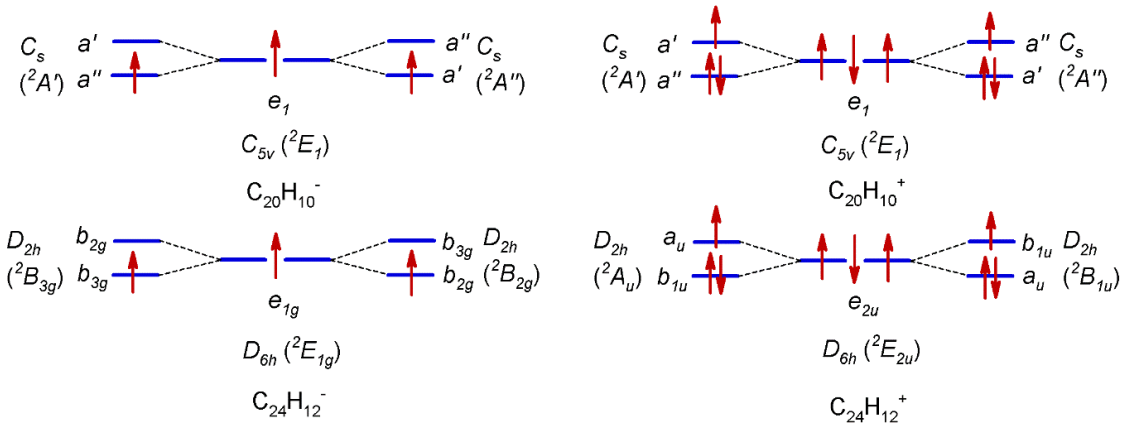

Figure 7.3.2. Schematic representation of the JT effect in $C_{20}H_{10}^{-}$, $C_{20}H_{10}^{+}$, $C_{24}H_{12}^{-}$ and $C_{24}H_{12}^{+}$.

Table 7.3.1. Summary of the group theory considerations for the JT distortions in $C_{20}H_{10}^-$, $C_{20}H_{10}^+$, $C_{24}H_{12}^-$ and $C_{24}H_{12}^+$. Γ_{el} is irrep of the electronic state; Γ_{JT} is irrep of the JT active vibrations; N is the number of atoms in a molecule; N_{a1} is the number of totally symmetrical vibrations in the LS point group. One component of the degenerate pairs of vibrations in the HS becomes a_1 in the LS point group.

Molecule	Distortion	Γ_{el}	Γ_{JT}	$3N$-6	N_{a1}	Origin of the LS a_1 vibs
$C_{20}H_{10}^-$	$C_{5v} \rightarrow C_s$	$E_1 \rightarrow A' + A''$	$E_2 \rightarrow A' + A''$	84	43	$9a_1$, $16e_1$, $18e_2$
$C_{20}H_{10}^+$	$C_{5v} \rightarrow C_s$	$E_1 \rightarrow A' + A''$	$E_2 \rightarrow A' + A''$	84	43	$9a_1$, $16e_1$, $18e_2$
$C_{24}H_{12}^-$	$D_{6h} \rightarrow D_{2h}$	$E_{1g} \rightarrow B_{2g} + B_{3g}$	$E_{2g} \rightarrow A_g + B_{1g}$	102	18	$6a_1$, $12e_{2g}$
$C_{24}H_{12}^+$	$D_{6h} \rightarrow D_{2h}$	$E_{2u} \rightarrow A_u + B_{1u}$	$E_{2g} \rightarrow A_g + B_{1g}$	102	18	$6a_1$, $12e_{2g}$

In order to elucidate whether the distortion in $C_{20}H_{10}^-$, $C_{20}H_{10}^+$, $C_{24}H_{12}^-$ and $C_{24}H_{12}^+$ is localized in the central ring of the investigated species, or spread over the whole molecules, molecular orbital (MO) analysis is performed, Figure 7.3.3. According to the careful inspection of doubly degenerate MOs (HS point group) containing unpaired electron, it is evident that the MOs are delocalized over the carbon skeleton of molecules and thus, all of the fragments (pentagons and hexagons depending on the molecule) play the role in the JT distortion.

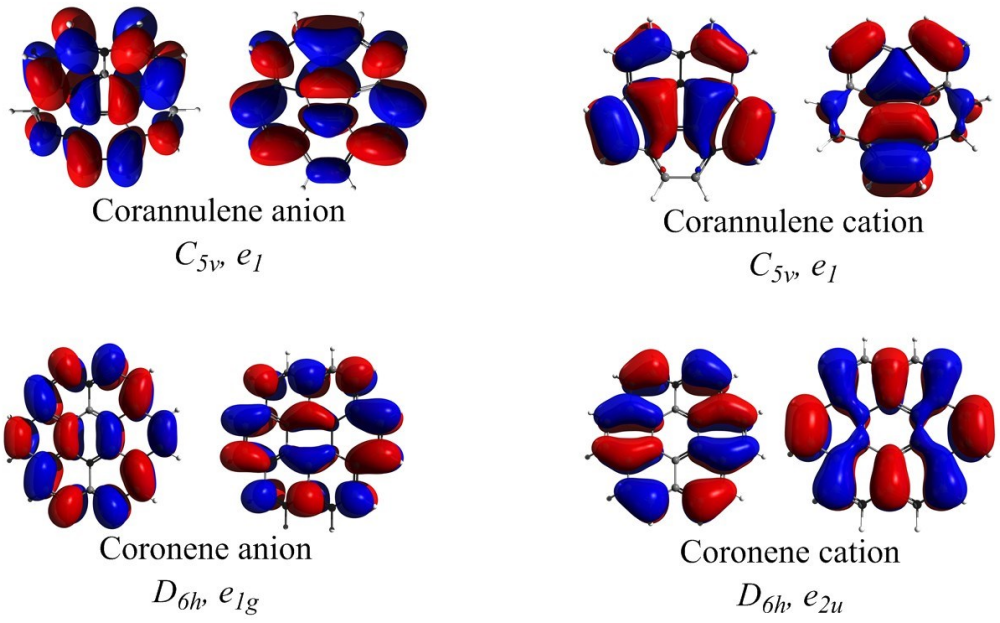

Figure 7.3.3. Schematic representation of doubly degenerate MOs containing unpaired electron in $C_{20}H_{10}^-$, $C_{20}H_{10}^+$, $C_{24}H_{12}^-$ and $C_{24}H_{12}^+$.

Bearing in the mind that calculated MD-DFT E_{JT} values using LDA for $C_5H_5^{\bullet}$, $C_6H_6^+$, fullerene cation and fullerene anion are 1244,[20, 78] 879,[20, 78] 599,[21] and 312 cm^{-1},[79] respectively, and that these values are in very good agreement with earlier experimental and theoretical investigations,[182, 184, 309-317] calculated E_{JT} for all investigated species give the confidence in the accuracy of the results, (See Chapter 6) . Particular choice of the XC functional for the determination of the JT parameters in $C_{20}H_{10}^-$, $C_{20}H_{10}^+$, $C_{24}H_{12}^-$ and $C_{24}H_{12}^+$ is not essential (Chapter 6). However, in all cases, E_{JT} obtained from IDP analysis is in a good agreement with DFT calculations using LDA, Table 7.3.2., confirming the validity of the model.

Table 7.3.2. Results of the DFT calculations performed to analyze the JT effect in $C_{20}H_{10}^-$, $C_{20}H_{10}^+$, $C_{24}H_{12}^-$ and $C_{24}H_{12}^+$. The JT parameters E_{JT} and Δ are given in cm^{-1} and R_{JT} in $(amu)^{1/2}$Å.

Molecule	JT parameters		Molecule	JT parameters	
	E_{JT}, $^2A'$	405		E_{JT}, $^2B_{2g}$	290
	E_{JT}, $^2A''$	403		E_{JT}, $^2B_{3g}$	279
	E_{JT}(IDP), $^2A'$	414		E_{JT}(IDP), $^2B_{2g}$	284
$C_{20}H_{10}^-$	E_{JT}(IDP), $^2A''$	396	$C_{24}H_{12}^-$	E_{JT}(IDP), $^2B_{3g}$	276
	Δ	1.6		Δ	12.1
	R_{JT}, $^2A'$	0.32		R_{JT}, $^2B_{2g}$	0.12
	R_{JT}, $^2A''$	0.23		R_{JT}, $^2B_{3g}$	0.12
	E_{JT}, $^2A'$	541		E_{JT}, ^2A_u	275
	E_{JT}, $^2A''$	548		E_{JT}, $^2B_{1u}$	287
	E_{JT}(IDP), $^2A'$	559		E_{JT}(IDP), ^2A_u	276
$C_{20}H_{10}^+$	E_{JT}(IDP), $^2A''$	577	$C_{24}H_{12}^+$	E_{JT}(IDP), $^2B_{1u}$	285
	Δ	-2.4		Δ	-12.9
	R_{JT}, $^2A'$	0.43		R_{JT}, ^2A_u	0.19
	R_{JT}, $^2A''$	0.53		R_{JT}, $^2B_{1u}$	0.19

In order to determine the linear vibronic coupling constants, and to get further insight into the multimode problem in $C_{20}H_{10}^-$, $C_{20}H_{10}^+$, $C_{24}H_{12}^-$ and $C_{24}H_{12}^+$, the forces at the HS point were calculated toward the distortion to the LS structures, Tables 7.3.3.-7.3.6. An analysis of the multimode JT distortion shows that, out of 43 totally symmetric normal modes in the LS minimum conformation, Table 7.3.1., in the case of $C_{20}H_{10}^-$ and $C_{20}H_{10}^+$, 10 and 15 normal modes describe the distortion, respectively, Tables 7.3.3. and 7.3.4. In the case of $C_{24}H_{12}^-$ and $C_{24}H_{12}^+$, out of 18 a_{1g} modes, 8 vibrations are sufficient, Tables 7.3.5. and 7.3.6. These selected normal modes contribute the most to the JT distortion (R_{JT}), and to the overall force at the HS point.

The IDP profiles for the distortion from the C_{5v} cusp to the C_s global minimum for both, $C_{20}H_{10}^-$ and $C_{20}H_{10}^+$, Figures 7.3.4. and 7.3.5. (top), clearly distinguishes two different regions. In the first region, the energy is changing fast, and most of the E_{JT} is obtained after 10% of the path. In the second region the molecules have just relaxed toward the global minima. The distortion starts with the hardest C-C stretching modes, mostly tangential in character, Figures 7.3.4. and 7.3.5. (bottom). In the case of $C_{20}H_{10}^-$ the vibrations at 1616 and 1481 cm^{-1} correspond to C-C stretch mainly localized in the central pentagon ring, and hexagon rings, respectively, Figure 7.3.6. These two modes have the largest linear vibronic coupling constants, Table 7.3.3. and Figure 7.3.4. (bottom), and their contributions to the total force decrease rapidly along the IDP path. According to the earlier work, only one mode at 1669 cm^{-1}, corresponding to C-C stretch delocalized over whole carbon skeleton, has a large coupling constant.[199] The data obtained for $C_{20}H_{10}^+$ show that only one force along C-C stretching mode at 1483 cm^{-1} is pushing the nuclei toward a minimum, Table 7.3.4. and Figure 7.3.5. (bottom). The difference in the motion of the atoms in normal modes around 1480 cm^{-1} of $C_{20}H_{10}^-$ and $C_{20}H_{10}^+$, Figure 7.3.6., lead to the different contributions to the driving forces, Tables 7.3.3. and 7.3.4. The contribution to the distortion of lower frequency modes for both, $C_{20}H_{10}^-$ and $C_{20}H_{10}^+$, is not negligible, Tables 7.3.3. and 7.3.4. In the second region of IDP, these soft modes, mostly with radial character, lead molecules toward the global minima. For both investigated species, wagging vibrations at 184 (for $C_{20}H_{10}^-$) and 150 cm^{-1} (for $C_{20}H_{10}^+$) do not contribute significantly to the total force, Figures 7.3.4. and 7.3.5. (bottom) and Tables 7.3.3. and 7.3.4, but play the main role concerning the JT radii.

Table 7.3.3. Analysis of the multimode JT effect in $C_{20}H_{10}^-$ at the C_{5v} nuclear configuration: the JT radii ($r_{JT,i}$, (amu)$^{1/2}$Å), contribution of the chosen C_{5v} normal modes to the distortion (c_i), and the forces (linear vibronic coupling constants, F_i^{HS}, cm^{-1}/ Å) of the chosen C_{5v} normal modes. Total force along all 43 JT active modes is 22019 cm^{-1}/Å. The total r_{JT} and F^{HS} are vector sum.

$C_{20}H_{10}^-$, $C_{5v} \rightarrow C_s$				
Assignment	Freq., cm^{-1}	$r_{JT,i}$, (amu)$^{1/2}$Å	c_i	F_i^{HS}, cm^{-1}/Å
wagging	184	0.2647	0.7031	229
wagging	333	0.0443	0.0196	78
C-C-C bending	428	0.0501	0.0252	892
wagging	601	0.1031	0.1067	3838
wagging	697	0.0483	0.0235	1699
C-C-C and C-C-H bending	1074	0.0440	0.0210	5109
C-C-H bending	1198	0.0209	0.0044	2574
C-C stretching	1414	0.0144	0.0021	3011
C-C stretching	1481	0.0594	0.0354	13010
C-C stretching	1616	0.0585	0.0343	15658
Total		0.3115	0.9753	21788

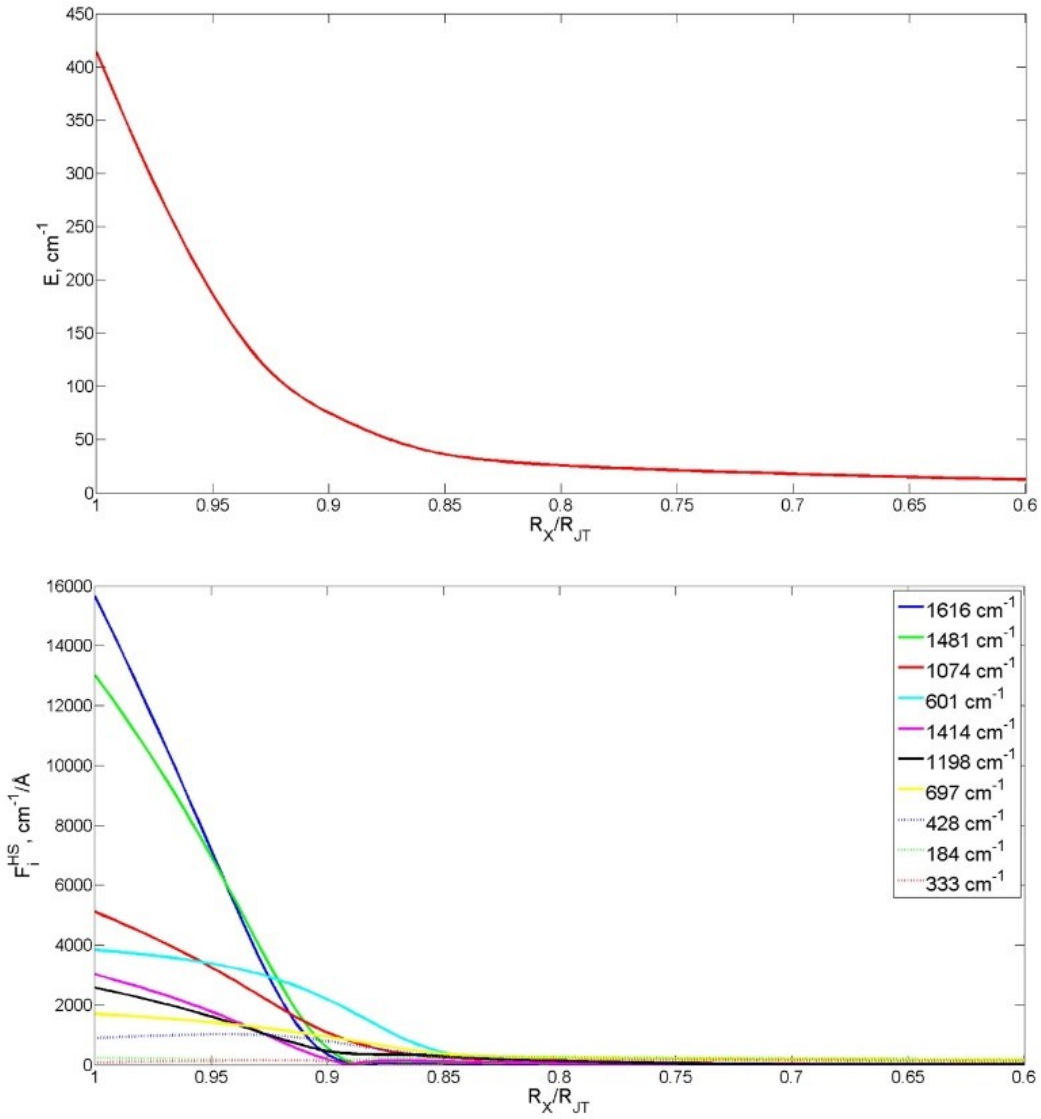

Figure 7.3.4. IDP analysis of the $C_{5v} \rightarrow C_s$ multimode JT distortion in $C_{20}H_{10}^{-}$: change of the energy from C_{5v} nuclear configuration to the C_s global minimum (top); changes of the forces along the important C_{5v} normal modes (bottom).

Table 7.3.4. Analysis of the multimode JT effect in $C_{20}H_{10}^{+}$ at the C_{5v} nuclear configuration: the JT radii (r_{JT},i, (amu)$^{1/2}$Å), contribution of the chosen C_{5v} normal modes to the distortion (c_i), and the forces (linear vibronic coupling constants, F_i^{HS}, cm^{-1}/ Å) of the chosen C_{5v} normal modes. Total force along all 43 JT active modes is 21244 cm^{-1}/Å. The total r_{JT} and F^{HS} are vector sum.

$C_{20}H_{10}^{+}$, $C_{5v}\rightarrow C_s$				
Assignment	Freq., cm^{-1}	$r_{JT,i}$, (amu)$^{1/2}$Å	c_i	F_i^{HS}, cm^{-1}/Å
wagging	150	0.4443	0.6889	746
wagging	276	0.0713	0.0177	996
C-C-C bending	434	0.2227	0.1732	3676
C-C-C and C-C-H bending	538	0.0300	0.0031	922
wagging	607	0.0805	0.0227	1971
wagging and C-C-H bending	650	0.1056	0.0390	4079
wagging	772	0.0455	0.0073	1912
wagging	821	0.0344	0.0041	2208
C-C-C and C-C-H bending	1087	0.0481	0.0081	5717
C-C-H bending	1133	0.0114	0.0005	818
C-C-H bending	1214	0.0203	0.0014	3245
C-C stretching	1378	0.0160	0.0008	3385
C-C stretching	1409	0.0174	0.0011	4205
C-C stretching	1483	0.0825	0.0238	17999
C-C stretching	1642	0.0126	0.0005	2368
Total		0.5331	0.9922	21156

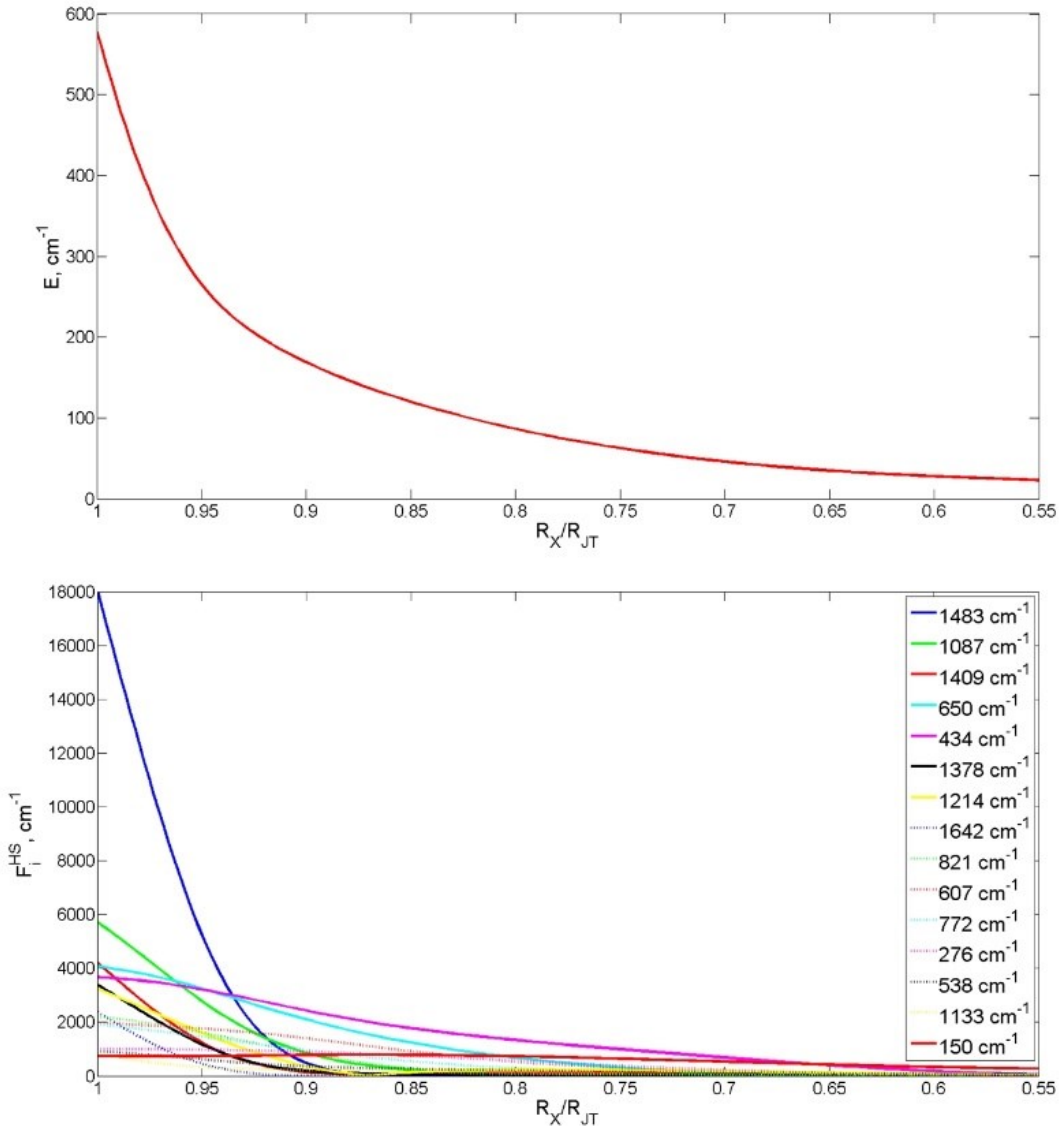

Figure 7.3.5. IDP analysis of the $C_{5v} \rightarrow C_s$ multimode JT distortion in $C_{20}H_{10}^{+}$: change of the energy from C_{5v} nuclear configuration to the C_s global minimum (top); changes of the forces along the important C_{5v} normal modes (bottom).

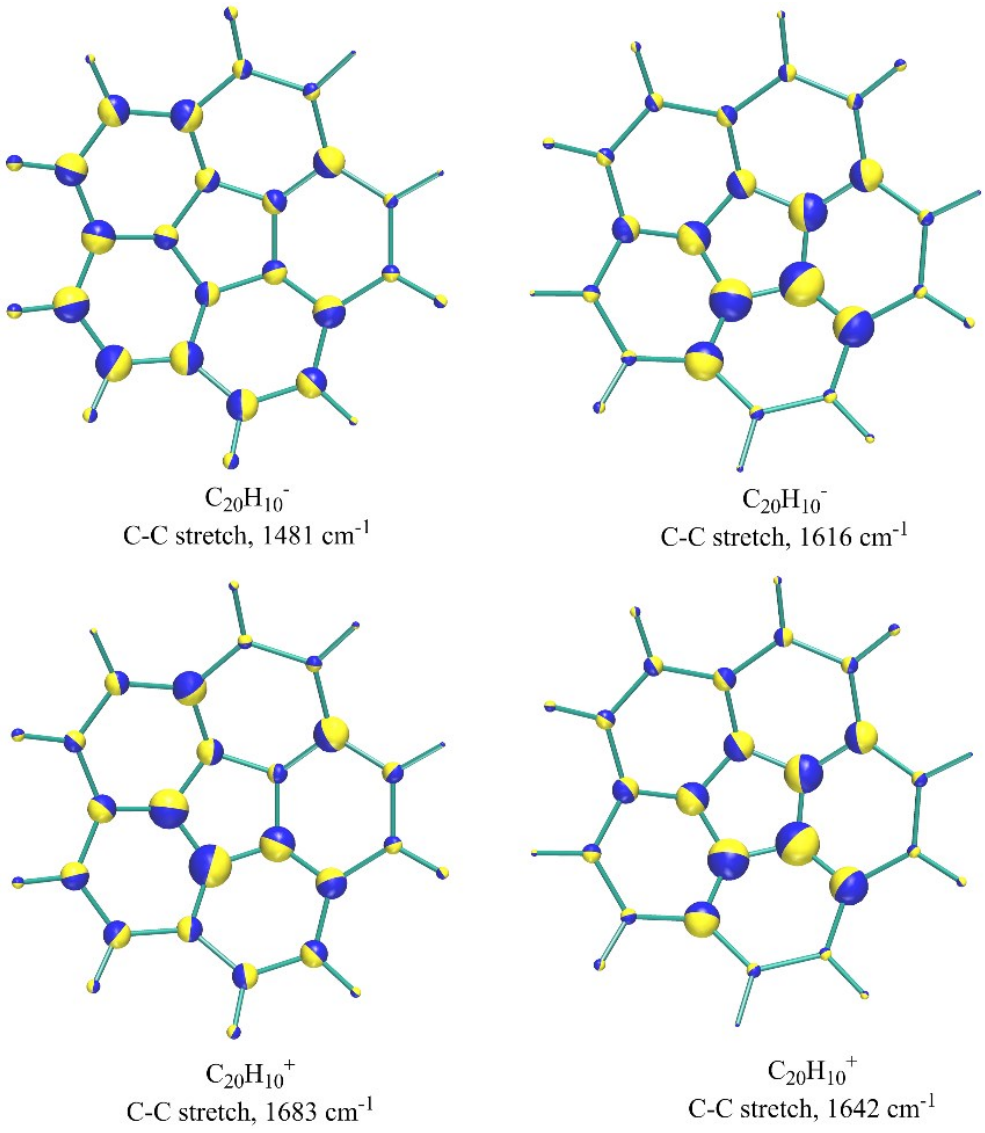

Figure 7.3.6. Schematic representation of the hardest C-C stretching modes in $C_{20}H_{10}^-$ and $C_{20}H_{10}^+$. The size of vibrational motion on a nucleus is represented as sphere with the radius depending on the magnitude of the motion. The different colors indicate the direction of the motion.

On the potential energy profiles of $C_{24}H_{12}^-$ and $C_{24}H_{12}^+$, again, two distinct regions were observed, Figures 7.3.7. and 7.3.8. (top), respectively. In the first 20-30 % of the path the most of the E_{JT} is obtained. The C-C stretching modes of 1655 and 1652 cm^{-1} for $C_{24}H_{12}^-$ and $C_{24}H_{12}^+$, respectively, afford the largest coupling constants, and hence stabilize the molecules, Tables 7.3.5. and 7.3.6. and Figures 7.3.7. and 7.3.8. (bottom), which is in very good agreement with results obtained by Kato et al.[202] In the second region of the IDP, molecules relax toward the LS minima, Figures 7.3.7. and 7.3.8. (top). Softer modes, C-C-C bending, which cause a deformation of the carbon skeleton, become

more important, allowing relaxation, and the APES is flat. The discrepancy with previous study[202] refers to the contribution of the two C-H stretching modes to the distortion. The IDP analysis did not find these modes to contribute significantly to the JT distortion in $C_{24}H_{12}^-$ and $C_{24}H_{12}^+$, because MO analysis, Figure 7.3.3., does not show any contribution of hydrogen *s* orbitals to the HOMOs of $C_{24}H_{12}^-$ and $C_{24}H_{12}^+$.

Table 7.3.5. Analysis of the multimode JT effect in $C_{24}H_{12}^-$ at the D_{6h} nuclear configuration: the JT radii ($r_{JT,i}$, (amu)$^{1/2}$Å), contribution of the chosen D_{6h} normal modes to the distortion (c_i), and the forces (linear vibronic coupling constants, F_i^{HS}, cm^{-1}/ Å) of the chosen D_{6h} normal modes. Total force along all 18 JT active modes is 21219 cm^{-1}/Å. The total r_{JT} and F^{HS} are vector sum.

$C_{24}H_{12}^-$, $D_{6h}\rightarrow D_{2h}$				
Assignment	Freq., cm^{-1}	$r_{JT,i}$, (amu)$^{1/2}$Å	c_i	F_i^{HS}, cm^{-1}/Å
C-C-C bending	359	0.0676	0.3017	760
C-C-C and C-C-H bending	489	0.0473	0.1477	1097
C-C-C and C-C-H bending	986	0.0233	0.0358	2060
C-C-H bending	1117	0.0309	0.0630	3041
C-C-H bending	1230	0.0243	0.0390	3341
C-C stretching	1454	0.0142	0.0133	2962
C-C stretching	1496	0.0326	0.0698	7024
C-C stretching	1652	0.0698	0.3218	18972
Total		0.1226	0.9921	21083

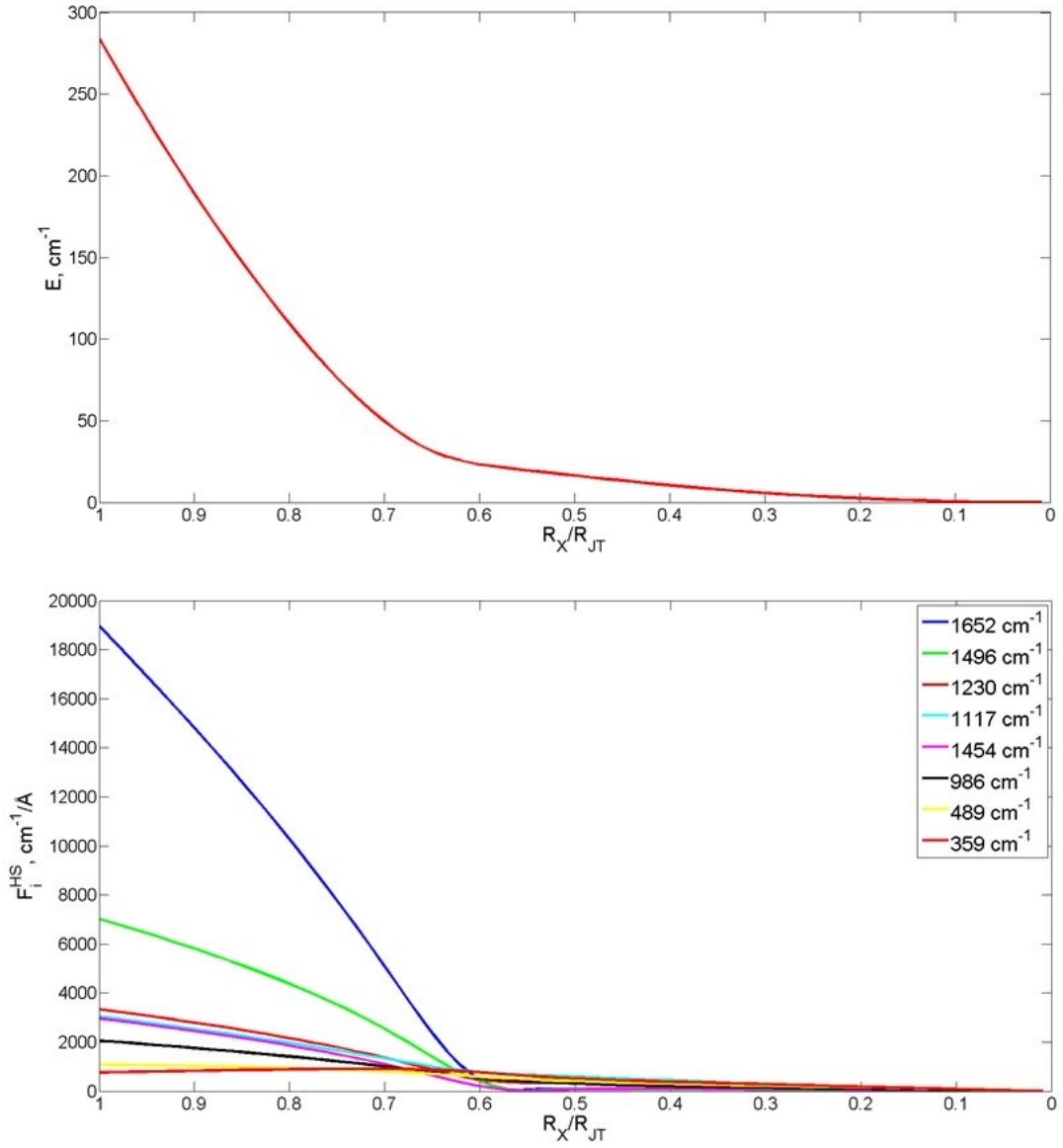

Figure 7.3.7. IDP analysis of the $D_{6h} \rightarrow D_{2h}$ multimode JT distortion in $C_{24}H_{12}^{-}$: change of the energy from D_{6h} nuclear configuration to the D_{2h} stationary point (top); changes of the forces along the important D_{6h} normal modes (bottom).

Table 7.3.6. Analysis of the multimode JT effect in $C_{24}H_{12}^{+}$ at the D_{6h} nuclear configuration: the JT radii ($r_{JT,i}$, (amu)$^{1/2}$Å), contribution of the chosen D_{6h} normal modes to the distortion (c_i), and the forces (linear vibronic coupling constants, F_i^{HS}, cm^{-1}/ Å) of the chosen D_{6h} normal modes. Total force along all 18 JT active modes is 19296 cm^{-1}/Å. The total r_{JT} and F^{HS} are vector sum.

$C_{24}H_{12}^{+}$, $D_{6h}\rightarrow D_{2h}$				
Assignment	Freq., cm^{-1}	$r_{JT,i}$, (amu)$^{1/2}$Å	c_i	F_i^{HS}, cm^{-1}/Å
C-C-C bending	368	0.1664	0.7460	2384
C-C-C and C-C-H bending	487	0.0500	0.0672	1058
C-C-C and C-C-H bending	1005	0.0187	0.0094	2245
C-C-H bending	1143	0.0320	0.0276	3819
C-C-H bending	1247	0.0262	0.0185	4197
C-C stretching	1475	0.0089	0.0021	2124
C-C stretching	1496	0.0408	0.0447	9359
C-C stretching	1655	0.0554	0.0827	15335
Total		0.1925	0.9982	19269

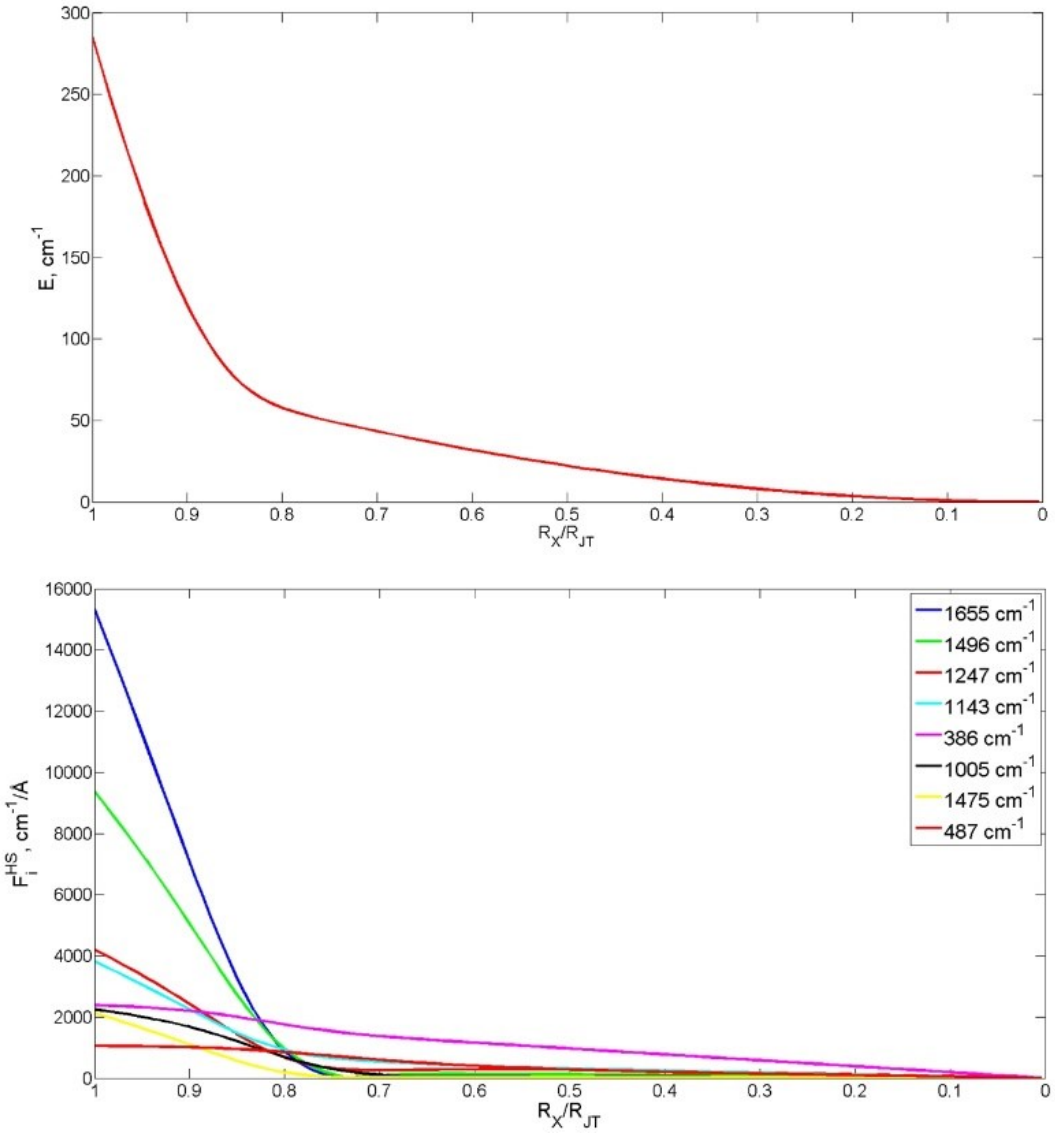

Figure 7.3.8. IDP analysis of the $D_{6h} \rightarrow D_{2h}$ multimode JT distortion in $C_{24}H_{12}^{+}$: change of the energy from D_{6h} nuclear configuration to the D_{2h} stationary point (top); changes of the forces along the important D_{6h} normal modes (bottom).

It is interesting to note that in $C_5H_5^{\bullet}$, $C_6H_6^{-}$ and $C_6H_6^{+}$ the distortion also always starts with the hardest C-C stretch modes,[20, 318] Table 7.3.7. Soft modes, C-C-C bend and C-C-H bend, relax molecules toward the global minima. The force along these three relevant modes in the case of $C_5H_5^{\cdot}$ is 37666 cm^{-1}/Å, Table 7.3.7. The forces along the selected important vibrations for $C_{20}H_{10}^{-}$ and $C_{20}H_{10}^{+}$ are around 21000 cm^{-1}/Å, Tables 7.3.3. and 7.3.4. The larger driving force in $C_5H_5^{\cdot}$ results in larger E_{JT}. As $C_{24}H_{12}^{-}$ and $C_{24}H_{12}^{+}$ are constructed out of six-member carbon rings, it is not surprising that the same trend is observed in the case of $C_{24}H_{12}^{-}$, $C_{24}H_{12}^{+}$, $C_6H_6^{-}$ and $C_6H_6^{+}$, Tables 7.3.5.-7.3.7.

Moreover, recent analysis of the multimode JT effect in fullerene cation and anion revealed that the distortion starts with hardest frequency anti-squashing modes, mainly C-C stretch modes, contributing the most to the total force.[21, 79] Thus, the IDP analysis may give a general trend in the distortion behavior of the JT active molecules with C-C bonds. In all the cases, direction of the distortion can be qualitatively understood from the shape and phase pattern of frontier MOs.[21, 79, 319] The distortion will always be directed in the way of maximizing the bonding interactions, and minimizing antibonding interactions of the orbitals partially occupied by an electron. This is related to the fact that mechanism of the distortion must be in close relationship with the electronic structure, as has been emphasized by Kato et al. in studying the JT effect in series of charged hydrocarbons.[318, 320-322] However, deeper analysis is needed to understand the different role of the normal modes to the distortion. Analysis of the multimode problem, as given by IDP analysis, explains this in a straightforward manner.

Table 7.3.7. Analysis of the multimode JT effect in $C_5H_5^{\bullet}$, $C_6H_6^-$ and $C_6H_6^+$ at the HS nuclear configuration: the JT radii (r_{JT},i, (amu)$^{1/2}$Å), contribution of the chosen HS normal modes to the distortion (c_i), and the forces (linear vibronic coupling constants, F_i^{HS}, cm^{-1}/ Å) of the chosen HS normal modes. The total r_{JT} and F^{HS} are vector sum.

Assignment	Freq., cm^{-1}	$r_{JT,i}$, (amu)$^{1/2}$Å	c_i	F_i^{HS}, cm^{-1}/Å
$C_5H_5^{\bullet}$, $D_{5h}\rightarrow C_{2v}$				
C-C-C bending	832	0.1541	0.3695	11749
C-C-H bending	1052	0.1242	0.2403	13084
C-C stretching	1426	0.1571	0.3842	33309
Total		0.2527	0.9940	37666
$C_6H_6^-$, $D_{6h}\rightarrow D_{2h}$				
C-C-C bending	593	0.2323	0.7658	9218
C-C-H bending	1168	0.0779	0.0861	11126
C-C stretching	1596	0.1018	0.1471	29440
Total		0.2653	0.9990	32795
$C_6H_6^+$, $D_{6h}\rightarrow D_{2h}$				
C-C-C bending	557	0.0990	0.2878	2867
C-C-H bending	1108	0.0907	0.2414	10218
C-C stretching	1545	0.1265	0.4691	34126
Total		0.1845	0.9983	35738

7.3.1. Conclusion

Analysis of the multimode JT distortion in $C_{20}H_{10}^-$, $C_{20}H_{10}^+$, $C_{24}H_{12}^-$ and $C_{24}H_{12}^+$ is presented, combining MD-DFT and IDP methods.

Since there are more than one set of degenerate JT active modes in investigated molecules, the JT distortions are derived from the sum of contributions of all possible vibrations. However, not all of them have the same role. The C-C stretching modes play the most important role in the stabilization of the systems, both in the anions and cations of corannulene and coronene, pushing the nuclei toward the minima on the potential energy surface. The further inspection of the IDP in $C_{20}H_{10}^-$, $C_{20}H_{10}^+$, $C_{24}H_{12}^-$ and $C_{24}H_{12}^+$ revealed that the relaxation of the geometry arrives in the final part of the path and is encountered by the lowest frequency vibrational modes. The present study hopefully

complements previous works on $C_5H_5^{\bullet}$, $C_6H_6^{+}$, $C_6H_6^{-}$, fullerene cation, and fullerene anion.[20, 21, 79, 319]

7.3.2. Computational Details

The DFT calculations have been carried out using the Amsterdam Density Functional program package, ADF2013.01.[229, 230, 238] Geometry optimization of all investigated molecules was performed using LDA characterized by the VWN parameterization.[61] TZP basis set has been used for all atoms. All calculations were spin-unrestricted. Separation of the orbital and the geometrical symmetry, as used in the calculation of the energies of the HS nuclear configurations, is done using SYMROT subblock in the QUILD program, version 2013.01,[239] provided in the ADF2013.01 program package. Analytical harmonic frequencies[231, 232] were calculated in order to ascertain that LS structures correspond to the stationary points on the potential energy surface. For the IDP analysis LDA geometries and information from corresponding frequency calculations were used.

7.4. Final Remarks on the Treatment of the Multimode Jahn-Teller Problem

A general approach to analyze the multimode JT distortion is presented and applied to study the APES in square-planar arsenic and antimony anions, small organic radicals and cations and anions of corannulene and coronene. The specific formulation of the JT distortion in terms of the Hessian of the LS minimum has several advantages. The LS structure is a true minimum on the APES, and the potential energy expression has a simple analytical form in the harmonic approximation. Expressing the distortion along the minimal energy path from the HS to LS minimum gives the change of contribution of different normal modes to the JT distortion. IDP analysis rigorously treats all the possible normal modes and provides important chemical information like an approximation to the minimum energy path, and the decomposition of the JT forces in a mode-per-mode basis without the requirement of case-by-case model. In fact, the contributions of each mode along the path are not fixed in IDP, allowing an analysis of the importance of each one depending on their distance to the HS configuration. The combination of the alternative methods for the analysis of the multimode problem, one starting from the HS nuclear configuration and reduction of the multimode problem to a single interaction mode[1] and IDP model starting from the LS nuclear configuration may be a possible general solution of the multimode problem and can be considered as a reliable tools for the better understanding of the JT phenomena.

8. Results and Discussion: The Influence of the Jahn-Teller Effect on the Aromaticity

Aromaticity, intuitive concept in chemistry and physics, is considered as a property of systems that are thermodynamically stabilized as a consequence of cyclic electron delocalization. The delocalized electronic structure of aromatic compounds yields enhanced planarity, equalized bond lengths, enhanced stability due to the resonance, favoring of the substitution instead of the addition that would be typical for isolated double bonds, and the ability to sustain ring currents when exposed to the external magnetic fields. Contrary to the concept of aromaticity, JT effect induces unequalization of bond lengths, leading to the stabilization of the system upon a distortion. The investigation of the influence of JT distortion on the aromaticity of 4n+1 π open-shell molecules is certainly of the increasing importance due to the rapid developments in material chemistry, for example considering magnetism and structure of graphene nanodots.[323] Understanding relation between aromatic 4n+2 π and antiaromatic 4n+1 π JT active systems is necessary for applying concept of aromaticity to a design of new molecules, and in general for the investigation of their electronic structure, chemical bonding and properties. Thus, finding a method of choice to determine both chemically relevant phenomena is essential since they lead to the different reaction pathways and the connection of aromaticity and vibronic coupling demands tremendous caution. In this Chapter, the impact of the JT distortion on the aromaticity in cyclopentadienyl radical, benzene cation and anion, bis(cyclopentadienyl)cobalt(II), fullerene ions and square planar arsenic and antimony anionic clusters is presented.

8.1. Magnetic Criteria of Aromaticity in a Benzene Cation and Anion: How Does the Jahn-Teller Effect Influence the Aromaticity?

NICS values for $C_6H_6^+$ and $C_6H_6^-$ were calculated along the relevant particular path of distortion, the IDP path, as well as evaluation of their magnetic susceptibility and anisotropy. It is worth noting that negative and positive NICS values are associated with aromatic and antiaromatic rings, respectively. Discussion whether the loss or gain of antiaromaticity occurs gradually along the IDP or suddenly at a certain point on the APES will help to gain insight into the relationship between the vibronic coupling and aromaticity.

$C_6H_6^+$ and $C_6H_6^-$, with 4n+1 π electrons, are JT unstable and prefer the conformation of lower symmetry, as discussed in Chapter 7. $C_6H_6^+$ adopts D_{2h} symmetry in the global minimum structure. Due to the PJT coupling of the ground π* electronic state with the excited σ* state in $C_6H_6^-$, the out-of-plane C_{2v} conformation is found to be the global minimum on the potential energy surface. The C_{2v} geometry obtained is a consequence of both, proper JT and PJT distortion. Analysis of the changes of the aromatic character of these JT active molecules along the IDP for $D_{6h} \rightarrow D_{2h}$ distortion for both $C_6H_6^+$ and $C_6H_6^-$, and $D_{6h} \rightarrow C_{2v}$ for $C_6H_6^-$ are shown in Figures 8.1.1., 8.1.2. and 8.1.3.a.

The benzene molecule is typical example of a π aromatic system, showing a minimum NICS value at certain distances from the center of the ring plane (Table 8.1.1.). Magnetic susceptibility data for benzene are presented in the Table 8.1.2. All calculations of NICS parameters on C_6H_6, performed for comparison purposes, were in good agreement with previous theoretical values [NICS(0) = -9.7 ppm[132]].

For both $C_6H_6^+$ and $C_6H_6^-$, NICS values were evaluated at the ring center above the ring plane (0 Å - 10 Å) along the IDP path from D_{6h} to D_{2h} structures and the values for the HS and LS points are reported in Table 8.1.1. Since the calculation of magnetic properties in species with a degenerate ground state may lead to incorrect results, the NICS values were calculated imposing HS (D_{6h}) nuclear arrangement and LS (D_{2h}) symmetry of electron density. NICS values monitored along the path for the $^2B_{2g}$ state in $C_6H_6^+$ and the ^2A_u state in $C_6H_6^-$, which are the minima on the corresponding D_{2h} potential energy surfaces, are presented. The results for other states are qualitatively the same. According to the obtained NICS index (Table 8.1.1.), $C_6H_6^+$ and $C_6H_6^-$ reveal antiaromatic character, as expected.[121] However, plotted NICS values versus the JT distortion, $\vec{R}_X$ / $\vec{R}_{JT}$

, and the distance from the ring center (Figures 8.1.1. and 8.1.2.) give a more detailed picture. Aromaticity favors bond equalization while antiaromaticity leads to bond alternation. Removing or adding an electron to the benzene molecule causes non-totally symmetric electron density in high symmetry, D_{6h} point group, while bond distances remain the same. Due to the non-totally symmetric electron density, $C_6H_6^+$ and $C_6H_6^-$, in D_{6h}, possess strong antiaromatic character. Near the point of electron degeneracy the HOMO-LUMO gap is significantly small, hence NICS parameters have large values in the first region of the distortion path (Figures 8.1.1. and 8.1.2.). Although the JT distortion leads to the bond unequalization, our results reveal lowering of antiaromatic behavior along the IDP. The forces, responsible for removing orbital degeneracy, lead to enhancement of the HOMO-LUMO gap.

Table 8.1.1. Calculated NICS values for C_6H_6, $C_6H_6^+$ and $C_6H_6^-$ at HS and LS geometries; NICS(0), NICS(1) and $NICS_{zz}(1)$ are given in ppm

	Geometry	Electronic state	NICS(0)	NICS(1)	$NICS_{zz}(1)$
C_6H_6	D_{6h}	$^1A_{1g}$	-7.9	-10.1	-29.0
$C_6H_6^+$	D_{6h}	$^2B_{2g}$	130.2	106.2	322.1
	D_{2h}	$^2B_{2g}$	28.3	18.5	59.1
$C_6H_6^-$	D_{6h}	^2A_u	220.3	172.6	502.7
	D_{2h}	^2A_u	57.3	45.0	129.2
	C_{2v}	$^2A_1$	9.7	5.4	17.9

Values of mean molar magnetic susceptibility (χ_M), molar magnetic anisotropy ($\Delta\chi$) and the z-component of the magnetic tensor (χ_{zz}) for the studied molecules, at their HS and LS conformations, are given in Table 8.1.2. In comparison to benzene, $C_6H_6^+$ in D_{6h} point group has large positive magnetic susceptibility data, while in the global minimum, D_{2h} symmetry, these values become slightly negative. In the case of $C_6H_6^-$, the z-component of the magnetic tensor has a large positive value for a molecule in HS conformation and becomes negative after the first descent in symmetry. The large negative magnetic anisotropy value for the benzene anion in D_{2h} symmetry cannot be an indicator for aromatic character since the x-component of the magnetic tensor has a large

positive value, while the y- and z-components have small negative values (χ_{xx}=192.7 cgs-ppm, χ_{yy}= -27.1 cgs-ppm, χ_{zz}= -23.7 cgs-ppm).

Table 8.1.2. Magnetic susceptibility data for C_6H_6, $C_6H_6^+$ and $C_6H_6^-$ at HS and LS geometries; χ_M, $\Delta\chi$ and χ_{zz} are given in cgs-ppm

	Geometry	Electronic state	χ_M	$\Delta\chi$	χ_{zz}
C_6H_6	D_{6h}	$^1A_{1g}$	-56.1	-64.9	-99.4
$C_6H_6^+$	D_{6h}	$^2B_{2g}$	75.1	293.0	270.5
	D_{2h}	$^2B_{2g}$	-16.1	-9.8	-22.6
$C_6H_6^-$	D_{6h}	^2A_u	286.2	818.2	831.7
	D_{2h}	^2A_u	47.3	-106.6	-23.7
	C_{2v}	$^2A_1$	-46.3	23.4	-30.7

The global minimum of $C_6H_6^-$, C_{2v} structure with $^2A_1$ electronic state, is slightly puckered, thus the NICS parameters were calculated at the center, above and below the average ring plane (-10 Å – 10 Å). The results obtained from D_{6h} toward distorted C_{2v} structure, considering the combined JT/PJT effect, are given in Table 8.1.1. Following NICS values along the IDP, from the HS point to C_{2v} minimum energy conformation, two regions could be distinguished. In the first 3% of the path the JT effect dominates, the molecule stays planar and NICS values decrease fast but smoothly, similar to the previously described case. In the second region, where the distortion is almost completely described by the out-of-plane vibration (see Chapter 7),[20] decreasing of NICS values is abrupt. At the point R_X/R_{JT}=0.97 an almost steep-like change in the NICS values occurs. At this point NICS parameters change from low positive to low negative values as the distance from the ring plane increases (Figure 8.1.3), revealing the non-aromatic character.[324] Explanation for this abrupt change of NICS values is associated with mixing of the ground π^* state with the first excited σ^* state at a certain point, which leads to a discontinuity in the values. It should be pointed out that from the same point, PJT mixing becomes very important, and determines the overall puckered structure.

Magnetic susceptibility data for $C_6H_6^-$ for distortion caused by combined JT/PJT effects are presented in Table 8.1.2. Observing reduction of symmetry from D_{6h} to C_{2v}, the magnetic susceptibility data have almost the same trend as in the $C_6H_6^+$ ion.

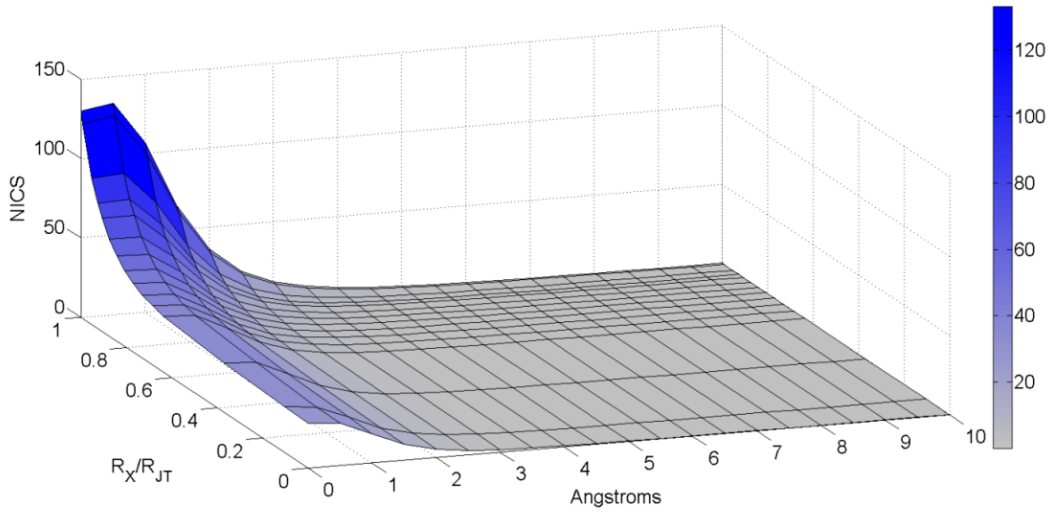

Figure 8.1.1. Schematic plots of the NICS values along the IDP for the benzene cation (D_{6h} to D_{2h}), $^2B_{2g}$ electronic state.

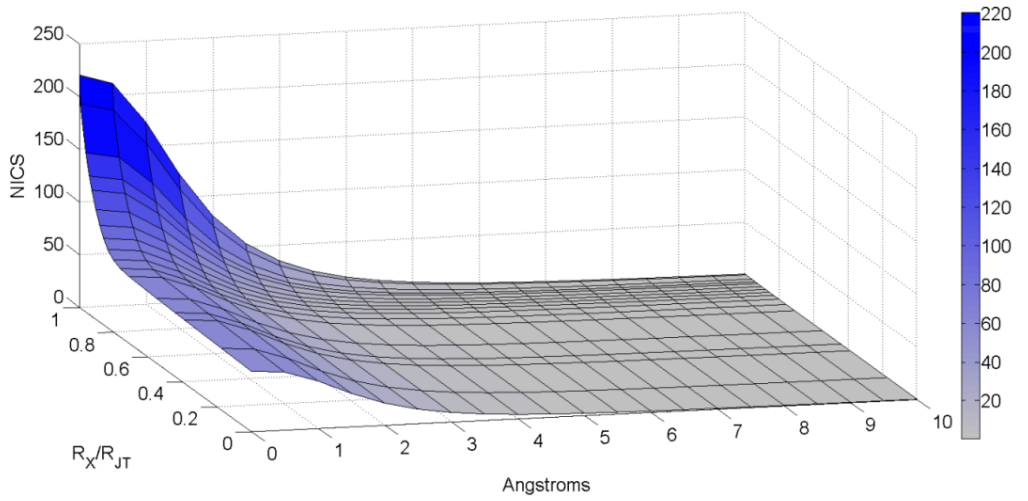

Figure 8.1.2. Schematic plots of the NICS values along the IDP for the benzene anion (D_{6h} to D_{2h}), ^2A_u electronic state.

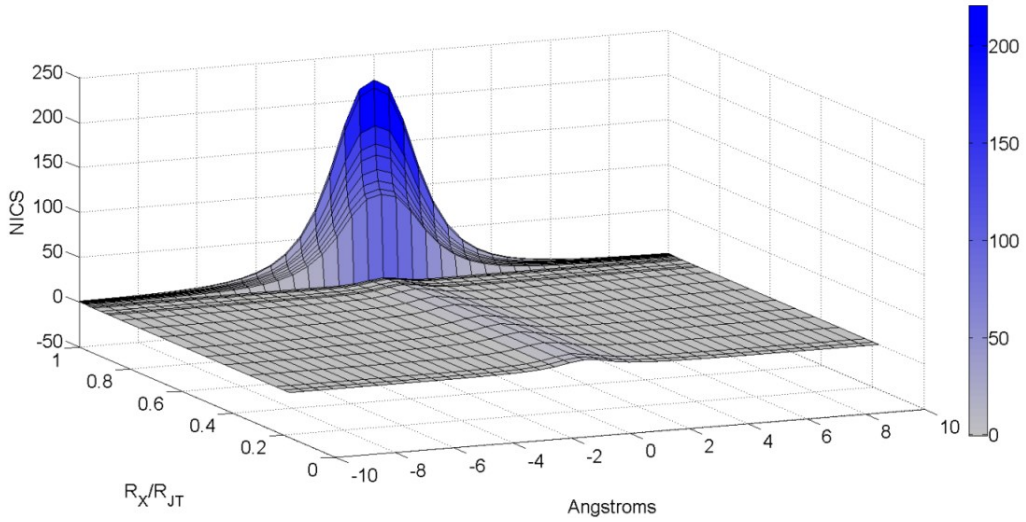

a)

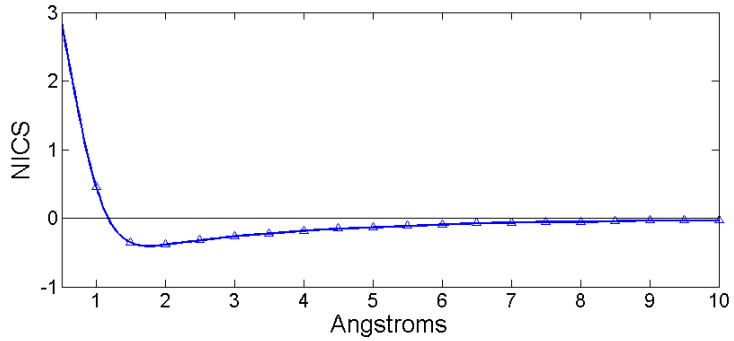

b)

Figure 8.1.3. a) Schematic plots of the NICS values along the IDP for the benzene anion (D_{6h} to C_{2v}), $^2A_1$ electronic state; b) Schematic plot of the NICS values from the ring center up to 10 Å above the ring following an axis perpendicular to the ring plane, at R_X/R_{JT}=0.97.

8.1.1. Conclusion

Monitoring the changes in NICS values for $C_6H_6^+$ and $C_6H_6^-$ along the IDP path indicate that antiaromaticity decreases with increasing deviation from D_{6h} to D_{2h} point group. $C_6H_6^-$ adopts a non-planar conformation in its global minimum as a consequence of the combined JT/PJT effect,[20] thus avoiding antiaromaticity. However, if we compute NICS values only in D_{6h} structure and C_{2v} global minimum conformation, wrong conclusions can be made and antiaromatic character could be determined. The full NICS profile along the IDP shows non-aromatic behavior.

8.1.2. Computational Details

The structures of $C_6H_6^+$ and $C_6H_6^-$ were optimized by DFT calculations using the Amsterdam Density Functional program package, ADF2010.01.[228-230] The LDA characterized by the VWN[61] parameterization have been used for the symmetry constrained geometry optimizations. TZP basis set was used for all atoms. Analytical harmonic frequencies[231, 232] were calculated and in all cases the global minimum was confirmed by the absence of imaginary frequency modes.

Calculations of NICS values and magnetic susceptibility data were performed at the B3LYP/6-311+G* level of theory[64, 325] using the Gaussian 09W program package[326] using LDA optimized geometries. To evaluate magnetic properties, the gauge-including atomic orbitals (GIAO) method was used.[327] NICS parameters were calculated for ghost atoms located at the center of C_6H_6, $C_6H_6^+$ and $C_6H_6^-$. In order to obtain the full profile of aromatic/antiaromatic behavior of the investigated molecules, calculations of NICS parameters were performed from 0 Å to 10 Å, in steps of 0.5 Å, along the IDP.

In addition to the nucleus-independent chemical shifts, mean molar magnetic susceptibility (χ_M) and molar magnetic anisotropy ($\Delta\chi$) became important tools to prove the term of aromaticity. The tensor normal to the aromatic ring (χ_{zz}) is much larger than the average of other tensors, thus the aromatic compounds have large negative magnetic anisotropy (Eqs. 10.2.1. and 10.2.2.).

$$\chi_M = \frac{\chi_{xx} + \chi_{yy} + \chi_{zz}}{3}$$

Eq. 8.2.1.

$$\Delta\chi = \chi_{zz} - \frac{\chi_{yy} + \chi_{xx}}{2}$$

Eq. 8.2.2.

8.2. Nucleus-Independent Chemical Shift Profiles Along the Intrinsic Distortion Path for Jahn-Teller Active Molecules. Study on Cyclopentadienyl Radical and Cobaltocene

In spite of relatively simple composition, aromaticity of the JT active $Cp^{\bullet}$ and $Co(Cp)_2$ have not been fully rationalized so far. The NICS were determined for the reference non JT active species, cyclopentadienyl anion (Cp^-) and bis(η^5-cyclopentadienyl)iron(II) ($Fe(Cp)_2$), and molecules prone to the JT effect, $Cp^{\bullet}$ and $Co(Cp)_2$. In order to preserve chemically important features, the full NICS profile of $Cp^{\bullet}$ and $Co(Cp)_2$ along the IDP was performed.

The planar Cp^-, in its singlet ground state with D_{5h} symmetry was optimized using several different levels of theory. All chosen XC functionals reproduced experimental geometrical parameters[328] with sufficient accuracy, Table 8.2.1. $Fe(Cp)_2$ molecule has two possible conformations, eclipsed D_{5h} and staggered D_{5d}. According to the previous studies, D_{5h} conformation is the global minimum on the potential energy surface, although the energy difference between two conformations is very small.[329-333] Calculated bond lengths, Table 8.2.1., are in excellent agreement with the experimental data.[334]

Since all the functionals reproduced geometrical parameters with good accuracy, the NICS were computed at B3LYP/6-311+G* level, using geometries obtained with the simplest LDA functional. Calculated NICS values for Cp^- and $Fe(Cp)_2$ are given in Table 8.2.2. Previous sophisticated computational studies, provide a rather satisfactory insight into the nature of aromaticity of Cp^- revealing that Cp^- is aromatic, which is in accordance with herein presented results.[115, 324, 335-338] It is important to emphasize that the NICS parameters for Cp^- were computed at the center of pentagon and at various distances form the center of the ring. In the case of $Fe(Cp)_2$, the starting point for NICS calculation was 1 Å above the central metal ion following the z-axis. The NICS value calculated at 1.6 Å represents the NICS in the center of pentagon ring of the cyclopentadienyl ligand. According to the results, both molecules show aromatic character, and the $Fe(Cp)_2$ is more aromatic, Table 8.2.2.[115, 324, 335-341] The isolated Cp^- ring has the NICS value of -12.52 ppm in the center, Table 8.2.2. When two Cp^- rings are placed at the distance which they have in $Fe(Cp)_2$ molecule (3.2 Å) the NICS parameter calculated at the center of one 5-membered ring is -12.13 ppm. Therefore, the difference in the NICS parameters

calculated for ghost atoms in the center of isolated Cp^- and Cp^- in $Fe(Cp)_2$ is rather due to the coordination to the central metal ion, than the presence of other ring.

It is worth noting that $Cp^{\bullet}$ and $Co(Cp)_2$ have a hole and an unpaired electron in a doubly degenerate highest occupied molecular orbital, respectively, referring to the JT problem. Since it has been previously shown that the eclipsed conformation is more stable and the JT effect does not depend on a rotation of the rings,[80] the discussion will be limited only to $Co(Cp)_2$ in eclipsed conformation. Average bond distances for distorted LS structures of $Cp^{\bullet}$, calculated at different levels of theory, are consistent, Table 8.2.1. Calculated bond lengths of $Co(Cp)_2$ are in accordance with average bond distances obtained by X-ray experiment,[342] regardless of the choice of selected XC functional, Table 8.2.1.

Table 8.2.1. Selected bond lengths (Å) for stationary points of investigated molecules calculated with different XC functionals.

Molecule	Bond	LDA	BP86	PW91	OPBE	S12g	B3LYP	S12h	Exp.
Cp^- (D_{5h}, $^1A_1'$)	C-C	1.406	1.420	1.417	1.413	1.414	1.410	1.404	1.413[328]
$Fe(Cp)_2$ (D_{5h}, $^1A_1'$)	Fe-C	2.004	2.055	2.049	2.006	2.033	2.082	2.048	2.03[334]
	C-C	1.422	1.434	1.432	1.429	1.429	1.422	1.417	1.43[334]
$Cp^{\bullet}$ (C_{2v}, $^2B_1$)	C-C	1.364 1.424	1.374 1.439	1.372 1.436	1.370 1.432	1.371 1.432	1.365 1.432	1.360 1.426	---
$Cp^{\bullet}$ (C_{2v}, $^2A_2$)	C-C	1.455 1.390	1.471 1.402	1.468 1.400	1.462 1.397	1.463 1.397	1.465 1.394	1.457 1.389	---
$Co(Cp)_2$ (C_{2v}, $^2B_1$)	Co-C	2.029 2.070 2.098	2.091 2.134 2.155	2.084 2.128 2.149	2.038 2.080 2.108	2.070 2.112 2.135	2.129 2.175 2.185	2.092 2.137 2.151	2.119[342]
	C-C	1.434 1.415 1.402	1.447 1.426 1.412	1.445 1.424 1.410	1.441 1.421 1.408	1.441 1.421 1.408	1.435 1.415 1.400	1.429 1.409 1.396	1.429[342]
$Co(Cp)_2$ (C_{2v}, $^2A_2$)	Co-C	2.090 2.047 2.022	2.150 2.111 2.083	2.143 2.104 2.076	2.101 2.056 2.031	2.129 2.089 2.062	2.184 2.153 2.118	2.149 2.115 2.083	2.119[342]
	C-C	1.406 1.426 1.438	1.416 1.438 1.450	1.414 1.436 1.448	1.412 1.432 1.444	1.412 1.432 1.444	1.404 1.427 1.439	1.400 1.421 1.432	1.429[342]

Although the JT effect in $Cp^{\bullet}$ and $Co(Cp)_2$ has been often studied,[182, 192, 227] the influence of the vibronic coupling on their aromatic character has not been investigated so far. The question is whether or not the distortion has a significant impact on the change of aromaticity. In the $Cp^{\bullet}$ and $Co(Cp)_2$, the degeneracy of the $^2E_1''$ state is broken by the JT distortion which stabilizes the system. Therefore, the NICS parameters were computed at LDA optimized geometries, for both the, HS and LS points on the potential energy surfaces. Observing the NICS values at the HS point of $Cp^{\bullet}$, high antiaromatic character is noticeable, Table 8.2.3. Calculated parameters for the global minimum of $Cp^{\bullet}$ show that it still possesses antiaromatic character,[120] but much weaker than in the HS point, Table 8.2.3. This is very similar to the case of benzene cation (Chapter 8, Section 8.1.). Moving from the center of pentagon ring along the z-axis, NICS indices decrease. In the case of $Co(Cp)_2$ it is evident that molecule at the HS point has high antiaromatic character, Table 8.2.4. In the global minimum structure, $Co(Cp)_2$ shows σ aromaticity and π antiaromaticity according to the NICS and $NICS_{zz}$ values, Tables 8.2.3. and 8.2.4.

Table 8.2.2. Calculated NICS values (ppm) for Cp^- and $Fe(Cp)_2$ using LDA optimized geometries at various distances (Å) from the center of the molecules (for $Fe(Cp)_2$ NICS calculated at 1.6 Å corresponds to the NICS value at the center of Cp^- ligand).

Distance / Å	NICS	$NICS_{zz}$
	Cp^-	
0.0	-12.52	-15.95
1.0	-9.44	-33.70
2.0	-3.97	-17.86
3.0	-1.63	-7.87
4.0	-0.77	-3.87
5.0	-0.40	-2.13
	$Fe(Cp)_2$	
1.0	-103.47	-65.35
1.6	-42.14	-29.40
2.0	-31.15	-29.73
3.0	-9.46	-29.07
4.0	-2.44	-13.37
5.0	-0.95	-6.38

Table 8.2.3. Calculated NICS values* (ppm) for $Cp^{\bullet}$ using LDA optimized geometries at HS and LS geometries at various distances (Å) from the center of the ring.

Electronic state	Distance / Å	NICS	$NICS_{zz}$
$Cp^{\bullet}$ (D_{5h})			
$^2B_1/^2A_2$	0.0	86.88	273.95
	1.0	72.10	217.30
	2.0	21.36	61.38
	3.0	6.65	18.12
	4.0	2.69	7.06
	5.0	1.34	3.40
$Cp^{\bullet}$ (C_{2v})			
$^2B_1/^2A_2$	0.0	20.78	77.09
	1.0	14.79	45.84
	2.0	3.58	8.00
	3.0	0.91	0.87
	4.0	0.31	-0.12
	5.0	0.13	-0.22

* NICS values for both LS structures are the same.

Table 8.2.4. Calculated NICS values* (ppm) for $Co(Cp)_2$ using LDA optimized geometries at HS and LS geometries at various distances (Å) from central metal ion. NICS value calculated at 1.7 Å corresponds to NICS parameter in the center of the pentagon in $Co(Cp)_2$.

Electronic state	Distance / Å	NICS	$NICS_{zz}$
$Co(Cp)_2$ (D_{5h})			
$^2B_1/^2A_2$	1.0	302.49	1135.98
	1.7	67.59	281.61
	2.0	42.20	182.76
	3.0	24.86	73.78
	4.0	9.80	24.48
	5.0	4.04	9.32
$Co(Cp)_2$ (C_{2v})			
$^2B_1/^2A_2$	1.0	-3.91	209.45
	1.7	-10.86	42.41
	2.0	-11.11	21.41
	3.0	-1.64	-5.91
	4.0	-0.10	-5.08
	5.0	-0.04	-2.92

* NICS values for both LS structures are the same.

Since dependence of the *NICS* parameters from the distortion, $\vec{R}_X / \vec{R}_{JT}$, and distances (Å) from the center of the molecules gives a more detailed picture, NICS were

monitored along the IDP for $Cp^{\bullet}$ and $Co(Cp)_2$, Figures 8.2.1. and 8.2.2. NICS were scanned only for $^2B_1$ state, since NICS parameters computed for $^2A_2$ state are almost the same. Due to the non-totally symmetric electron density, both molecules, in D_{5h}, possess strong antiaromatic character. Near the point of electron degeneracy, i.e. near the HS nuclear arrangement, the HOMO-LUMO gap is substantially small, thus the NICS parameters have large positive values in the first region of the IDP (Figures 8.2.1. and 8.2.2.). Going toward the global minimum point on the potential energy surface, the NICS values decrease, hence initially strong antiaromatic character lowers, and finally, in the case of $Co(Cp)_2$ the NICS indices become negative, Figures 8.2.1. and 8.2.2. It is worth noting that the negative NICS values in $Co(Cp)_2$ occur after 40 % of the IDP where the most of the JT stabilization is attained. The driving force responsible for the removal of orbital degeneracy leads to the enlargement of the HOMO-LUMO gap. Considering $Cp^{\bullet}$, for both, the HS and LS nuclear arrangement, calculations revealed that the NICS decrease gradually along the z-axis, Figure 8.2.1. Moving apart along the z-axis in HS configuration of $Co(Cp)_2$, abrupt decrease of NICS parameters is observed until distance of 1.7 Å (center of pentagon ring), Figure 8.2.2. Going even further, NICS show a smooth decreasing trend, as expected.

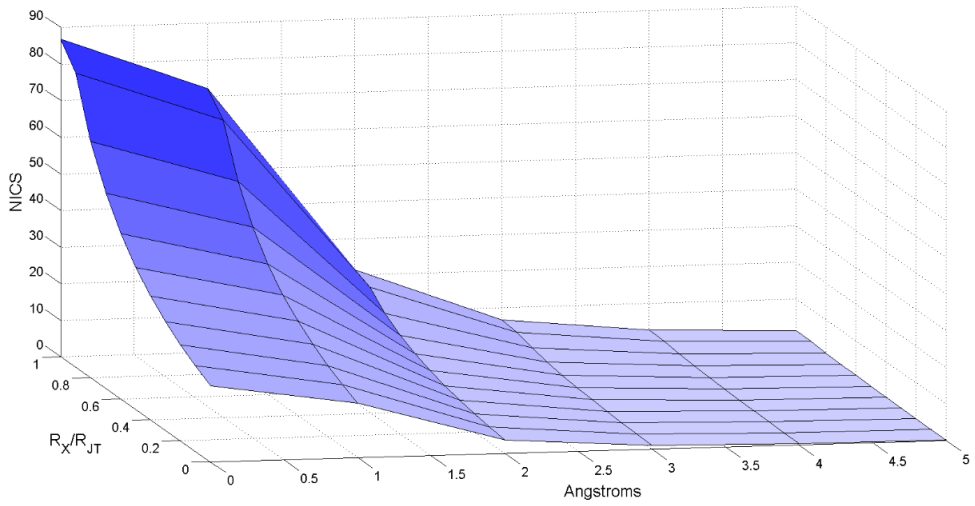

Figure 8.2.1. Schematic plot of the NICS values along the IDP for $Cp^{\bullet}$ (from D_{5h} to C_{2v}), $^2B_1/^2A_2$ electronic states.

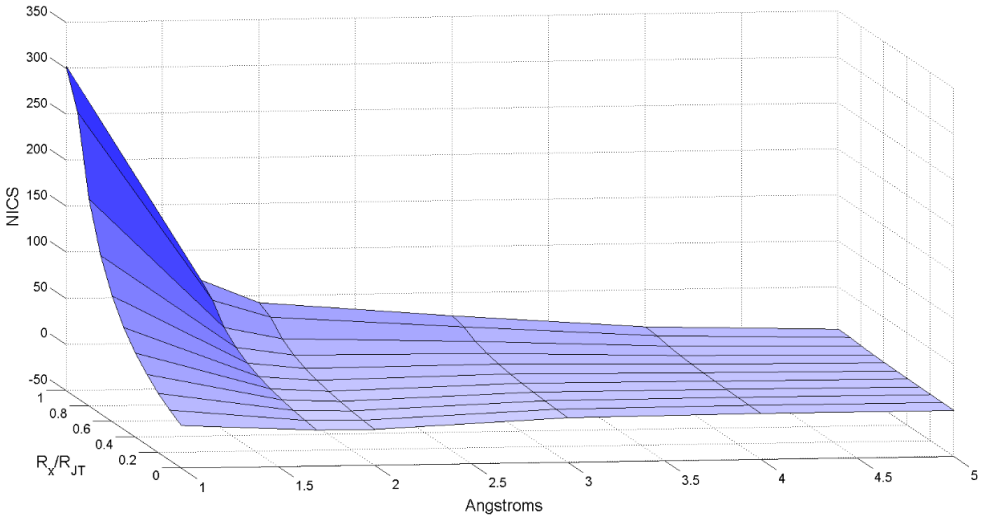

Figure 8.2.2. Schematic plot of the NICS values along the IDP for $Co(Cp)_2$ (from D_{5h} to C_{2v}), $^2B_1/^2A_2$ electronic states.

8.2.1. Conclusion

The detail analysis of the NICS parameters, as one of the most widely used and efficient magnetic criteria, in Cp^-, $Fe(Cp)_2$, $Cp^{\cdot}$ and $Co(Cp)_2$ is presented by the means of DFT. Calculations revealed that Cp^- and $Fe(Cp)_2$ are highly aromatic molecules. According to the NICS, Cp^- ring in $Fe(Cp)_2$ is far more aromatic than isolated Cp^-, showing the impact of the Fe^{2+} ion. In other words, these results would be highly attractive in applied sciences for the design of new advanced materials with desired properties, and the understanding of electronic structure, chemical bonding and properties in a moiety of aromatic species.

In the case of $Cp^{\cdot}$ and $Co(Cp)_2$ the monitoring of the NICS along the IDP has been performed. Similarly to the previous study (Chapter 8, Section 8.1.),[123] antiaromaticity decreases with increasing deviation from the high symmetry D_{5h} structures to the low symmetry C_{2v} global minimum structures, confirming that the JT distortion represents a mechanism for reducing the antiaromatic character. In the LS structure of $Co(Cp)_2$ the NICS become even negative, revealing aromatic character, in contrast to the $Cp^{\cdot}$. This is again due to the coordination to the Co^{2+} ion.

8.2.2. Computational Details

The DFT calculations have been carried out using the Amsterdam Density Functional program package, ADF2013.01.[229, 230, 238] Geometry optimization of all investigated molecules was performed using LDA characterized by the VWN parameterization,[61] as well as GGA such as BP86,[63, 64] PW91,[343] OPBE,[65] and S12g,[344] and hybrids, B3LYP[178, 179] and S12h[344]. TZP basis set has been used for all atoms. All calculations were spin-unrestricted. Analytical harmonic frequencies[231, 232] were calculated in order to ascertain that LS structures correspond to the stationary points on the potential energy surface. Calculations of the NICS values were performed at the B3LYP/6-311+G* level of theory[64, 325] using the Gaussian 09W program package[326] using LDA optimized geometries. To evaluate magnetic properties, the GIAO method was used.[327] NICS parameters were calculated for ghost atoms located at the center of Cp^- and $Cp^\bullet$. In order to obtain the full profile of aromatic/antiaromatic behavior, calculations of the NICS parameters were performed from 0 Å to 5 Å, in steps of 0.5 Å. In order to avoid the influence of the magnetic field of the central metal ion in metallocenes, the first NICS value was calculated 1 Å above the metal ion along the z-axis. For JT active species in the HS nuclear arrangement the NICS values were calculated imposing HS (D_{5h}) nuclear arrangement and LS (C_{2v}) of electron density. The NICS parameters for JT active species, $Cp^\bullet$ and $Co(Cp)_2$, were scanned along the IDP. The details about IDP analysis for $Cp^\bullet$ can be found in Chapter 7, Section 7.2., and for $Co(Cp)_2$ in the literature[22].

8.3. Spherical Aromaticity of the Jahn-Teller Active Fullerene Ions

The well-known concept of aromaticity can be applied not only to the planar molecules, but also onto 3D spherical species, therefore defined as spherical aromaticity.[136, 345-349] According to the Hirsch's rule,[345-347] spherical structures with $2(N+1)^2$ π electrons are aromatic, where N is an arbitrary positive integer, analogously to 4n+2 Hückel rule for cyclic annulenes. π shells in the fullerene molecule (C_{60}) are full-filled with $2(N+1)^2$ electrons, thus implying the aromatic character.[350] Moreover, according to endohedral helium (^{3}He) chemical shifts, charged fullerenes obeying $2(N+1)^2$ rule present even more aromatic species than neutral one.[345, 347] However, the structures with partially filled π orbitals demand more extensive examination of aromaticity, due to the violation of the $2(N+1)^2$ rule. An additional problem arises in species with the degenerate ground state due to the presence of the JT effect. Hence, the examination of the spherical aromaticity in the JT active species is rather interesting and requires detailed analysis. Among many techniques, NICS are certainly the most useful indicator of aromatic character,[131, 351] as well as of the spherical aromaticity. Additionally, ^{3}He NMR chemical shifts have proven to be powerful tools to probe the interior magnetic fields of the cage compounds, and give significant data about aromatic behavior.[352-359]

In order to explain the relationship between the vibronic coupling and spherical aromaticity, the NICS values were calculated for fullerene anion (C_{60}^-) and fullerene cation (C_{60}^+), Figure 12.1., along the IDP. With the aim of getting even deeper insight into the origin of aromatic behavior and to elucidate the influence of the JT distortion on the spherical aromaticity, the NICS parameters were also computed for the JT inactive species, neutral fullerene molecule and charged one, C_{60}^{10+}, examples of the $2(N+1)^2$ rule, Figure 8.3.1., for comparison purposes. NMR chemical shifts of ^{3}He nucleus placed in the cavity of C_{60}, C_{60}^{10+},C_{60}^- and C_{60}^+ species were determined, to complement the NICS analysis.

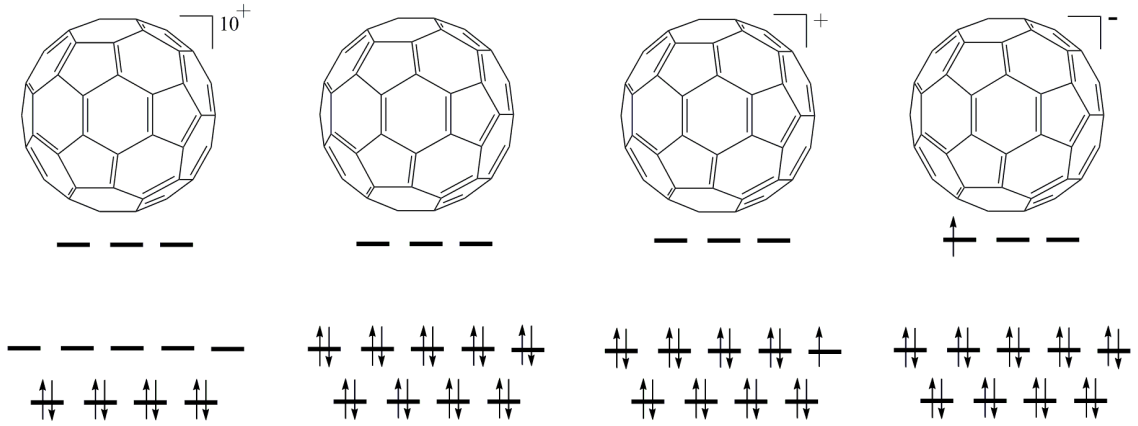

Figure 8.3.1. Structures of C_{60}^{10+},C_{60}, C_{60}^{+} and C_{60}^{-}; simple molecular orbital scheme.

The calculated NICS values for C_{60} (I_h) and C_{60}^{10+} (I_h) structures, along the C_5, C_3 and C_2 symmetry axis from the center of the cages toward centers of pentagon rings, hexagon rings and mutual bond of two hexagons, Figure 8.3.2., are summarized in Table 8.3.1.

Table 8.3.1. NICS parameters (ppm) for C_{60} and C_{60}^{10+} calculated along C_5, C_3 and C_2 symmetry axis at various distances (Å) from the center of the molecules.

	I_h, C_{60}			I_h, C_{60}^{10+}		
Distance/Å	C_5	C_3	C_2	C_5	C_3	C_2
0	-3.11	-3.11	-3.11	-83.20	-83.20	-83.20
1	-3.07	-3.13	-3.17	-83.20	-86.08	-83.23
2	0.21	-4.19	-4.94	-81.93	-79.81	-82.54
3	12.81	-2.86	-35.14	-45.40	-39.84	-68.44
4	9.09	0.68	-24.50	-12.48	-11.23	-33.94
5	3.32	-0.32	-2.83	-1.01	-1.89	-1.19

It is clear from Table 8.3.1. that C_{60} pentagons are antiaromatic while hexagons possess weak aromatic character. Since the mutually opposite effects of five- and six-membered rings are practically canceled near the cage center, the moderate aromaticity is noticed. However, the precise definition of aromatic behavior of C_{60} is still ambiguous in accordance with previous studies.[360, 361] In contrast to the neutral fullerene molecule, the calculations on hypothetical C_{60}^{10+} reveal strong shielding in all possible directions, C_5,

C_3 and C_2 axis, as expected,[125, 348] Table 8.3.1. The five-membered and six-membered rings of the C_{60}^{10+} show a synergistic diatropic (aromatic) effect, so this highly charged fullerene has a large homogeneous magnetic field region.

By adding or removing one electron from neutral C_{60} molecule, the JT active C_{60}^- and C_{60}^+ are obtained, Figure 8.3.1. Fullerene anion has an $^2T_{1u}$ electronic ground state in icosahedral (I_h) point group, and the descent in symmetry goes to the D_{3d} global minimum structure with an $^2A_{2u}$ ground electronic state.[79] The ground electronic state of C_{60}^+, in I_h symmetry is ^2H_u. It has been shown that the distortion leads to structures belonging either to D_{5d} or D_{3d} point groups,[311, 362] where the first one is the global minimum. Descent in symmetry from the HS point to the LS conformation leads to the loss of symmetry elements, i.e. descent in symmetry from I_h point group to D_{3d} leads to the loss of C_5 symmetry axis, while the lowering of symmetry to D_{5d} point group leads to the loss of C_3 axis. For this purpose, the NICS values of the JT active fullerene ions were determined along C_3 and C_2 axis for C_{60}^- and C_5 and C_2 axis for C_{60}^+, Figure 8.3.2.

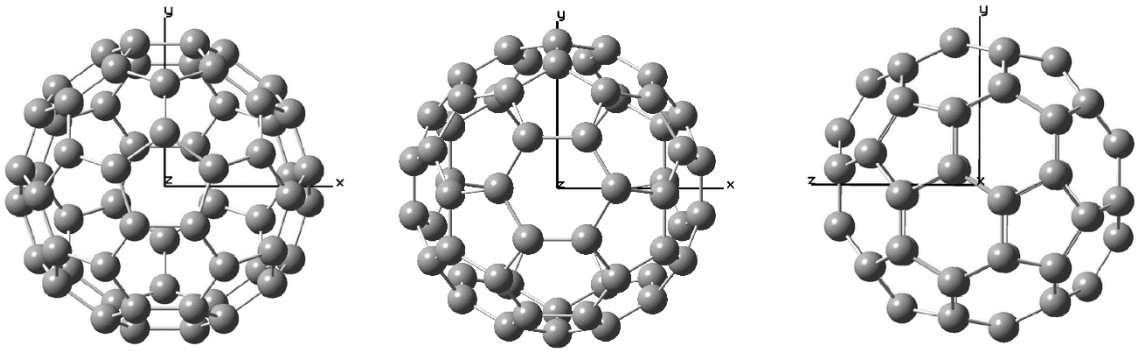

Figure 8.3.2. C_5, C_3 and C_2 rotation axis in fullerene, respectively.

NICS parameters for C_{60}^- and C_{60}^+ were calculated imposing HS (I_h) nuclear arrangement and LS (D_{3d} and D_{5d}, respectively) electron density. NICS values for the C_{60}^- cage in the HS point show strong antiaromatic character in both directions, along C_3 and C_2 axis, Table 8.3.2. In the global minimum structure, D_{3d} symmetry, paratropic (anitaromatic) character is observed. However, in comparison to the HS structure antiaromatic effect is weaker. Moving toward the surface of the C_{60}^- along C_3 and C_2 symmetry axis, the decrease of antiaromaticity is spotted, Table 8.3.2. The analysis of

local effects leads to the conclusion that pentagon rings in D_{3d} structure have aromatic character, while the hexagons are non-aromatic, Table 8.3.3. In order to explain how the JT distortion affects the spherical aromaticity, NICS parameters were scanned along the IDP for JT active C_{60}^- from I_h to the D_{3d} global minimum structure, moving from the center of the cage toward the surface, following C_3 and C_2 symmetry axis, Figures 8.3.3. and 8.3.4., respectively. Due to the non-totally symmetric electron density, C_{60}^-, in I_h, possesses strong antiaromatic character. Near the point of electron degeneracy the HOMO-LUMO gap is significantly small, hence NICS parameters have large values which decrease with increasing distortion, Figure 8.3.3. Near the center of the cage, approximately in the first five percent of the path, NICS values change abruptly, while in the second region the changes become smoother. Since NICS parameters remain roughly constant near the surface of the molecule, JT distortion has insignificant influence on the change of antiaromaticity, Figure 8.3.3. The similar trend was observed moving toward the C-C bond of hexagon rings, Figure 8.3.4.

Evaluated NICS values for the C_{60}^+ in its HS point show antiaromatic character, which is more pronounced along the C_2 axis than in the direction along the C_5 axis, Table 8.3.2. The open-shell icosahedral C_{60}^- is somewhat more antiaromatic than icosahedral C_{60}^+ as indicated by NICS indices, Table 8.3.2. Considering the global minimum structure of C_{60}^+ cage, very weak aromatic character can be observed in its interior, similar to the neutral C_{60}. Moving toward the surface of the molecule along two chosen directions, i.e. C_5 and C_2 symmetry axis, the same trend is noticed as in the case of neutral fullerene. NICS parameters calculated at the centers of pentagon and hexagon for the global minimum structure of C_{60}^+ indicate local antiaromatic characters, Table 8.3.3. NICS values have been scanned along the IDP, following the directions along C_5 and C_2, Figures 8.3.5. and 8.3.6., respectively. As it can be seen from Figure 8.3.5., the NICS indices calculated near the center of the cage, change rapidly versus the JT distortion, R_X/R_{JT}, in the first ten percent of the path. In the second region, the NICS parameters decrease gradually toward the global minimum. Moving towards the surface of the pentagon rings, JT distortion has even less influence on the changes of the NICS indices. Hence, the JT distortion has a significant impact on the aromaticity/antiaromaticity only in the interior of C_{60}^+, along C_5 axis. Following the C_2 symmetry axis, Figure 8.3.6., opposite effect is noticed in contrast to the scanned NICS parameters along C_5, which is

in accordance with results given in Table 8.3.2. The largest decrease in NICS parameters is between 2 and 4 Å, where I_h point, i.e. C_{60}^+ with I_h geometry and D_{5d} electron density, shows great antiaromatic character, while global minimum structure is highly aromatic. Evidently, the JT effect strongly affects not only the aromaticity inside the cage but also near the surface of the six-membered rings in contrast to the effect toward the five-membered rings.

Table 8.3.2. NICS parameters (ppm) of the cage compounds: C_{60}^- and C_{60}^+ at HS and LS geometries calculated along C_3 and C_2 symmetry axis for C_{60}^- and C_5 and C_2 axis for C_{60}^+ at various distances (Å) from the center of the molecules

	I_h, C_{60}^-		D_{3d}, C_{60}^-		I_h, C_{60}^+		D_{5d}, C_{60}^+	
Distance/Å	C_3	C_2	C_3	C_2	C_5	C_2	C_5	C_2
0	254.84	254.84	22.30	22.30	92.62	92.62	-1.82	-1.82
1	251.93	251.70	21.93	21.08	75.28	102.82	-2.72	-1.28
2	217.78	251.00	17.02	21.30	42.81	140.06	-1.37	-0.55
3	87.51	316.58	4.19	9.46	25.88	107.17	9.88	-24.88
4	11.39	85.42	-0.09	-9.82	10.28	46.06	7.21	-16.13
5	-20.75	57.17	-3.98	5.02	0.46	16.75	1.76	0.58

Table 8.3.3. NICS parameters (ppm) for global minimum structures of C_{60}^- and C_{60}^+ calculated at the center of pentagon and hexagon rings (NICS (0)) and one angstrom above the ring center (NICS (1))

	D_{3d}, C_{60}^-			D_{5d}, C_{60}^+		
	NICS (0)	NICS (1)	NICS $(1)_{zz}$	NICS (0)	NICS (1)	NICS $(1)_{zz}$
Pentagon	-18.54	-6.38	-17.55	9.89	5.28	16.39
Hexagon	2.43	-1.46	-3.85	12.60	7.86	24.88

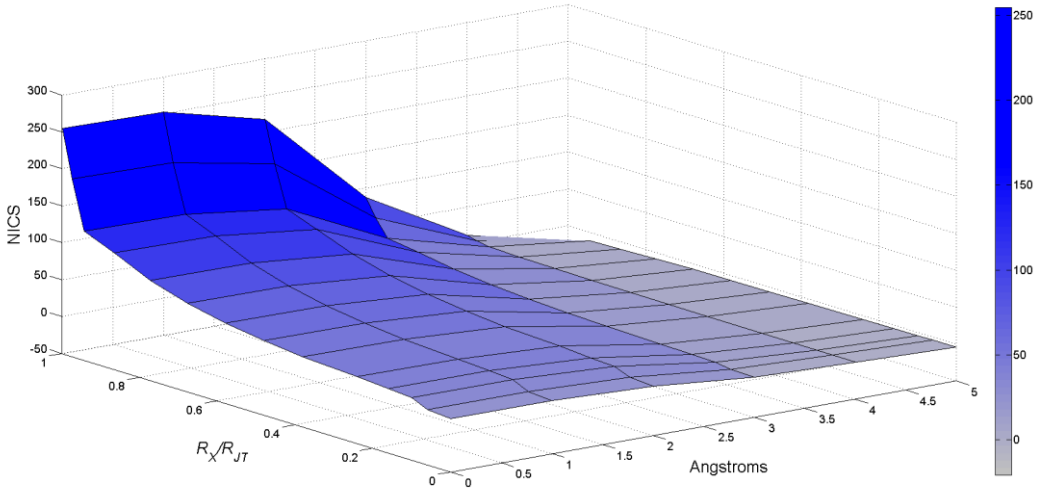

Figure 8.3.3. Schematic plot of the NICS values along the IDP for the fullerene anion along C_3 axis.

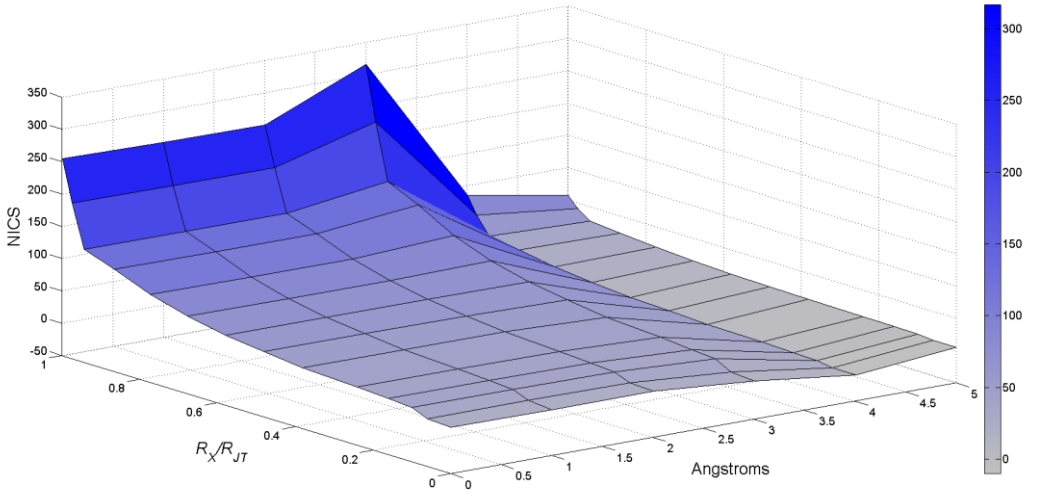

Figure 8.3.4. Schematic plot of the NICS values along the IDP for the fullerene anion along C_2 axis.

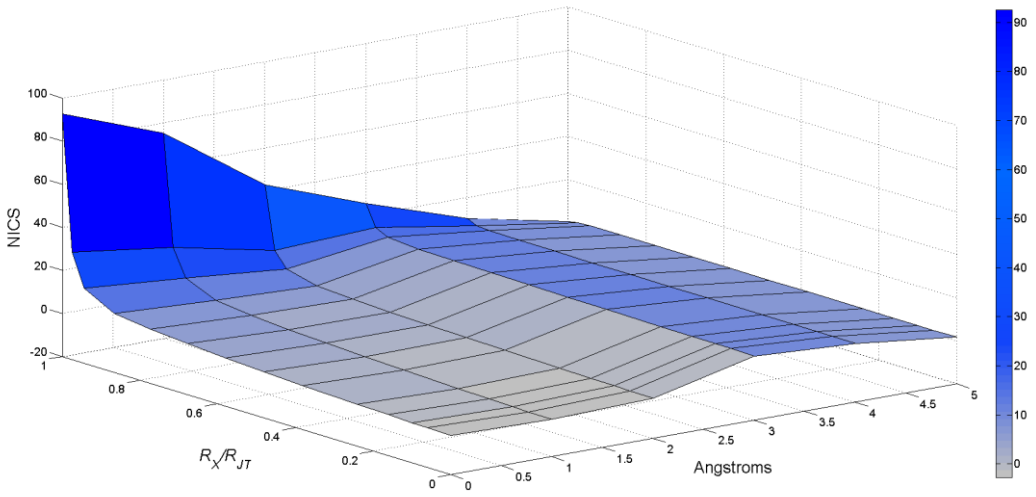

Figure 8.3.5. Schematic plot of the NICS values along the IDP for the fullerene cation along C_5 axis.

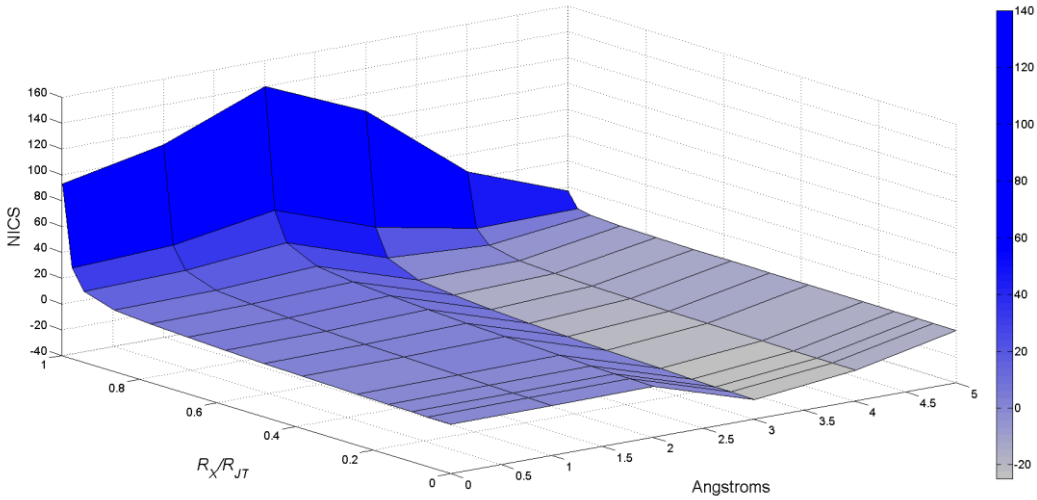

Figure 8.3.6. Schematic plot of the NICS values along the IDP for the fullerene cation along C_2 axis.

The analysis of ^{3}He NMR isotropic chemical shielding tensors data, Table 8.3.4., are in agreement with results obtained by NICS methodology. The isotropic chemical shielding tensors of C_{60} and C_{60}^{10+} minima conformations are positive, indicating aromatic character of the species. High positive value of the ^{3}He shielding tensors of C_{60}^{10+} is a consequence of the strong aromaticity, as expected.[360] The high negative value of ^{3}He NMR chemical shielding tensor for C_{60}^- in its I_h symmetry confirms strong antiaromatic character, which is decreasing by reducing the symmetry to D_{3d}. Observing and comparing ^{3}He shielding tensors of C_{60} and C_{60}^+ in I_h geometries, the great change in the aromaticity appears. However, the global minimum conformation of C_{60}^+ possesses similar weak aromatic character as neutral fullerene.

Table 8.3.4. ^{3}He NMR chemical shielding tensors (ppm) of the cage compounds: C_{60}, C_{60}^{10+}, C_{60}^- and C_{60}^+ at HS and LS geometries calculated at the center of the molecules.

	^{3}He NMR chemical shielding tensor
I_h, C_{60}	62.50
I_h, C_{60}^{10+}	143.00
I_h, C_{60}^-	-194.21
D_{3d}, C_{60}^-	37.50
I_h, C_{60}^+	-33.88
D_{5d}, C_{60}^+	61.17

8.3.1. Conclusion

Derived NICS indices revealed that the magnetic field inside C_{60} and C_{60}^{10+} is practically uniform throughout the interior cavity until reaching the walls, where the local effects are decisive. Addition of the one electron to the LUMO of C_{60} while retaining the I_h geometry leads to the appearance of the intense antiaromaticity, while the removal of one electron from HOMO orbital causes the less pronounced paratropic character. Monitoring the changes of the NICS values for C_{60}^- and C_{60}^+ along IDP, indicate that the antiaromaticity decreases with increasing deviation from the HS to the LS point group. C_{60}^- remains antiaromatic in the global minimum structure. In the global minimum conformation C_{60}^+ has a quite similar aromatic character as neutral, non-JT active C_{60}. In

the analogy to the benzene cation and anion (Chapter 8, Section 8.1.)[123] and cyclopentadienyl radical (Chapter 8, Section 8.2.), the JT effect acts to reduce the antiaromaticity, representing a mechanism of lowering it.

8.3.2. Computational Details

The structures of C_{60}, C_{60}^{10+}, C_{60}^{-} and C_{60}^{+} were optimized by DFT calculations using the Amsterdam Density Functional program package, ADF2010.01.[228-230] The LDA characterized by the VWN parameterization[61] was used for the symmetry-constrained geometry optimizations. TZP basis set was used for all atoms. In all cases, the global minimum was confirmed by the absence of the imaginary frequency modes.

NICS values and ^{3}He NMR chemical shifts were calculated at the B3LYP/6-311+G* level of theory[64, 325] using the Gaussian 09W program package[326]. To evaluate magnetic properties, the GIAO method was used.[327] NICS parameters were calculated for ghost atoms located at the center of investigated molecules, as well as in the center and 1 Å above the pentagon and hexagon rings. In order to obtain the full profile of spherical aromatic behavior, calculations of NICS parameters were performed from 0 Å to 5 Å, in steps of 1 Å, following C_5, C_3 and C_2 symmetry axis of C_{60} and C_{60}^{10+}. NICS parameters for JT active fullerenes were scanned along the IDP, following C_3 and C_2 symmetry axis for C_{60}^{-} and C_5 and C_2 axis for C_{60}^{+}. Calculations of ^{3}He NMR chemical shifts were done at the center of C_{60}, C_{60}^{10+}, C_{60}^{-} and C_{60}^{+} molecules.

8.4. DFT Investigation of the Influence of Jahn-Teller Distortion on the Aromaticity in Square-Planar Arsenic and Antimony Clusters

Aromaticity in metal and metalloid clusters is subject of intensive research[139, 363-367] since the discovery of Al_4^{2-}, using photoelectron spectroscopy and *ab initio* calculations.[368, 369] The aromaticity in these species is unusual and its analysis is challenging task due to the so-called multifold aromaticity and conflicting aromaticity,[363, 364, 367, 370] necessitating careful inspection of typical counting rules [371] and application of different aromaticity criteria.[117, 124, 125, 366, 372]

The investigation of aromaticity in four-atomic metalloid clusters based on arsenic and antimony is presented. More specifically, DFT analysis of the JT active 4n+1 π $As_4^-$and Sb_4^- and their parent, square-planar, 4n+2 π As_4^{2-} and Sb_4^{2-}species has been performed. The full NICS profile along the IDP has been scanned in order to understand the aromatic behavior of the species prone to the JT distortion.

Square-planar, As_4^{2-} and $Sb_4^{2-}$are well-known building blocks of solid materials, for example in (2,2,2-crypt-K^+)$_2$$Sb_4$ crystal,[373] (K@18-crown-6)$_2$$As_4$,[374] [$Na(NH_3)_5$]$_2$$As_4$·$2NH_3$,[375] [Nb(η^5-Cp*)(CO)$_2$(η^4-$As_4$)][376]. These clusters are valent isoelectronic to the classical aromatic $C_4H_4^{2-}$ di-anion, and often considered to be examples of inorganic aromatic compounds. Aromatic character of $2Na^+As_4^{2-}$and $2Na^+Sb_4^{2-}$, and antiaromatic character of $Na^+As_4^-$ and $Na^+Sb_4^-$, was confirmed from MO analyses and verified by experimental photodetachment spectra[122]. Contrary to this findings, NICS profile of As_4^{2-} and Sb_4^{2-}show anti-aromoaticity,[324] or non-aromaticity[377] and electron localization function for As_4^{2-} exhibit delocalization through the lone pairs.[374] It seems that, in spite of relatively simple composition, the structure and aromatic properties of four-member metalloid rings, though studied experimentally[122, 374, 378, 379] and computationally[122, 374, 377, 380-383] have not been fully rationalized so far. Thus, in addition to answering the important issue of the JT influence on the aromatic behavior of As_4^- and Sb_4^-, the above mentioned discrepancies in determination of aromaticity in As_4^{2-} and Sb_4^{2-} have potentially been rationalized. The standard NICS analysis is supplemented by determination of the most significant $T_{x,y}$ (translationally)- and R_z (rotationally)-allowed occupied→unoccupied MO transitions[129] and with adaptive natural density partitioning (AdNDP) analysis[130] and compared to the well-known aromatic Al_4^{2-}.

Square-planar, D_{4h}, arsenic and antimony di-anionic four-atoms clusters ($As_4^{2-}$and Sb_4^{2-}), have $^1A_{1g}$ electronic ground state. Considering their electronic structure and planar geometry, one could expect appearance of aromatic character according to the Hückel 4n+2 π electrons rule. Contrary to these expectations calculated NICS values for $As_4^{2-}$and Sb_4^{2-} at the various distances from the centers of the molecules planes, Table 8.4.1., revealed antiaromatic character. The obtained data are in accordance with previous study of J. Oscar et al.[324] For comparison purposes, NICS values were calculated for di-anionic 4-atoms aluminum cluster, Al_4^{2-}, Table 8.4.1., which are also in full accordance with previous studies and its aromatic properties.[363] Investigation of aromaticity in metalloid clusters demands deeper insight, and observation of isotropic NICS parameter only, is not satisfactory because isotropic NICS values of two-dimensional rings do not reflect the ring current exclusively, owing to the contamination by local σ currents. The out-of-plane component of the NICS tensor ($NICS_{zz}$) has been recommended as an alternative aromaticity criterion for planar systems.[129, 384] Closer analysis of calculated $NICS_{zz}$ values, Table 8.4.1., indicates that investigated metalloid species exhibit conflicting aromatic/antiaromatic behavior. Namely, with increasing the distance from the ring centers $NICS_{zz}$ indices adopt slightly negative values, Table 8.4.1.

Table 8.4.1. Calculated NICS values (ppm) for Al_4^{2-}, As_4^{2-} and Sb_4^{2-} at various distances (Å) from the center of the molecules.

Distance / Å	NICS	$NICS_{zz}$
	Al_4^{2-}	
0	-34.45	-66.15
1	-27.39	-54.86
2	-15.03	-33.73
3	-7.34	-18.91
4	-3.67	-10.80
5	-2.00	-6.47
	As_4^{2-}	
0	9.10	76.67
1	4.39	22.18
2	0.90	-2.92
3	0.22	-3.35
4	0.05	-2.03
5	0.02	-1.20
	Sb_4^{2-}	
0	9.30	66.11
1	4.13	30.53
2	0.78	3.17
3	0.51	-1.32
4	0.41	-1.22
5	0.29	-0.81

Rationalization of which effect, aromatic or antiaromatic, dominates is given by the group theory. The contribution to the induced ring current can be estimated through the analysis of σ and π type diatropic (aromatic) translationally allowed, $T_{x,y}$, and paratropic (antiaromatic), rotationally allowed – R_z, transitions.[129] Diatropic and paratropic contributions to the induced ring current are described with following equation:

$$\sigma = \frac{1}{2c^2}\sum_{i}^{occ}\langle\Psi_i\left|\frac{rr_N I - r_N \otimes \mathrm{r}}{|r-R_N|^3}\right|\Psi_i\rangle - \frac{2}{c}\sum_{i}^{occ}\sum_{a}^{unocc}\frac{1}{\varepsilon_i-\varepsilon_a}\langle\Psi_i\left|\frac{L_N}{|r-R_N|^3}\right|\Psi_a\rangle \otimes \langle\Psi_a|L_N|\Psi_i\rangle$$

Eq. 8.4.1.

The symbol r refers to the electronic position and R_N to the vector position where the shielding is calculated. L_N is the angular momentum operator, ε_i and ε_a are the eigenvalues of the occupied and unoccupied molecular orbital, respectively. In D_{4h} point group, $T_{x,y}$ and R_z transform as E_u and A_{2g} irreps, respectively. This implies that only ${}^1A_{1g}\otimes E_u \otimes {}^1E_u$,

and ${}^1A_{1g}\otimes A_{2g}\otimes {}^1A_{2g}$ transitions are allowed according to the mentioned criteria. The most important magnetically active MOs of Al_4^{2-}, As_4^{2-} and Sb_4^{2-}, participating in the $T_{x,y}$ and R_z allowed transitions, are presented in the Figures 8.4.1., 8.4.2. and 8.4.3., respectively. Considering highly aromatic Al_4^{2-} molecule, transitions $5a_{1g}\rightarrow 6e_u$, $2b_{2g}\rightarrow 6e_u$ and $2a_{2u}\rightarrow 2e_g$ are $T_{x,y}$ allowed, Figure 8.4.1. The rotational transitions between relevant orbitals are forbidden, leading to the high diatropic character. Differently to the observations for Al_4^{2-}, metalloid clusters As_4^{2-} and Sb_4^{2-} exhibit rotationally allowed R_z transitions, that induce strong antiaromatic behavior, Figures 8.4.2. and 8.4.3., respectively. Namely, $12e_u \rightarrow 13e_u$ and $18e_u \rightarrow 19e_u$ are R_z allowed, for arsenic and antimony cluster, respectively. The lowest $T_{x,y}$ transitions are $4a_{2u}\rightarrow 6e_g$ for As_4^{2-}, and $6a_{2u}\rightarrow 9e_g$ for Sb_4^{2-}. Hence, opposed to the strong double (σ+π) aromatic character of Al_4^{2-}, metalloid clusters As_4^{2-} and Sb_4^{2-} posses conflicting, weak π aromaticity and strong σ antiaromaticity.

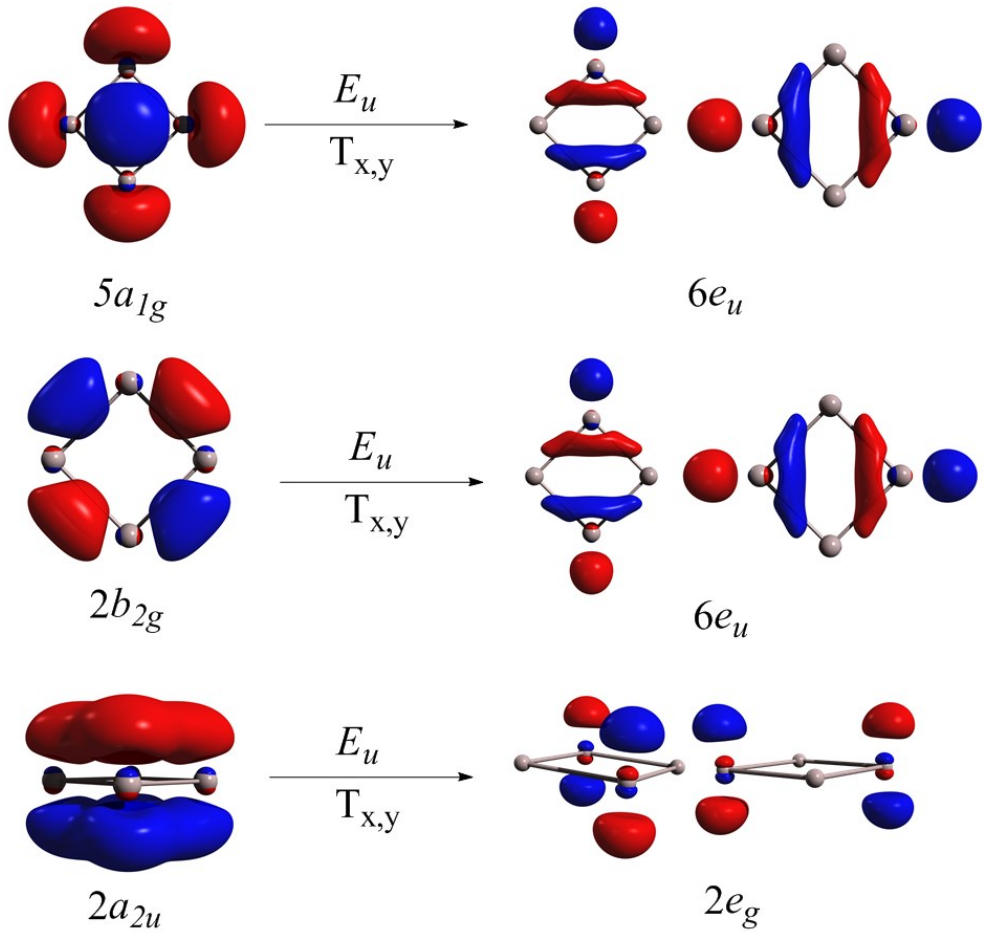

Figure 8.4.1. The molecular orbital diagram of Al_4^{2-}, showing symmetries, 3D molecular orbital pictures, and the $T_{x,y}$-allowed transitions leading to the diamagnetic ring currents.

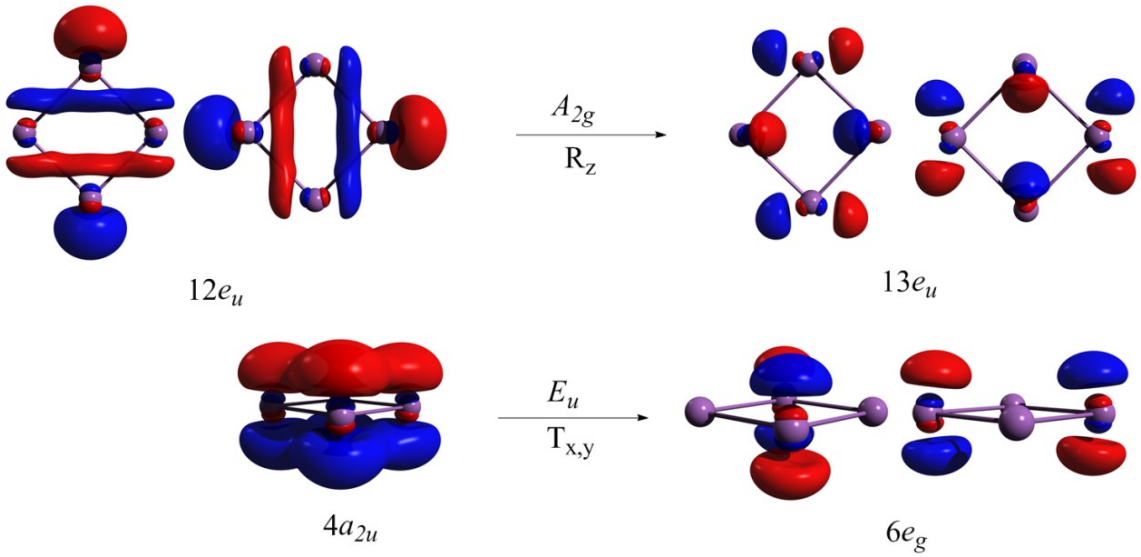

Figure 8.4.2. The molecular orbital diagram of As_4^{2-}, showing symmetries, 3D molecular orbital pictures, and the $T_{x,y}$- and R_z-allowed transitions leading to the diamagnetic and paramagnetic ring currents, respectively.

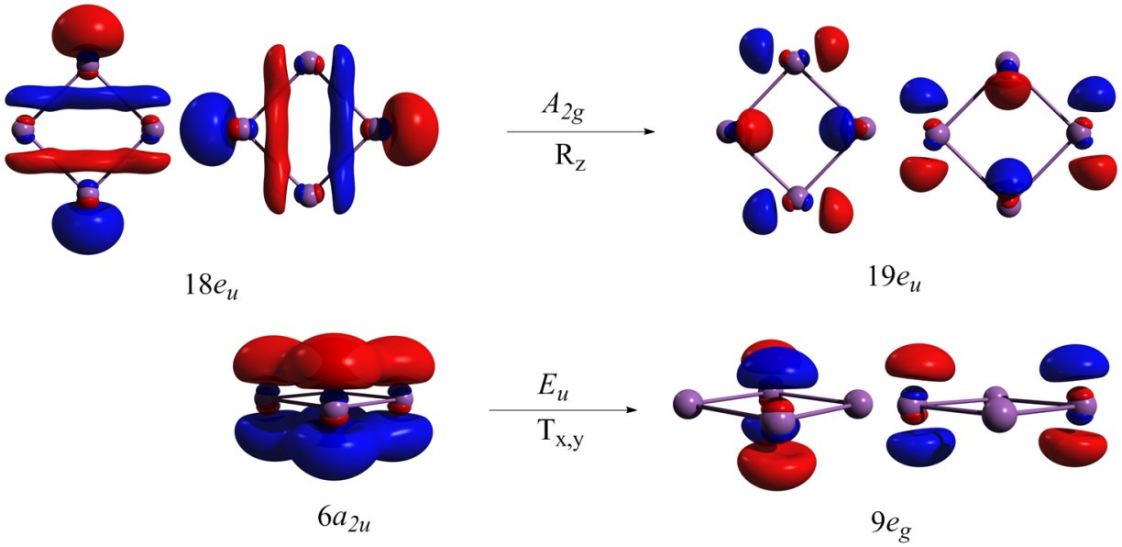

Figure 8.4.3. The molecular orbital diagram of Sb_4^{2-}, showing symmetries, 3D molecular orbital pictures, and the $T_{x,y}$- and R_z-allowed transitions leading to the diamagnetic and paramagnetic ring currents, respectively.

The detail AdNDP analysis for Al_4^{2-} confirms double σ aromaticity in addition to π aromaticity derived from 4c-2e π bond, (Figure 8.4.4.). This findings are in accordance with previous studies of Boldyrev et al.[385] In the case of As_4^{2-} and Sb_4^{2-}, the part of the electron density due to the valence electrons is partitioned into four lone pairs, four 2c-2e σ bonds, two 2c-2e π bonds, and one aromatic 4c-2e π bond (Figure 8.4.5.). This is consistent to the observations derived through the analysis of NICS values.

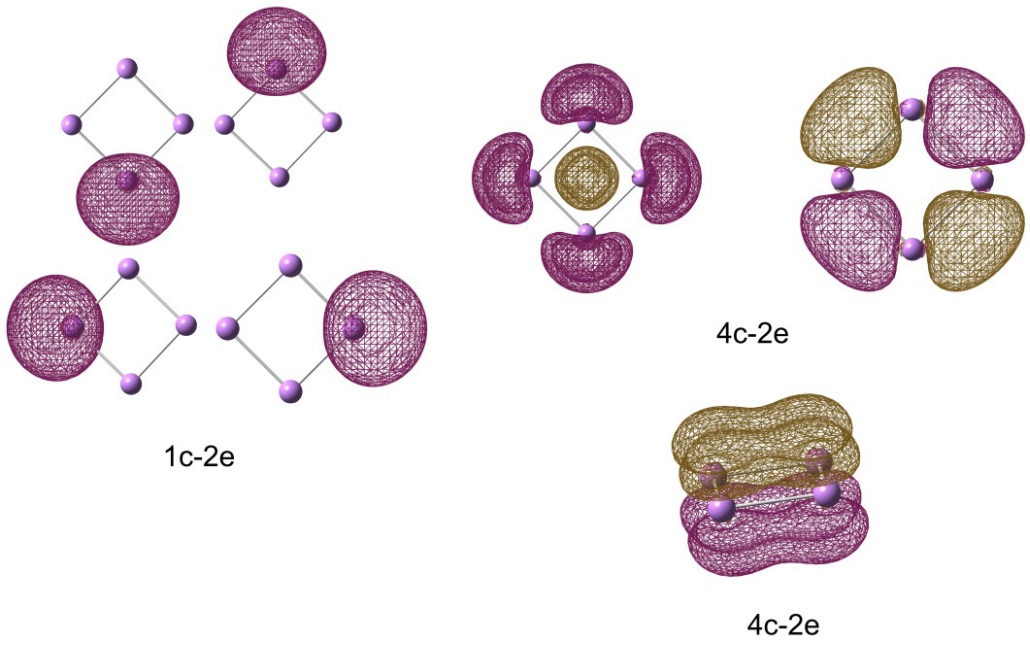

Figure 8.4.4. Results of the AdNDP localization for Al_4^{2-}.

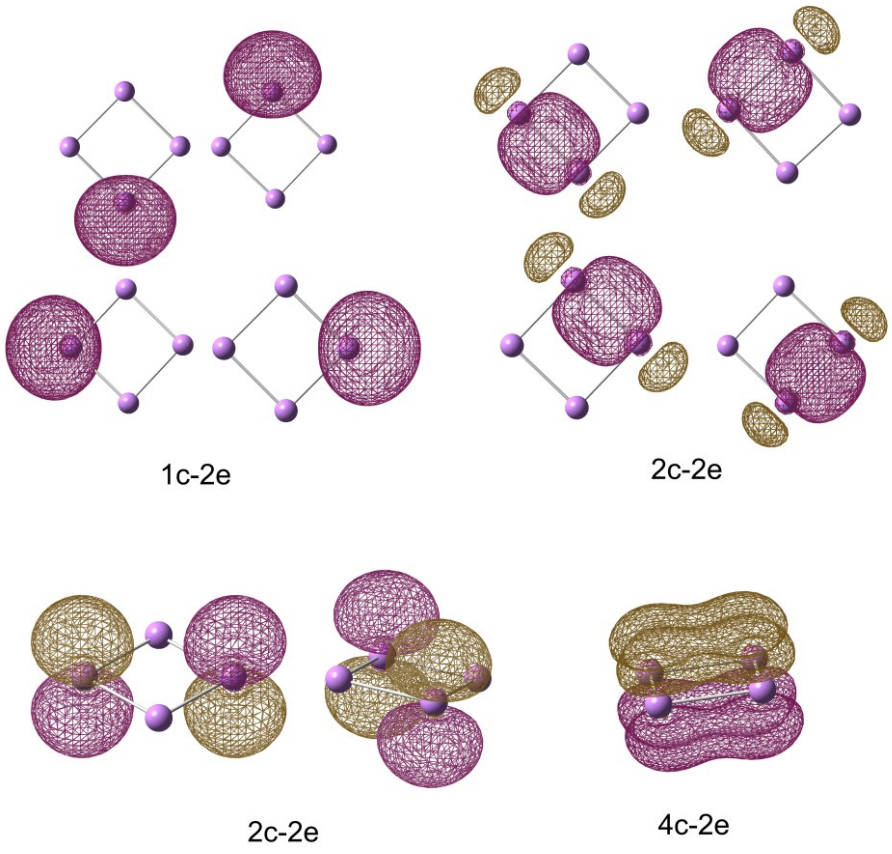

Figure 8.4.5. Results of the AdNDP localization for As_4^{2-} and Sb_4^{2-}.

NICS values were evaluated at the ring center and above the ring plane (0 Å - 5 Å) along the IDP from D_{4h} to D_{2h} structures in the JT active As_4^- and Sb_4^-. The values for the HS and LS points are reported in Table 8.4.2. Since the calculation of magnetic properties of open-shell species with a degenerate ground state may lead to incorrect results, NICS were calculated and monitored imposing HS (D_{4h}) nuclear arrangement and LS (D_{2h}) symmetry of electron density (See Chapter 8, Section 8.1.). According to the obtained NICS indices, $As_4^{2-}$and Sb_4^{2-} have antiaromatic character, Table 8.4.2. Obviously, the removal of one electron from HOMO orbitals destroys originally present weak π aromaticity, as confirmed by highly positive $NICS_{zz}(1)$ values in both D_{4h} and D_{2h} structures. This findings were complemented with detail AdNDP analysis (Figure 8.4.6.). The total density is partitioned into four lone pairs, four 2c-2e σ bonds and two 2c-2e π bonds. In contrast to As_4^{2-} and Sb_4^{2-} fully delocalized aromatic 4c-2e π bond is not present.

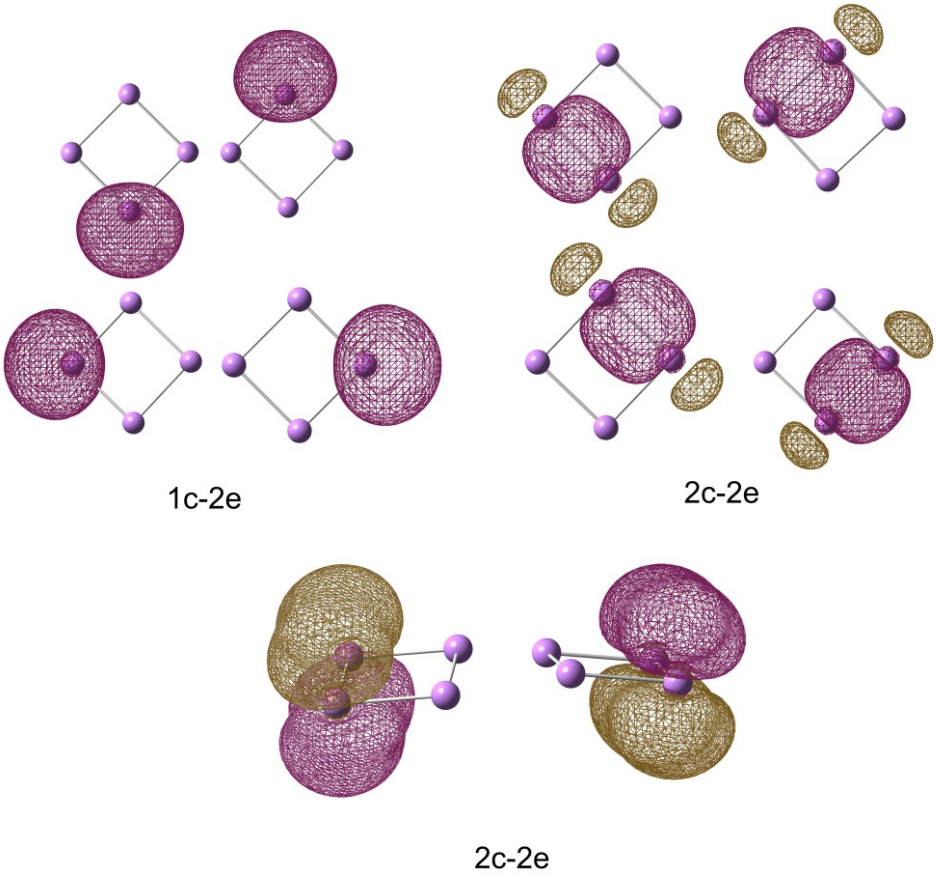

Figure 8.4.6. Results of the AdNDP localization for As_4^- and Sb_4^-.

The full NICS profile along the distortion path, i.e. NICS values versus the JT distortion, $\vec{R}_X/\vec{R}_{JT}$, and the distance from the ring center, Figures 8.4.7. and 8.4.8. (down), give a more detailed interpretation of antiaromatic behavior. Moving from the center of the ring, sudden increase of NICS parameters is observed until distance of 1 Å. Going even further from the center of the ring, NICS show a decreasing trend, as expected. $E\otimes(b_1+b_2)$ JT effect is the main mechanism of distortion, triggering the abrupt change in NICS values, in the first 20 % of the IDP path. After the first 20 % NICS continue to decrease gradually toward the global minimum structure, due to the changes in electronic wave function, or in other words by PJT effect.

Above presented analysis shows that high antiaromaticity of D_{4h} structures indicates JT instability of square-planar configuration. AdNDP orbitals, Figure 8.4.6., correctly reflect changes in electron density upon removal of one electron from parent π aromatic $As_4^{2-}$and Sb_4^{2-}that result in non-zero forces leading to the rectangular minima

with two isolated double bonds. It should be mentioned that rectangular forms of As_4^- and Sb_4^- are still relatively highly antiaromatic, Table 8.4.2., and are in fact only local minima. Global minima of As_4^- and Sb_4^- are C_{2v} "roof" structures with $^2B_2$ electronic state,[122, 382] as confirmed by our calculations, Chapter 7, Section 7.1., Tables 7.1.1. and 7.1.2. This is a consequence of the JT distortion of ^2T state in tetrahedral isomers created by addition of an electron to the neutral tetrahedral clusters.

Table 8.4.2. Calculated NICS values (ppm) for As_4^- and Sb_4^- at HS and LS minimum geometries.

	Geometry	Electronic state	NICS(0)	NICS(1)	$NICS_{zz}(1)$
As_4^-	D_{4h}	$^2B_{3g}$	268.32	285.74	867.53
	D_{2h}	$^2B_{3g}$	35.97	28.24	95.22
Sb_4^-	D_{4h}	$^2B_{3g}$	527.47	618.94	1867.73
	D_{2h}	$^2B_{3g}$	34.44	29.12	98.24

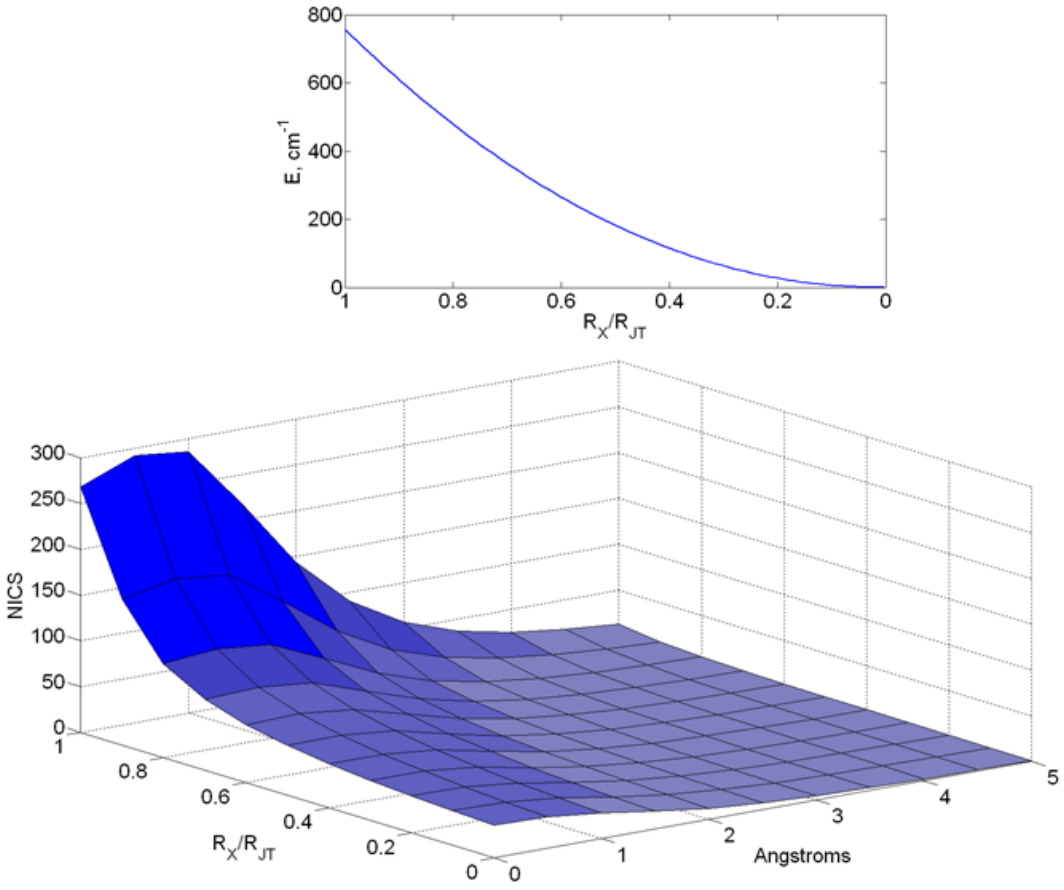

Figure 8.4.7. Changes in energy, IDP model (up); Schematic plots of the NICS values along the IDP for the As_4^- (D_{4h} to D_{2h}), $^2B_{3g}$ electronic state (down).

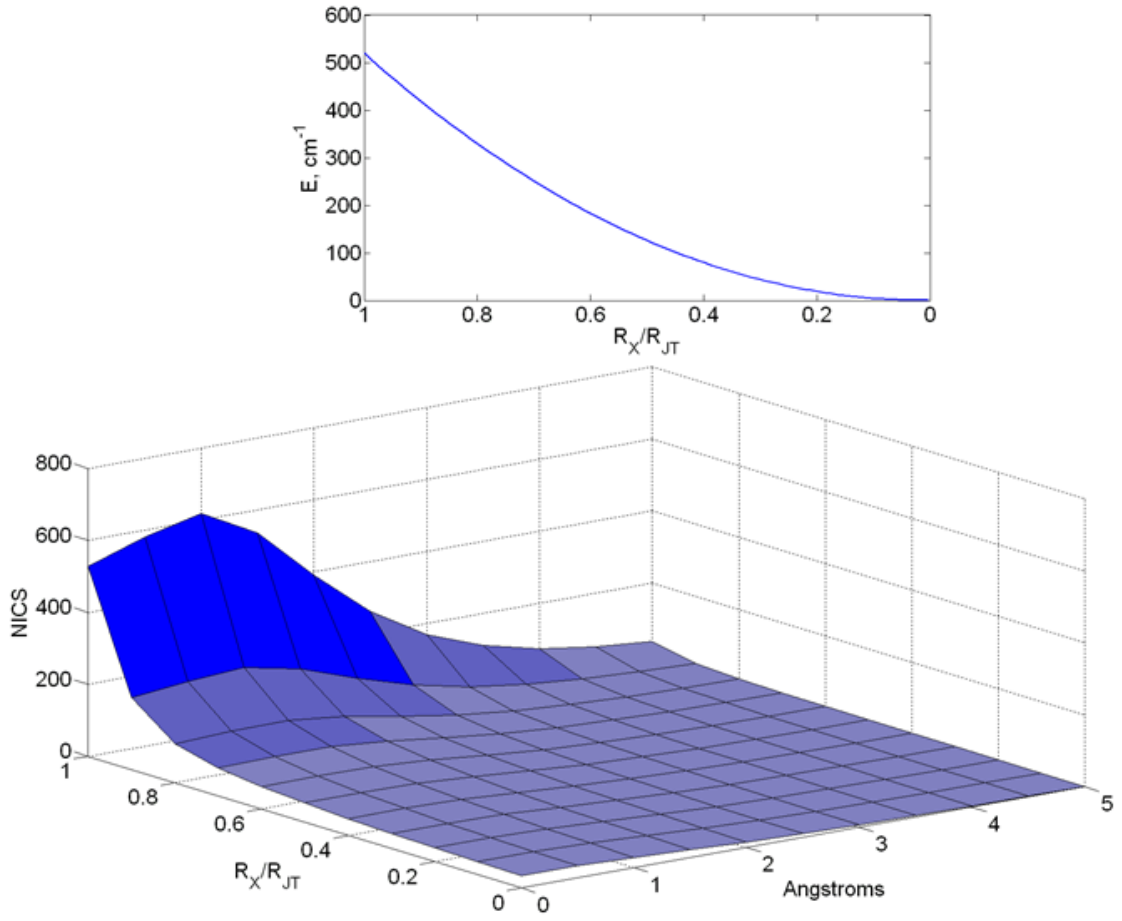

Figure 8.4.8. Changes in energy, IDP model (up); Schematic plots of the NICS values along the IDP for the Sb_4^- (D_{4h} to D_{2h}), $^2B_{3g}$ electronic state (down).

8.4.1. Conclusion

The four-atomic anionic planar forms of arsenic and antimony clusters were studied. Aromatic properties of these systems was rationalized by the means of detailed analysis of NICS values, analysis of occupied→unoccupied MO transitions that contribute to the calculated NICS values and by the means of AdNDP analysis. As_4^{2-} and Sb_4^{2-} are found to possess conflicting, weak π aromaticity and strong σ antiaromaticity. π aromaticity of As_4^{2-} and Sb_4^{2-} is completely lost after detachment of one electron from HOMO orbitals, resulting in antiaromatic, JT active As_4^- and Sb_4^- species. It was shown that high antiaromaticity of square-planar As_4^- and Sb_4^- is a signature of JT effect that was examined in detail by MD-DFT and IDP model (Chapter 6, Chapter 7, Section 7.1.). In both examined clusters, antiaromaticity decreases with increasing deviation from high symmetry D_{4h} structures to low symmetry rectangular minima.

8.4.2. Computational Details

All investigated molecules were optimized by DFT calculations using the Amsterdam Density Functional program package, ADF2013.01.[229, 230, 238] The LDA characterized by the VWN parameterization[61] was used for the symmetry-constrained geometry optimizations. In addition BP86[63, 64] and B3LYP[178, 179] XC functionals were employed. TZP basis set was used for all atoms. Separation of the orbital and the geometrical symmetry, as used in the calculation of the energies of the HS nuclear configurations, is done using SYMROT subblock in the QUILD program, version 2013.01,[239] provided in the ADF2013.01 program package. In all cases, the global minimum was confirmed by the absence of the imaginary frequency modes.

NICS values were calculated at the B3LYP/6-311+G* level of theory[64, 325] using the Gaussian 09W program package[326] using LDA optimized geometries. To evaluate magnetic properties, the GIAO method was used.[327] NICS indices were calculated with 6-311+G* basis set for Al_4^{2-}, As_4^{2-} and As_4^-, while LANL2DZ was used for antimony clusters, since the 6-311+G* basis set is not available for Sb. NICS parameters were calculated for ghost atoms located at the center of Al_4^{2-}, As_4^{2-}, Sb_4^{2-}, As_4^- and Sb_4^-. In order to obtain the full profile of aromatic behavior, calculations of NICS parameters were performed from 0 Å to 5 Å from the center of the rings, in steps of 0.5 Å. Moreover,

NICS parameters for JT active molecules were scanned along the IDP. The AdNDP analysis was performed with Multiwfn3.2 program package.[386]

8.5. Final Remarks on the Influence of the Jahn-Teller Distortion on the Aromaticity

The connection of aromaticity and the JT effect is of utmost importance, since both effects have been very useful in the characterization and interpretation of the structure, stability and reactivity of many molecules. The IDP model gives direct insight on microscopic origin, mechanism and consequences of distortion. The deeper inspection of the magnetic criteria along the IDP indicate that antiaromaticity decreases with increasing deviation from the HS to LS point on the potential energy surface. Thus, the JT effect is not a source of antiaromaticity, and rather is the mechanism of lowering it. The fact that JT distortion is a mechanism for reducing the antiaromatic character, seems to be of general validity, as similar behavior was observed for the various JT active molecules: benzene cation and anion, cyclopentadienyl radical, cobaltocene, fullerene cation and anion, and arsenic and antimony anionic clusters. These results suggest that without analyzing details on how NICS values change along the distortion path, chemically important features could be lost.

9. Results and Discussion: A Simple Monomer-Based Model-Hamiltonian Approach to Combine Excitonic Coupling and Jahn-Teller Theory

Excitonic coupling is the physical quantity that determines the function and efficiency of many photo-biological processes like light harvesting or light reception, or of technological devices like organic light emitting diodes or organic photovoltaics. The model for the reliable description, interpretation and prediction of excitonic coupling taking into account vibronic coupling, and the interplay between these two effects is presented. The necessary quantities for the dimer Hamiltonian can be derived from monomer calculations alone. The proposed theory is validated using the benzene dimer as test case, since it presents one of the simplest, aromatic systems with π-π interaction, representative of more complex chromophores. In addition, extensive experimental and theoretical data are available in the bibliography, which can be compared to the computed data.[387-396] For the purpose of this work, TD-DFT was chosen as standard method for the calculation of the excited states, due to its computational efficiency. Its accuracy is here clearly sufficient despite its well-known drawbacks.[397]

9.1. Vibronic Model for Excitonic Coupling

In order to develop a theory, which takes excitonic and vibronic coupling into account, and to understand their mutual influence at least in a qualitative manner, one needs to start with some basic assumptions: (a) It is assumed that the monomer is a closed-shell species (see Figure 9.1.1., left) which should be correct for most systems not containing transition metal ions. (b) The first excited state of the monomer is mainly described by a single excitation from the HOMO to the LUMO. While this condition implies a very small configuration interaction, this later condition is reasonable if excited states with other configurations are sufficiently separated from the HOMO-LUMO ones. (c) In order to take advantage of a JT-type formulation it is assumed that some kind of symmetry element relating the two monomers in a dimer exists. In the case of the benzene dimer shown in Figure 9.1.1. (right) this operation can be taken to be a reflection or inversion but the theory is not limited to them in its application to other cases as, for example, it could be applied to an n-monomer system with a C_n axis in the system.

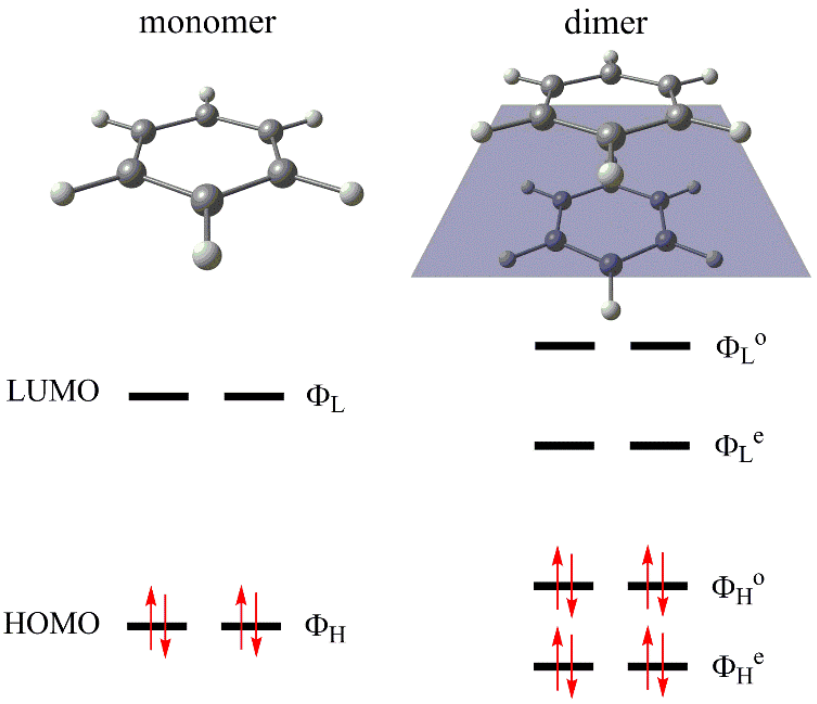

Figure 9.1.1. Scheme of the frontier orbitals of the monomer and the dimer, in which, a symmetry operation relates the monomer orbitals to the dimer ones. Hence it is possible to classify the dimer orbitals accordingly, here with respect to the coplanar reflection plane.

The nature of the lowest excited states in a symmetric dimer will be firstly discussed. For simplicity, it is first supposed that monomer HOMO and LUMO are non-degenerate, however this restriction can be easily lifted and the solutions for the degenerate case will be given also below for benzene. Using the symmetry condition (c) we can write the dimer orbitals as symmetrized combinations of the monomer orbitals:

$$\Phi_H^\alpha = \frac{1}{\sqrt{2(1 \pm S_H)}}(\Phi_H^1 \pm \Phi_H^2)$$

Eq. 9.1.1.

$$\Phi_L^\alpha = \frac{1}{\sqrt{2(1 \pm S_L)}}(\Phi_L^1 \pm \Phi_L^2)$$

Eq. 9.1.2.

In the equations above the sign corresponds to the character of the wavefunction with respect to the considered symmetry operation. The combination with the + sign will be

called *even* (α=*e*) and the combination with the - sign *odd* (α=*o*). It is important to note that the even and odd notations here refer exclusively to the main symmetry operation and they should not be understood as proper even or odd character with respect to inversion in real space which, in many cases, the studied molecules lack. The symbols S_H and S_L denote the HOMO-HOMO and LUMO-LUMO orbital overlaps. Note that in deriving expressions 9.1.1. and 9.1.2. the interactions of the HOMO of a monomer with the LUMO of the other, and vice versa are neglected. This is justified, because the HOMO-LUMO interaction is small. Using conditions (a) and (b) all singly excited determinants that give rise to the lowest dimer singlet excited states can be generated (Figure 9.1.2.), which can be classified with respect to the position of the electron and hole of the exciton, as well as from a symmetry point-of-view.

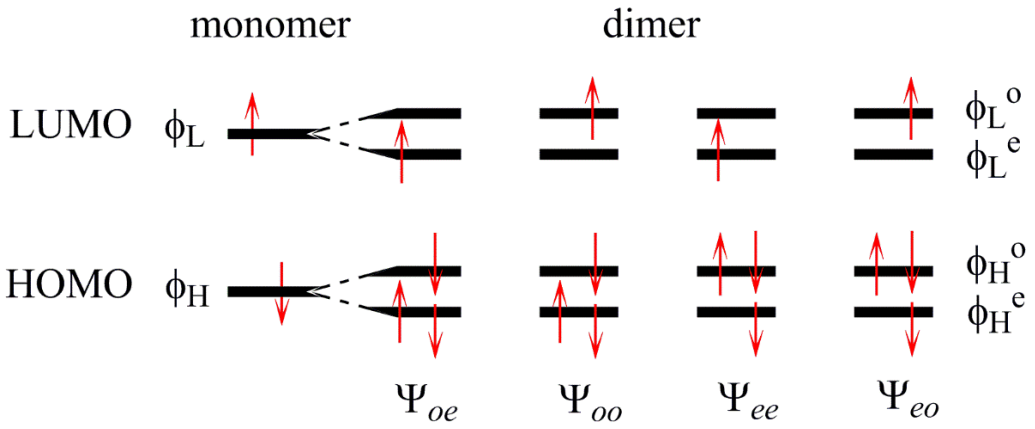

Figure 9.1.2. Scheme of all singly excited determinants within the dimer orbital space composed only of linear combinations of the HOMOs and the LUMOs of the monomer units, and the notation used to differentiate the different excited states arising from it.

In a second step the structural distortion that occurs on the monomer when the system is excited into the excited state will be taken into account. If this distortion is described by an effective mode $\vec{Q}$, using symmetry, we can construct two distortion modes for the dimer:

$$\vec{Q}_e = \frac{1}{\sqrt{2}}(\vec{Q}_1 + \vec{Q}_2)$$

Eq. 9.1.3.

$$\vec{Q}_o = \frac{1}{\sqrt{2}}(\vec{Q}_1 - \vec{Q}_2)$$

Eq. 9.1.4.

Here, and similar to previous notation, $\vec{Q}_e$ and $\vec{Q}_o$ have +1 and -1 character with respect to the symmetry operation, and $\vec{Q}_1$ and $\vec{Q}_2$ are local distortions in each of the monomers. In Figure 9.1.3. a schematic representation of these modes for the benzene dimer in a D_{6h} configuration is given.

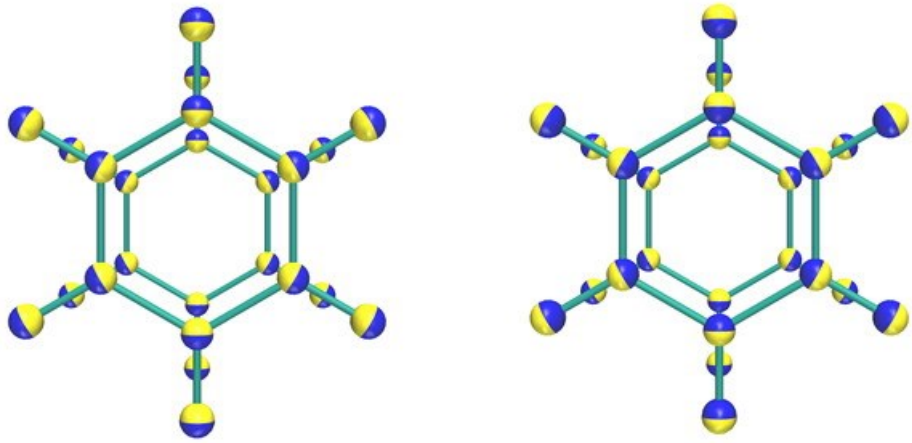

Figure 9.1.3. Schematic representation of a symmetric $\vec{Q}_e$ (left) and anti-symmetric distortion $\vec{Q}_o$ (right) of the benzene dimer. The size of vibrational motion on a nucleus is represented as sphere with the radius depending on the magnitude of the motion. The different colours indicate the direction of the motion.

Finally, the system Hamiltonian as a sum of electronic, vibrational and vibronic parts will be built. The electronic contribution ($\hat{H}_{el}(\{\vec{r}\};R)$) depends on the electron coordinates, $\{\vec{r}\}$, and the distance between the monomers, R, the vibrational on the distortion coordinates ($\vec{Q}_e$, $\vec{Q}_o$) while the vibronic part depends on both:

$$\hat{H} = \hat{H}_{el}(\{\vec{r}\};R) + \hat{H}'_o(\{\vec{r}\};R)Q_o + \hat{H}'_e(\{\vec{r}\};R)Q_e + \hat{H}_v(Q_e,Q_o;R)$$

Eq. 9.1.5.

Using this Hamiltonian a vibronic matrix $\langle\Psi_i|\hat{H}|\Psi_j\rangle$ can now be created using the states shown in Figure 9.1.2. This matrix can be simplified using symmetry to determine only non-zero elements to yield:

$$H_{JT} = \frac{1}{2}K_e Q_e^2 + \frac{1}{2}K_o Q_o^2 + \begin{pmatrix} \Delta_{ee} + F_{ee}Q_e & F_{ee}^{oo}Q_e & F_{ee}^{eo}Q_o & F_{ee}^{oe}Q_o \\ F_{ee}^{oo}Q_e & \Delta_{oo} + F_{oo}Q_e & F_{oo}^{eo}Q_o & F_{oo}^{oe}Q_o \\ F_{ee}^{eo}Q_o & F_{oo}^{eo}Q_o & \Delta_{eo} + F_{eo}Q_e & F_{eo}^{oe}Q_e \\ F_{ee}^{oe}Q_o & F_{oo}^{oe}Q_o & F_{eo}^{oe}Q_e & \Delta_{oe} + F_{oe}Q_e \end{pmatrix}$$

Eq. 9.1.6.

where we have defined the excitonic coupling constants $\Delta_i = \langle \Psi_i | \hat{H} | \Psi_i \rangle$ and the diagonal $F_i = \langle \Psi_i | d\hat{H}/dQ_\alpha | \Psi_i \rangle$ and off-diagonal $F_i^j = \langle \Psi_i | d\hat{H}/dQ_\alpha | \Psi_j \rangle$ vibronic coupling constants (here the index i and j run along the states ee, oo, eo and oe as defined in Figure 9.1.2. and α stands for e or o). Using the singlet wavefunctions of the electronic configurations and taking into account that the diagonal terms represent the force exerted by the excited electrons with respect to the ground state, the following expressions for the diagonal vibronic coupling elements is:

$$F_{ee} = F_{oo} = F_{eo} = F_{oe} = -\langle \Phi_H^e | \hat{f}_e | \Phi_H^e \rangle + \langle \Phi_L^e | \hat{f}_e | \Phi_L^e \rangle$$

Eq. 9.1.7.

in which $\hat{f}_e$ represents the vibronic operator for a single-electron along Q_e. Thus, all diagonal vibronic coupling elements are approximately the same. The expressions for the off-diagonal elements are:

$$F_{ee}^{oo} = F_{eo}^{oe} = 0$$

Eq. 9.1.8.

$$F_{ee}^{eo} = F_{oo}^{oe} = \langle \Phi_L^e | \hat{f}_o | \Phi_L^o \rangle$$

Eq. 9.1.9.

$$F_{ee}^{oe} = F_{oo}^{eo} = \langle \Phi_H^e | \hat{f}_o | \Phi_H^o \rangle$$

Eq. 9.1.10.

Expression 9.1.7. suggests that the force with respect to the ground state on the dimer comes from the removal of an electron from the HOMO (due to the negative sign) that is placed into the LUMO, while expressions 9.1.9. and 9.1.10. suggest that they are related

to the forces of individual electrons in the LUMO and the HOMO, respectively. Indeed, using expressions 9.1.1. and 9.1.2. the integrals are observed:

$$\langle \Phi_H^e | \hat{f}_o | \Phi_H^o \rangle = \frac{1}{\sqrt{2(1-S_H^2)}} [\langle \Phi_{1H} | \hat{f}_1 | \Phi_{1H} \rangle - \langle \Phi_{1H} | \hat{f}_2 | \Phi_{1H} \rangle]$$

Eq. 9.1.11.

This integrals can be further simplified taking into account that vibronic operators decay very quickly (typically αr^{-3}) to neglect the second term in the sum when compared to the first one. Moreover, the first product, whose meaning is that of a reduction factor due to the delocalization of the electron in between the two individual monomers orbitals, can in fact be simplified since our first-principles calculations indicate that $S_H^2 \ll 1$. Under these conditions Eqs. 9.1.7., 9.1.9. and 9.1.10. in terms of integrals depending just on a single monomer can be written as:

$$F_{ee} = F_{oo} = F_{eo} = F_{oo} = \frac{1}{\sqrt{2}} \left(-\langle \Phi_H | \hat{f} | \Phi_H \rangle + \langle \Phi_L | \hat{f} | \Phi_L \rangle \right) = \frac{1}{\sqrt{2}} f_{mono}$$

Eq. 9.1.12.

$$F_{ee}^{eo} = F_{oo}^{oe} = \frac{1}{\sqrt{2}} f_L$$

Eq. 9.1.13.

$$F_{ee}^{oe} = F_{oo}^{eo} = \frac{1}{\sqrt{2}} f_H$$

Eq. 9.1.14.

Here $f_{mono} = f_L - f_H$ is the force experienced in the monomer by removing an electron from the HOMO and placing it in the LUMO, i.e. the force in the excited state of the monomer, while f_L and f_H are the individual forces created by adding an electron to the LUMO or removing an electron from the HOMO of a monomer, respectively. These two last quantities can be associated with the force on the monomer along the effective mode Q when an electron is added or removed, i.e. the forces for the anion and the cation. In order to check expressions 9.1.12.-9.1.14. and the assumptions leading to them the *ab initio* forces of the anion and cation (Eqs. 9.1.13. and 9.1.14.) are compared with that of the neutral excited monomer (given by Eq. 9.1.12.). Acting in a similar way for the

vibrational part, and imposing that at long range the frequencies of vibration of the dimer need to be those of the monomer we obtain:

$$K_e = K_o = K_{mono}$$

Eq. 9.1.15.

Thus, the full vibronic matrix (Eq. 9.1.6.) can finally be reduced to:

$$H = \frac{1}{2}K_{mono}(Q_e^2 + Q_o^2) + \begin{pmatrix} \Delta_{ee} + \frac{1}{\sqrt{2}}f_{mono}Q_e & 0 & \frac{1}{\sqrt{2}}f_L Q_o & \frac{1}{\sqrt{2}}f_H Q_o \\ 0 & \Delta_{oo} + \frac{1}{\sqrt{2}}f_{mono}Q_e & \frac{1}{\sqrt{2}}f_H Q_o & \frac{1}{\sqrt{2}}f_L Q_o \\ \frac{1}{\sqrt{2}}f_L Q_o & \frac{1}{\sqrt{2}}f_H Q_o & \Delta_{eo} + \frac{1}{\sqrt{2}}f_{mono}Q_e & 0 \\ \frac{1}{\sqrt{2}}f_H Q_o & \frac{1}{\sqrt{2}}f_L Q_o & 0 & \Delta_{oe} + \frac{1}{\sqrt{2}}f_{mono}Q_e \end{pmatrix}$$

Eq. 9.1.16.

Here one can see that all vibronic interactions in the dimer can be reduced to quantities obtainable from the monomer. This is a very desirable property since it may allow estimation of the role of vibronic coupling in exciton transport without the need to carry out costly dimer calculations, but to do so is generally advised to validate the model with *ab initio* calculations.

Now, the physical content of the derived model can be analyzed. The coupling to $\vec{Q}_e$ occurs on the diagonal of the Hamiltonian and connected with f_{mono}, while, on the other hand, the coupling to $\vec{Q}_o$ is always accompanied by vibronic constants f_H and f_L. Taking into account that $f_{mono}=f_L-f_H$, there will be systems in which the coupling to $\vec{Q}_e$ dominates (f_L and f_H are very different), while in others the coupling to $\vec{Q}_o$ dominates ($f_L \sim f_H \rightarrow |f_{mono}| << |f_L|, |f_H|$). The emerging picture is that in the first case the distortion is the same and the solution that dominates the vibronic problem (Eq. 9.1.16.) is an exciton where electron and hole travel together. On the other hand, the case where $f_L \sim f_H$ leads to different distortions in the two monomers favoring the localization of the electron and hole separately, i.e. formation of polarons. Thus, even though the model does not contain several important key ingredients like electrostatic attraction between hole and electron,

it provides a very sensible picture of which conditions would favor the separation of the exciton in polarons. These limit solutions can be obtained from Eq. 9.1.16. when the excitonic coupling energy Δ is much smaller than the vibronic coupling energy (f·Q). In that case the solutions take the form:

$$\Psi_{\pm}^{e} = \frac{1}{\sqrt{2}}(\Psi_{oo} \pm \Psi_{ee})$$

Eq. 9.1.17.

$$\Psi_{\pm}^{o} = \frac{1}{\sqrt{2}}(\Psi_{oe} \pm \Psi_{eo})$$

Eq. 9.1.18.

While the (+) combinations correspond to two excitonically coupled local excited states, the (-) combinations represent two symmetrized CT excitations.[398] Later in this Chapter will be shown that the CT states do not play a role in the benzene dimer due to their symmetry.

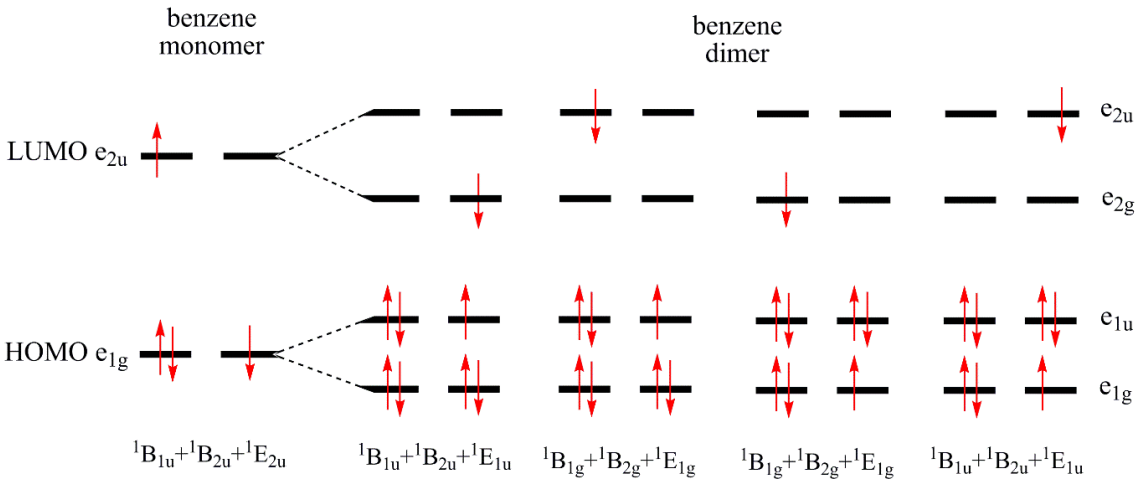

Figure 9.1.4. Singly excited determinants arising from single HOMO-LUMO excitations in the benzene monomer (left) and benzene dimer (right).

The changes between the above model and the one that arises when the HOMO and LUMO are doubly degenerate, as in the case of benzene will be given in the following. The main difference between these models is that in the latter case many more states are

involved (see Figure 9.1.4. and compare with Figure 9.1.2.). Observing the monomer states in Figure 9.1.4., in principle, the vibronic coupling problem is more complicated since vibrations belonging to a_{1g}, a_{2g} and e_{1g} can be involved. However, *ab initio* calculations indicate that in the benzene molecule the effective mode $\vec{Q}$ belongs to a_{1g} and as a consequence the other possibilities will not be taken into account. When constructing all excited states in the benzene dimer involving only the doubly degenerate HOMO and LUMO, instead of the previously four possibilities, now sixteen different states are possible. However, since the effective mode in the monomer is a_{1g}, the resulting even ($\vec{Q}_e$) and odd ($\vec{Q}_o$) dimer modes have a_{1g} and a_{2u} symmetry, respectively. As a consequence, the lower ^1B states do not couple with the higher-lying ^1E ones. Therefore the *E* states can be completely neglected in the model. Because the charge transfer states belong to these *E* states, they do not play any role in the derived excitonic coupling model due to the symmetry restrictions of the distortion modes. Thus, the dimensionality of the vibronic matrix can be reduced to eight, and using the same approximations as in Eqs. 9.1.7. to 9.1.14., it is found:

$$H = \frac{1}{2}K_{mono}(Q_e^2 + Q_o^2) + \begin{pmatrix} \Delta_{1e}^{ee} + \frac{f_m Q_e}{\sqrt{2}} & 0 & 0 & 0 & 0 & 0 & \frac{f_L}{\sqrt{2}}Q_o & 0 \\ 0 & \Delta_{1o}^{oo} + \frac{f_m Q_e}{\sqrt{2}} & 0 & 0 & 0 & 0 & 0 & \frac{f_L}{\sqrt{2}}Q_o \\ 0 & 0 & \Delta_{1o}^{eo} + \frac{f_m Q_e}{\sqrt{2}} & 0 & \frac{f_H}{\sqrt{2}}Q_o & 0 & 0 & 0 \\ 0 & 0 & 0 & \Delta_{1o}^{oe} + \frac{f_m Q_e}{\sqrt{2}} & 0 & \frac{f_H}{\sqrt{2}}Q_o & 0 & 0 \\ 0 & 0 & \frac{f_H}{\sqrt{2}}Q_o & 0 & \Delta_{2e}^{ee} + \frac{f_m Q_e}{\sqrt{2}} & 0 & 0 & 0 \\ 0 & 0 & 0 & \frac{f_H}{\sqrt{2}}Q_o & 0 & \Delta_{2e}^{oo} + \frac{f_m Q_e}{\sqrt{2}} & 0 & 0 \\ \frac{f_L}{\sqrt{2}}Q_o & 0 & 0 & 0 & 0 & 0 & \Delta_{2o}^{eo} + \frac{f_m Q_e}{\sqrt{2}} & 0 \\ 0 & \frac{f_L}{\sqrt{2}}Q_o & 0 & 0 & 0 & 0 & 0 & \Delta_{2o}^{oe} + \frac{f_m Q_e}{\sqrt{2}} \end{pmatrix}$$

Eq. 9.1.19.

Note again that, as in the previous case, only information from monomer calculations are required to arrive at a complete description of the benzene dimer coupling Hamiltonian.

The underlying computational procedure for the construction of the dimer model Hamiltonian consists of the following steps:

1. Geometry optimization of the monomer and calculation of verical excitation energies using different TD-DFT levels of theory and comparison with experimental data.
2. Geometry optimization of the monomer in the first excited state and identification of the distortion mode.
3. Choice of mutual orientations of monomer units in the dimer, followed by calculations of vertical excitation energies at different intermolecular separations between two monomer units; selection of particular intermolecular distances from the potential energy curves.
4. Performing calculations along the symmetric ($\vec{Q}_e$) and anti-symmetric ($\vec{Q}_o$) distortion of the excimer at chosen intermolecular separations.
5. Determination of all parameters in the model Hamiltonian (Eq. 9.1.19.); comparison of the results obtained using the model Hamiltonian with *ab initio* computed ones; validation of proposed model.

As already mentioned, the parameters f_H and f_L correspond to the forces acting on the monomer HOMO and LUMO at the ground state geometry, and their difference should be practically equal to the force acting on the excited neutral molecule, f_{mono}. These parameters have been obtained by fitting the curves of HOMO and LUMO energies along the monomer distortion coordinate. K_e and K_o correspond to the monomer force constant in the excited state and can be extracted by fitting the curves of the first excited state along the particular distortion. $\vec{Q}_e$ and $\vec{Q}_o$ have been constructed over the distortion mode of monomer, $\vec{Q}_1$ and $\vec{Q}_2$.

In order to study the localization mechanism of the excited benzene dimer and to calculate the model Hamiltonian, it is first necessary to compute properties of the benzene monomer to extract the required constants. For this purpose, equilibrium distances and vertical excitation energies have been calculated at different levels of theory and

compared with available data. Afterwards, TD-DFT results will be presented and compared to the proposed model for the excitonically coupled benzene dimer.

9.2. The Benzene Monomer

The optimized structure of the benzene molecule, in D_{6h} symmetry, at B3LYP-D3/TZP level of theory, has equilibrium bond lengths values of r_{CC} = 1.39 Å and r_{CH} = 1.08 Å, in perfect agreement with CCSD(T)/cc-pVQZ results.[399]

The excited states of benzene have been the subject of various theoretical and experimental studies.[393, 400-410] The obtained TD-DFT values of the excitation energies of the seven lowest excited states of benzene are given in Table 9.2.1. and compared with experimental data. The three well-known absorption bands in the UV spectrum of benzene at 4.90, 6.20, and 6.94 eV are assigned to the transitions $^1A_{1g} \rightarrow {}^1B_{2u}$, $^1A_{1g} \rightarrow {}^1B_{1u}$, and $^1A_{1g} \rightarrow {}^1E_{1u}$, respectively. Although, the transitions to 1^1B_{2u}, and 1^1B_{1u} excited states, are symmetry forbidden in benzene,[411] due to vibronic interactions they still occur in the experimental spectrum.[409] The excitation energies are calculated at different levels of theory.. The results are consistent to each other, and to the previous theoretical considerations,[410] and do not show large basis set or exchange/correlation functional dependance (Table 9.2.1). For further studies we have chosen TD-B3LYP/TZP level, although it is clear that it does not exhibit the necessary accuracy to perform a quantitative state-of-the-art study of the excited states of benzene.[410] Qualitatevely same results could be obtained with other levels of theory. However, the focus of the present study is not the investigation of the exicted states of benzene, but the rationalization of the electronic structure of the excited benzene dimer and the verification of the proposed model Hamiltonian approach. It is also important to note that the CT problem of TD-DFT is irrelevant here, since the CT states are excluded from the investigation based on their symmetry and the fact that they do thus not play a role in the excitonic coupling.

Table 9.2.1. Vertical excitation energies of C_6H_6 (eV) calculated at the level of TD-DFT using different functionals and basis sets. All calculations were performed in D_{6h} symmetry with r_{CC}=1.39 Å and r_{CH}=1.08 Å.

E_{ex}/eV	Singlet π→π*			Triplet π→π*			
	1^1B_{1u}	1^1B_{2u}	1^1E_{1u}	1^3B_{1u}	1^3E_{1u}	1^3B_{2u}	1^3E_{2g}
B3LYP							
DZP	5.53	6.34	7.31	4.07	4.84	5.23	7.23
TZP	5.41	6.18	7.14	4.01	4.76	5.13	6.56
TZ2P	5.43	6.18	7.14	4.02	4.77	5.14	6.57
QZ4P	5.44	6.15	6.99	4.04	4.76	5.11	6.24
BP86							
DZP	5.34	6.21	7.20	4.46	4.83	5.10	7.49
TZP	5.26	6.08	7.05	4.41	4.77	5.02	6.77
TZ2P	5.27	6.08	7.05	4.42	4.77	5.03	6.77
QZ4P	5.29	6.07	6.98	4.43	4.77	5.02	6.47
PBEsol							
DZP	5.34	6.22	7.20	4.47	4.83	5.11	7.44
TZP	5.27	6.09	7.06	4.42	4.77	5.03	6.70
TZ2P	5.27	6.09	7.05	4.43	4.78	5.04	6.71
QZ4P	5.29	6.06	6.96	4.43	4.78	5.02	6.32
SAOP							
DZP	5.32	6.20	7.16	4.44	4.81	5.09	7.14
TZP	5.28	6.09	7.05	4.42	4.78	5.04	6.59
TZ2P	5.28	6.10	7.05	4.43	4.79	5.05	6.61
QZ4P	5.30	6.07	6.96	4.43	4.78	5.03	6.56
PBE0							
DZP	5.58	6.36	7.35	3.98	4.86	5.27	7.52
TZP	5.51	6.25	7.22	3.94	4.81	5.20	6.87
TZ2P	5.51	6.24	7.21	3.95	4.81	5.20	6.89
QZ4P	5.53	6.22	7.14	3.97	4.81	5.17	6.54
Experiment[400-404]	4.90	6.20	6.94	3.94	4.76	5.60	6.83/7.24

TD-DFT geometry optimization, without constraining the symmetry, has shown that the equilibrium structure of the first excited singlet state has D_{6h} symmetry and bond lengths of r_{CC} = 1.43 Å and r_{CH} = 1.08 Å. It is obvious that the structural relaxation, which leads from the ground state geometry of benzene to the equilibrium geometry of the first excited state, occurs along the totally symmetric breathing mode. Following this breathing mode from the ground state geometry, the potential energy curves of the three lowest singlet excited electronic states of benezene, in D_{6h} symmetry, have been

computed (Figure 9.2.1.). These three states of $^1B_{1u}$, $^1B_{2u}$ and $^1E_{1u}$ symmetry are the lowest singlet states arising from HOMO-LUMO excitations.

In order to verify the applicability and accuracy of the proposed model Hamiltonian, which requires only intrinsic features of the constituting monomer to reproduce the excited states of the dimer, we have calculated the necessary parameters f_H and f_L and obtained values of 14.53 eV/Å and 23.30 eV/Å, respectively. According to the model, the difference between these forces (8.77 eV/Å) acting on the monomer cation on removal of an electron from the HOMO or on the anion on addition of an electron to the LUMO, perfectly corresponds to the force (8.48 eV/Å) acting on the excited neutral monomer.

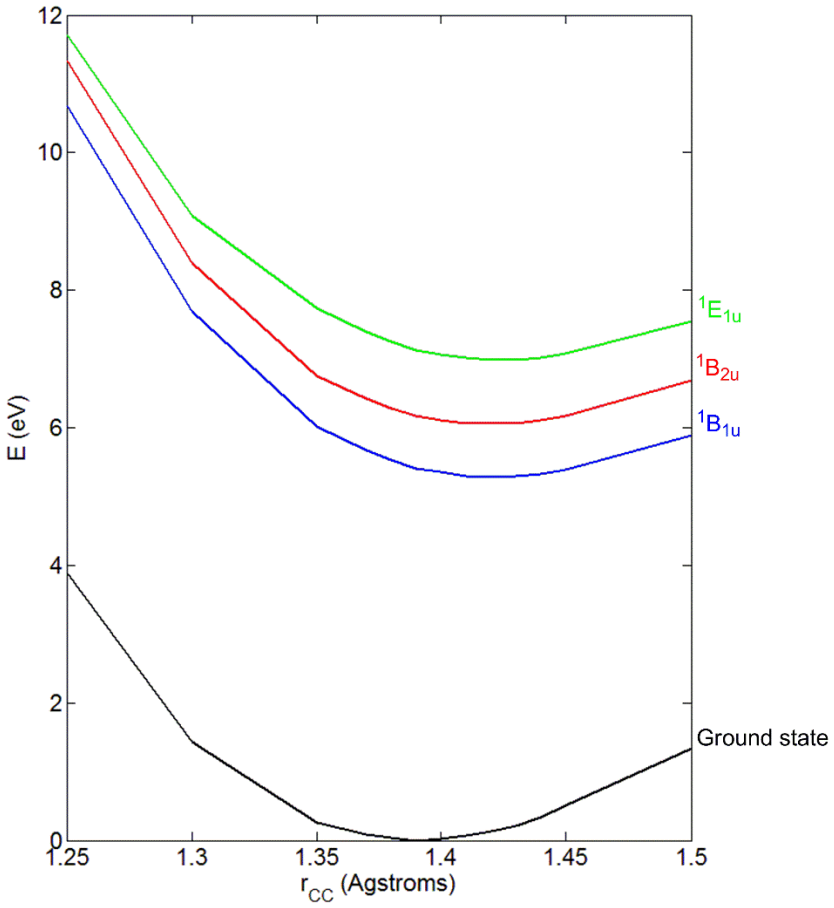

Figure 9.2.1. Potential energy curves of the ground and the three lowest excited singlet states of benzene along its totally symmetric vibrational breathing mode.

9.3. The Benzene Dimer

Selected possible mutual orientations of two benzene molecules forming a dimer, i.e. parallel (sandwich-shaped) (D_{6h}), T-shaped (C_{2v}), parallel-displaced (C_{2h}) and parallel-twisted (D_6), are presented in Figure 9.3.1. In the case of the D_{6h}, C_{2v} and D_6 structures, the intermolecular separation coordinate R was defined as the distance between the centers of masses of the two benzene molecules. In C_{2h} orientation, the intermolecular separation coordinate R was chosen to be the distance between the center of mass of one benzene ring and center of the closest C-C bond of the other benzene ring.

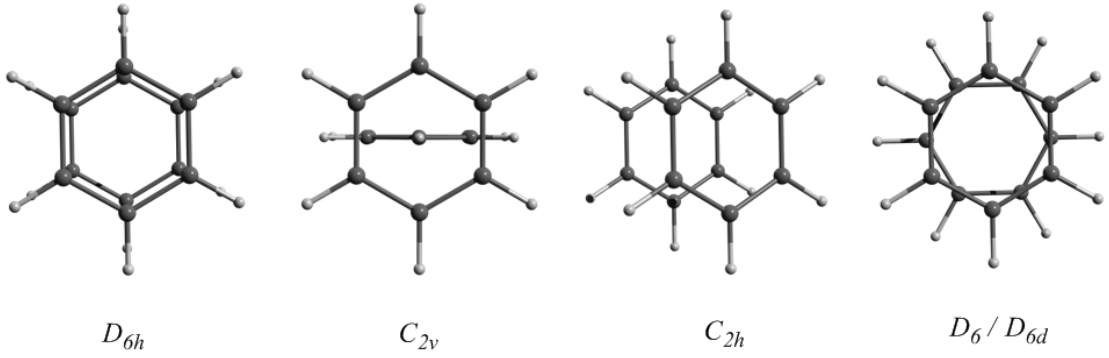

Figure 9.3.1. Investigated mutual orientations of the benzene dimer.

Numerous theoretical studies have nowadays shown that the T-shaped and the parallel-displaced structures are minima on the potential energy surface of the benzene dimer,[412, 413] which is in agreement with the calculations. Symmetry constrained geometry optimizations of the benzene dimer in all investigated mutual orientations result in equilibrium bond distances r_{CC} = 1.39 Å and r_{CH} = 1.08 Å, which are equal to the bond lengths of the benzene monomer. Since the equilibrium bond distances are the same as in the isolated monomer, the ground state geometry is practically not affected by the presence of another benzene molecule at this intermolecular distance. The optimal intermolecular separation between two benzene units, R_{eq}, is 3.89 Å for D_{6h}, 3.63 Å for C_{2h}, 4.97 Å for C_{2v} and 3.82 Å for D_6 at the theoretical level of DFT/B3LYP-D3, with splitting of the first two excited states of 0.28 eV for D_{6h}, 0.04 eV for C_{2h}, 0.08 eV for C_{2v} and 0.00 eV for D_6 minima structures, respectively, at the theoretical level of TD-DFT/B3LYP (Figure 9.3.2.).

The potential energy curves of the energetically lowest electronic states of all studied dimer orientations along the intermolecular separation coordinate R, going from 7 Å to 3 Å in steps of 0.5 Å, are shown in Figure 9.3.2. At distances R < 3 Å strong repulsive Coulomb interaction appears resulting in a steep increase of the energies of the electronic states and consequently in their mixing.

The potential energy curves of the electronic states of the parallel, eclipsed, D_{6h}, benzene dimer at various intermolecular separations, R (Figure 9.3.2., top left), show that the two first excited states are practically degenerate at intermolecular distances larger than 5 Å. At separations < 5 Å, a significant excitonic splitting of these states becomes apparent. With decreasing monomer distances, the splitting becomes more significant, and at R = 3 Å, it has a value of 1.39 eV. In the other studied dimer orientations, the splitting of the first two excited states at R = 3 Å is smaller. In the parallel-displaced orientation, C_{2h}, it has a value of 0.47 eV (Figure 9.3.2., top right), while in the D_6 orientation, the splitting is completely absent (Figure 9.3.2., bottom left). In the T-shaped orientation (Figure 9.3.2., bottom right), the splitting of first two excited states is 0.07 eV at an intermolecular separations of 4.5 Å.

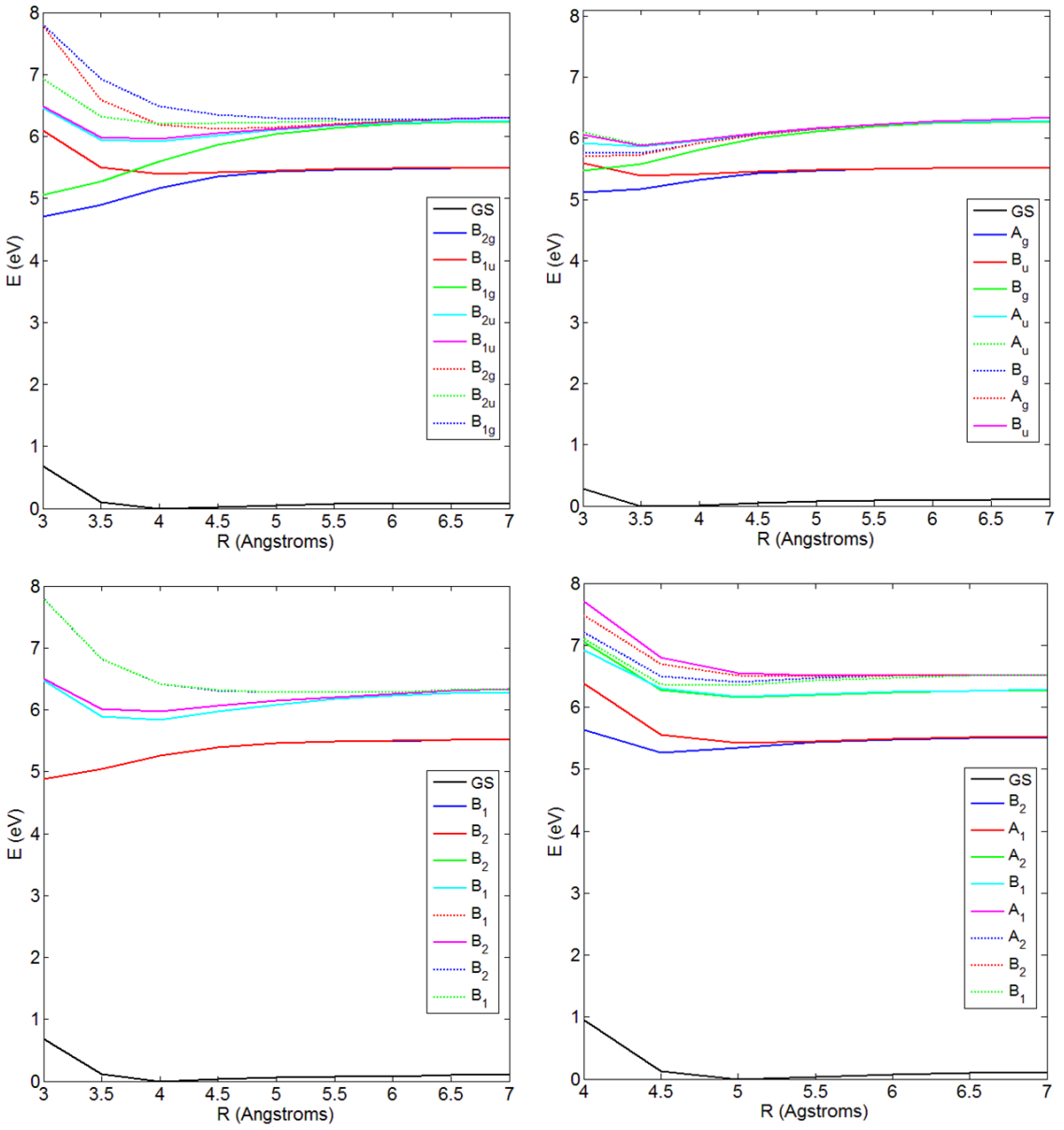

Figure 9.3.2. Potential energy curves along the intermolecular separation coordinate R of the benzene dimer in D_{6h} (top left), C_{2h} (top right), D_6 (bottom left) and C_{2v} (bottom right) orientation with $r_{CC1} = r_{CC2} = 1.39$ Å at the theoretical level of TD-DFT/B3LYP-D3.

The largest EC, i.e. the most pronounced splitting of the excited states, appears in the D_{6h} parallel sandwich orientation. It has been shown previously that a minimum on the potential energy surface of the lowest excited state exists in this D_{6h} orientation corresponding to a benzene excimer ($^1B_{2g}$) with an intermolecular separation of only 3.05 Å.[414] Hence, we studied the localization of the exciton in this parallel D_{6h} conformation. The relevant potential energy curves of the benzene dimer were determined at fixed values of R (3 Å – excimer minimum, 3.89 Å – ground state minimum and 5 Å –

borderline case) by following the symmetric and anti-symmetric combinations of the breathing mode, which belong to a_{1g} and a_{2u} irreducible representations in the D_{6h} point group, by varying the bond distance r_{CC} from 1.25-1.50 Å in steps of 0.025 Å. By elongation of all C-C bonds in one benzene monomer and simultaneous compression of all C-C bonds in the other one, i.e. following the anti-symmetric distortion, the symmetry of the benzene dimer is reduced from D_{6h} to C_{6v}. Therefore, calculations were performed in D_{6h} ($r_{CC1} = r_{CC2}$) and C_{6v} ($r_{CC1} \neq r_{CC2}$) point groups.

Cuts through the potential energy surfaces obtained at TD-DFT/B3LYP-D3 level along the symmetric and anti-symmetric distortions, at intermolecular separation of 3, 3.89 and 5 Å are displayed in Figures 9.3.3., 9.3.4. and 9.3.5. (top), respectively. In the same Figures (bottom), results obtained using the model Hamiltonian (Eq. 9.1.19.) are shown. Remember that all necessary parameters for the model Hamiltonian, except the Δ, are extracted from *ab initio* calculations of the monomer alone.[ii] However, it is straightforward to derive also Δ from monomer calculations alone knowing the relative orientation of the monomers using the classical Förster equation (see Chapter 5) for the coupling of the transition dipole moments.

The overall agreement between *ab initio* and model curves is excellent, despite of the simplicity of the proposed model. The only discrepancy can be found for the slope of the four highest considered excited states in the model, Figures 9.3.3., 9.3.4. and 9.3.5. (bottom right). This is not surprising, since in PJT theory higher excited states are generally needed to soften these curves.[36, 415] However, for the localization of the exciton, i.e. the correct description of the shape of the $^1B_{2g}$ curve, which is reproduced perfectly, only eight states are needed, which are included in the model. In addition, a slight

[ii] The obtained force of the dimer at small R corresponds to the force derived from Eq. 12 and can be presented through the force calculated for the monomer. At intermolecular separation of 3 Å, the force obtained by TD-DFT calculations of the dimer is 5.68 eV/Å, and correspond to the value of 6.01 eV/Å obtained using Eq. 12 in the model. With increasing the separation between monomer units total force that drives the nuclei to the minimum increases, and at R = 3.89 Å it has the value of 6.96 eV/Å. The total force at intermolecular distance of 5 Å is 8.54 eV/Å, which is in the excellent agreement with the force obtained for the monomer in the first excited state (8.48 eV/Å). K_e and K_o were obtained from the monomer force constant in the excited state. Following the model and Eq. 15 the dimer force constants are equal to the monomer force constant. K_{mono} has a value of 313.07 eV/Å^2. The dimer forces, K_e and K_o, where the monomer units are strongly separated, are 318.10 eV/Å^2 and 269.82 eV/Å^2, respectively. Moving to smaller intermolecular separations, K_e and K_o have almost constant values. At intermolecular distance of 3.89 Å Ke is 316.49 eV/Å^2 and at R = 3 Å it has value of 318.28 eV/Å^2. K_o calculated at intermolecular separation of 3.89 Å is 262.43 eV/Å^2 and at intermolecular separation of 3 Å the constant has a value of 283.45 eV/Å^2.

anharmonicity of the TD-DFT computed curves can generally be noted (Figures 9.3.3., 9.3.4. and 9.3.5., top left). Obviously, this remains undetected in the purely harmonic model (Figures 9.3.3., 9.3.4. and 9.3.5., bottom left).

At an intermolecular separation of 3 Å, the splitting of the first two excited states, $^1B_{2g}$ and $^1B_{1u}$, is apparent (Figure 9.3.3., left). Along the anti-symmetric distortion of the first exicted state, only one minimum exists (Figure 9.3.3., right). Having a closer look at Figure 9.3.3. (top right), the minimum of the curve of the first excited state lies at $r_{CC1} = r_{CC2}$, though at longer bond lengths of 1.41 Å, which is between the equilibrium bond lengths of the benzene molecule in the ground and first excited state.

Moving to the intermolecular separation of 3.89 Å, the splitting of the states decreases, as expected (Figure 9.3.4., left), because excitonic coupling decreases with intermolecular distance as R^{-6}. Regarding the anti-symmetric distortion (Figure 9.3.4., top right), the interaction between the two first excited states at the point $r_{CC1} = r_{CC2} = 1.41$ Å can be noticed. Consequently, two very weakly visible minima in the first excited state, where one monomer unit has C-C bond lengths 1.43 Å and the other 1.39 Å and vice versa, arise, which represent characteristic examples of PJT distortion. This situation can be seen as an intermediate case where weak localization of the exciton due to the PJT distortion can occur. The curve of the first excited state along the anti-symmetric distortion coordinate Q_o obtained from the model Hamiltonian (Figure 9.3.4., bottom right) is in excellent agreement with the *ab initio* curve.

Finally, at R = 5 Å, the first two excited states, $^1B_{2g}$ and $^1B_{1u}$, are practically degenerate (Figure 9.3.5., left). At this intermolecular separation, only a very weak interaction exists between the two monomer units. Removal of the degeneracy is achieved along anti-symmetric distortion and a symmetric double minimum emerges (Figure 9.3.5., right). The obtained minima correspond to structures in which one benzene monomer has C-C bond lengths of 1.43 Å and the other of 1.39 Å and vice versa. It is obvious that one monomer takes on the equilibrium bond distance of the electronic ground state, while the other the one of the first excited state. In other words, localization of the exciton on one of the monomers in the excited benzene dimer can occur at this intermolecular separation of 5 Å.

It should be noted that in this case degeneracy exists by construction i.e. by putting two equivalent molecules in spatial proximity exhibiting D_{6h} symmetry. However, the

distortion that the system undergoes is not due to the JT effect. The reasons can be found in point group theory as the final state representation must come from the sum of the two initial irreducible representations. Therefore, the subspace of the degenerate B_{2g} and B_{1u} state corresponds to a double irrep ($B_{2g} + B_{1u}$). Taking the direct product with itself, the result is the total symmetric representation A_{1g} plus the asymmetric A_{2u}, which is exactly the connecting mode between the D_{6h} and C_{6v} symmetric structures, representing the anti-symmetric distortion mode of the benzene C-C bonds. Moreover, the strong mixing of these two initial wavefunctions strongly changes the initial character of the state transferring charge from one molecule to the other clearly indicating that this is a strong PJT effect with a very small gap.

Similarly to previous results for the CO dimer,[158] distance dependent EC can either quench the PJT effect (R = 3 Å), or lead to the formation of PJT (R = 3.89 Å) that becomes very strong with quasi-degeneracy at (R = 5 Å). In the two later cases, breaking the symmetry results in asymmetrically distorted molecular geometries with lower energy and concomitant localization of the excitation energy on one monomer unit.

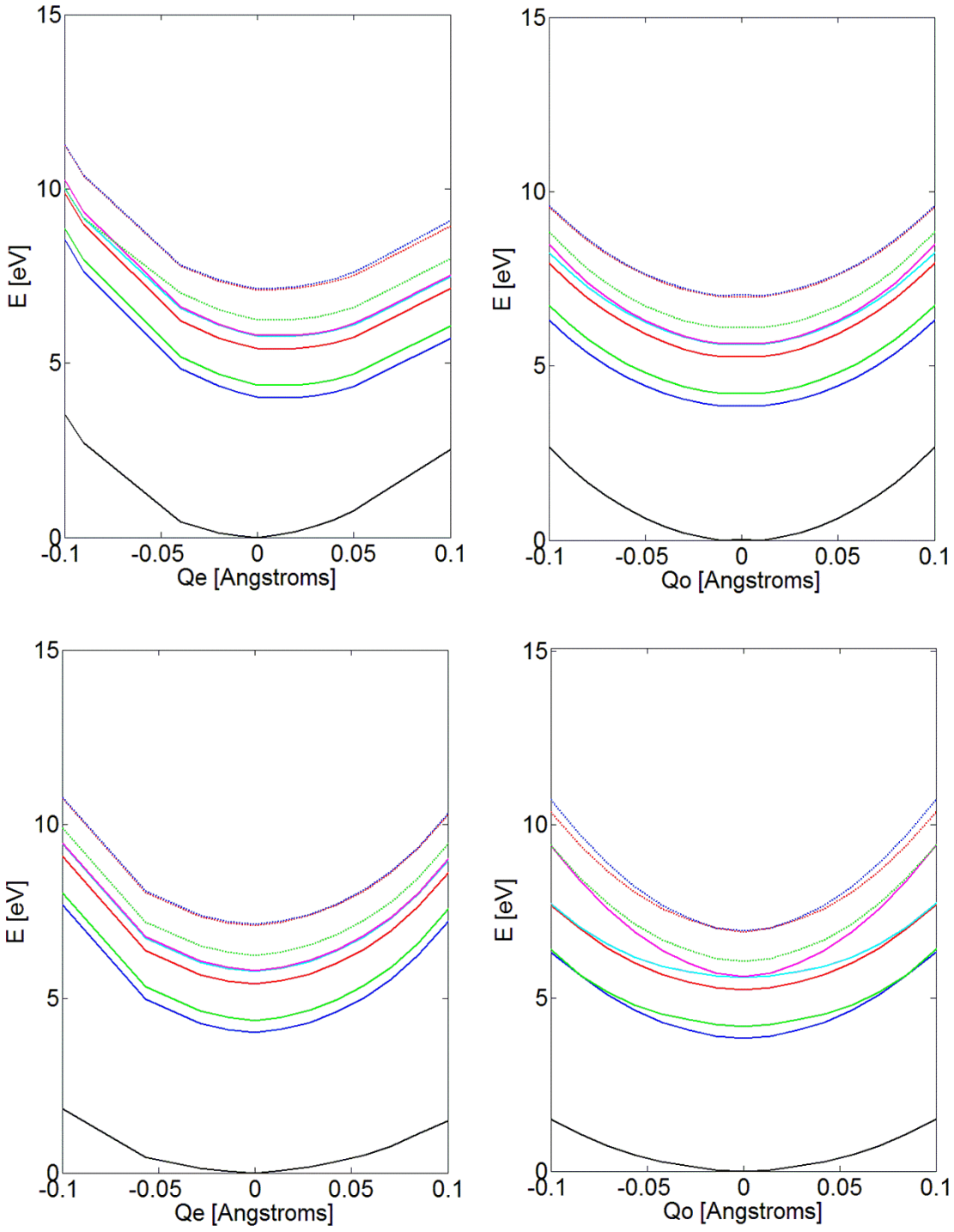

Figure 9.3.3. Potential energy curves of the lowest excited states along the symmetric and the anti-symmetric distortion coordinates Q_e (left) and Q_o (right) at an intermolecular separation R of 3 Å of the D_{6h} benzene dimer; TD-DFT/B3LYP-D3 calculated plots are given on the top, while the plots obtained using the model Hamiltonian are given at the bottom.

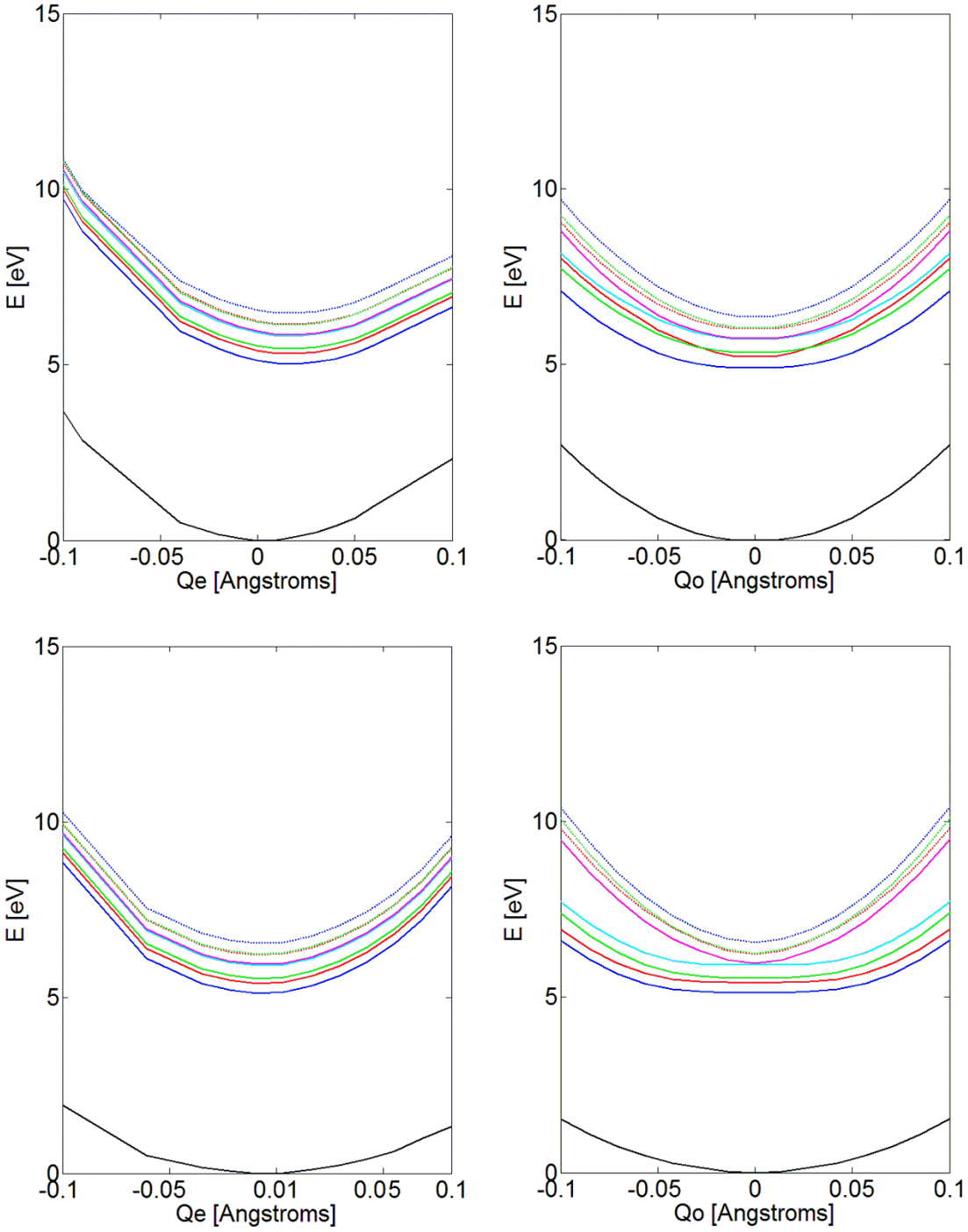

Figure 9.3.4. Potential energy curves of the lowest excited states along the symmetric and the anti-symmetric distortion coordinates Q_e (left) and Q_o (right) at an intermolecular separation R of 3.89 Å of the D_{6h} benzene dimer; TD-DFT/B3LYP-D3 calculated plots are given on the top, while the plots obtained using the model Hamiltonian are given at the bottom.

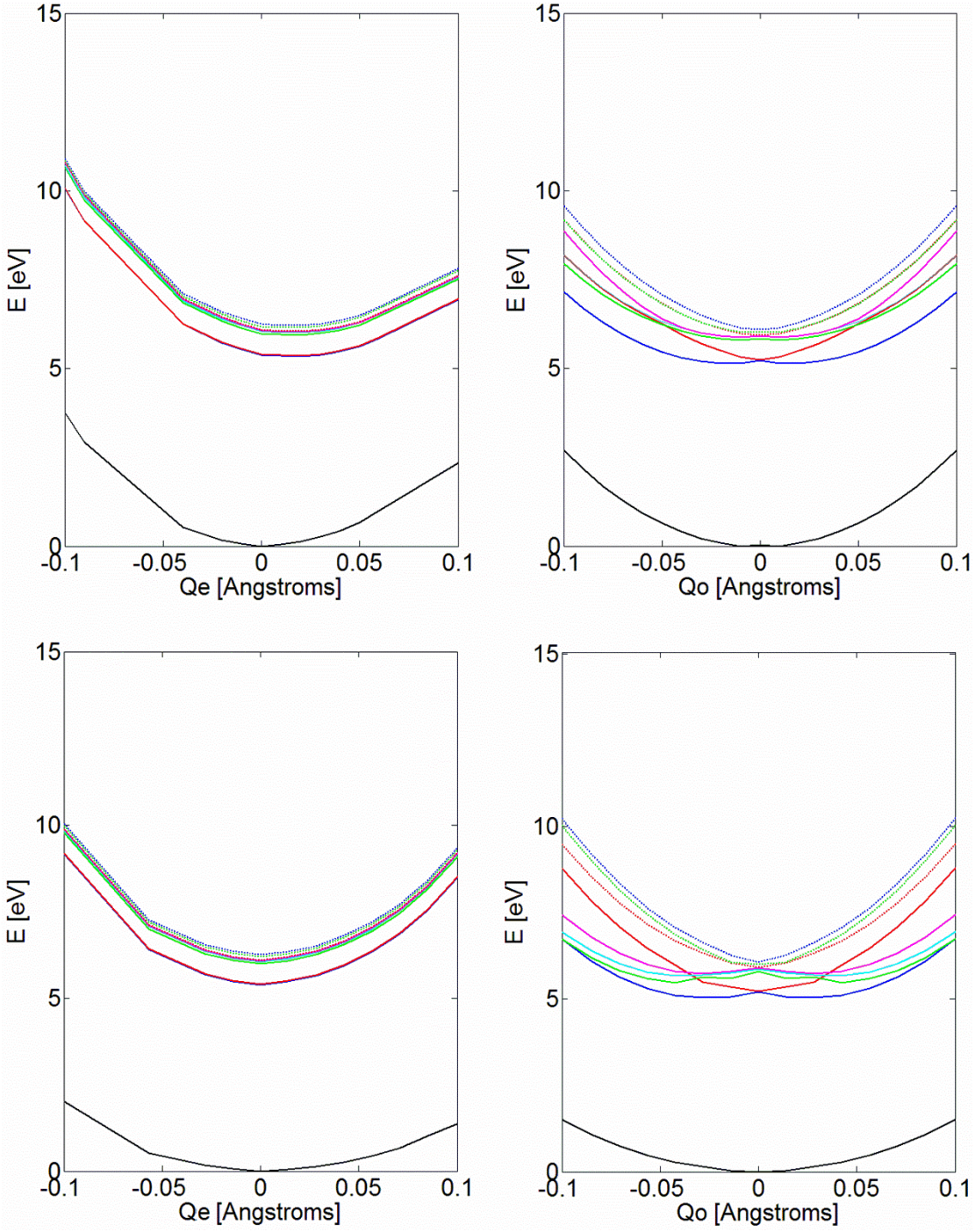

Figure 9.3.5. Potential energy curves of the lowest excited states along the symmetric and the anti-symmetric distortion coordinates Q_e (left) and Q_o (right) at an intermolecular separation R of 5 Å of the D_{6h} benzene dimer; TD-DFT/B3LYP-D3 calculated plots are given on the top, while the plots obtained using the model Hamiltonian are given at the bottom.

9.4. Conclusion

A novel scheme for analyzing exciton localization or equivalently excitation energy transfer in excitonically coupled dimers taking vibronic coupling into account is presented, which can be derived from intrinsic properties of the constituting monomers alone. The derived model has here been exemplified using the benzene dimer and its validity and applicability has been tested against *ab initio* results. Most importantly, the derived Hamiltonian forms the basis for more advanced quantum simulations of excitons in coupled chromophores.

Spatially separated equivalent molecules have degenerate excited states by construction. In principle, two possibilities exist to lift the degeneracy, either by lowering the intermolecular separation between two monomer units to increase EC, or by vibronic coupling where only a small displacement of the atoms removes the degeneracy and lowers the energy of the states, indicating strong vibronic coupling in the excited states, whereas the ground state is not affected. In other words, if two chromophores are close enough that excitonic coupling plays the main role for splitting of the excited states, this situation corresponds to the coherent regime of excitation energy transfer as the exciton remains delocalized over both chromophores. With increasing the intermolecular separation, EC strength decreases, and as soon as the vibronic coupling approaches a similar magnitude than EC, pseudo JT distortion occurs and the exciton tends to localize on one monomer. Going to even larger intermolecular separation, a very strong PJT effect removes the excited states degeneracy.

In order to rationalize the effects that are taking place in the process of exciton localization, we have developed this model based on the vibronic coupling theory, to elucidate the mechanism of exciton localization vs. excitation energy transfer, in strong, weak and intermediate EC case. The key role of the PJT coupling, especially in intermediate EC situations has been illuminated. In particular, neglecting the PJT coupling between excited states in the model would always lead to a delocalized picture of the exciton.

9.5. Computational Details

The structures of the benzene monomer and its dimer were optimized at the level of DFT using the Amsterdam Density Functional program package, ADF2010.01.[228-230] The hybrid B3LYP,[179, 180] with included dispersion,[416] B3LYP-D3, was used for the symmetry-constrained geometry optimizations. TZP basis set was used for all atoms. The difference in energy between two optimized monomers and the dimer, where two monomer units are placed at large intermolecular separation, i.e. there is practically no interaction between them, was 0.0047 eV, confirming the size-consistency of the calculations.

Vertical excitation energies of benzene were calculated using TD-DFT, at B3LYP-D3 optimized geometry with B3LYP,[179, 180] BP86,[63, 64] PBEsol,[417] SAOP[418, 419] and PBE0[420, 421] levels of theory. In order to elucidate the best combination of functional and basis set the vertical excitation energies were calculated with DZP, TZP, TZ2P and QZ4P basis set for all used XC functionals. Vertical excitation energies and potential energy curves of the excited states of benzene dimer were approximated by adding the excitation energies to the B3LYP-D3 ground state.

10. General Conclusion and Outlook

The results presented in this thesis demonstrate state-of-art approach for the analysis of the multimode JT problems, combining MD-DFT and IDP model, and the influence of the vibronic coupling on the important molecular properties.

Simple algorithm of MD-DFT allows quantifying the JT distortion and its energy stabilization in fast and efficient way and thus, can be successfully applied for the calculation of the JT parameters, as well as geometries of chemically different molecules prone to the JT distortion. The performance of the MD-DFT approach using various XC functionals has been evaluated for: small, organic radicals, C_nH_n (n=4-7); open-shell corannulenes and coronenes; organometallic compound - bis(cyclopentadienyl)cobalt(II) (cobaltocene); small metal clusters - sodium cluster (Na_3) and silver cluster (Ag_3); square-planar arsenic and antimony anionic clusters and Werner-type complexes - hexaflurocuprat(II) ion ($[CuF_6]^{4-}$) and tris(acetylacetonato)manganese(III) ($[Mn(acac)_3]$). The JT distortion is a consequence of electronic factors, but strongly depends on the geometry. The selection of the XC functional is strictly connected to the chemical system at hand, but to obtain qualitatively reliable results, the simplest LDA is satisfactory, regardless of the diversity of the systems prone to the JT distortion. Although other XC functionals perform better in the quantification of other properties of molecules, that is, the B3LYP for magnetic couplings,[173] the BP86 for EPR hyperfine data,[174] the OPBE for reliable spin-state energies for iron complexes,[422] the LDA appears to be the most accurate for the determination of the JT parameters by the means of MD-DFT. Quantification of the JT distortion in this simple and efficient way is of great interest as the experimental determination of the JT parameters is very difficult and there is often uncertainty in the obtained values. Conversely, multireference wavefunction methods are usually not affordable for large systems, giving the advantage to MD-DFT as a reliable tool for the study of vibronic coupling.

In addition the analysis of the multimode JT effect using concept of the IDP model is shown. Systematic analysis of the JT distortion of essentially different organic and inorganic molecules, i.e. arsenic and antimony anionic clusters, examples of $E \otimes b_1 + b_2$ JT problem, and small, organic radicals and anions and cations of corannulene and

coronene, examples of $E \otimes e$ JT problem, has provided confidence in the validity of the model. The distortion is always dominated by the modes that fulfill symmetry requirements, and that mostly affect the corresponding, partially occupied frontier orbitals. If there are several appropriate vibrations, harder modes will always be more important in the beginning of the distortion, because they reduce energy in the most efficient way, while the softer modes are important in the relaxation part of the distortion path. The importance of both, the harder and softer normal modes, needs to be included in the proper analysis of the JT effect. Since the IDP approach, within the harmonic approximation, assumes the energy surface to be quadratic, the potential energy surface has a simple analytical form, and it is possible directly to separate the contributions of the different vibrations to the JT distortion, the forces at the HS point, as well as how these forces change along a relevant particular path of distortion. IDP in conjunction with MD-DFT presents an effective method, not only for quantifying the distortion of the JT active molecules with C-C bonds, but also for a broad palette of the JT active molecules.[22, 423, 424] Therefore, this fully non-empirical approach can be considered as a reliable tool for better understanding of the JT effect and getting deeper insight into the origin and the mechanism of the vibronic coupling. Moreover, important features in the coupling between the electron distribution and the motion of the nuclei could be lost without employment of this conceptually simple model.

Since the discovery of the JT effect has become a source of inspiration for many researchers, not only as an adoption of new cognitions, but as the effect which affects many fundamental properties of molecules, the influence of the JT distortion on the aromaticity and excitonic coupling is presented.

The development in material chemistry is relentlessly growing and takes up a monopoly in modern science. Therefore, the relation between two fundamentally opposite effects, vibronic coupling and aromaticity certainly represents the topic of great interest. The investigation and understanding of the influence of the JT distortion on the aromaticity of 4n+1 π open-shell molecules, i.e. cyclopentadienyl radical, benzene cation and anion, bis(cyclopentadienyl)cobalt(II), fullerene ions and square planar arsenic and antimony clusters, is presented. The changes of the most famous magnetic criteria, NICS, were scanned along the particular path of distortion, IDP. The deeper inspection of the magnetic criteria along the IDP indicate that antiaromaticity decreases with increasing

deviation from the HS to LS point on the potential energy surface, for all investigated species. Thus, the JT effect can be surely considered as the unique mechanism of lowering the antiaromaticity.

Since the understanding of excitonics will help in the optimization of solar energy conversion efficiency, the study of excitons represents great and recurring interest in scientific community. The investigation of excitons, which determine the efficiency of EET, leads to the possible rational design of better manmade devices, i.e., organic photovoltaic devices, electroluminescence and solar energy cells, or light-emitting diodes. The exciton coupling parameter, has been studied and a novel scheme for analyzing exciton localization or equivalently excitation energy transfer in excitonically coupled dimers taking vibronic coupling into account is presented. The proposed theory has been validated using the benzene dimer as the model of more complex systems. More importantly, the derived Hamiltonian forms the basis for more advanced quantum simulations of excitons in coupled chromophores. The purpose of the new developed model is to represent and predict the properties of coupled identical chromophores based on intrinsic features of the constituting monomers alone, allowing the study of much larger biological or chemical systems, but still to achieve microscopic insights into the details of exciton localization vs. excitation energy transfer in complex systems. It is noteworthy that the developed simplified model leads to the same conclusions as computationally demanding *ab initio* calculations, bearing the advantage of giving detailed insight in the behavior of excitonically coupled chromophores. Conceptually simple model introduced in this thesis will give the direct insight into the one of the nowadays problems in the design of new functional materials and devices - the EET between the chromophores. Potential applications of these results, apart from the purely fundamental understanding of EET, lie in the framework of molecular nanoengineering, optoelectronics, use in biomimeting technical applications and photobiology where excitations in nearby proteins are coupled, allowing energy to be captured by antenna systems and transported to the protein active sites.

In the framework of vibronic coupling theory it is possible to find rationalizations of different molecular phenomena and to gather detailed information on the interplay between electronic structure and nuclear motions. This is an important prerequisite for the analysis of various properties in complex systems. Such a new perspective will allow

the novel analysis and deeper understanding of fundamental chemical problems. Application of this theory and new models developed in this thesis will hopefully pave the road to a computational design of new functional materials and devices.

11. References

1. I. Bersuker, *The Jahn-Teller Effect*, Cambridge University Press, 2006.
2. H. Köppel, W. Domcke and L. S. Cederbaum, in *Advances in Chemical Physics*, John Wiley & Sons, Inc., 1984, vol. 57, pp. 59-246.
3. H. A. Jahn and E. Teller, *Proceedings of the Royal Society of London A*, 1937, **161**, 220-235.
4. R. Renner, *Z. Physik*, 1934, **92**, 172-193.
5. U. Öpik and P. M. H. L., *Proceedings of the Royal Society of London A: Mater. Phys. Sci. S*, 1957, **238**, 425-447.
6. A. J. Millis, *Nature*, 1998, **392**, 147-150.
7. O. Gunnarsson, *Nature Materials*, 2008, **7**, 176-177.
8. T. T. M. Palstra, *Nature Materials*, 2008, **7**, 350-351.
9. O. Gunnarsson, *Reviews of Modern Physics*, 1997, **69**, 575-606.
10. O. Gunnarsson, J. E. Han, E. Koch and V. H. Crespi, in *Superconductivity in Complex Systems*, eds. K. A. Müller and A. Bussmann-Holder, Springer Berlin Heidelberg, 2005, vol. 114, ch. 3, pp. 71-101.
11. I. B. Bersuker, *Electronic Structure and Properties of Transition Metal Compounds*, John Wiley & Sons, Inc., 2010.
12. R. G. Pearson, *Symmetry Rules for Chemical reactions*, A Willey-Interscience Publication, 1976.
13. J. G. Bednorz and K. A. Müller, *Zeitschrift für Physik B Condensed Matter*, 1986, **64**, 189-193.
14. J. G. Bednorz and K. A. Müller, *Angewandte Chemie*, 1988, **100**, 757-770.
15. V. V. Gudkov and I. B. Bersuker, in *Vibronic Interactions and the Jahn-Teller Effect*, eds. M. Atanasov, C. Daul and P. L. W. Tregenna-Piggott, Springer Netherlands, 2012, vol. 23, ch. 7, pp. 143-161.
16. R. M. Dreizler and E. K. U. Gross, *Density Functional Theory, An Approach to Quantum Many-Body Problem*, Springer -Verlag, Berlin, Heidelberg, New York, London, Paris, Tokyo, Hong Kong, Barcelona, 1990.
17. R. G. Parr and Y. Weitao, *Density-Functional Theory of Atoms and Molecules (International Series of Monographs on Chemistry)*, Oxford University Press, 1994.
18. R. Bruyndonckx, C. Daul, P. T. Manoharan and E. Deiss, *Inorganic Chemistry*, 1997, **36**, 4251-4256.
19. M. Zlatar, C.-W. Schläpfer and C. Daul, in *The Jahn-Teller Effect*, eds. H. Köppel, D. R. Yarkony and H. Barentzen, Springer Berlin Heidelberg, 2009, vol. 97, ch. 6, pp. 131-165.
20. M. Gruden-Pavlović, P. García-Fernández, L. Andjelković, C. Daul and M. Zlatar, *The Journal of Physical Chemistry A*, 2011, **115**, 10801-10813.
21. H. Ramanantoanina, M. Zlatar, P. Garcia-Fernandez, C. Daul and M. Gruden-Pavlovic, *Physical Chemistry Chemical Physics*, 2013, **15**, 1252-1259.
22. M. Zlatar, M. Gruden-Pavlović, C.-W. Schläpfer and C. Daul, *Journal of Molecular Structure: THEOCHEM*, 2010, **954**, 86-93.
23. I. B. Bersuker and V. Z. Polinger, *Vibronic interactions in Molecules and Crystals*, Springer-Verlag, Berlin, 1989.
24. M. Born and J. R. Oppenheimer, *Annals of Physics*, 1927, **84**, 457–484.
25. H. Hellmann, *Einführung in die Quantenchemie*, Franz Deuticke, Leipzig, 1937.
26. R. P. Feynman, *Physical Review*, 1939, **56**, 340-343.
27. W. L. Clinton and B. Rice, *The Journal of Chemical Physics*, 1959, **30**, 542-546.

28. J. M. García-Lastra, M. T. Barriuso, J. A. Aramburu and M. Moreno, *Chemical Physics*, 2005, **317**, 103-110.
29. A. Ceulemans, D. Beyens and L. G. Vanquickenborne, *Journal of the American Chemical Society*, 1984, **106**, 5824-5837.
30. A. Ceulemans and L. G. Vanquickenborne, in *Stereochemistry and Bonding*, Springer Berlin Heidelberg, 1989, vol. 71, ch. 4, pp. 125-159.
31. C. A. Coulson and R. P. Bell, *Transactions of the Faraday Society*, 1945, **41**, 141-149.
32. P. Garcia-Fernandez and I. B. Bersuker, *International Journal of Quantum Chemistry*, 2012, **112**, 3025-3032.
33. P. Garcia-Fernandez, J. A. Aramburu and M. Moreno, *Physical Review B*, 2011, **83**, 174406.
34. W. Domcke, H. Köppel and L. S. Cederbaum, *Molecular Physics*, 1981, **43**, 851-875.
35. P. García-Fernández, I. B. Bersuker, J. A. Aramburu, M. T. Barriuso and M. Moreno, *Physical Review B*, 2005, **71**, 184117.
36. P. García-Fernández and I. B. Bersuker, *Physical Review Letters*, 2011, **108**, 246406
37. H. Nakatsuji, *Journal of the American Chemical Society*, 1974, **96**, 30-37.
38. W. Hug and M. Fedorovsky, *Theoretical Chemistry Accounts*, 2008, **119** 113-131.
39. M. Bacci, *Physical Review B*, 1978, **17**, 4495- 4498.
40. F. Duschinsky, *Acta physicochimica URSS*, 1937, **7**, 551–566.
41. C. J. Cramer, *Essentials of Computational Chemistry: Theories and Models, 2nd Edition*, John Wiley & Sons, Ltd, England, 2004.
42. P. Garcia-Fernandez, A. Trueba, M. T. Barriuso, J. A. Aramburu and M. Moreno, in *Vibronic Interactions and the Jahn-Teller Effect*, eds. M. Atanasov, C. Daul and P. L. W. Tregenna-Piggott, Springer Netherlands, 2012, vol. 23, ch. 6, pp. 105-142.
43. P. H. P. Harbach and A. Dreuw, *Chemical Physics*, 2010, **377**, 78-85.
44. P. Mondal, D. Opalka, L. V. Poluyanov and W. Domcke, *The Journal of Chemical Physics*, 2012, **136**, 084308.
45. M. J. Paterson, M. J. Bearpark, M. A. Robb, L. Blancafort and G. A. Worth, *Physical Chemistry Chemical Physics*, 2005, **7**, 2100-2115.
46. E. J. Baerends and O. V. Gritsenko, *The Journal of Physical Chemistry A*, 1997, **101**, 5383-5403.
47. P. Geerlings, F. De Proft and W. Langenaeker, *Chemical Reviews*, 2003, **103**, 1793-1874.
48. R. Stowasser and R. Hoffmann, *Journal of the American Chemical Society*, 1999, **121**, 3414-3420.
49. G. te Velde, F. M. Bickelhaupt, S. J. A. van Gisbergen, C. F. Guerra, E. J. Baerends, J. G. Snijders and T. Ziegler, *Journal of Computational Chemistry*, 2001, **22**, 931–967.
50. W. Koch and M. C. Holthausen, *A Chemist's Guide to Density Functional Theory, 2nd Edition*, Wiley-VCH, 2001.
51. T. Ziegler, *Chemical Reviews*, 1991, **91**, 651-667.
52. L. H. Thomas, *Mathematical Proceedings of the Cambridge Philosophical Society*, 1927, **23**, 542-548.
53. E. Fermi, *Rendiconti Accademia Nazionale dei Lincei*, 1927, **6**, 602–607.
54. P. A. M. Dirac, *Mathematical Proceedings of the Cambridge Philosophical Society*, 1930, **26**, 376-385.
55. E. Wigner, *Physical Review*, 1932, **40**, 749-759.
56. J. C. Slater, *Physical Review*, 1951, **81**, 385-390.
57. P. Hohenberg and W. Kohn, *Physical Review*, 1964, **136**, B864-B871.
58. W. Kohn and L. J. Sham, *Physical Review*, 1965, **140**, A1133-A1138.
59. A. J. Cohen, P. Mori-Sánchez and W. Yang, *Science*, 2008, **321**, 792-794.

60. J. P. Perdew and K. Schmidt, *AIP Conference Proceedings*, 2001, **577**, 1-20.
61. S. H. Vosko, L. Wilk and M. Nusair, *Canadian Journal of Physics*, 1980, **58**, 1200-1211.
62. D. M. Ceperley and B. J. Alder, *Physical Review Letters*, 1980, **45**, 566-569.
63. A. D. Becke, *Physical Review A*, 1988, **38**, 3098-3100.
64. J. P. Perdew, *Physical Review B*, 1986, **33**, 8822-8824.
65. M. Swart, A. W. Ehlers and K. Lammertsma, *Molecular Physics*, 2004, **102**, 2467-2474.
66. Y. Zhao and D. G. Truhlar, *Journal of Chemical Theory and Computation*, 2005, **1**, 415-432.
67. Y. Zhao and D. G. Truhlar, *The Journal of Physical Chemistry A*, 2005, **109**, 5656-5667.
68. J. Heyd, J. E. Peralta, G. E. Scuseria and R. L. Martin, *The Journal of Chemical Physics*, 2005, **123**, 174101.
69. E. N. Brothers, A. F. Izmaylov, J. O. Normand, V. Barone and G. E. Scuseria, *The Journal of Chemical Physics*, 2008, **129**, 011102.
70. H. J. Wörner and F. Merkt, *Angewandte Chemie International Edition*, 2009, **48**, 6404-6424.
71. A. J. Cohen, P. Mori-Sánchez and W. Yang, *Chemical Reviews*, 2012, **112**, 289-320.
72. I. B. Bersuker, *Journal of Computational Chemistry*, 1997, **18**, 260-267.
73. I. G. Kaplan, *Journal of Molecular Structure*, 2007, **838**, 39-43.
74. M. Atanasov and C. Daul, *CHIMIA*, 2005, **59**, 504-510.
75. M. Levy, *International Journal of Quantum Chemistry*, 2010, **110**, 3140-3144.
76. A. K. Theophilou, *J. Phys. C: Solid State Phys.*, 1979 **12** 5419.
77. A. K. Theophilou and P. G. Papaconstantinou, *Physical Review A*, 2000, **61**, 022502.
78. L. Andjelković, M. Gruden-Pavlović, C. Daul and M. Zlatar, *International Journal of Quantum Chemistry*, 2013, **113**, 859-864.
79. H. Ramanantoanina, M. Gruden-Pavlovic, M. Zlatar and C. Daul, *International Journal of Quantum Chemistry*, 2013, **113**, 802-807.
80. M. Zlatar, C.-W. Schläpfer, E. P. Fowe and C. A. Daul, *Pure and Applied Chemistry*, 2009, **81**, 1397-1411.
81. S. G. Wang and W. H. E. Schwarz, *The Journal of Chemical Physics*, 1996, **105**, 4641-4648.
82. P. R. T. Schipper, O. V. Gritsenko and E. J. Baerends, *Theoretical Chemistry Accounts*, 1998, **99**, 329-343.
83. Y. Zhang and W. Yang, *The Journal of Chemical Physics*, 1998, **109**, 2604-2608.
84. H. Chermette, *Coordination Chemistry Reviews*, 1998, **178–180, Part 1**, 699-721.
85. C. Daul, *International Journal of Quantum Chemistry*, 1994, **52**, 867-877.
86. C. Daul, E. J. Baerends and P. Vernooijs, *Inorganic Chemistry*, 1994, **33**, 3538-3543.
87. M. Atanasov, C. A. Daul and C. Rauzy, in *Optical Spectra and Chemical Bonding in Inorganic Compounds*, eds. D. Mingos and T. Schönherr, Springer Berlin Heidelberg, 2004, vol. 106, ch. 8, pp. 97-125.
88. M. A. L. Marques and E. K. U. Gross, *Annual Review of Physical Chemistry*, 2004, **55**, 427-455.
89. F. Furche and K. Burke, in *Annual Reports in Computational Chemistry*, ed. C. S. David, Elsevier, 2005, vol. Volume 1, pp. 19-30.
90. E. Runge and E. K. U. Gross, *Physical Review Letters*, 1984, **52**, 997-1000.
91. E. K. U. Gross and W. Kohn, in *Advances in Quantum Chemistry*, ed. L. Per-Olov, Academic Press, 1990, vol. Volume 21, pp. 255-291.

92. P. Elliott, F. Furche and K. Burke, in *Reviews in Computational Chemistry*, John Wiley & Sons, Inc., 2009, DOI: 10.1002/9780470399545.ch3, pp. 91-165.
93. Á. Nagy, *Physical Review A*, 1998, **57**, 1672-1677.
94. M. E. Casida and M. Huix-Rotllant, *Annual Review of Physical Chemistry*, 2012, **63**, 287-323.
95. M. E. Casida, in *Recent Advances in Density Functional Methods (Part I)*, ed. D. P. Chong, Singapore: World Sci., 1995, vol. 1, pp. 155-192.
96. A. Rosa, G. Ricciardi, E. J. Baerends, M. Zimin, M. A. J. Rodgers, S. Matsumoto and N. Ono, *Inorganic Chemistry*, 2005, **44**, 6609-6622.
97. K. A. Nguyen, P. N. Day and R. Pachter, *The Journal of Physical Chemistry A*, 2009, **113**, 13943-13952.
98. S. J. A. van Gisbergen, J. A. Groeneveld, A. Rosa, J. G. Snijders and E. J. Baerends, *The Journal of Physical Chemistry A*, 1999, **103**, 6835-6844.
99. D. Jacquemin, B. Mennucci and C. Adamo, *Physical Chemistry Chemical Physics*, 2011, **13**, 16987-16998.
100. Z. Pawlowska, A. Lietard, S. Aloise, M. Sliwa, A. Idrissi, O. Poizat, G. Buntinx, S. Delbaere, A. Perrier, F. Maurel, P. Jacques and J. Abe, *Physical Chemistry Chemical Physics*, 2011, **13**, 13185-13195.
101. J. Autschbach, F. E. Jorge and T. Ziegler, *Inorganic Chemistry*, 2003, **42**, 2867-2877.
102. Y.-M. Sang, L.-K. Yan, N.-N. Ma, J.-P. Wang and Z.-M. Su, *The Journal of Physical Chemistry A*, 2013, **117**, 2492-2498.
103. M. E. Casida, B. Natarajan and T. Deutsch, in *Fundamentals of Time-Dependent Density Functional Theory*, eds. M. A. L. Marques, N. T. Maitra, F. M. S. Nogueira, E. K. U. Gross and A. Rubio, Springer Berlin Heidelberg, 2012, vol. 837, ch. 14, pp. 279-299.
104. E. Tapavicza, I. Tavernelli and U. Rothlisberger, *Physical Review Letters*, 2007, **98**, 023001.
105. M. Barbatti, J. Pittner, M. Pederzoli, U. Werner, R. Mitrić, V. Bonačić-Koutecký and H. Lischka, *Chemical Physics*, 2010, **375**, 26-34.
106. R. Send and F. Furche, *The Journal of Chemical Physics*, 2010, **132**, 044107.
107. E. Tapavicza, I. Tavernelli, U. Rothlisberger, C. Filippi and M. E. Casida, *The Journal of Chemical Physics*, 2008, **129**, 124108.
108. M. E. Casida and T. A. Wesołowski, *International Journal of Quantum Chemistry*, 2004, **96**, 577-588.
109. C. Konig and J. Neugebauer, *Physical Chemistry Chemical Physics*, 2011, **13**, 10475-10490.
110. J. Neugebauer, *The Journal of Physical Chemistry B*, 2008, **112**, 2207-2217.
111. A. Dreuw and M. Head-Gordon, *Journal of the American Chemical Society*, 2004, **126**, 4007-4016.
112. P. J. Aittala, O. Cramariuc, T. I. Hukka, M. Vasilescu, R. Bandula and H. Lemmetyinen, *The Journal of Physical Chemistry A*, 2010, **114**, 7094-7101.
113. A. R. Katritzky, *Chemical Reviews*, 2004, **104**, 2125-2126.
114. P. J. Garrat, *Aromaticity*, Wiley, New York, 1986.
115. V. I. Minkin, M. N. Glukhovtsev and B. Y. Simkin, *Aromaticity and Antiaromaticity: Electronic and Structural Aspects*, Wiley, New York, 1994.
116. P. v. R. Schleyer, *Chemical Reviews*, 2005, **105**, 3433-3435.
117. P. v. R. Schleyer, *Chemical Reviews*, 2001, **101**, 1115-1118.
118. E. Hückel, *Z. Physik*, 1931, **70**, 204-286.
119. E. Hückel, *Z. Physik*, 1932, **78**, 628-648.
120. A. D. Allen and T. T. Tidwell, *Chemical Reviews*, 2001, **101**, 1333-1348.

121. A. C. Tsipis, *Physical Chemistry Chemical Physics*, 2009, **11**, 8244-8261.
122. A. E. Kuznetsov, H.-J. Zhai, L.-S. Wang and A. I. Boldyrev, *Inorganic Chemistry*, 2002, **41**, 6062-6070.
123. L. Andjelković, M. Perić, M. Zlatar, S. Grubišić and M. Gruden-Pavlović, *Tetrahedron Lett.*, 2012, **53**, 794-799.
124. P. v. R. Schleyer and H. Jiao, *Pure and Applied Chemistry*, 1996, **68**, 209-218.
125. Z. Chen, C. S. Wannere, C. Corminboeuf, R. Puchta and P. v. R. Schleyer, *Chemical Reviews*, 2005, **105**, 3842-3888.
126. P. von Ragué Schleyer, M. Manoharan, Z.-X. Wang, B. Kiran, H. Jiao, R. Puchta and N. J. R. van Eikema Hommes, *Organic Letters*, 2001, **3**, 2465-2468.
127. A. R. Katritzky, K. Jug and D. C. Oniciu, *Chemical Reviews*, 2001, **101**, 1421-1450.
128. J. A. N. F. Gomes and R. B. Mallion, *Chemical Reviews*, 2001, **101**, 1349-1384.
129. C. Corminboeuf, R. B. King and P. v. R. Schleyer, *ChemPhysChem*, 2007, **8**, 391 – 398.
130. D. Y. Zubarev and A. I. Boldyrev, *Phys. Chem. Chem. Phys.*, 2008, **10**, 5207–5217.
131. P. v. R. Schleyer, C. Maerker, A. Dransfeld, H. Jiao and N. J. R. van Eikema Hommes, *Journal of the American Chemical Society*, 1996, **118**, 6317-6318.
132. C. Corminboeuf, T. Heine, G. Seifert, P. v. R. Schleyer and J. Weber, *Physical Chemistry Chemical Physics*, 2004, **6**, 273-276.
133. V. Gogonea, P. v. R. Schleyer and P. R. Schreiner, *Angewandte Chemie International Edition in English*, 1998, **37**, 1945-1948.
134. H. Jiao and P. v. R. Schleyer, *Journal of Physical Organic Chemistry*, 1998, **11**, 655-662.
135. D. Ajami, O. Oeckler, A. Simon and R. Herges, *Nature*, 2003, **426**, 819-821.
136. Z. Chen and R. B. King, *Chemical Reviews*, 2005, **105**, 3613-3642.
137. H. Masui, *Coordination Chemistry Reviews*, 2001, **219–221**, 957-992.
138. J. E. Maslowsky, *Coordination Chemistry Reviews*, 2011, **255**, 2746– 2763.
139. F. Feixas, E. Matito, J. Poater and M. Solà, in *Metalloaromaticity. WIREs Comput. Mol. Sci.*, ed. P. R. Schreiner, Wiley, 2013, vol. 3(2), pp. 105–122.
140. T. O. Pullerits and V. Sundström, *Advanced Materials*, 2001, **13**, 1053–1067.
141. T. O. Pullerits and V. Sundström, *Accounts of Chemical Research*, 1996, **29**, 381–389.
142. A. C. Grimsdale and K. Müllen, *Angewandte Chemie International Edition*, 2005, **44**, 5592–5629.
143. J. C. Sancho-García and A. J. Pérez-Jiménez, *The Journal of Chemical Physics*, 2008, **129**, 024103.
144. A. Damjanović, I. Kosztin, U. Kleinekathöfer and K. Schulten, *Physical Review B*, 2002, **65**, 031919.
145. A. Hadipour, B. de Boer, J. Wildeman, F. Kooistra, J. Hummelen, M. Turbiez, M. Wienk, R. Janssen and P. Blom, *Advanced Functional Materials*, 2006, **16**, 1897–1903.
146. G. Gustafsson, Y. Cao, G. M. Treacy, F. Klavetter, N. Colaneri and A. J. Heeger, *Nature*, 1992, **357**, 477–479.
147. C. J. Brabec, A. Cravino, D. Meissner, N. S. Sariciftci, T. Fromherz, M. T. Rispens, L. Sanchez and J. C. Hummelen, *Advanced Functional Materials*, 2001, **11**, 374–380.
148. K. M. Coakley and M. D. McGehee, *Chemistry of Materials*, 2004, **16**, 4533–4542.
149. S. R. Forrest, *Chemical Reviews*, 1997, **97**, 1793–1896.
150. P. Peumans, A. Yakimov and S. R. Forrest, *Journal of Applied Physics*, 2003, **93**, 3693–3723.
151. J.-L. Brédas, D. Beljonne, V. Coropceanu and J. Cornil, *Chemical Reviews*, 2004, **104**, 4971-5004.
152. J.-L. Brédas, J. Cornil and A. J. Heeger, *Advanced Materials*, 1996, **8**, 447–452.

153. S. E. Shaheen, G. E. Jabbour, B. Kippelen, N. Peyghambarian, J. D. Anderson, S. R. Marder, N. R. Armstrong, E. Bellmann and R. H. Grubbs, *Applied Physics Letters*, 1999, **74**, 3212–3214.
154. H. E. Katz, A. J. Lovinger, J. Johnson, C. Kloc, T. Siegrist, W. Li, Y. Y. Lin and A. Dodabalapur, *Nature*, 2000, **404**, 478–481.
155. Z. Bao, *Advanced Materials*, 2000, **12**, 227–230.
156. S.-B. Rim, R. F. Fink, J. C. Schöneboom, P. Erk and P. Peumans, *Applied Physics Letters*, 2007, **91**, 173504.
157. A. Dreuw, G. R. Fleming and M. Head-Gordon, *The Journal of Physical Chemistry B*, 2003, **107**, 6500.
158. P. H. P. Harbach and A. Dreuw, *Chemical Physics*, 2010, **377**, 78–85.
159. W.Zinth and J. Wachveitl, *ChemPhysChem*, 2005, **6**, 871.
160. V. May and O. Kühn, *Charge and Energy Transfer Dynamics in Molecular Systems*, Wiley-VCH, Weinheim, 3rd edn., 2011.
161. S. Mukamel, D. S. Franchi and R. F. Loring, *Chemical Physics*, 1988, **128**, 99-123.
162. E. Hennebicq, G. Pourtois, G. D. Scholes, L. M. Herz, D. M. Russell, C. Silva, S. Setayesh, A. C. Grimsdale, K. Müllen, J.-L. Brédas and D. Beljonne, *Journal of the American Chemical Society*, 2005, **127**, 4744-4762.
163. T. Förster, *Annalen der Physik*, 1948, **437**, 55-75.
164. T. Förster, in *Modem Quantum Chemistry, Istanbul lectures, Part III: Action of light and organic crystals*, ed. O. Sinanoglu, Academic Press, Inc., New York, 1965, pp. 97-137.
165. P. Petelenz, *Chemical Physics Letters*, 1977, **47**, 603-605.
166. P. Ottiger, S. Leutwyler and H. V. Köppel, *The Journal of Chemical Physics*, 2012, **136**, 174308.
167. P. Ottiger, S. Leutwyler and H. Köppel, *The Journal of Chemical Physics*, 2009, **131**, 204308.
168. S. Polyutov, O. Kühn and T. Pullerits, *ChemPhysChem*, 2012, **394**, 21-28.
169. H.-M. Wu, M. Ratsep, I.-J. Lee, R. J. Cogdell and G. J. Small, *The Journal of Physical Chemistry B*, 1997, **101**, 7654-7663.
170. V. I. Novoderezhkin, M. A. Palacios, H. van Amerongen and R. van Grondelle, *Journal of Physical Chemistry B*, 2004, **108**, 10363-10375.
171. I. B. Bersuker, *The Jahn-Teller Effect*, Cambridge University Press, 2006.
172. S. F. Sousa, P. A. Fernandes and M. J. Ramos, *The Journal of Physical Chemistry A*, 2007, **111**, 10439-10452.
173. A. Rodríguez-Fortea, P. Alemany, S. Alvarez and E. Ruiz, *Inorganic Chemistry*, 2002, **41**, 3769-3778.
174. S. Kababya, J. Nelson, C. Calle, F. Neese and D. Goldfarb, *Journal of the American Chemical Society*, 2006, **128**, 2017-2029.
175. M. Swart and F. M. Bickelhaupt, *Journal of Computational Chemistry*, 2008, **29**, 724-734.
176. M. R. Bray, R. J. Deeth, V. J. Paget and P. D. Sheen, *International Journal of Quantum Chemistry*, 1997, **61**, 85-91.
177. N. I. Gidopoulos, P. G. Papaconstantinou and E. K. U. Gross, *Physical Review Letters*, 2002, **88**, 033003.
178. C. Lee, W. Yang and R. G. Parr, *Physical Review B*, 1988, **37**, 785.
179. A. D. Becke, *Journal of Chemical Physics*, 1993, **98**, 5648-5652.
180. P. J. Stephens, F. J. Devlin, C. F. Chabalowski and M. J. Frisch, *The Journal of Physical Chemistry*, 1994, **98**, 11623-11627.
181. S. Saddique and G. A. Worth, *Chemical Physics*, 2006, **329**, 99-108.

182. B. E. Applegate, T. A. Miller and T. A. Barckholtz, *The Journal of Chemical Physics*, 2001, **114**, 4855-4868.
183. T. Ichino, S. W. Wren, K. M. Vogelhuber, A. J. Gianola, W. C. Lineberger and J. F. Stanton, *The Journal of Chemical Physics*, 2008, **129**, 084310.
184. B. E. Applegate and T. A. Miller, *The Journal of Chemical Physics*, 2002, **117**, 10654-10674.
185. K. Tokunaga, T. Sato and K. Tanaka, *The Journal of Chemical Physics*, 2006, **124**, 154303.
186. V. Perebeinos, P. B. Allen and M. Pederson, *Physical Review A*, 2005, **72**, 012501.
187. I. Sioutis, V. L. Stakhursky, G. Tarczay and T. A. Miller, *The Journal of Chemical Physics*, 2008, **128**, 084311.
188. J. Paier, M. Marsman and G. Kresse, *The Journal of Chemical Physics*, 2007, **127**, 024103.
189. R. Lindner, K. Müller-Dethlefs, E. Wedum, K. Haber and E. R. Grant, *Science*, 1996, **271**, 1698-1702.
190. W. T. Borden, E. R. Davidson and D. Feller, *Journal of the American Chemical Society*, 1981, **103**, 5725-5729.
191. M. Roeselová, T. Bally, P. Jungwirth and P. Čársky, *Chemical Physics Letters*, 1995, **234**, 395-404.
192. B. E. Applegate, A. J. Bezant and T. A. Miller, *The Journal of Chemical Physics*, 2001, **114**, 4869-4882.
193. S. Zilberg and Y. Haas, *Journal of the American Chemical Society*, 2002, **124**, 10683-10691.
194. T. Sato, K. Tokunaga and K. Tanaka, *The Journal of Chemical Physics*, 2006, **124**, 024314.
195. H. J. Silverstone, D. E. Wood and H. M. McConnell, *The Journal of Chemical Physics*, 1964, **41**, 2311-2323.
196. R. F. Gunion, W. Karney, P. G. Wenthold, W. T. Borden and W. C. Lineberger, *Journal of the American Chemical Society*, 1996, **118**, 5074-5082.
197. E. P. F. Lee and T. G. Wright, *The Journal of Physical Chemistry A*, 1998, **102**, 4007-4013.
198. T. Pino, F. Güthe, H. Ding and J. P. Maier, *The Journal of Physical Chemistry A*, 2002, **106**, 10022-10026.
199. T. Yamabe, K. Yahara, T. Kato and K. Yoshizawa, *The Journal of Physical Chemistry A*, 2000, **104**, 589-595.
200. T. Sato, A. Yamamoto and T. Yamabe, *The Journal of Physical Chemistry A*, 2000, **104**, 130-137.
201. T. Sato, Y. Kuzumoto, K. Tokunaga, H. Tanaka and H. Imahori, in *Advances in Quantum Chemistry*, Academic Press, 2003, vol. Volume 44, pp. 239-255.
202. T. Kato, K. Yoshizawa and T. Yamabe, *The Journal of Chemical Physics*, 1999, **110**, 249-255.
203. T. Sato, H. Tanaka, A. Yamamoto, Y. Kuzumoto and K. Tokunaga, *Chemical Physics*, 2003, **287**, 91-102.
204. M. Sato, K. Yamamoto, H. Sonobe, K. Yano, H. Matsubara, H. Fujita, T. Sugimoto and K. Yamamoto, *Journal of the Chemical Society, Perkin Transactions 2*, 1998, DOI: 10.1039/A803306D, 1909-1914.
205. H. von Busch, V. Dev, H. A. Eckel, S. Kasahara, J. Wang, W. Demtröder, P. Sebald and W. Meyer, *Physical Review Letters*, 1998, **81**, 4584-4587.
206. J. Gaus, K. Kobe, V. Bonacic-Koutecky, H. Kuehling, J. Manz, B. Reischl, S. Rutz, E. Schreiber and L. Woeste, *The Journal of Physical Chemistry*, 1993, **97**, 12509-12515.

207. S. P. Walch, C. W. Bauschlicher and S. R. Langhoff, *The Journal of Chemical Physics*, 1986, **85**, 5900-5907.
208. K. Balasubramanian and M. Z. Liao, *Chemical Physics*, 1988, **127**, 313-324.
209. J. A. Howard, K. F. Preston and B. Mile, *Journal of the American Chemical Society*, 1981, **103**, 6226-6227.
210. J. A. Howard, R. Sutcliffe and B. Mile, *Surface Science*, 1985, **156, Part 1**, 214-227.
211. K. Knox, *The Journal of Chemical Physics*, 1959, **30**, 991-993.
212. H. G. von Schnering, *Zeitschrift für anorganische und allgemeine Chemie*, 1967, **353**, 1-12.
213. H. G. von Schnering, *Zeitschrift für anorganische und allgemeine Chemie*, 1967, **353**, 13-25.
214. P. J. Ellis, H. C. Freeman, M. A. Hitchman, D. Reinen and B. Wagner, *Inorganic Chemistry*, 1994, **33**, 1249-1250.
215. D. Reinen and M. A. Hitchman, *Journal*, 1997, **200**, 11.
216. H. Stratemeier, B. Wagner, E. R. Krausz, R. Linder, H. H. Schmidtke, J. Pebler, W. E. Hatfield, L. ter Haar, D. Reinen and M. A. Hitchman, *Inorganic Chemistry*, 1994, **33**, 2320-2329.
217. P. García-Fernández, M. Moreno and J. A. Aramburu, *The Journal of Physical Chemistry C*, 2014, **118**, 7554-7561.
218. L. Dubicki, M. J. Riley and E. R. Krausz, *The Journal of Chemical Physics*, 1994, **101**, 1930-1938.
219. M. J. Riley, L. Dubicki, G. Moran, E. R. Krausz and I. Yamada, *Inorganic Chemistry*, 1990, **29**, 1614-1626.
220. W. Kleemann and Y. Farge, *Journal de Physique Lettres*, 1974, **35**, 135-137.
221. R. Haegele and D. Babel, *Zeitschrift für anorganische und allgemeine Chemie*, 1974, **409**, 11-22.
222. W. Massa and D. Babel, *Chemical Reviews*, 1988, **88**, 275-296.
223. D. Reinen, M. Atanasov, P. Köhler and D. Babel, *Coordination Chemistry Reviews*, 2010, **254**, 2703 – 2754.
224. I. Diaz-Acosta, J. Baker, J. F. Hinton and P. Pulay, *Spectrochimica Acta Part A: Molecular and Biomolecular Spectroscopy*, 2003, **59**, 363-377.
225. B. R. Stults, R. S. Marianelli and V. W. Day, *Inorganic Chemistry*, 1979, **18**, 1853-1858.
226. T. K. Kundu, R. Bruyndonckx, C. Daul and P. T. Manoharan, *Inorganic Chemistry*, 1999, **38**, 3931–3934.
227. J. H. Ammeter, L. Zoller, J. Bachmann, P. Baltzer, E. Gamp, R. Bucher and E. Deiss, *Helvetica Chimica Acta*, 1981, **64**, 1063-1082.
228. E. J. Baerends, J. Autschbach, A. Bérces, J. A. Berger, F. M. Bickelhaupt, C. Bo, P. L. de Boeij, P. M. Boerrigter, L. Cavallo, D. P. Chong, L. Deng, R. M. Dickson, D. E. Ellis, M. van Faassen, L. Fan, T. H. Fischer, C. Fonseca Guerra, S. J. A. van Gisbergen, J. A. Groeneveld, O. V. Gritsenko, M. Grüning, F. E. Harris, P. van den Hoek, C. R. Jacob, H. Jacobsen, L. Jensen, E. S. Kadantsev, G. van Kessel, R. Klooster, F. Kootstra, E. van Lenthe, D. A. McCormack, A. Michalak, J. Neugebauer, V. P. Nicu, V. P. Osinga, S. Patchkovskii, P. H. T. Philipsen, D. Post, C. C. Pye, W. Ravenek, P. Romaniello, P. Ros, P. R. T. Schipper, G. Schreckenbach, J. G. Snijders, M. Solà, M. Swart, D. Swerhone, G. teVelde, P. Vernooijs, L. Versluis, L. Visscher, O. Visser, F. Wang, T. A. Wesolowski, E. M. van Wezenbeek, G. Wiesenekker, S. K. Wolff, T. K. Woo, A. L. Yakovlev and T. Ziegler, *ADF2010.01.*, SCM, Theoretical Chemistry, Vrije Universiteit Amsterdam, Amsterdam, The Netherlands, 2010.

229. C. F. Guerra, J. G. Snijders, G. teVelde and E. Baerends, *Theoretical Chemistry Accounts*, 1998, **99**, 391-403.
230. G. te Velde, F. M. Bickelhaupt, E. J. Baerends, C. Fonseca Guerra, S. J. A. van Gisbergen, J. G. Snijders and T. Ziegler, *Journal of Computational Chemistry*, 2001, **22**, 931-967.
231. A. Bérces, R. M. Dickson, L. Fan, H. Jacobsen, D. Swerhone and T. Ziegler, *Computer Physics Communications*, 1997, **100**, 247-262.
232. H. Jacobsen, A. Bérces, D. P. Swerhone and T. Ziegler, *Computer Physics Communications*, 1997, **100**, 263-276.
233. A. Klamt and G. Schuurmann, *Journal of the Chemical Society, Perkin Transactions 2*, 1993, DOI: 10.1039/P29930000799, 799-805.
234. A. Klamt, *The Journal of Physical Chemistry*, 1995, **99**, 2224-2235.
235. A. Klamt and V. Jonas, *The Journal of Chemical Physics*, 1996, **105**, 9972-9981.
236. C. C. Pye and T. Ziegler, *Theoretical Chemistry Accounts*, 1999, **101**, 396-408.
237. V. P. Khlopin, V. Z. Polinger and I. B. Bersuker, *Theoretica chimica acta*, 1978, **48**, 87-101.
238. E. J. Baerends, J. Autschbach, A. Bérces, J. A. Berger, F. M. Bickelhaupt, C. Bo, P. L. de Boeij, P. M. Boerrigter, L. Cavallo, D. P. Chong, L. Deng, R. M. Dickson, D. E. Ellis, M. van Faassen, L. Fan, T. H. Fischer, C. Fonseca Guerra, S. J. A. van Gisbergen, J. A. Groeneveld, O. V. Gritsenko, M. Grüning, F. E. Harris, P. van den Hoek, C. R. Jacob, H. Jacobsen, L. Jensen, E. S. Kadantsev, G. van Kessel, R. Klooster, F. Kootstra, E. van Lenthe, D. A. McCormack, A. Michalak, J. Neugebauer, V. P. Nicu, V. P. Osinga, S. Patchkovskii, P. H. T. Philipsen, D. Post, C. C. Pye, W. Ravenek, P. Romaniello, P. Ros, P. R. T. Schipper, G. Schreckenbach, J. G. Snijders, M. Solà, M. Swart, D. Swerhone, G. teVelde, P. Vernooijs, L. Versluis, L. Visscher, O. Visser, F. Wang, T. A. Wesolowski, E. M. van Wezenbeek, G. Wiesenekker, S. K. Wolff, T. K. Woo, A. L. Yakovlev and T. Ziegler, *ADF2013.01*, SCM, Theoretical Chemistry, Vrije Universiteit Amsterdam, Amsterdam, The Netherlands, 2013.
239. M. Swart and F. M. Bickelhaupt, *J. Comput. Chem.*, 2008, ***29***, 724-734.
240. K. Ruedenberg, *Reviews of Modern Physics*, 1962, **34**, 326-376.
241. M. J. Feinberg and K. Ruedenberg, *The Journal of Chemical Physics*, 1971, **54**, 1495-1511.
242. T. Bitter, K. Ruedenberg and W. H. E. Schwarz, *Journal of Computational Chemistry*, 2007, **28**, 411-422.
243. R. J. Boyd, *Nature*, 1984, **310**, 480-481.
244. A. Zhong and S. Liu, *Journal of Theoretical and Computational Chemistry*, 2005, **04**, 833-847.
245. T. Oyamada, K. Hongo, Y. Kawazoe and H. Yasuhara, *The Journal of Chemical Physics*, 2010, **133**, 164113.
246. H. Ichikawa and Y. Ebisawa, *Journal of the American Chemical Society*, 1985, **107**, 1161-1165.
247. H. Ichikawa and H. Kagawa, *The Journal of Physical Chemistry*, 1995, **99**, 2307-2311.
248. C. Rong, S. Lian, D. Yin, B. Shen, A. Zhong, L. Bartolotti and S. Liu, *The Journal of Chemical Physics*, 2006, **125**, 174102.
249. A. Toyota and S. Koseki, *The Journal of Physical Chemistry*, 1996, **100**, 2100-2106.
250. S. Koseki and A. Toyota, *The Journal of Physical Chemistry A*, 1997, **101**, 5712-5718.
251. A. Toyota and S. Koseki, *The Journal of Physical Chemistry A*, 1998, **102**, 490-495.
252. A. Toyota and S. Koseki, *The Journal of Physical Chemistry A*, 1998, **102**, 6668-6675.
253. A. Toyota, S. Koseki and M. Shiota, *The Journal of Physical Chemistry A*, 2000, **104**, 5343-5350.

254. A. Toyota, M. Shiota, Y. Nagae and S. Koseki, *The Journal of Physical Chemistry A*, 2001, **105**, 1334-1342.
255. A. Toyota, S. Koseki, H. Umeda, M. Suzuki and K. Fujimoto, *The Journal of Physical Chemistry A*, 2003, **107**, 2749-2756.
256. S. Liu, *The Journal of Chemical Physics*, 2007, **126**, 244103.
257. S. Liu, N. Govind and L. G. Pedersen, *The Journal of Chemical Physics*, 2008, **129**, 094104.
258. S. Liu and N. Govind, *The Journal of Physical Chemistry A*, 2008, **112**, 6690-6699.
259. İ. Uğur, F. De Vleeschouwer, N. Tüzün, V. Aviyente, P. Geerlings, S. Liu, P. W. Ayers and F. De Proft, *The Journal of Physical Chemistry A*, 2009, **113**, 8704-8711.
260. S. Liu, H. Hu and L. G. Pedersen, *The Journal of Physical Chemistry A*, 2010, **114**, 5913-5918.
261. D. H. Ess, S. Liu and F. De Proft, *The Journal of Physical Chemistry A*, 2010, **114**, 12952-12957.
262. Y. Huang, A.-G. Zhong, Q. Yang and S. Liu, *The Journal of Chemical Physics*, 2011, **134**, 084103.
263. R. J. Boyd, K. V. Darvesh and P. D. Fricker, *The Journal of Chemical Physics*, 1991, **94**, 8083-8088.
264. J. Wang and R. J. Boyd, *The Journal of Chemical Physics*, 1992, **96**, 1232-1239.
265. F. De Proft and P. Geerlings, *Chemical Physics Letters*, 1996, **262**, 782-788.
266. S. Liu and R. G. Parr, *Physical Review A*, 1996, **53**, 2211-2219.
267. J. I. Rodríguez, P. W. Ayers, A. W. Götz and F. L. Castillo-Alvarado, *The Journal of Chemical Physics*, 2009, **131**, 021101.
268. C. F. v. Weizsäcker, *Z. Physik*, 1935, **96**, 431-458.
269. N. H. March, *Physics Letters A*, 1986, **113**, 476-478.
270. M. Levy and O.-Y. Hui, *Physical Review A*, 1988, **38**, 625-629.
271. C. Herring, *Physical Review A*, 1986, **34**, 2614-2631.
272. C. Herring and M. Chopra, *Physical Review A*, 1988, **37**, 31-42.
273. A. Holas and N. H. March, *Physical Review A*, 1991, **44**, 5521-5536.
274. Á. Nagy, *International Journal of Quantum Chemistry*, 2010, **110**, 2117-2120.
275. Q. Zhao and R. G. Parr, *Physical Review A*, 1992, **46**, 2337-2343.
276. V. F. Weisskopf, *Science*, 1975, **187**, 605-612.
277. R. Bader, *Atoms in Molecules: A Quantum Theory*, Clarendon Press: Oxford, U.K., 1994.
278. S. Liu, *The Journal of Chemical Physics*, 2007, **126**, 191107.
279. R. O. Esquivel, S. Liu, J. C. Angulo, J. S. Dehesa, J. Antolín and M. Molina-Espíritu, *The Journal of Physical Chemistry A*, 2011, **115**, 4406-4415.
280. A. D. Becke and K. E. Edgecombe, *The Journal of Chemical Physics*, 1990, **92**, 5397-5403.
281. A. Savin, O. Jepsen, J. Flad, O. K. Andersen, H. Preuss and H. G. von Schnering, *Angewandte Chemie International Edition in English*, 1992, **31**, 187-188.
282. L. N. Shchegoleva, I. V. Beregovaya and P. V. Schastnev, *Chemical Physics Letters*, 1999, **312**, 325-332.
283. P. Garcia-Fernandez, I. B. Bersuker and J. E. Boggs, *Physical Review Letters*, 2006, **96**, 163005.
284. I. Bersuker, in *The Jahn-Teller Effect*, eds. H. Köppel, D. R. Yarkony and H. Barentzen, Springer Berlin Heidelberg, 2009, vol. 97, ch. 1, pp. 3-23.
285. M. Valiev, E. J. Bylaska, N. Govind, K. Kowalski, T. P. Straatsma, H. J. J. Van Dam, D. Wang, J. Nieplocha, E. Apra, T. L. Windus and W. A. de Jong, *Computer Physics Communications*, 2010, **181**, 1477-1489.

286. M. A. Petrukhina and L. T. Scott, *Fragments of Fullerenes and Carbon Nanotubes*, John Wiley & Sons, Inc., 2011.
287. O. A. Shenderova, V. V. Zhirnov and D. W. Brenner, *Critical Reviews in Solid State and Materials Sciences*, 2002, **27**, 227-356.
288. W. E. Barth and R. G. Lawton, *Journal of the American Chemical Society*, 1966, **88**, 380-381.
289. R. G. Lawton and W. E. Barth, *Journal of the American Chemical Society*, 1971, **93**, 1730-1745.
290. M. S. Newman, *Journal of the American Chemical Society*, 1940, **62**, 1683-1687.
291. G. Valenti, C. Bruno, S. Rapino, A. Fiorani, E. A. Jackson, L. T. Scott, F. Paolucci and M. Marcaccio, *The Journal of Physical Chemistry C*, 2010, **114**, 19467-19472.
292. Y.-T. Wu, D. Bandera, R. Maag, A. Linden, K. K. Baldridge and J. S. Siegel, *Journal of the American Chemical Society*, 2008, **130**, 10729-10739.
293. S. Sanyal, A. K. Manna and S. K. Pati, *ChemPhysChem*, 2014, **15**, 885-893.
294. S. Sanyal, A. K. Manna and S. K. Pati, *The Journal of Physical Chemistry C*, 2012, **117**, 825-836.
295. Y. Yoshida, M. Maesato, Y. Kumagai, M. Mizuno, K. Isomura, H. Kishida, M. Izumi, Y. Kubozono, A. Otsuka, H. Yamochi, G. Saito, K. Kirakci, S. Cordier and C. Perrin, *European Journal of Inorganic Chemistry*, 2014, **2014**, 3871-3878.
296. T. Kato and T. Yamabe, *The Journal of Chemical Physics*, 2002, **117**, 2324-2331.
297. A. V. Zabula, S. N. Spisak, A. S. Filatov, V. M. Grigoryants and M. A. Petrukhina, *Chemistry – A European Journal*, 2012, **18**, 6476-6484.
298. D. Schröder, J. Loos, H. Schwarz, R. Thissen, D. V. Preda, L. T. Scott, D. Caraiman, M. V. Frach and D. K. Böhme, *Helvetica Chimica Acta*, 2001, **84**, 1625-1634.
299. J. Janata, J. Gendell, C.-Y. Ling, W. E. Barth, L. Backes, H. B. Mark and R. G. Lawton, *Journal of the American Chemical Society*, 1967, **89**, 3056-3058.
300. H. A. Galué, C. A. Rice, J. D. Steill and J. Oomens, *The Journal of Chemical Physics*, 2011, **134**, 054310.
301. M. G. Townsend and S. I. Weissman, *The Journal of Chemical Physics*, 1960, **32**, 309-310.
302. T. Kato, K. Yoshizawa and T. Yamabe, *Synthetic Metals*, 2001, **119**, 217-218.
303. T. Kato and T. Yamabe, *Chemical Physics Letters*, 2005, **403**, 113-118.
304. T. Kato and K. Hirao, in *Advances in Quantum Chemistry*, Academic Press, 2003, vol. Volume 44, pp. 257-271.
305. M. Breza, *Chemical Physics*, 2003, **291**, 207-212.
306. A. S. Filatov, N. J. Sumner, S. N. Spisak, A. V. Zabula, A. Y. Rogachev and M. A. Petrukhina, *Chemistry – A European Journal*, 2012, **18**, 15753-15760.
307. T. Kato and T. Yamabe, *The Journal of Physical Chemistry A*, 2006, **110**, 2785-2795.
308. T. Sato, A. Yamamoto and H. Tanaka, *Chemical Physics Letters*, 2000, **326**, 573-579.
309. V. Perebeinos, P. B. Allen and M. Pederson, *Phys. Rev. A*, 2005, **72**, 012501.
310. K. Tokunaga, T. Sato and K. Tanaka, *J. Chem. Phys*, 2006, **124**, -.
311. N. Manini, A. Dal Corso, M. Fabrizio and E. Tosatti, *Philosophical Magazine Part B*, 2001, **81**, 793-812.
312. M. Saito, *Phys. Rev. B*, 2002, **65**, 220508.
313. N. Iwahara, T. Sato, K. Tanaka and L. F. Chibotaru, *Phys. Rev. B*, 2010, **82**, 245409.
314. I. D. Hands, J. L. Dunn, C. A. Bates, M. J. Hope, S. R. Meech and D. L. Andrews, *Phys. Rev. B*, 2008, **77**, 115445.
315. O. Gunnarsson, H. Handschuh, P. S. Bechthold, B. Kessler, G. Ganteför and W. Eberhardt, *Phys. Rev. Lett.*, 1995, **74**, 1875-1878.

316. N. Iwahara, T. Sato, K. Tanaka and L. Chibotaru, in *Vibronic Interactions and the Jahn-Teller Effect*, eds. M. Atanasov, C. Daul and P. L. W. Tregenna-Piggott, Springer Netherlands, 2012, vol. 23, ch. 13, pp. 245-264.
317. I. D. Hands, J. L. Dunn and C. A. Bates, *Phys. Rev. B*, 2001, **63**, 245414.
318. T. Kato and T. Yamabe, *J. Chem. Phys*, 2001, **115**, 8592-8602.
319. M. Zlatar, J.-P. Brog, A. Tschannen, M. Gruden-Pavlović and C. Daul, in *Vibronic Interactions and the Jahn-Teller Effect*, eds. M. Atanasov, C. Daul and P. L. W. Tregenna-Piggott, Springer Netherlands, 2012, vol. 23, ch. 2, pp. 25-38.
320. T. Kato, K. Yoshizawa and K. Hirao, *J. Chem. Phys*, 2002, **116**, 3420-3429.
321. T. Kato and T. Yamabe, *J. Chem. Phys*, 2004, **120**, 3311-3322.
322. T. Kato, T. Kambe and Y. Kubozono, *Phys. Rev. Lett.*, 2011, **107**, 077001.
323. M. R. Philpott and Y. Kawazoe, *The Journal of Chemical Physics*, 2012, **137**, 054715.
324. J. Oscar, C. Jimenez-Halla, E. Matito, J. Robles and M. Sola, *Journal of Organometallic Chemistry*, 2006, **691**, 4359–4366.
325. A. D. Becke, *The Journal of Chemical Physics*, 1986, **84**, 4524-4529.
326. M. J. Frisch, G. W. Trucks, H. B. Schlegel, G. E. Scuseria, M. A. Robb, J. R. Cheeseman, G. Scalmani, V. Barone, B. Mennucci, G. A. Petersson, H. Nakatsuji, M. Caricato, X. Li, H. P. Hratchian, A. F. Izmaylov, J. Bloino, G. Zheng, J. L. Sonnenberg, M. Hada, M. Ehara, K. Toyota, R. Fukuda, J. Hasegawa, M. Ishida, T. Nakajima, Y. Honda, O. Kitao, H. Nakai, T. Vreven, J. Montgomery, J. A., J. E. Peralta, F. Ogliaro, M. Bearpark, J. J. Heyd, E. Brothers, K. N. Kudin, V. N. Staroverov, R. Kobayashi, J. Normand, K. Raghavachari, A. Rendell, J. C. Burant, S. S. Iyengar, J. Tomasi, M. Cossi, N. Rega, N. J. Millam, M. Klene, J. E. Knox, J. B. Cross, V. Bakken, C. Adamo, J. Jaramillo, R. Gomperts, R. E. Stratmann, O. Yazyev, A. J. Austin, R. Cammi, C. Pomelli, J. W. Ochterski, R. L. Martin, K. Morokuma, V. G. Zakrzewski, G. A. Voth, P. Salvador, J. J. Dannenberg, S. Dapprich, A. D. Daniels, Ö. Farkas, J. B. Foresman, J. V. Ortiz, J. Cioslowski and D. J. Fox, *Gaussian 09, Revision A.1*, Gaussian, Inc., Wallingford CT, 2009.
327. K. Wolinski, J. F. Hinton and P. Pulay, *Journal of the American Chemical Society*, 1990, **112**, 8251-8260.
328. R. E. Dinnebier, U. Behrens and F. Olbrich, *Organometallics*, 1997, **16**, 3855-3858.
329. N. Mohammadi, A. Ganesan, C. T. Chantler and F. Wang, *Journal of Organometallic Chemistry*, 2012, **713**, 51-59.
330. H. Koch, P. Jørgensen and T. Helgaker, *The Journal of Chemical Physics*, 1996, **104**, 9528-9530.
331. U. Hohm, D. Goebel and S. Grimme, *Chemical Physics Letters*, 1997, **272**, 328-334.
332. K. Pierloot, B. J. Persson and B. O. Roos, *The Journal of Physical Chemistry*, 1995, **99**, 3465-3472.
333. M. Swart, *Inorganica Chimica Acta*, 2007, **360**, 179-189.
334. E. A. Seibold and L. E. Sutton, *The Journal of Chemical Physics*, 1955, **23**, 1967-1967.
335. T. M. Krygowski and M. K. Cyrański, *Chemical Reviews*, 2001, **101**, 1385-1420.
336. V. Y. Lee and A. Sekiguchi, *Angewandte Chemie International Edition*, 2007, **46**, 6596-6620.
337. H. Jiao, P. v. R. Schleyer, Y. Mo, M. A. McAllister and T. T. Tidwell, *Journal of the American Chemical Society*, 1997, **119**, 7075-7083.
338. L. Nyulászi and P. v. R. Schleyer, *Journal of the American Chemical Society*, 1999, **121**, 6872-6875.
339. M. Laskoski, W. Steffen, M. D. Smith and U. H. F. Bunz, *Chemical Communications*, 2001, DOI: 10.1039/B009696M, 691-692.

340. D. E. Bean, P. W. Fowler and M. J. Morris, *Journal of Organometallic Chemistry*, 2011, **696**, 2093-2100.
341. T. N. Gribanov, R. M. Minyaev and V. I. Minkin, *The Open Organic Chemistry Journal*, 2011, **5**, 62-78.
342. M. Y. Antipin, R. Boese, N. Augart and G. Schmid, *Struct Chem*, 1993, **4**, 91-101.
343. J. P. Perdew, J. A. Chevary, S. H. Vosko, K. A. Jackson, M. R. Pederson, D. J. Singh and C. Fiolhais, *Physical Review B*, 1992, **46**, 6671-6687.
344. M. Swart, *Chemical Physics Letters*, 2013, **580**, 166-171.
345. A. Hirsch, Z. Chen and H. Jiao, *Angewandte Chemie International Edition*, 2000, **39**, 3915-3917.
346. A. Hirsch, Z. Chen and H. Jiao, *Angewandte Chemie International Edition*, 2001, **40**, 2834-2838.
347. Z. Chen, H. Jiao, A. Hirsch and W. Thiel, *J Mol Model*, 2001, **7**, 161-163.
348. J. Poater and M. Sola, *Chemical Communications*, 2011, **47**, 11647-11649.
349. M. Bühl and A. Hirsch, *Chemical Reviews*, 2001, **101**, 1153-1184.
350. D. E. Bean, J. T. Muya, P. W. Fowler, M. T. Nguyen and A. Ceulemans, *Physical Chemistry Chemical Physics*, 2011, **13**, 20855-20862.
351. H. Jiao and P. v. R. Schleyer, *Angewandte Chemie International Edition in English*, 1996, **35**, 2383-2386.
352. E. Kleinpeter, S. Klod and A. Koch, *The Journal of Organic Chemistry*, 2008, **73**, 1498-1507.
353. M. Bühl, S. Patchkovskii and W. Thiel, *Chemical Physics Letters*, 1997, **275**, 14-18.
354. M. Bühl and W. Thiel, *Chemical Physics Letters*, 1995, **233**, 585-589.
355. E. Shabtai, A. Weitz, R. C. Haddon, R. E. Hoffman, M. Rabinovitz, A. Khong, R. J. Cross, M. Saunders, P.-C. Cheng and L. T. Scott, *Journal of the American Chemical Society*, 1998, **120**, 6389-6393.
356. M. Saunders, R. J. Cross, H. A. Jiménez-Vázquez, R. Shimshi and A. Khong, *Science*, 1996, **271**, 1693-1697.
357. M. Saunders, H. A. Jimenez-Vazquez, R. J. Cross, W. E. Billups, C. Gesenberg, A. Gonzalez, W. Luo, R. C. Haddon, F. Diederich and A. Herrmann, *Journal of the American Chemical Society*, 1995, **117**, 9305-9308.
358. M. Saunders, H. A. Jimenez-Vazquez, B. W. Bangerter, R. J. Cross, S. Mroczkowski, D. I. Freedberg and F. A. L. Anet, *Journal of the American Chemical Society*, 1994, **116**, 3621-3622.
359. M. Saunders, H. A. Jimenez-Vazquez, R. J. Cross, S. Mroczkowski, D. I. Freedberg and F. A. L. Anet, *Nature*, 1994, **367**, 256-258.
360. M. P. Johansson, J. Jusélius and D. Sundholm, *Angewandte Chemie International Edition*, 2005, **44**, 1843-1846.
361. R. Zanasi and P. W. Fowler, *Chemical Physics Letters*, 1995, **238**, 270-280.
362. A. Ceulemans and P. W. Fowler, *The Journal of Chemical Physics*, 1990, **93**, 1221-1234.
363. A. I. Boldyrev and L.-S. Wang, *Chemical Reviews*, 2005, **105**, 3716-3757.
364. C. A. Tsipis, *Coordination Chemistry Reviews*, 2005, **249**, 2740–2762.
365. D. Y. Zubarev, B. B. Averkiev, H.-J. Zhai, L.-S. Wang and A. I. Boldyrev, *Physical Chemistry Chemical Physics*, 2008, **10**, 257−267.
366. T. R. Galeev and A. I. Boldyrev, *Annual Reports on the Progress of Chemistry, Section C: Physical Chemistry*, 2011, **107**, 124-147.
367. D. Y. Zubarev and A. I. Boldyrev, in *Science and Technology of Atomic, Molecular, Condensed Matter & Biological Systems*, eds. P. Jena and A. W. Castleman, Elsevier, 2010, vol. 1, ch. 5, pp. 219-267.

368. X. Li, A. E. Kuznetsov, H.-F. Zhang, A. I. Boldyrev and L.-S. Wang, *Science*, 2001, **291**, 859-861.
369. A. E. Kuznetsov, A. I. Boldyrev, X. Li and L.-S. Wang, *Journal of the American Chemical Society*, 2001, **123**, 8825–8831.
370. A. N. Alexandrova, A. I. Boldyrev, H.-J. Zhai and L. S. Wang, *Coordination Chemistry Reviews*, 2006, **250**, 2811-2866.
371. R. W. A. Havenith, P. W. Fowler, E. Steiner, S. Shetty, D. Kanhere and S. Pal, *Physical Chemistry Chemical Physics*, 2004, **6**, 285–288.
372. D. Y. Zubarev and A. I. Boldyrev, *Physical Chemistry Chemical Physics*, 2008, **10**, 5207–5217.
373. S. C. Critchlow and J. D. Corbett, *Inorganic Chemistry*, 1984, **23**, 770-774.
374. F. Kraus, T. Hanauer and N. Korber, *Inorganic Chemistry*, 2006, **45**, 1117-1123.
375. N. Korber and M. Reil, *Chemical Communications*, 2002, **108**, 84-85.
376. O. J. Scherer, J. Vondung and G. Wolmershäuse, *Journal of Organometallic Chemistry*, 1989, **376**, C35-C38.
377. W. G. Xu and B. Jin, *Computational and Theoretical Chemistry*, 2005, **731**, 61–66.
378. L.-S. Wang, B. Niu, Y. T. Lee, D. A. Shirley, E. Ghelichkhani and E. R. Grant, *The Journal of Chemical Physics*, 1990, **93**, 6318-6326.
379. T. P. Lippa, S. J. Xu, S. A. Lyapustina, J. M. Nilles and K. H. Bowen, *The Journal of Chemical Physics*, 1998, **109**, 10727-10731.
380. T. Baruah, M. R. Pederson, R. R. Zope and M. R. Beltran, *Chemical Physics Letters*, 2004, **387**, 476–480.
381. Y. Zhao, W. Xu, Q. Li, Y. Xie and H. F. Schaefer, *J. Comput. Chem.*, 2004, **25**, 907-920.
382. G. Liang, Q. Wu and J. Yang, *The Journal of Physical Chemistry A*, 2011, **115**, 8302–8309.
383. X. Zhou, J. Zhao, X. Chen and W. Lu, *Physical Review A, Atomic, Molecular and Optical Physics*, 2005, **72**, 053203-053208.
384. A. C. Tsipis, I. G. Depastas, E. E. Karagiannis and C. A. Tsipis, *Journal of Computational Chemistry*, 2010, **31**, 431–446.
385. D. Y. Zubarev and A. I. Boldyrev, *The Journal of Physical Chemistry A*, 2008, **112**, 7984–7985.
386. T. Lu and F. Chen, *Journal of Computational Chemistry*, 2012, **33**, 580-592.
387. J. B. Birks, *Reports on Progress in Physics*, 1975, **38**, 903.
388. A. Waldman and S. Ruhman, *Chemical Physics Letters*, 1993, **215**, 470.
389. T. Hirata, H. Ikeda and H. Saigusa, *The Journal of Physical Chemistry A*, 1999, **103**, 1014.
390. H. Saigusa, M. Morohoshi and S. Tsuchiya, *The Journal of Physical Chemistry A*, 2001, **105**, 7334.
391. K. Law, M. Schauer and E. R. Bernstein, *The Journal of Chemical Physics*, 1984, **81**, 4871.
392. N. Nakashima, M. Sumitani, I. Ohmine and K. Yoshihara, *The Journal of Chemical Physics*, 1980, **72**, 2226.
393. J. T. Richards and J. K. Thomas, *Chemical Physics Letters*, 1970, **5**, 527.
394. R. Bonneau, R. Josset-Dubien and R. Bensasson, *Chemical Physics Letters*, 1969, **3**, 353.
395. R. Cooper and J. K. Thomas, *The Journal of Chemical Physics*, 1968, **48**, 5097.
396. J. B. Hopkins, D. E. Powers and R. E. Smalley, *The Journal of Physical Chemistry*, 1981, **85**, 3739.
397. A. Dreuw and M. Head-Gordon, *Chemical Reviews*, 2005, **105**, 4009–4037.

398. A. Dreuw and M. Head-Gordon, *Chemical Physics Letters*, 2006, **426**, 231.
399. J. Gaus and J. F. Stanton, *The Journal of Physical Chemistry A*, 2000, **104**, 2865.
400. A. Hiraya and K. Shobatake, *The Journal of Chemical Physics*, 1991, **94**, 7700.
401. N. Nakashima, H. Inoue, M. Sumitani and K. Yoshihara, *The Journal of Chemical Physics*, 1980, **73**, 5976.
402. J. P. Doering, *The Journal of Chemical Physics*, 1969, **51**, 2866.
403. R. Astier and Y. H. Meyer, *Chemical Physics Letters*, 1969, **3**, 399.
404. E. N. Lassettre, A. Skerbele, M. A. Dillon and K. J. Ross, *The Journal of Chemical Physics*, 1968, **48**, 5066.
405. T. Hashimoto, H. Nakano and K. Hirao, *The Journal of Chemical Physics*, 1996, **104**, 6244.
406. T. Hashimoto, H. Nakano and K. Hirao, *Journal of Molecular Structure: THEOCHEM*, 1998, **451**, 25-33.
407. C. Adamo, G. E. Scuseria and V. Barone, *Journal of Chemical Physics*, 1999, **111**, 2889.
408. M. Schreiber, M. R. Silva-Junior, S. P. A. Sauer and W. Thiel, *The Journal of Chemical Physics*, 2008, **128**, 134110.
409. K. Diri and A. I. Krylov, *The Journal of Physical Chemistry A*, 2012, **116**, 653.
410. R. F. Fink, J. Pfister, H. M. Zhao and B. Engels, *Chemical Physics*, 2008, **346**, 275–285.
411. M. Nooijen, *Spectrochimica Acta Part A*, 1999, **55**, 539.
412. T. C. Dinadayalane and L. J., *Struct Chem*, 2009, **20**, 11-20.
413. P. Hobza, V. Spirko, H. L. Selzle and E. W. Schlag, *The Journal of Physical Chemistry A*, 1998, **102**, 2501.
414. T. Rocha-Rinza, L. D. Vico, V. Veryazov and B. O. Roos, *Chemical Physics Letters*, 2006, **426**, 268272.
415. P. García-Fernández, Y. Liu, I. B. Bersuker and J. E. Boggs, *Physical Chemistry Chemical Physics*, 2011, **13**, 3502-3513.
416. S. Grimme, S. Ehrlich and L. Goerigk, *Journal of Computational Chemistry*, 2011, **32**, 1457.
417. J. P. Perdew, A. Ruzsinszky, G. I. Csonka, O. A. Vydrov and G. E. Scuseria, *Physical Review Letters*, 2008, **100**, 136406.
418. O. V. Gritsenko, P. R. T. Schipper and E. J. Baerends, *Chemical Physics Letters*, 1999, **302**, 199.
419. P. R. T. Schipper, O. V. Gritsenko, S. J. A. van Gisbergen and E. J. Baerends, *The Journal of Chemical Physics*, 2000, **112**, 1344.
420. S. Grimme, *Journal of Computational Chemistry*, 2004, **25**, 1463.
421. M. Ernzerhof and G. Scuseria, *The Journal of Chemical Physics*, 1999, **10**, 5029.
422. M. Swart, *Journal of Chemical Theory and Computation*, 2008, **4**, 2057-2066.
423. M. Gruden-Pavlović, M. Zlatar, C.-W. Schläpfer and C. Daul, *Theochem. J. Mol. Struct.*, 2010, **954**, 80-85.
424. M. Zlatar, M. Gruden-Pavlovic, M. Guell and M. Swart, *Phys. Chem. Chem. Phys.*, 2013, **15**, 6631-6639.

Biography

Ljubica Anđelković (born in 1983, Kraljevo) finished elementary and high school in Vrnjačka Banja. She graduated in 2008 at the Faculty of Chemistry, University of Belgrade, at study program Chemistry. She finished master studies at the Faculty of Chemistry, University of Belgrade in 2009, and in the same year she started the PhD studies. She was employed as a research trainee at the Center for Chemistry of the Institute of Chemistry, Technology and Metallurgy in Belgrade at the end of 2009. She became a research associate in 2012 at the same institution. She is also associate of the Regional Center for talents "Mihajlo Pupin" in Pančevo since 2012. She is a member of the Serbian Chemical Society. She is coauthor on 10 scientific papers.

List of scientific papers that are part of the doctoral dissertation:

1. **Andjelković, Lj.**; Gruden-Pavlović, M. Zlatar, M. *Density functional theory study of the multimode Jahn-Teller problem in the open-shell corannulenes and coronenes.* Chemical Physics **2015**, 460, 64-74.
2. **Andjelković, Lj.**; Perić, M.; Zlatar, M.; Gruden-Pavlović, M. *Nucleus-independent chemical shift profiles along the Intrinsic Distortion Path for Jahn-Teller active molecules. Study on cyclopentadienyl radical and cobaltocene.* Journal of the Serbian Chemical Society **2015,** 80, 877-888.
3. Perić, M.; **Andjelković, Lj.**; Zlatar, M.; Daul, C.; Gruden-Pavlović, M. *DFT investigation of the influence of Jahn–Teller distortion on the aromaticity in square-planar arsenic and antimony clusters.* Polyhedron **2014**, 80, 69-80.
4. García-Fernández, P.; **Andjelković, Lj.**; Zlatar, M.; Gruden-Pavlović, M.; Dreuw, A. *A simple monomer-based model-Hamiltonian approach to combine excitonic coupling and Jahn-Teller theory***.** Journal of Chemical Physics **2013**, 139, 174101.
5. **Andjelković, Lj.**; Gruden-Pavlović, M.; Daul, C.; Zlatar, M. *The Choice of the Exchange-Correlation Functional for the Determination of the Jahn–Teller Parameters by the Density Functional Theory.* International Journal of Quantum Chemistry **2013**, 113, 859–864.

6. Perić, M.; **Andjelković, Lj.**; Zlatar, M.; Nikolić, A. S.; Daul, C.; Gruden-Pavlović, M.; *Spherical aromaticity of Jahn–Teller active fullerene ions.* Monatshefte fur Chemie **2013**, 144, 817-823.
7. **Andjelković, Lj.**; Perić, M.; Zlatar, M.; Grubišić, S.; Gruden-Pavlović, M. *Magnetic criteria of aromaticity in a benzene cation and anion: how does the Jahn–Teller effect influence the aromaticity?* Tetrahedron Letters **2012**, 53, 794–799.
8. Gruden-Pavlović, M.; García-Fernández, P.; **Andjelković, Lj.**; Daul, C.; Zlatar, M. *Treatment of the Multimode Jahn–Teller Problem in Small Aromatic Radicals.* Journal of Physical Chemistry A **2011**, 115, 10801–10813.

Biografija

Ljubica Anđelković (rođ. 1983. godine u Kraljevu) završila je osnovnu školu i gimnaziju u Vrnjačkoj Banji. Diplomirala je 2008. godine na Hemijskom fakultetu Univerziteta u Beogradu, na smeru Hemija. Završila je master studije na Hemijskom fakultetu Univerziteta u Beogradu 2009. godine, a iste godine je upisala i doktorske studije. Zaposlila se kao istraživač-pripravnik pri Centru za hemiju Instituta za hemiju, tehnologiju i metalurgiju u Beogradu, krajem 2009. godine. 2012. godine izabrana je u zvanje istraživač-saradnik. Saradnik je Regionalnog centra za talente "Mihajlo Pupin" iz Pančeva od 2012. godine. Član je Srpskog hemijskog društva. Koautor je na 10 naučnih radova.

Spisak naučnih radova koji čine deo doktorske disertacije:

1. **Andjelković, Lj.**; Gruden-Pavlović, M. Zlatar, M. *Density functional theory study of the multimode Jahn-Teller problem in the open-shell corannulenes and coronenes.* Chemical Physics **2015**, 460, 64-74.
2. **Andjelković, Lj.**; Perić, M.; Zlatar, M.; Gruden-Pavlović, M. *Nucleus-independent chemical shift profiles along the Intrinsic Distortion Path for Jahn-Teller active molecules. Study on cyclopentadienyl radical and cobaltocene.* Journal of the Serbian Chemical Society **2015,** 80, 877-888.
3. Perić, M.; **Andjelković, Lj.**; Zlatar, M.; Daul, C.; Gruden-Pavlović, M. *DFT investigation of the influence of Jahn–Teller distortion on the aromaticity in square-planar arsenic and antimony clusters.* Polyhedron **2014**, 80, 69-80.
4. García-Fernández, P.; **Andjelković, Lj.**; Zlatar, M.; Gruden-Pavlović, M.; Dreuw, A. *A simple monomer-based model-Hamiltonian approach to combine excitonic coupling and Jahn-Teller theory***.** Journal of Chemical Physics **2013**, 139, 174101.
5. **Andjelković, Lj.**; Gruden-Pavlović, M.; Daul, C.; Zlatar, M. *The Choice of the Exchange-Correlation Functional for the Determination of the Jahn–Teller Parameters by the Density Functional Theory.* International Journal of Quantum Chemistry **2013**, 113, 859–864.

6. Perić, M.; **Andjelković, Lj.**; Zlatar, M.; Nikolić, A. S.; Daul, C.; Gruden-Pavlović, M.; *Spherical aromaticity of Jahn–Teller active fullerene ions.* Monatshefte fur Chemie **2013**, 144, 817-823.
7. **Andjelković, Lj.**; Perić, M.; Zlatar, M.; Grubišić, S.; Gruden-Pavlović, M. *Magnetic criteria of aromaticity in a benzene cation and anion: how does the Jahn–Teller effect influence the aromaticity?* Tetrahedron Letters **2012**, 53, 794–799.
8. Gruden-Pavlović, M.; García-Fernández, P.; **Andjelković, Lj.**; Daul, C.; Zlatar, M. *Treatment of the Multimode Jahn–Teller Problem in Small Aromatic Radicals.* Journal of Physical Chemistry A **2011**, 115, 10801–10813.

Прилог 1.

Изјава о ауторству

Потписани-а Љубица Анђелковић

број индекса ДХ26/2009

Изјављујем

да је докторска дисертација под насловом

Theoretical investigation of the Jahn-Teller effect and the influence of the Jahn-Teller distortion on the properties of chemical systems (Teorijsko proučavanje *Jahn-Teller*-ovog efekta i njegovog uticaja na osobine hemijskih sistema)

- резултат сопственог истраживачког рада,
- да предложена дисертација у целини ни у деловима није била предложена за добијање било које дипломе према студијским програмима других високошколских установа,
- да су резултати коректно наведени и
- да нисам кршио/ла ауторска права и користио интелектуалну својину других лица.

Потпис докторанда

У Београду, _____

_____

Прилог 2.

Изјава о истоветности штампане и електронске верзије докторског рада

Име и презиме аутора Љубица Анђелковић

Број индекса ДХ26/2009

Студијски програм Доктор хемијских наука

Наслов рада: Theoretical investigation of the Jahn-Teller effect and the influence of the Jahn-Teller distortion on the properties of chemical systems (Teorijsko proučavanje *Jahn-Teller*-ovog efekta i njegovog uticaja na osobine hemijskih sistema)

Ментори др Маја Груден-Павловић, ванредни професор Хемијског факултета Универзитета у Београду и др Матија Златар, научни сарадник при Центру за хемију, Института за Хемију, Технологију и Металургију, Универзитет у Београду

Потписани/а _____

Изјављујем да је штампана верзија мог докторског рада истоветна електронској верзији коју сам предао/ла за објављивање на порталу **Дигиталног репозиторијума Универзитета у Београду.**

Дозвољавам да се објаве моји лични подаци везани за добијање академског звања доктора наука, као што су име и презиме, година и место рођења и датум одбране рада.

Ови лични подаци могу се објавити на мрежним страницама дигиталне библиотеке, у електронском каталогу и у публикацијама Универзитета у Београду.

Потпис докторанда

У Београду, _____

_____

Прилог 3.

Изјава о коришћењу

Овлашћујем Универзитетску библиотеку „Светозар Марковић“ да у Дигитални репозиторијум Универзитета у Београду унесе моју докторску дисертацију под насловом:

Theoretical investigation of the Jahn-Teller effect and the influence of the Jahn-Teller distortion on the properties of chemical systems (Teorijsko proučavanje *Jahn-Teller*-ovog efekta i njegovog uticaja na osobine hemijskih sistema)

која је моје ауторско дело.

Дисертацију са свим прилозима предао/ла сам у електронском формату погодном за трајно архивирање.

Моју докторску дисертацију похрањену у Дигитални репозиторијум Универзитета у Београду могу да користе сви који поштују одредбе садржане у одабраном типу лиценце Креативне заједнице (Creative Commons) за коју сам се одлучио/ла.

1. Ауторство

2. Ауторство - некомерцијално

3. Ауторство – некомерцијално – без прераде

4. Ауторство – некомерцијално – делити под истим условима

5. Ауторство – без прераде

6. Ауторство – делити под истим условима

(Молимо да заокружите само једну од шест понуђених лиценци, кратак опис лиценци дат је на полеђини листа).

Потпис докторанда

У Београду, _____

_____

1. Ауторство - Дозвољавате умножавање, дистрибуцију и јавно саопштавање дела, и прераде, ако се наведе име аутора на начин одређен од стране аутора или даваоца лиценце, чак и у комерцијалне сврхе. Ово је најслободнија од свих лиценци.

2. Ауторство – некомерцијално. Дозвољавате умножавање, дистрибуцију и јавно саопштавање дела, и прераде, ако се наведе име аутора на начин одређен од стране аутора или даваоца лиценце. Ова лиценца не дозвољава комерцијалну употребу дела.

3. Ауторство - некомерцијално – без прераде. Дозвољавате умножавање, дистрибуцију и јавно саопштавање дела, без промена, преобликовања или употребе дела у свом делу, ако се наведе име аутора на начин одређен од стране аутора или даваоца лиценце. Ова лиценца не дозвољава комерцијалну употребу дела. У односу на све остале лиценце, овом лиценцом се ограничава највећи обим права коришћења дела.

4. Ауторство - некомерцијално – делити под истим условима. Дозвољавате умножавање, дистрибуцију и јавно саопштавање дела, и прераде, ако се наведе име аутора на начин одређен од стране аутора или даваоца лиценце и ако се прерада дистрибуира под истом или сличном лиценцом. Ова лиценца не дозвољава комерцијалну употребу дела и прерада.

5. Ауторство – без прераде. Дозвољавате умножавање, дистрибуцију и јавно саопштавање дела, без промена, преобликовања или употребе дела у свом делу, ако се наведе име аутора на начин одређен од стране аутора или даваоца лиценце. Ова лиценца дозвољава комерцијалну употребу дела.

6. Ауторство - делити под истим условима. Дозвољавате умножавање, дистрибуцију и јавно саопштавање дела, и прераде, ако се наведе име аутора на начин одређен од стране аутора или даваоца лиценце и ако се прерада дистрибуира под истом или сличном лиценцом. Ова лиценца дозвољава комерцијалну употребу дела и прерада. Слична је софтверским лиценцама, односно лиценцама отвореног кода.